Qualitative and Quantitative Imaging in Electromagnetic Inverse Scattering Theory

Sun, Shilong

DOI
10.4233/uuid:edf396c5-5c3a-4b5c-9fc4-b8bb5ff6eeee

Publication date
2017

Document Version
Final published version

Citation (APA)
Sun, S. (2017). *Qualitative and Quantitative Imaging in Electromagnetic Inverse Scattering Theory*. [Dissertation (TU Delft), Delft University of Technology]. https://doi.org/10.4233/uuid:edf396c5-5c3a-4b5c-9fc4-b8bb5ff6eeee

Qualitative and Quantitative Imaging in Electromagnetic Inverse Scattering Theory

QUALITATIVE AND QUANTITATIVE IMAGING IN ELECTROMAGNETIC INVERSE SCATTERING THEORY

Proefschrift

ter verkrijging van de graad van doctor
aan de Technische Universiteit Delft,
op gezag van de Rector Magnificus prof. dr. ir. T. H. J. J. van der Hagen,
voorzitter van het College voor Promoties,
in het openbaar te verdedigen op vrijdag 2 februari 2018 om 10:00 uur

door

Shilong SUN

Master of Science in Information and Communication Engineering
National University of Defense Technology, China,
geboren te Zhangqiu, Shandong, China.

Dit proefschrift is goedgekeurd door de

promotor: prof. dr. A. G. Yarovoy
copromotor: dr. ir. B. J. Kooij

Samenstelling promotiecommissie:

Rector Magnificus	voorzitter
Prof. dr. A. G. Yarovoy	Technische Universiteit Delft
Dr. ir. B. J. Kooij	Technische Universiteit Delft
Onafhankelijke leden:	
Prof. ir. F. le Chevalier	Technische Universiteit Delft
Prof. dr. ir. E. C. Slob	Technische Universiteit Delft
Prof. dr. ir. C. P. A. Wapenaar	Technische Universiteit Delft
Prof. dr. T. Isernia	Università Mediterranea di Reggio Calabria
Prof. dr. C. Pichot	Université Nice Sophia Antipolis

This research was financially supported by the China Scholarship Council and the EEMCS faculty of Delft University of Technology.

ISBN 978-94-028-0912-1
PhD Dissertation, Delft University of Technology.

An electronic version of this dissertation is available at
http://repository.tudelft.nl/.

Dedicated to my family

CONTENTS

LIST OF FIGURES

LIST OF TABLES

1

INTRODUCTION

We live in a world full of waves, such as acoustic waves, ElectroMagnetic (EM) waves, even the newly detected gravitational waves. The full grasp of the fundamentals governing the propagation of the variant waves and the effective perception and interpretation of them have greatly extended the capability of human beings to unfold the mysteries of the world from the micro-scale of an atom to the macro-scale of the whole cosmos. Among all probing techniques, imaging science plays an important role in human's historical discoveries.

Knowing the principles of the wave propagation, it is possible to exactly determine how waves are scattered based on relevant properties of the scatterer. However, due to many reasons, such as the incompleteness of the measurement data and the inherent ill-posedness, it is intractable to exactly determine the characteristics of an object based on the collected data of how it scatters incident waves. The former problem is referred to as direct scattering problem, and, in the contrary, the latter one is referred to as inverse scattering problem. In essence, imaging is a procedure of reconstructing the scatterer's shape using different probing substances, such as acoustic fields, EM fields, neutrons, etc. As it is too comprehensive to give a complete account of imaging science in a thesis of a few hundred pages, efforts have been made in this thesis for the investigation of the EM inverse scattering problem in the framework of classical scattering theory (as opposed to quantum scattering theory).

The characteristics of EM scattering are dependent on the ratio of the targets' dimensions to the wavelength of the incident wave and are ultimately determined by Maxwell's equations. In general, the frequency dependence can be categorized into three overall regions: the Rayleigh region, the resonance region, and the optical region. One way of defining these regions in terms of wavelength, λ, and the maximum body dimension, L, is as follows [2]:

- Rayleigh or low-frequency region — The wavelength is large compared to the target dimension ($L/\lambda \ll 1$);

- Resonance region — The wavelength is on the same order as the target dimensions ($0.5 < L/\lambda < 10$);
- Optical or high-frequency region — The wavelength is much smaller than the target dimensions ($L/\lambda > 10$).

In the Rayleigh region, since the wavelength is much larger than the body size, there is essentially no variation in phase of the incident wave over the scattering body; all portions of the target are exposed to the same incident field level (magnitude and phase) at the same time. Except for the temporal variations, this is almost the same as a statics problem and is commonly referred to as a quasi-static problem. This static approximation was recognized by Rayleigh. The quasi-static locally incident field causes the charge on the body to polarize to the two ends of the body creating a dipole moment. The strength of this induced dipole moment is a function of the size of the body relative to the vector direction of the incident field. The scattered field is then proportional to this dipole moment and to the square of the frequency. In the optical or high-frequency scattering region, the scattering is not a result of the field interacting with the total body, while it is more useful to think of the scattering as coming from a collection of independent scattering edges and shadow boundaries based on the linear physical optics approximation. The inverse scattering problem we discussed herein is the one with frequencies in the resonance region, which turns out to be nonlinear and improperly posed [3]. It is nonlinear because, given the incident field and the measurement data of the scattered fields, both the total fields and the dielectric parameters of the region under test are the unknowns, and the former are functions of the latter; It is improperly posed because the scattering operator is compact and the inverse of a compact operator cannot be continuous for both single-view problem and multi-view problem [4].

The aim of research in this thesis is to retrieve not only the morphological information but also the dielectric parameters of the targets using EM fields. The former is referred to as qualitative imaging, and the latter is referred to as quantitative imaging. Quantitative imaging is of much more importance for identifying the targets in the applications of non-destructive detection, such as Ground Penetrating Radar (GPR) [5], Through-the-Wall Imaging (TWI) [6], seismic exploration [7–10], and etc. As pointed out in [11] concerning the problem of locating unexploded ordinance, "Target identification is the great unsolved problem. We detect almost everything, we identify nothing." One more advantage of this imaging technique is the safety and security when applied to a human body. In the field of medical diagnosis, the use of traditional X-ray systems is limited to the sensitive group of patients due to the high doses of ionizing radiation. For security application, the use of ionizing radiation is prohibited in the passengers scanning devices at airport or railway station due to safety concerns. In the contrary, imaging equipment using the microwave frequency (< 300 GHz) is less physically detrimental on human bodies due to its safe level of radiation, and could be widely used for assisting the present medical imaging devices, such as Computed Tomography (CT) and Magnetic Resonance Imaging (MRI), and the surveillance tools for various security purposes, such as Concealed Weapon Detection (CWD).

In this thesis, imaging techniques are developed using EM field data in the frequency

domain, in which we do not consider the assumptions of plane waves, far-field pattern, or weak scattering phenomenon throughout all chapters. The EM scattering is numerically modeled by means of the Finite Difference Frequency Domain (FDFD) method, resulting in a versatile applicability of the proposed imaging techniques to not only far-field but also intermediate and near-field imaging problems of both 2-Dimensional (2-D) and 3-Dimensional (3-D) cases. More generally, it is also straightforward to apply the inversion theory proposed herein to acoustic inverse scattering problems governed by the Helmholtz Equation, which highly resembles the Transverse Magnetic (TM) case of the EM inverse scattering problem.

1.1 RESEARCH OBJECTIVE

Recent developments in the field of inverse scattering problems are mainly focused on the aspects of improving the computational efficiency (such as the study on linear model and approach [12–14], and multi-resolution methods [15–19]), incorporation of *a priori* information [20–23], and calibration to the real antenna radiating pattern especially in near-field scenarios [24–26]. Specifically in this thesis, the main research objectives can be primarily stated as the following:

1. To improve the robustness of the inversion methods based on the nonlinear optimization techniques.
2. To develop a linear qualitative imaging approach which is able to efficiently retrieve the morphology of the scatterers with higher resolution.
3. To develop an quantitative imaging method which is able to provide 3-D inversion image with acceptable computational complexity.
4. To utilize the frequency diversity in the proposed imaging methods for achieving better inversion performance.
5. To verify the proposed qualitative and quantitative imaging techniques with experimental data.

Calibration to the real antenna radiating pattern will not be considered in this thesis. For processing the experimental data, the incident fields are modelled approximately in accordance with the antennas pattern, and the amplitude and phase are calibrated using the measurement data of the incident fields.

1.2 CHALLENGES AND APPROACHES

The challenges of dealing with the inverse scattering problems arise from two aspects: technical issues and theoretical issues. The former concerns the design of the imaging system. One key issue when dealing with the inverse scattering problems is to ensure

that the scattered field contains a sufficient amount of information about the targets. Normally, more useful information is sought by exploitation of the angular diversity of the incident/scattered fields. However, it is limited in some special configurations, for instance, the half space configuration where the inversion domain can only be illuminated by incident waves coming from one side and the scattered field data can only be collected at the same side. Another challenge is that, since the scattered field measurement data are normally extracted by subtracting the incident field (the measurements without targets) from the total field (the measurements in the presence of targets), the main difficulty encountered with weak scatterers is the low level of the signal of interest in comparison with the measured field level. Any variations between the two measurements can therefore completely disrupt the scattered field measurements. In addition, to be able to realize quantitative inversion, i.e., reconstructions where the shape of the target is not the only information extracted, but the dielectric characteristics are also of interest, quantitative values of the fields, as well as the modelling of the incident fields, are required. An accurate calibration procedure has therefore to be applied.

In summary, the system design required by the quantitative inversion is of much higher intricacy in comparison to the EM imaging system operated with frequencies in the optical region, and the latter is out of the scope of this thesis.

The research work of this thesis has been mainly focused on theoretical issues. As mentioned previously, solving the inverse scattering problem is full of challenges due to both non-linearity and ill-posedness. Most of the existing iterative methods are local optimization techniques, which are inherently prone to the occurrence of false solutions [27]. For quantitative imaging, the total fields are required to be updated while recovering the dielectric parameters of the scatterers. As a result, the inversion procedure can be very time consuming when it comes to large-scale inversion domain. In such cases, high performance computer and parallel computing technique are needed to do the full inversion. Global optimization techniques [19, 28, 29] perform better in avoiding the occurrence of local minima. However, it is still intractable due to the huge computational complexity in real applications. Weak scattering approximations enable us to linearize the inverse problem and achieve faster convergence. However, the applicability is very limited when considering large contrast scenarios and/or large electric size of the scatterer. An alternative is attempting the direct estimation of the contrast source that is defined as the multiplication of the contrast and the total fields. In doing so, a linearization of the inverse scattering problem is achieved. However, the inversion accuracy and robustness of this approach are very poor due to the severe inherent ill-posedness. Therefore, regularization methods are required for ensuring a stable, approximate solution. Another challenge is the estimation of the noise level, which is equivalent with the termination criterion in the iterative inversion methods or the determination of the regularization parameter.

To deal with the aforementioned problems, we have considered the following approaches in this thesis:

- The direct scattering is modeled by means of the Finite Defference (FD) approach. The inversion domain is discretized into staggered grids which consist of primal and dual meshes. The scheme based on the FDFD technique shows

computational advantages compared to the Electric Field Integral Equation (EFIE) formulation, especially when a non-homogeneous background, like the half-space configuration in GPR, is involved.

- Propose a so-called cross-correlated error term and revolutionize the classical formulation of the cost functional. Since the measurement matrix has typically a large condition number, a minor state error in the field space may cause a large error in the measurement space. However, this potential mismatch is totally ignored in classical cost functional. In this thesis, a cross-correlated error term is proposed and introduced to the cost functional. In doing so, the robustness of the contrast source inversion method is obviously enhanced.

- Linearize the inverse problem by formulating it into a Multiple Measurement Vectors (MMV) inverse source problem. If we consider the inverse scattering problem of highly conductive scatterers, the ill-posedness can be successfully overcome by exploiting the joint sparsity of the contrast sources. The idea is implemented by reformulating the problem to a linear optimization problem regularized by a sum-of-norm constraint.

- A statistical technique — Cross-Validation (CV) method is used to circumvent the estimation of the noise level. Specifically, the original scattering matrix is separated into a reconstruction matrix and a CV matrix. The measurement vector is also separated accordingly to a reconstruction measurement vector and a CV measurement vector. In doing so, every iteration can be viewed as two separate parts: reconstructing the contrast sources and evaluating the outcome by the CV technique. The iteration arrives at the optimal solution when the least CV residual occurs.

- By exploitation of the frequency diversity, the MMV model is extended to non-sparse targets based on the Generalized Multiple Measurement Vectors (GMMV) model. The row-structure is utilized in the estimation of the contrast source vectors, resulting in higher resolution images.

- Synthetic data are generated by solving the EM direct scattering problem using a MATLAB-based 3-D FDFD package "MaxwellFDFD" [30]. Perfectly Matched Layers (PMLs) are used to simulate the anechoic chamber environment. Periodic Boundary Conditions (PBCs) are used to simulate the invariant axis in solving the 2-D scattering problem.

- The experimental data provided by the Institut Fresnel, France [31, 32] are selected and processed for validating the proposed methods. The scattered field is extracted from the subtraction of the total field and the incident field. Post-processing is applied to the measurement data with one single complex coefficient which multiplies the computed fields to match energy and phase to the measured ones. This calibration factor is simply derived from the ratio of the measured incident field and the simulated one at the receiver located at the opposite of the source.

1

1.3 NOVELTIES AND MAIN RESULTS

The novelties and main results presented in this thesis are listed as follows:

- I have demonstrated that, in some challenging situations where the initial guess is far from the real solution, the Multiplicative Regularized Contrast Source Inversion (MR-CSI) method shows poor performance, and the introduction of the Total Variation (TV) constraint even disrupts the convergence. Meanwhile, a new cost functional is proposed for the first time, which cross-correlates the mismatch of the contrast sources in the field domain with the data error in the measurement domain. Based upon this new error term, a Cross-Correlated Contrast Source Inversion (CC-CSI) method is developed, which shows less dependence on the initial guess and better inversion results.

- A multi-frequency version of the CC-CSI method, referred to as Multi-Frequency Cross-Correlated Contrast Source Inversion (MF-CC-CSI), is developed. By simultaneous processing of the multi-frequency data, this algorithm presents higher reliability and inversion accuracy. It is also demonstrated that the additional robustness brought by introducing the cross-correlated error term is still significant in the multi-frequency cases.

- A linear shape reconstruction method has been developed based on the MMV model for solving the inverse scattering problem of highly conductive scatterers. The exploitation of the joint sparsity of the induced currents makes it possible to estimate the contrast sources with linear optimization techniques. The intensity of the estimated contrast sources is able to indicate the position and profile of the highly conductive scatterers.

- 3-D inverse scattering problem in a half-space configuration is a realistic problem encountered in real applications. With partial measurements, the nonlinear iterative inversion methods are prone to false local optimal solutions, while global optimization inversion can hardly be done due to the huge demand for the computation resources. In this thesis, I have proposed an approach by transferring this problem to a cascade of inverse source problems and a linear optimization problem. With the proposed method, lots of computation time has been saved in comparison to the nonlinear iterative methods. In addition, the proposed method, to some extent, circumvents the occurrence of false local optimal solutions when only partial measurement data are available.

- A multi-frequency version of the MMV-based linear shape reconstruction method has been proposed based on the GMMV model. By exploiting the frequency diversity, the proposed GMMV-based linear inversion method shows good inversion performance for a variety of scatterers, including dielectric, lossy, and metallic scatterers. Due to the exploitation of the sum-of-norm constraint, the row-structure information of the contrast source vectors is exploited, which plays an extra focusing role. Therefore, the proposed method possesses higher resolving

ability in comparison to existing shape reconstruction methods, such as Linear Sampling Method (LSM).

1.4 OUTLINE OF THE THESIS

The rest of the thesis is organized as follows:

- **Chapter 2** — *Electromagnetic scattering theory.* This chapter introduces the rudiments of EM direct/inverse scattering theory. The FDFD method is introduced and a MATLAB-based solver package, "MaxwellFDFD", and its companion C program, "FD3D", are tested in both 2-D and 3-D configurations. The inverse scattering problem is formulated using the FDFD scheme. Considering the important roles of the following concepts in the field of inverse scattering problem, Singular Value Decomposition (SVD), nonlinearity, ill-posedness, and regularization are discussed. Finally, reviews of the state-of-the-art of inversion techniques are presented in the end of this chapter.
- **Chapter 3** — *Cross-correlated contrast source inversion.* This chapter focuses on the development of a CC-CSI method which is more robust than the known ones. The classical cost functional is a superposition of the data error and the state error. In this chapter, we defined a cross-correlated error term which is the mapping of the state error in the measurement domain. Subsequently, we changed the classical cost functional by introducing this new error term and develop a novel inversion method, referred to as CC-CSI. The extended version of this novel method for processing the multi-frequency data, MF-CC-CSI, is also given in this chapter. Numerical and experimental results demonstrate that the proposed method is more robust than both classical Contrast Source Inversion (CSI) and MR-CSI.
- **Chapter 4** — *Linear model for solving highly conductive inverse scattering problem.* This chapter aims to develop a linear model for reconstructing the boundary of the highly conductive scatterers. Considering the sparsity of the induced currents generated on the surface of the highly conductive scatterer when illuminated by external fields, I reformulate the inverse problem as an MMV inverse source problem, and a joint sparsity of the contrast sources is exploited by introducing the sum-of-norm regularization constraint. The proposed linear method turns out to be of higher resolving ability than LSM.
- **Chapter 5** — *Linearized 3-D inversion.* This chapter aims to develop a linearized inversion method for solving 3-D inverse scattering problem. The linearized 3-D inversion method is a cascade of two steps: 1) an extended 3-D version of the MMV method proposed in Chapter 4; and 2) a linear optimization process. Since the solution to the direct scattering problem is required only once, it is therefore more efficient in comparison to the nonlinear iterative inversion methods. In addition, this method is robust against the occurrence of local optimal solutions, especially in half space configurations, such as GPR, TWI, etc.

- **Chapter 6** — *GMMV linear inversion.* In this chapter, a linear shape reconstruction method based on the GMMV model is proposed. The contrast source vectors with respect to different incident angles and different operating frequencies are estimated jointly by exploitation of the row-structure information. It has been demonstrated that the regularized solutions of the contrast sources sought by the GMMV method are sufficient to indicate the spatial profile of non-sparse targets, including both metallic scatterers and dielectric scatterers.
- **Chapter 7** — *Conclusions and recommendation for future work.* This chapter presents the conclusions of this thesis and recommendations for future research.

2

ELECTROMAGNETIC SCATTERING THEORY

In classical scattering theory, the propagation of ElectroMagnetic (EM) waves is perfectly governed by Maxwell's equations. Therefore, in this chapter, an introduction to Maxwell's equations is first given in Subsection 2.1.1. In this thesis, the background medium and the material of the targets are assumed to be isotropic. Finite Difference Frequency Domain (FDFD) is considered as a numerical method for solving the direct scattering problem and a discretization approach for solving the inverse scattering problem. Details of FDFD are introduced in Subsection 2.1.2. In Subsection 2.1.3, a "MaxwellFDFD" solver package and its companion C program, "FD3D", for solving the EM direct scattering problems are introduced and tested using 2-Dimensional (2-D) and 3-Dimensional (3-D) benchmark problems. The EM inverse scattering problem is formulated subsequently in Subsection 2.2.1 based upon the FDFD scheme. Some important concepts — nonlinearity, ill-posedness, and regularization are discussed in Subsection 2.2.2 and Subsection 2.2.3. Section 2.3 gives a review of the state-of-the-art of the inversion techniques.

2.1 ELECTROMAGNETIC DIRECT SCATTERING PROBLEM

2.1.1 MAXWELL'S EQUATIONS

Suppose the time factor is $\exp(\mathrm{i}\omega t)$, where $\mathrm{i}^2 = -1$, and let $\vec{x} = [x_1, x_2, x_3]^T$ denotes the position vector, Maxwell's equations in the frequency domain can be written as follows

$$\begin{bmatrix} -\mathrm{i}\omega\overline{\overline{\varepsilon}} - \overline{\overline{\sigma}} & \nabla\times \\ \nabla\times & \mathrm{i}\omega\overline{\overline{\mu}} \end{bmatrix} \begin{bmatrix} \vec{E} \\ \vec{H} \end{bmatrix} = \begin{bmatrix} \vec{J} \\ -\vec{M} \end{bmatrix}, \tag{2.1}$$

where, $\vec{E} = \left[E_{x_1}, E_{x_2}, E_{x_3}\right]^T$ and $\vec{H} = \left[H_{x_1}, H_{x_2}, H_{x_3}\right]^T$ are the electric and magnetic fields, respectively; $\vec{J} = \left[J_{x_1}, J_{x_2}, J_{x_3}\right]^T$ and $\vec{M} = \left[M_{x_1}, M_{x_2}, M_{x_3}\right]^T$ are the electric and magnetic current source densities, respectively; $\overline{\overline{\sigma}}$, $\overline{\overline{\varepsilon}}$ and $\overline{\overline{\mu}}$ are the rank-2 tensors (in other words, 3×3 matrices) of the electric conductivity, dielectric permittivity and magnetic permeability, respectively. All these quantities are functions of the position vector, $\vec{x}$, and the angular frequency, ω.

Given the dielectric parameters and the sources, the EM direct scattering problem is to find the solutions to Maxwell's equations, $\vec{E}$ and $\vec{H}$. Like any differential equation, boundary conditions and initial conditions are necessary for the uniqueness of the solution, which is however not easily obtained [33]. And the analytical solutions to most of the direct scattering problems in inhomogeneous medium do not even exist. Numerical methods for differential equations can be used to approximately solve Maxwell's equations when an exact solution is not available, such as the Finite Element (FE) method [34] and Finite Defference (FD) method [33, 35]. In this thesis, we selected the FDFD method to formulate the EM direct/inverse scattering problem, which enables a straightforward incorporation of complicated background medium. We assume that the scattering problems considered in this thesis only involve isotropic background medium and scatterers. In doing so, the dielectric parameters, $\overline{\overline{\sigma}}$, $\overline{\overline{\varepsilon}}$ and $\overline{\overline{\mu}}$, are reduced to scalar variables, σ, ε and μ. For simplicity, we neglect σ by including it into a complex permittivity defined as $\epsilon = \varepsilon - \mathrm{i}\sigma/\omega$.

2.1.2 FINITE DIFFERENCE FREQUENCY DOMAIN

The FDFD method is a numerical method based on the FD approximations of the derivative operators in the differential equations to be solved. The basic idea is that, by eliminating the E-field and the H-field respectively from Eq. (2.1), we first obtain the differential equations of the E-field and the H-field given by

$$\nabla \times \mu^{-1} \nabla \times \vec{E} - \omega^2 \epsilon \vec{E} = -\mathrm{i}\omega \vec{J} - \nabla \times \mu^{-1} \vec{M}, \tag{2.2}$$

and

$$\nabla \times \epsilon^{-1} \nabla \times \vec{H} - \omega^2 \mu \vec{H} = -\mathrm{i}\omega\epsilon \vec{M} + \nabla \times \epsilon^{-1} \vec{J}, \tag{2.3}$$

respectively. Then the FD approximation (second-order or higher orders) is used to implement the *curl* operator in a discretization manner, yielding a system of linear equations. Finally, the electric/magnetic fields can be numerically calculated by inverting a so-called stiffness matrix.

Specifically, in the Cartesian coordinate system, let us write the frequency domain Maxwell's equations, Eqs. (2.1), in the form of

$$\partial_{x_2} E_{x_3} - \partial_{x_3} E_{x_2} = -\mathrm{i}\omega\mu H_{x_1} - M_{x_1}, \tag{2.4a}$$
$$\partial_{x_3} E_{x_1} - \partial_{x_1} E_{x_3} = -\mathrm{i}\omega\mu H_{x_2} - M_{x_2}, \tag{2.4b}$$
$$\partial_{x_1} E_{x_2} - \partial_{x_2} E_{x_1} = -\mathrm{i}\omega\mu H_{x_3} - M_{x_3}, \tag{2.4c}$$

and

$$\partial_{x_2} H_{x_3} - \partial_{x_3} H_{x_2} = \mathrm{i}\omega\epsilon E_{x_1} + J_{x_1}, \tag{2.5a}$$

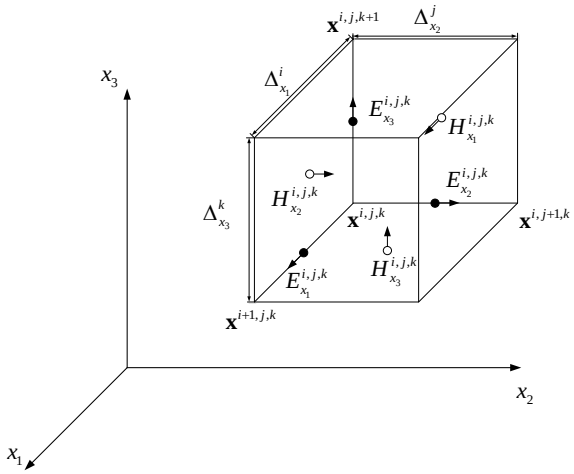

Figure 2.1: Yee's finite difference grid.

$$\partial_{x_3} H_{x_1} - \partial_{x_1} H_{x_3} = \mathrm{i}\omega\epsilon E_{x_2} + J_{x_2}, \tag{2.5b}$$
$$\partial_{x_1} H_{x_2} - \partial_{x_2} H_{x_1} = \mathrm{i}\omega\epsilon E_{x_3} + J_{x_3}. \tag{2.5c}$$

Using Yee's staggered grids (see Fig. 2.1) and a second-order FD approximation, Eqs. (2.4) and (2.5) can be approximately discretized as follows

$$\frac{E^{i,j+1,k}_{x_3} - E^{i,j,k}_{x_3}}{\Delta^j_{x_2}} - \frac{E^{i,j,k+1}_{x_2} - E^{i,j,k}_{x_2}}{\Delta^k_{x_3}} = -\mathrm{i}\omega\mu^{i,j,k} H^{i,j,k}_{x_1} - M^{i,j,k}_{x_1}, \tag{2.6a}$$
$$\frac{E^{i,j,k+1}_{x_1} - E^{i,j,k}_{x_1}}{\Delta^k_{x_3}} - \frac{E^{i+1,j,k}_{x_3} - E^{i,j,k}_{x_3}}{\Delta^i_{x_1}} = -\mathrm{i}\omega\mu^{i,j,k} H^{i,j,k}_{x_2} - M^{i,j,k}_{x_2}, \tag{2.6b}$$
$$\frac{E^{i+1,j,k}_{x_2} - E^{i,j,k}_{x_2}}{\Delta^i_{x_1}} - \frac{E^{i,j+1,k}_{x_1} - E^{i,j,k}_{x_1}}{\Delta^j_{x_2}} = -\mathrm{i}\omega\mu^{i,j,k} H^{i,j,k}_{x_3} - M^{i,j,k}_{x_3}, \tag{2.6c}$$

and

$$\frac{H^{i,j,k}_{x_3} - H^{i,j-1,k}_{x_3}}{\widetilde{\Delta}^j_{x_2}} - \frac{H^{i,j,k}_{x_2} - H^{i,j,k-1}_{x_2}}{\widetilde{\Delta}^k_{x_3}} = \mathrm{i}\omega\epsilon^{i,j,k} E^{i,j,k}_{x_1} + J^{i,j,k}_{x_1}, \tag{2.7a}$$
$$\frac{H^{i,j,k}_{x_1} - H^{i,j,k-1}_{x_1}}{\widetilde{\Delta}^k_{x_3}} - \frac{H^{i,j,k}_{x_3} - H^{i-1,j,k}_{x_3}}{\widetilde{\Delta}^i_{x_1}} = \mathrm{i}\omega\epsilon^{i,j,k} E^{i,j,k}_{x_2} + J^{i,j,k}_{x_2}, \tag{2.7b}$$
$$\frac{H^{i,j,k}_{x_2} - H^{i-1,j,k}_{x_2}}{\widetilde{\Delta}^i_{x_1}} - \frac{H^{i,j,k}_{x_1} - H^{i,j-1,k}_{x_1}}{\widetilde{\Delta}^j_{x_2}} = \mathrm{i}\omega\epsilon^{i,j,k} E^{i,j,k}_{x_3} + J^{i,j,k}_{x_3}, \tag{2.7c}$$

where, $\epsilon^{i,j,k}$ and $\mu^{i,j,k}$ are the complex dielectric permittivity and magnetic permeability evaluated at the locations where $E^{i,j,k}_\gamma$ and $H^{i,j,k}_\gamma$ are defined, respectively, and $\widetilde{\Delta}^l_\gamma = \left(\Delta^l_\gamma + \Delta^{l-1}_\gamma\right)/2$ with $\gamma \in \{x_1, x_2, x_3\}$.

The three difference equations, Eqs. (2.6), are obtained for each grid cell. We collect them from all grid cells to construct

$$\boldsymbol{C}_e^{\mathrm{sc}}\boldsymbol{e} = -\mathrm{i}\omega\boldsymbol{D}_\mu\boldsymbol{h} - \boldsymbol{m}, \tag{2.8}$$

where,

$$\boldsymbol{C}_e^{\mathrm{sc}} = \begin{bmatrix} \boldsymbol{0} & -\boldsymbol{D}^{\mathrm{e}}_{x_3} & \boldsymbol{D}^{\mathrm{e}}_{x_2} \\ \boldsymbol{D}^{\mathrm{e}}_{x_3} & \boldsymbol{0} & -\boldsymbol{D}^{\mathrm{e}}_{x_1} \\ -\boldsymbol{D}^{\mathrm{e}}_{x_2} & \boldsymbol{D}^{\mathrm{e}}_{x_1} & \boldsymbol{0} \end{bmatrix}, \quad \boldsymbol{D}_\mu = \begin{bmatrix} \mathrm{diag}\{\boldsymbol{\mu}\} & \boldsymbol{0} & \boldsymbol{0} \\ \boldsymbol{0} & \mathrm{diag}\{\boldsymbol{\mu}\} & \boldsymbol{0} \\ \boldsymbol{0} & \boldsymbol{0} & \mathrm{diag}\{\boldsymbol{\mu}\} \end{bmatrix},$$

$$\boldsymbol{e} = \begin{bmatrix} \boldsymbol{e}_{x_1} \\ \boldsymbol{e}_{x_2} \\ \boldsymbol{e}_{x_3} \end{bmatrix}, \quad \boldsymbol{h} = \begin{bmatrix} \boldsymbol{h}_{x_1} \\ \boldsymbol{h}_{x_2} \\ \boldsymbol{h}_{x_3} \end{bmatrix}, \quad \boldsymbol{m} = \begin{bmatrix} \boldsymbol{m}_{x_1} \\ \boldsymbol{m}_{x_2} \\ \boldsymbol{m}_{x_3} \end{bmatrix}.$$

Similarly, collecting Eq. (2.7) from all grid cells produces

$$\boldsymbol{C}_{\mathrm{h}}^{\mathrm{sc}}\boldsymbol{h} = \mathrm{i}\omega\boldsymbol{D}_\epsilon\boldsymbol{e} + \boldsymbol{j}, \tag{2.9}$$

where,

$$\boldsymbol{C}_{\mathrm{h}}^{\mathrm{sc}} = \begin{bmatrix} \boldsymbol{0} & -\boldsymbol{D}^{\mathrm{h}}_{x_3} & \boldsymbol{D}^{\mathrm{h}}_{x_2} \\ \boldsymbol{D}^{\mathrm{h}}_{x_3} & \boldsymbol{0} & -\boldsymbol{D}^{\mathrm{h}}_{x_1} \\ -\boldsymbol{D}^{\mathrm{h}}_{x_2} & \boldsymbol{D}^{\mathrm{h}}_{x_1} & \boldsymbol{0} \end{bmatrix},$$

$$\boldsymbol{D}_\epsilon = \begin{bmatrix} \mathrm{diag}\{\boldsymbol{\epsilon}\} & \boldsymbol{0} & \boldsymbol{0} \\ \boldsymbol{0} & \mathrm{diag}\{\boldsymbol{\epsilon}\} & \boldsymbol{0} \\ \boldsymbol{0} & \boldsymbol{0} & \mathrm{diag}\{\boldsymbol{\epsilon}\} \end{bmatrix}, \quad \boldsymbol{j} = \begin{bmatrix} \boldsymbol{j}_{x_1} \\ \boldsymbol{j}_{x_2} \\ \boldsymbol{j}_{x_3} \end{bmatrix}.$$

Corresponding to Eqs (2.6) and (2.7), $\boldsymbol{D}^{\mathrm{e}}_\gamma$ and $\boldsymbol{D}^{\mathrm{h}}_\gamma$ are the first order *curl* matrices, which are highly sparse. Now, by eliminating $\boldsymbol{h}$ from Eqs. (2.8) and (2.9), we can easily formulate the FD approximation of Eq. (2.2) as follows

$$\left(\boldsymbol{C}_{\mathrm{h}}^{\mathrm{sc}}\boldsymbol{D}_\mu^{-1}\boldsymbol{C}_{\mathrm{e}}^{\mathrm{sc}} - \omega^2\boldsymbol{D}_\epsilon\right)\boldsymbol{e} = -\mathrm{i}\omega\boldsymbol{j} - \boldsymbol{C}_{\mathrm{h}}^{\mathrm{sc}}\boldsymbol{D}_\mu^{-1}\boldsymbol{m}, \tag{2.10}$$

which is simply a system of linear equations of the form

$$\boldsymbol{A}\boldsymbol{e} = \boldsymbol{b}, \tag{2.11}$$

where, $\boldsymbol{A}$ is referred to as the stiffness matrix; $\boldsymbol{e}$ represents the E-field we solve for; $\boldsymbol{b}$ is a column vector determined by a given electric current source density. Inverting $\boldsymbol{A}$ yields the E-fields, and the H-field can be obtained by

$$\boldsymbol{h} = \boldsymbol{D}_\mu^{-1}\left(\boldsymbol{C}_{\mathrm{e}}^{\mathrm{sc}}\boldsymbol{e} + \boldsymbol{m}\right)\Big/(-\mathrm{i}\omega)\,. \tag{2.12}$$

Note that $\boldsymbol{C}_{\mathrm{e}}^{\mathrm{sc}}$ and $\boldsymbol{C}_{\mathrm{h}}^{\mathrm{sc}}$ represent the discretized *curl* operators on the electric field and the magnetic field, respectively. The superscript "sc" means that the scattering domain is truncated by the stretched-coordinate Perfectly Matched Layers (PMLs). In the FD method, PMLs are used to truncate the computational region, which can strongly absorb the outgoing waves from the interior of a computational region without reflecting them back into the interior. We refer to [33] for the design of PMLs.

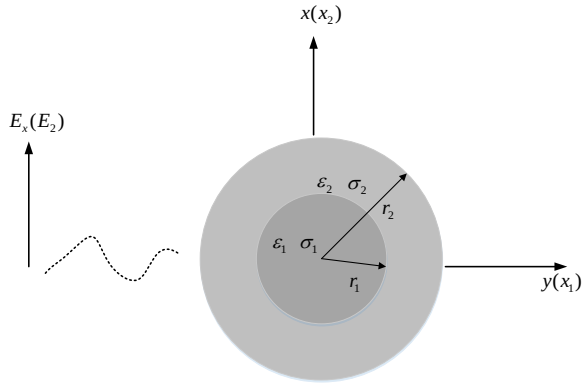

Figure 2.2: Geometry of the coaxially layered cylinder of the test cases for testing the performance of the "MaxwellFDFD" solver package.

Table 2.1: Simulation parameters of testing the performance of the "MaxwellFDFD" solver package.

Value / Case / Parameter	Case 1	Case 2
r_1, cm	7.9	9.4
r_2, cm	15	15
$\epsilon_{r,1}$	72	54
$\epsilon_{r,2}$	7.5	5.7
σ_1, S/m	0.9	1.4
σ_2, S/m	0.048	0.05
f, MHz	100	300

2.1.3 A SOLVER PACKAGE: "MAXWELLFDFD"

The "MaxwellFDFD" solver [36] is a MATLAB-based package that solves the frequency-domain Maxwell's equations. In this package, a second order FD approximation is used (see Eqs. (2.6) and (2.7)). In addition, "FD3D", a companion C program of "MaxwellFDFD", allows the users of "MaxwellFDFD" to solve the frequency-domain Maxwell's equations in a 3-D domain. "FD3D" uses iterative methods to avoid the large memory requirement of direct methods for 3-D problems. Since the "MaxwellFDFD" solver package and the companion C program are essential tools for the research work throughout the thesis, a performance test is first introduced with benchmark problems.

2-D BENCHMARK PROBLEM

In this subsection, 2-D benchmark problems, which have already been tested in reference [1], are used to test the "MaxwellFDFD" solver package. Fig. 2.2 shows the geometry

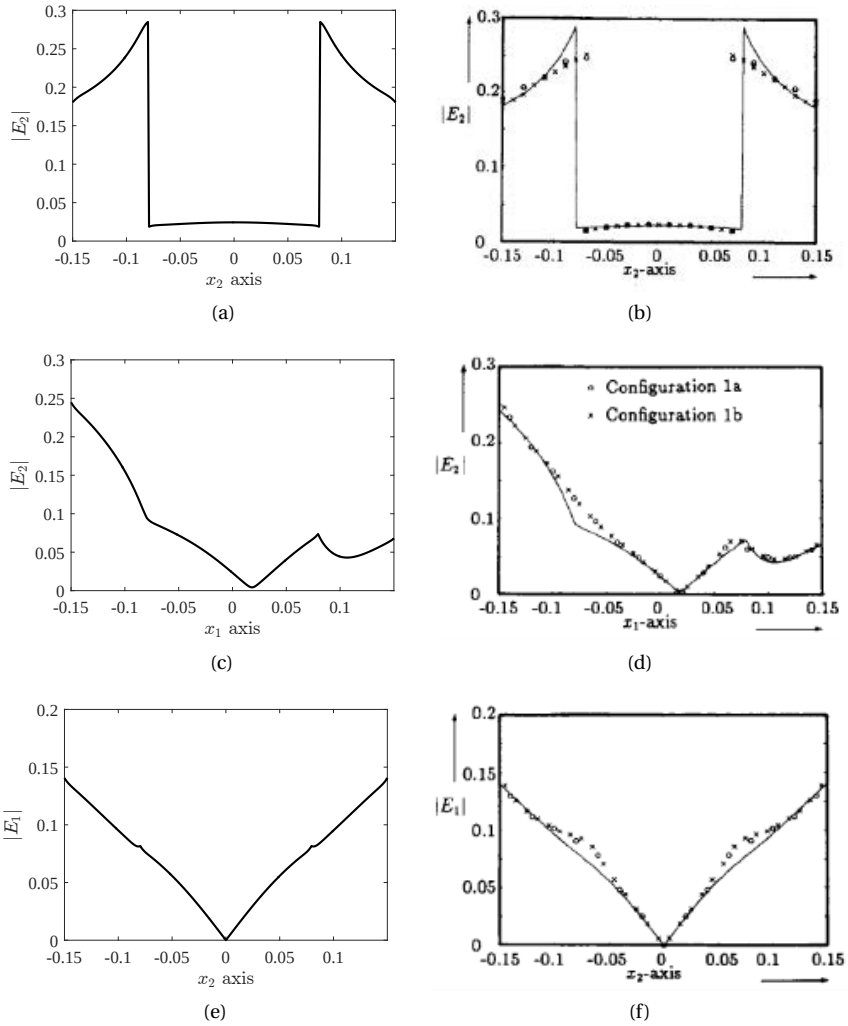

Figure 2.3: $|E_2|$ on the planes of $x_1 = 0$ and $x_2 = 0$ and $|E_1|$ on the plane of $x_1 = 0$ in Case 1. Left: results obtained by "MaxwellFDFD"; Right: analytical solutions reported in [1].

of the coaxially layered cylinder of the two test cases, and the simulation parameters are given in Table 2.1. The x_1- and x_2-normal boundaries are covered by PMLs to simulate the anechoic chamber environment. In order to simulate 2-D scattering model, the two x_3-normal boundaries are subject to Periodic Boundary Conditions (PBCs). A uniform plane wave is used as the incident wave propagating along the x_1 axis, with the unit electric field vector parallel to the x_2 axis. Let E_1^{inc}, E_2^{inc}, and E_3^{inc} represent the three components of the incident electric field, then we have

$$\left|E_1^{\text{inc}}\right| = 0, \quad \left|E_2^{\text{inc}}\right| = 1, \quad \left|E_3^{\text{inc}}\right| = 0. \tag{2.13}$$

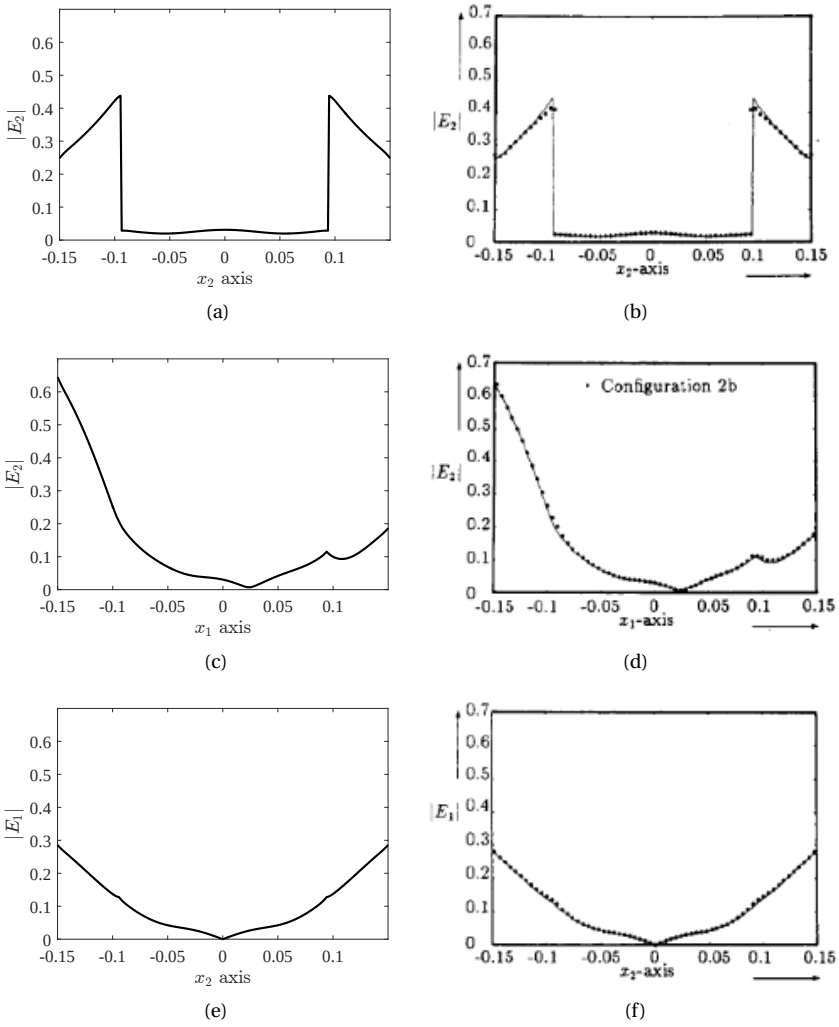

Figure 2.4: $|E_2|$ on the planes of $x_1 = 0$ and $x_2 = 0$ and $|E_1|$ on the plane of $x_1 = 0$ in Case 2. Left: results obtained by "MaxwellFDFD"; Right: analytical solutions reported in [1].

Since the time factor used in this package is $\exp(\mathrm{i}\omega t)$, the complex permittivity is defined as follows

$$\epsilon = \varepsilon_r \varepsilon_0 - \mathrm{i}\sigma/\omega \,, \tag{2.14}$$

where, ε_r denotes the relative permittivity of the object; the background medium is lossless and homogeneous with permittivity ε_0; and σ denotes the electric conductivity of the object.

Fig. 2.3 and Fig. 2.4 give the comparison of the FDFD results and the analytical solutions given by [1]. Fig. 2.5 shows the amplitude images of the x_1- and x_2-components

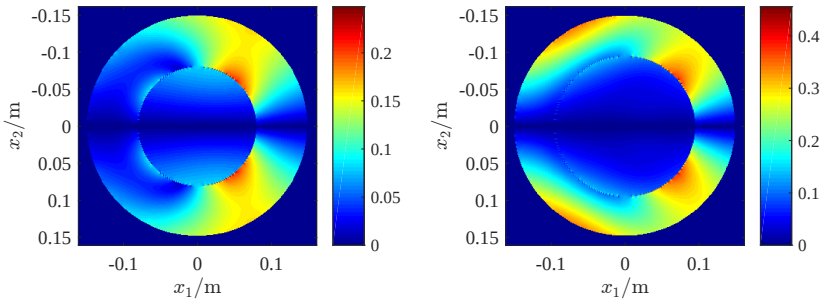

(a) $|E_1|$, Case 1 (b) $|E_1|$, Case 2

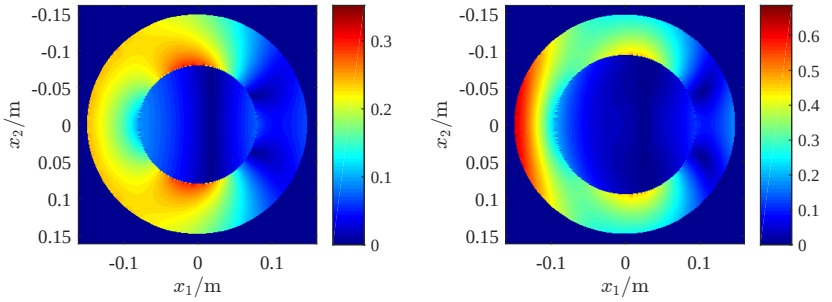

(c) $|E_2|$, Case 1 (d) $|E_2|$, Case 2

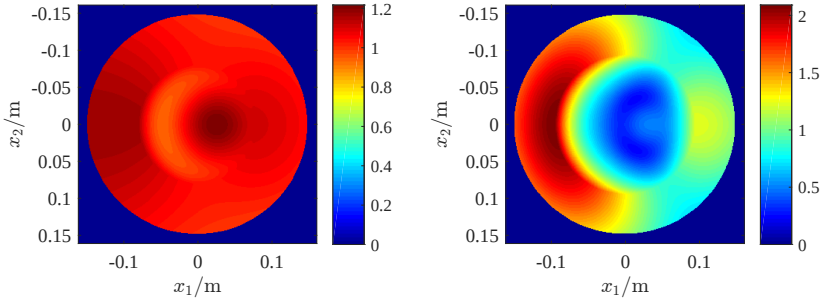

(e) $|H_3|$, Case 1 (f) $|H_3|$, Case 2

Figure 2.5: Amplitude images of the x_1- and x_2-components of the electric field, E_1, E_2 and the x_3-component of the magnetic field H_3, on the cross sectional plane of the cylinders. Left: Case 1; Right: Case 2.

of the electric field, E_1 and E_2, and the x_3-component of the magnetic field, H_3, in both cases. From Fig. 2.3 and Fig. 2.4, one can see that the results obtained by this FDFD solver coincide exactly with the analytical solution, demonstrating the good accuracy for high contrast and lossy medium cases.

For FD methods, grid point number per wavelength must satisfy $N_\lambda \geq 15$ so as to

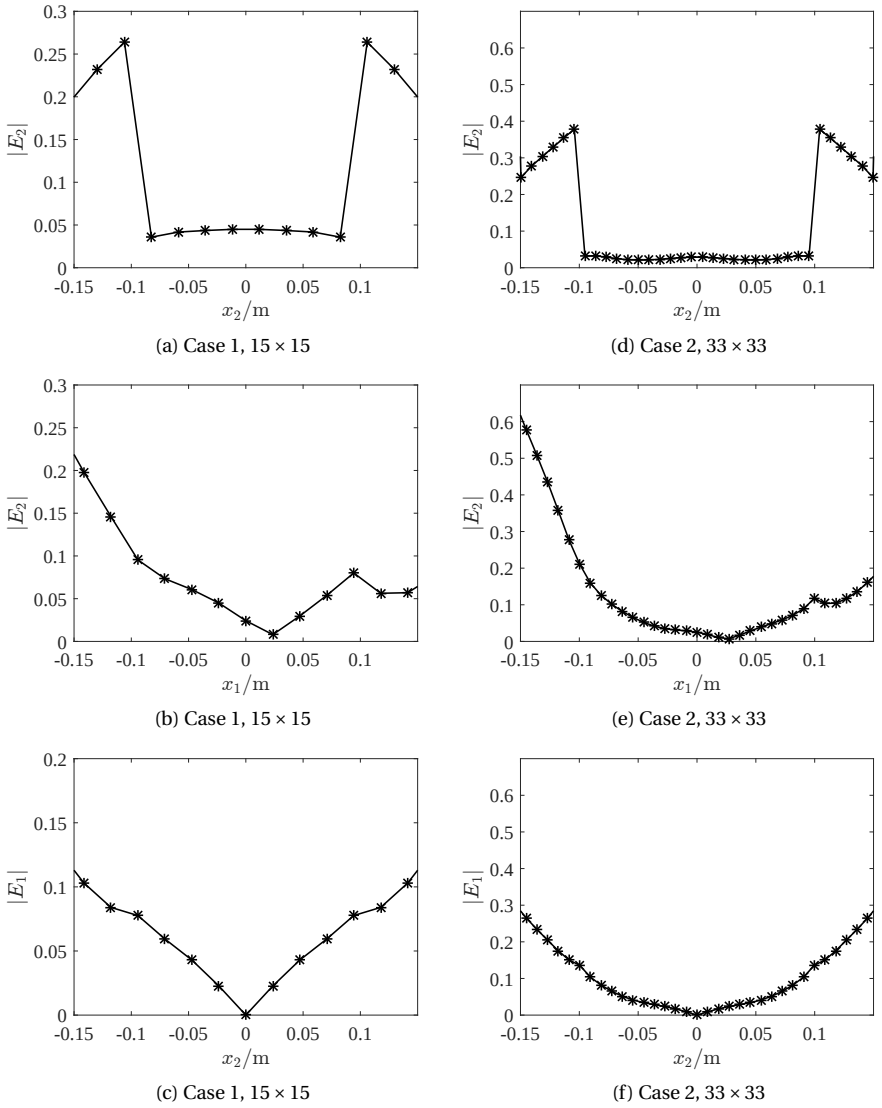

(a) Case 1, 15 × 15

(d) Case 2, 33 × 33

(b) Case 1, 15 × 15

(e) Case 2, 33 × 33

(c) Case 1, 15 × 15

(f) Case 2, 33 × 33

Figure 2.6: $|E_2|$ on the planes of $x_1 = 0$ and $x_2 = 0$ and $|E_1|$ on the plane of $x_1 = 0$ with $N_\lambda = 15$. Left: Case 1; Right: Case 2.

circumvent the numerical dispersion. To test the performance of "MaxwellFDFD" with coarse grids, we consider the lower limit $N = 15$. Fig. 2.6 gives the results with coarse grid points in both cases. By comparison of Fig. 2.6, Fig. 2.3 and Fig. 2.4, only a slight degradation of the accuracy can be observed. 3-D configuration can be easily realized by replacing the two x_3-normal boundaries with PMLs.

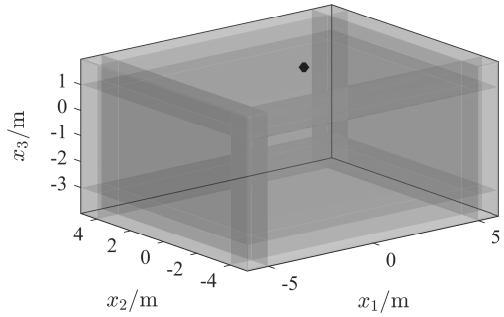

Figure 2.7: Configuration of the 3-D benchmark problem: an ideal electric dipole located at (−0.0495 m, 0 m, 0 m) of a unlimited free space.

3-D BENCHMARK PROBLEM

"FD3D" is a companion C program of the "MaxwellFDFD" solver package. It allows the users of "MaxwellFDFD" to solve the frequency-domain Maxwell's equations in a 3-D domain. "FD3D" uses iterative methods to avoid the large memory requirement in direct methods for solving 3-D scattering problems. To test the accuracy of the "FD3D" package, an ideal electric dipole in a homogeneous unlimited space is considered as a benchmark problem because the analytical solution of its 3-D electric field can be easily obtained. Without loss of generality, we assume the polarization of the ideal electric dipole is $\vec{q} = (1,0,0)$ (for other orientations, the solutions can be obtained by a rotation operation), then the electric field has an analytical expression of

$$\vec{E}(\vec{x},\vec{y},\vec{q}) = -\frac{\mathrm{i}}{4\pi k}\begin{bmatrix} -\frac{\partial^2}{\partial x_2 \partial x_2} - \frac{\partial^2}{\partial x_3 \partial x_3} \\ \frac{\partial^2}{\partial x_1 \partial x_2} \\ \frac{\partial}{\partial x_1 \partial x_3} \end{bmatrix} \frac{\exp(-\mathrm{i}kr)}{r}, \tag{2.15}$$

where, $r = \left\|\vec{x}-\vec{y}\right\|_2$. Here, k represents the wave number. Further, without loss of generality, let us assume $\vec{y} = (0,0,0)$ (for other locations, the solutions can be obtained by a simple shift operation), then we obtain

$$\vec{E}(\vec{x},\mathbf{0},\vec{q}) = -\frac{\mathrm{i}\exp(-\mathrm{i}kr)}{4\pi k}\begin{bmatrix} \frac{2\mathrm{i}k}{r^2} + \frac{k^2(x_2^2+x_3^2)+2}{r^3} - \frac{3\mathrm{i}k(x_2^2+x_3^2)}{r^4} - \frac{3x_2^2+3x_3^2}{r^5} \\ -\frac{k^2 x_1 x_2}{r^3} + \frac{3\mathrm{i}k x_1 x_2}{r^4} + \frac{3x_1 x_2}{r^5} \\ -\frac{k^2 x_1 x_3}{r^3} + \frac{3\mathrm{i}k x_1 x_3}{r^4} + \frac{3x_1 x_3}{r^5} \end{bmatrix}. \tag{2.16}$$

See Appendix B for the derivation.

Let us now use "FD3D" to solve the 3-D EM direct scattering problem discussed in the previous subsection. The linear system of equations is solved iteratively. The termination condition is

$$\frac{\|\boldsymbol{A}\hat{\boldsymbol{e}}-\boldsymbol{b}\|_2}{\|\boldsymbol{b}\|_2} \le 10^{-6}, \tag{2.17}$$

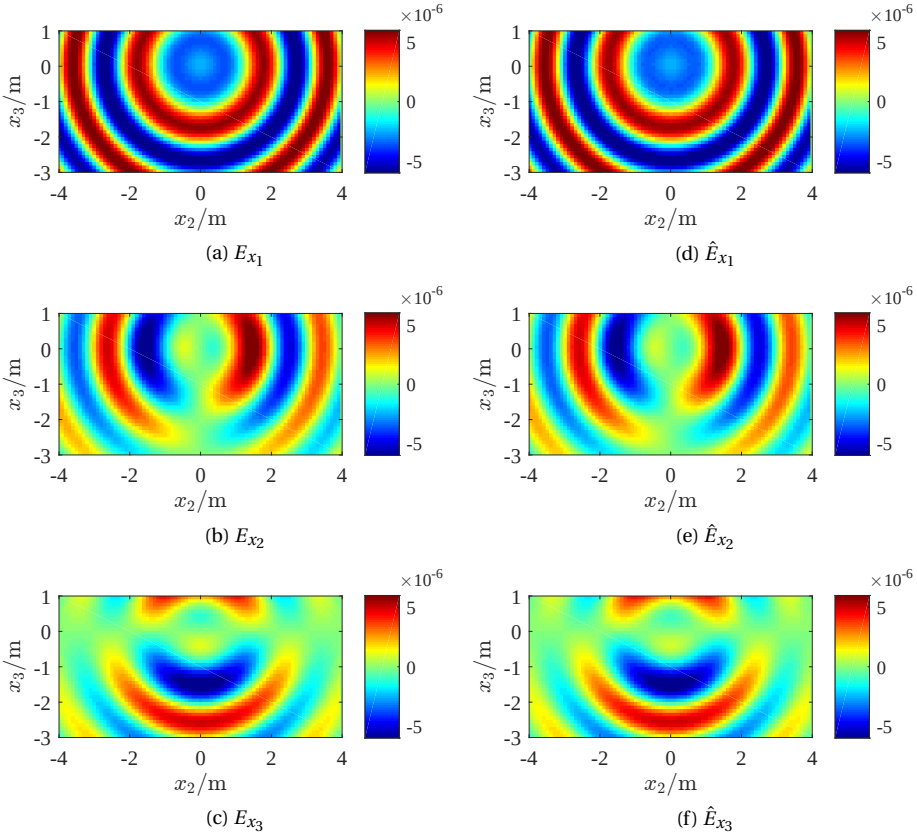

Figure 2.8: Real part of the three components of the analytical solution and the numerical solution on the cross section of $x_1 = -0.1$. Left: analytical solution; Right: numerical solution.

where, $\boldsymbol{A}$ is the FDFD stiffness matrix, $\boldsymbol{b}$ represents the source, and $\hat{\boldsymbol{e}}$ is the electric field to be calculated. The geometry of the test domain is shown in Fig. 2.7. The ideal dipole is located at (−0.0495 m, 0 m, 0 m), oscillating along x_1-axis at 200 MHz.

For comparison, the real part of the analytical solution and the numerical solution are shown in Fig. 2.8 on the cross section of $x_1 = -0.1$ m, from which we can see the analytical solution and the numerical solution match well, indicating that the direct scattering problem has been accurately solved by "FD3D". To evaluate the computation accuracy quantitatively, let us define the computation error as follows

$$err = \left|E_\gamma - \hat{E}_\gamma\right| / \left|E_\gamma\right|, \quad \gamma \in \{x_1, x_2, x_3\}, \tag{2.18}$$

where, E_γ represents the analytical solution, and $\hat{E}_\gamma$ represents the numerical solution. Fig. 2.9 shows the computation error images, from which we observe that the largest computation error remains no greater than 10%. Most of the relatively large errors are near the boundaries, and the errors in the central region are much less. Empirically, such

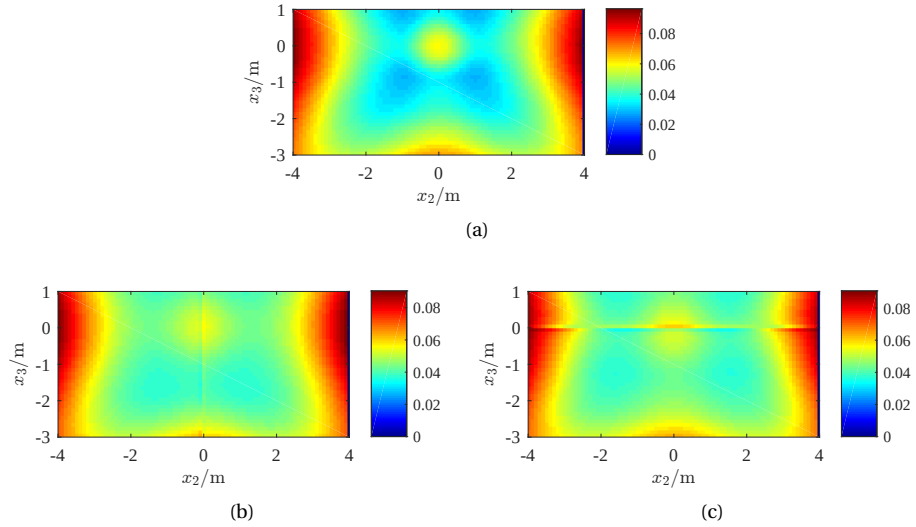

Figure 2.9: Computation error of the three components of the electric field on the cross section of $x_1 = -0.1$. (a) E_{x_1}; (b) E_{x_2}; (c) E_{x_3}.

a level of numerical errors does not have a significant effect to the method proposed in Chapter 5.

2.2 ELECTROMAGNETIC INVERSE SCATTERING PROBLEM

In contrast to the direct scattering problem, the inverse scattering problem is inherently nonlinear and, more seriously from the viewpoint of numerical computations, improperly posed. Unless regularization methods are used, small variations in the measured data can lead to large errors in the inverted results. Nevertheless, the inverse scattering problem is basic in areas such as radar, sonar, geophysical exploration, medical imaging and nondestructive testing. Indeed, it is safe to say that the inverse problem is at least of equal interest as the direct problem [37].

2.2.1 FORMULATION

We consider a scattering configuration as depicted in Fig. 2.10, which can be a 2-D or 3-D configuration. The scattering configuration consists of a bounded, simply connected, inhomogeneous domain of interest, $\mathcal{D}$, located in an inhomogeneous background medium. The domain of interest, $\mathcal{D}$, contains an object, $\mathcal{B}$, whose location and index of refraction are unknowns. According to Eq. (2.2), and meanwhile assuming the magnetic permeability is a constant, i.e., $\mu = \mu_0$, the total electric fields, $\vec{E}_p^{\text{tot}}$, and the incident

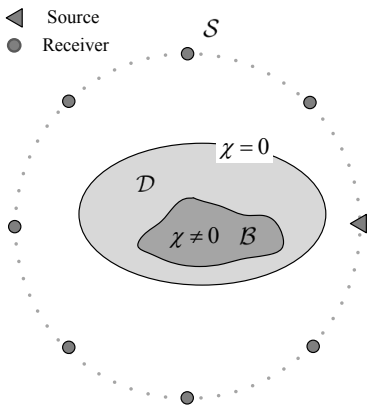

Figure 2.10: General configuration of the EM inverse scattering problem.

electric fields, $\vec{E}_p^{\text{inc}}$, satisfy the following equations

$$\nabla \times \mu_0^{-1} \nabla \times \vec{E}_p^{\text{tot}} - \omega^2 \epsilon \vec{E}_p^{\text{tot}} = -\mathrm{i}\omega \vec{J}_p - \nabla \times \mu_0^{-1} \vec{M}_p, \tag{2.19a}$$

$$\nabla \times \mu_0^{-1} \nabla \times \vec{E}_p^{\text{inc}} - \omega^2 \epsilon_{\text{bg}} \vec{E}_p^{\text{inc}} = -\mathrm{i}\omega \vec{J}_p - \nabla \times \mu_0^{-1} \vec{M}_p, \tag{2.19b}$$

respectively, where $p \in \{1, 2, 3, \cdots, P\}$ represents the p-th position of the transmitting antenna. The scattered electric fields, $\vec{E}_p^{\text{sct}}$, are defined as follows

$$\vec{E}_p^{\text{sct}} = \vec{E}_p^{\text{tot}} - \vec{E}_p^{\text{inc}} \quad p = 1, 2, 3, \cdots, P. \tag{2.20}$$

Subtracting Eq. (2.19a) from Eq. (2.19b), and using the definition in Eq. (2.20), we obtain

$$\nabla \times \mu_0^{-1} \nabla \times \vec{E}_p^{\text{sct}} - \omega^2 \epsilon_{\text{bg}} \vec{E}_p^{\text{sct}} = \omega^2 \chi \vec{E}_p^{\text{tot}}, \quad p = 1, 2, 3, \cdots, P, \tag{2.21}$$

in which the contrast function, χ, is defined as

$$\chi = \epsilon - \epsilon_{\text{bg}}. \tag{2.22}$$

Eq. (2.21) have the same form as Eq. (2.2), which means the scattered fields, $\vec{E}_p^{\text{sct}}$, can be solved by means of the FDFD scheme. Specifically, we have

$$\boldsymbol{A} \boldsymbol{e}_p^{\text{sct}} = \omega^2 \boldsymbol{\chi}^{\text{iso}} \boldsymbol{e}_p^{\text{tot}}, \quad p = 1, 2, 3, \cdots, P, \tag{2.23}$$

where,

$$\boldsymbol{A} = \mu_0^{-1} \boldsymbol{C}_{\text{h}}^{\text{sc}} \boldsymbol{C}_{\text{e}}^{\text{sc}} - \omega^2 \boldsymbol{D}_{\epsilon_{\text{bg}}}, \quad \boldsymbol{e}_p^{\text{sct}} = \begin{bmatrix} \boldsymbol{e}_{p,x_1}^{\text{sct}} \\ \boldsymbol{e}_{p,x_2}^{\text{sct}} \\ \boldsymbol{e}_{p,x_3}^{\text{sct}} \end{bmatrix}, \quad \boldsymbol{e}_p^{\text{tot}} = \begin{bmatrix} \boldsymbol{e}_{p,x_1}^{\text{tot}} \\ \boldsymbol{e}_{p,x_2}^{\text{tot}} \\ \boldsymbol{e}_{p,x_3}^{\text{tot}} \end{bmatrix}. \tag{2.24}$$

Since the problems we consider are isotropic, the contrast, $\boldsymbol{\chi}^{\text{iso}}$, is defined as follows

$$\boldsymbol{\chi}^{\text{iso}} = \left[\boldsymbol{\chi}^T \; \boldsymbol{\chi}^T \; \boldsymbol{\chi}^T \right]^T. \tag{2.25}$$

Note that the multiplication of two vectors is defined in default as Hadamard product in the remainder of this thesis. Then it is easy to get the solution to Eq. (2.23) by $\boldsymbol{e}_p^{\text{sct}} = \boldsymbol{A}^{-1}\omega^2\boldsymbol{\chi}_{\text{iso}}\boldsymbol{e}_p^{\text{tot}}$, and we obtain the data equations

$$\boldsymbol{y}_p = \mathcal{M}_{\mathcal{S},p}\boldsymbol{A}^{-1}\omega^2\boldsymbol{\chi}^{\text{iso}}\boldsymbol{e}_p^{\text{tot}}, \quad p = 1,2,3,\cdots,P, \tag{2.26}$$

and the state equations

$$\boldsymbol{e}_p^{\text{tot}} = \boldsymbol{e}_p^{\text{inc}} + \boldsymbol{A}^{-1}\omega^2\boldsymbol{\chi}^{\text{iso}}\boldsymbol{e}_p^{\text{tot}}, \quad p = 1,2,3,\cdots,P, \tag{2.27}$$

where, $\mathcal{M}_{\mathcal{S},p}$ is an operator that interpolates field values defined at the FD grids to the appropriate receiver positions. Let us now define a new matrix as follows

$$\boldsymbol{\Phi}_p = \mathcal{M}_{\mathcal{S},p}\boldsymbol{A}^{-1}\omega^2, \tag{2.28}$$

which is referred to as the sensing matrix throughout this thesis. Then Eq. (2.26) is simplified as

$$\boldsymbol{\Phi}_p\boldsymbol{\chi}^{\text{iso}}\boldsymbol{e}_p^{\text{tot}} = \boldsymbol{y}_p, \quad p = 1,2,3,\cdots,P. \tag{2.29}$$

The inverse scattering problem considered in this thesis is to solve the contrast, χ, using measurements of the scattered fields, $\boldsymbol{y}_1$, $\boldsymbol{y}_2$, $\boldsymbol{y}_3$, $\cdots$, $\boldsymbol{y}_P$. The reconstruction of the profile of the scatterer, i.e., the support of the contrast is referred to as qualitative imaging, and the inversion of the dielectric properties of the scatterer, i.e., the values of the contrast, is referred to as quantitative imaging.

2.2.2 NONLINEARITY AND ILL-POSEDNESS

Let us first rewrite the discretized formulation of the direct and inverse scattering problems

$$\boldsymbol{A}\boldsymbol{e} = \boldsymbol{b}, \tag{2.30}$$

$$\boldsymbol{\Phi}_p\boldsymbol{\chi}^{\text{iso}}\boldsymbol{e}_p^{\text{tot}} = \boldsymbol{y}_p, \quad p = 1,2,3,\cdots,P. \tag{2.31}$$

respectively, where, $\boldsymbol{A} = \mu_0^{-1}\boldsymbol{C}_{\text{h}}^{\text{sc}}\boldsymbol{C}_{\text{e}}^{\text{sc}} - \omega^2\boldsymbol{D}_{\epsilon_{\text{bg}}}$ and $\boldsymbol{b} = -\text{i}\omega\boldsymbol{j} - \boldsymbol{C}_{\text{h}}^{\text{sc}}\boldsymbol{D}_{\mu}^{-1}\boldsymbol{m}$. By noting that the total fields, $\boldsymbol{e}_p^{\text{tot}}$, are functions of the contrast, $\boldsymbol{\chi}$, it is obvious that the discretized inverse scattering problem is a nonlinear problem.

A well-posed problem in the Hadamard's sense [3] is given by:

- Existence of the solution;
- Uniqueness of the solution;
- The solution depends continuously on the data.

The third postulate is motivated by the fact that in all applications the data will be measured quantities. Therefore, one wants to make sure that small errors in the data will cause only small errors in the solution. A problem is said ill-posed if it does not satisfy at least one of the three Hadamard's criteria.

Since the scattering operator has an analytical kernel, it is completely continuous (or compact). As the inverse of a compact operator cannot be continuous [38], the inverse scattering problem is ill-posed. In fact, the analyticity of the radiation operator kernel implies that its singular values have a step-like behavior with an exponential decay after the knee. It can also be proved that the larger the scatterer is, the steeper the transition [4].

2.2.3 REGULARIZATION

Methods for constructing a stable approximate solution to an ill-posed problem are referred to as *regularization methods*. We shall now introduce the classical regularization concepts for linear equations of the first kind. In the sequel, we shall assume that the linear operator $A : X \to Y$ is injective. This is not a significant loss of generality since uniqueness for a linear equation always can be achieved by a suitable modification of the solution space X.

We wish to approximate the solution φ to the equation $A\varphi = y$ from a knowledge of a perturbed right hand side y^δ with a known error level

$$\left\| y^\delta - y \right\|_2 \leq \delta. \tag{2.32}$$

When y belongs to the range $A(X) := \{A\varphi : \varphi \in X\}$, there exists a unique solution φ to $A\varphi = y$. For a perturbed right hand side, in general, we cannot expect $y^\delta \in A(X)$. Using the erroneous data, y^δ, we want to construct a reasonable approximation, φ^δ, to the exact solution, φ, to the unperturbed equation $A\varphi = y$. Therefore, our task requires finding an approximation of the unbounded inverse operator, $A^{-1} : A(X) \to X$, by a bounded linear operator, $R : Y \to X$.

Definition 2.2.1. *Let X and Y be normed spaces and let $A : X \to Y$ be an injective bounded linear operator. Then a family of bounded linear operators, $R_\alpha : Y \to X, \alpha > 0$, with the property of point-wise convergence*

$$\lim_{\alpha \to 0} R_\alpha A\varphi = \varphi, \tag{2.33}$$

for all $\varphi \in X$ is called a regularization scheme for the operator A. The parameter α is called the regularization parameter.

One of the most classical regularization methods is the Tikhonov's regularization [39]. To give preference to a particular solution with desirable properties, a regularization term can be included in this minimization:

$$\left\| A\varphi - y \right\|_2^2 + \left\| \Gamma\varphi \right\|_2^2, \tag{2.34}$$

for some suitably chosen Tikhonov matrix, Γ. In many cases, this matrix is chosen as a multiple of the identity matrix ($\Gamma = \alpha \boldsymbol{I}$), giving preference to solutions with smaller norms; this is known as ℓ_2-norm regularization. Another group of regularization methods is designed by exploiting the sparsity of the scatterer in a certain domain [40–42]. We refer to [37, 43–45] for more introduction to regularization methods. In the following chapters, we shall see that the inversion methods developed in this thesis essentially belong to the family of regularization methods.

2.3 INVERSION TECHNIQUES: STATE-OF-THE-ART

Inversion techniques are developed mostly in the research of acoustic and EM inverse scattering problem. There are, of course, important differences in the practical implementation in each of these efforts. For example, some methods are based on the far field assumption, while sometimes near field condition is of more interest; In addition, the optimization scheme is numerically solved by different methods. However, the basic ideas embodied in the inversion techniques to be mentioned below and developed in this thesis are more general and are not restricted by the variety of the waves or the far/near field assumptions.

Initial efforts in this field attempted to linearize the problem by reducing it to the problem of solving a linear integral equation of the first kind. The main techniques used to accomplish this were the Born or Rytov approximation for the inverse scattering problem of penetrable scatterers, which is referred to as *inverse medium problem*, and the Kirchhoff, or physical optics, approximation of the solution to the inverse scattering problem of impenetrable scatterers, which is referred to as *inverse obstacle problem* [46–48]. While such linearized models are attractive because of their mathematical simplicity, they have the defect of ignoring the basic nonlinear nature of the inverse scattering problem, e.g., multiple reflections are essentially ignored.

The earliest attempts to treat the inverse scattering problem without linearizing it were due to [49] and [50], in which the inverse obstacle problem was studied with acoustic wave and EM wave, respectively. Then, beginning in the 1980's, a number of methods were given which explicitly acknowledged the nonlinear and ill-posed nature of the problem. The *inverse obstacle problem*, in particular, was formulated by either integral equations or Green's formulas as a nonlinear optimization problem that required the solution to the direct scattering problem for different domains at each step of the iteration procedure used to arrive at a solution [51–60]. Approaches which avoid the problem of solving a direct scattering problem at each iteration step and, furthermore, attempt to separate the ill-posedness and non-linearity of the *inverse obstacle problem* were introduced and theoretically and numerically analyzed by Kirsch and Kress in [61] and Colton and Monk in [62–64]. A method that is closely related to the approach suggested by Kirsch and Kress was also introduced by Angell, Kleinman and Roach [65]. These methods are collectively called decomposition methods and their main idea is to break up the inverse obstacle scattering problem into two parts: the first part deals with the ill-posedness by constructing the scattered wave from its far field pattern; and the second part deals with the nonlinearity by determining the unknown boundary of the scatterer as the location where the boundary condition for the total field is satisfied in a least-squares sense. A more recently developed decomposition method is the point source method of Potthast [66]. The hybrid method suggested by Kress and Serranho [67] combines ideas of the method of Kirsch and Kress with Newton type iterations as mentioned above.

To deal with the inverse medium problem, one approach is to use Linear Sampling Method (LSM) together with a knowledge of the first transmission eigenvalue [68] or with several so-called "virtual experiments" [13, 69–72]. Another group of methods seek for a solution of the contrast, $\boldsymbol{\chi}$, and the total fields, $\boldsymbol{e}_p^{\text{tot}}$, such that both Eq. (2.29) and

Eq. (2.27) are satisfied. This is done by reformulating the inverse problem as a nonlinear optimization problem in which Eq. (2.27) is considered as a regularization constraint. Variations of this category of methods include the Newton-Kantorovich (NK) method [51, 73–75], the Conjugate Gradient (CG) method [76], the Modified Gradient (MG) method [74, 77–79], the Born Iterative Method (BIM) and the Distorted Born Iterative Method (DBIM)) [80–83], the Contrast Source Extended Born (CS-EB) method [84], and the Contrast Source Inversion (CSI) method (including its variations) proposed by van den Berg et al. for solving EM inverse scattering problems [85–87]. A second method for solving the acoustic inverse medium problem was introduced by Colton and Monk [88–90] and can be viewed as a decomposition method for approaching the inverse medium problem. Alternate methods of modifying the method of Colton and Monk than that described above can be found in [91–93]. The theoretical basis of this decomposition method for EM waves has been developed in [91, 94, 95].

Alternative methods have been developed which, as apposed to nonlinear optimization techniques, only seek limited information about the scattering objects. Among them are LSM [96–99], the factorization method [100, 101], and the method of singular sources [102, 103], which determine the shape of the scattering obstacle but in general provide only limited information about the material properties of the scatterer. In addition, the quantitative inverse scattering methods based on LSM and CSI have also been studied in [13, 69–72, 104].

Since the CSI method and the LSM method are considered for comparison in Chapter 3, Chapter 4, and Chapter 6, and the ideas of both methods are closely related to the novel methods proposed in this thesis, we shall now briefly outline the CSI method and the LSM method respectively in the following two subsections, in which the Multiplicative Regularized Contrast Source Inversion (MR-CSI) method and the idea of "virtual experiments" are also introduced.

2.3.1 CONTRAST SOURCE INVERSION

CLASSICAL CSI

Classical CSI is an iterative method of solving the inverse scattering problem by minimizing a cost functional which is defined as the superposition of the data error and the state error. Specifically, let us first give the data equation and the state equation as follows

$$\boldsymbol{y}_p = \boldsymbol{\Phi}_p \boldsymbol{j}_p, \tag{2.35a}$$

$$\boldsymbol{j}_p = \boldsymbol{\chi}^{\text{iso}} \boldsymbol{e}_p^{\text{inc}} + \boldsymbol{\chi}^{\text{iso}} \mathcal{M}_{\mathcal{D}} \boldsymbol{A}^{-1} \boldsymbol{j}_p, \tag{2.35b}$$

where, $p = 1,2,3,\cdots,P$, $\mathcal{M}_{\mathcal{D}}$ is an operator that selects fields only inside the field domain, $\mathcal{D}$, and $\boldsymbol{\chi}^{\text{iso}}$ is given by Eq. (2.25). Note that the angular frequency, ω, is included into matrix $\boldsymbol{A}$ and therefore does not appear in the above equation. In classical CSI iterations, the contrast sources are first updated and then the contrast. The data error and the state error equation for updating the contrast sources are defined as

$$\boldsymbol{\rho}_{p,\ell-1/2} = \boldsymbol{y}_p - \boldsymbol{\Phi}_p \boldsymbol{j}_{p,\ell-1}, \tag{2.36a}$$

$$\boldsymbol{\gamma}_{p,\ell-1/2} = \boldsymbol{\chi}^{\text{iso}}_{\ell-1} \boldsymbol{e}_p^{\text{inc}} + \boldsymbol{\chi}^{\text{iso}}_{\ell-1} \boldsymbol{A}^{-1} \boldsymbol{j}_{p,\ell-1} - \boldsymbol{j}_{p,\ell-1}, \tag{2.36b}$$

respectively. Here, $\ell-1/2$ means the update of the contrast sources taking place after the $(\ell-1)$-th iteration and before the ℓ-th update of the contrast. Since $\mathcal{M}_{\mathcal{D}}$ always exists together with the stiffness matrix, $\boldsymbol{A}$, it is neglected for better readability in the remainder of this thesis. Let us first define the cost functional, $C_{\text{CSI},\ell-1/2}$, as follows

$$C_{\text{CSI},\ell-1/2} = \eta^{\mathcal{S}} \sum_{p=1}^{P} \left\| \boldsymbol{\rho}_{p,\ell-1/2} \right\|_{\mathcal{S}}^2 + \eta_{\ell-1}^{\mathcal{D}} \sum_{p=1}^{P} \left\| \boldsymbol{\gamma}_{p,\ell-1/2} \right\|_{\mathcal{D}}^2, \tag{2.37}$$

where, $\eta^{\mathcal{S}}$ and $\eta_{\ell}^{\mathcal{D}}$ are defined as

$$\eta^{\mathcal{S}} = \frac{1}{\sum_{p=1}^{P} \left\| \boldsymbol{y}_p \right\|_{\mathcal{S}}^2} \tag{2.38}$$

and

$$\eta_{\ell}^{\mathcal{D}} = \frac{1}{\sum_{p=1}^{P} \left\| \boldsymbol{\chi}_{\ell}^{\text{iso}} \boldsymbol{e}_p^{\text{inc}} \right\|_{\mathcal{D}}^2}, \tag{2.39}$$

respectively. Here, $\|\cdot\|_{\mathcal{S}}$ and $\|\cdot\|_{\mathcal{D}}$ represent the norms on the measurement space $L^2(\mathcal{S})$ and the field space $L^2(\mathcal{D})$, respectively.

Suppose both $\boldsymbol{\chi}_{\ell-1}$ and $\boldsymbol{j}_{p,\ell-1}$ are known, the contrast sources are first updated by

$$\boldsymbol{j}_{p,\ell} = \boldsymbol{j}_{p,\ell-1} + \alpha_n \boldsymbol{\nu}_{p,\ell}, \tag{2.40}$$

where, α_ℓ is the step size, and

$$\boldsymbol{\nu}_{p,\ell} = \begin{cases} 0, & \ell = 0, \\ \boldsymbol{g}_{p,\ell} + \dfrac{\sum_{p'} \left\langle \boldsymbol{g}_{p',\ell}, \boldsymbol{g}_{p',\ell} - \boldsymbol{g}_{p',\ell-1} \right\rangle_{\mathcal{D}}}{\sum_{p'} \left\| \boldsymbol{g}_{p',\ell-1} \right\|_{\mathcal{D}}^2} \boldsymbol{\nu}_{p,\ell-1}, & \ell \geq 1, \end{cases} \tag{2.41}$$

in which $\langle\cdot\rangle_{\mathcal{D}}$ represents the inner product defined in the field space, $L^2(\mathcal{D})$, and $\boldsymbol{g}_{p,\ell}$ is the gradient (Fréchet derivative) of $C_{\text{CSI},\ell-1/2}$ with respect to $\boldsymbol{j}_p$ by setting $\boldsymbol{j}_p = \boldsymbol{j}_{p,\ell-1}$, followed by the update of the contrast by minimizing the cost functional

$$C_{\text{CSI},\ell} = \eta^{\mathcal{S}} \sum_{p=1}^{P} \left\| \boldsymbol{\rho}_{p,\ell} \right\|_{\mathcal{S}}^2 + \eta_{\ell-1}^{\mathcal{D}} \sum_{p=1}^{P} \left\| \boldsymbol{\gamma}_{p,\ell} \right\|_{\mathcal{D}}^2, \tag{2.42}$$

where,

$$\boldsymbol{\rho}_{p,\ell} = \boldsymbol{y}_p - \boldsymbol{\Phi}_p \boldsymbol{j}_{p,\ell}, \tag{2.43}$$

and

$$\boldsymbol{\gamma}_{p,\ell} = \boldsymbol{\chi}_{\ell-1}^{\text{iso}} \boldsymbol{e}_{p,\ell}^{\text{tot}} - \boldsymbol{j}_{p,\ell}, \tag{2.44}$$

with

$$\boldsymbol{e}_{p,\ell}^{\text{tot}} = \boldsymbol{e}_p^{\text{inc}} + \boldsymbol{A}^{-1} \boldsymbol{j}_{p,\ell}. \tag{2.45}$$

If no *a priori* information about the scatterer is available, Eq. (2.42) is minimized when

$$\boldsymbol{\chi}_{\ell} = \frac{\sum_{p=1}^{P} \sum_{\gamma} \boldsymbol{j}_{p,\gamma,\ell} \overline{\boldsymbol{e}_{p,\gamma,\ell}^{\text{tot}}}}{\sum_{p=1}^{P} \sum_{\gamma} \boldsymbol{e}_{p,\gamma,\ell}^{\text{tot}} \overline{\boldsymbol{e}_{p,\gamma,\ell}^{\text{tot}}}}, \tag{2.46}$$

where, $\gamma \in \{x_1, x_2, x_3\}$, and $\overline{(\cdot)}$ represents the conjugate of a complex scalar/vector/matrix. More details of classical CSI can be found in [85, 86, 105]

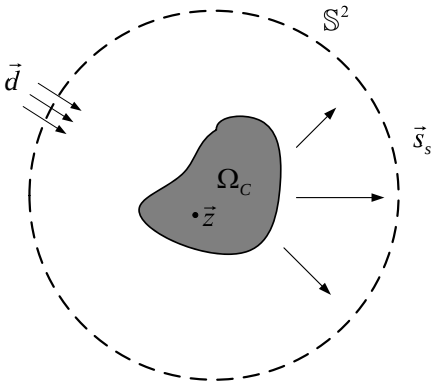

Figure 2.11: Geometry of the far-field LSM.

MULTIPLICATIVE REGULARIZED CSI

MR-CSI is the regularized CSI method with a multiplicative weighted Total Variation (TV) constraint, which was first introduced by van den Berg et al. [45]. In comparison to CSI, the contrast, $\boldsymbol{\chi}$, in MR-CSI is updated by minimizing the cost functional of the form

$$C_{\mathrm{CSI},\ell} \times \frac{1}{V}\int_{\mathcal{D}} \frac{\left\|\nabla \boldsymbol{\chi}\right\|^2 + \delta_{\ell-1}^2}{\left\|\nabla \boldsymbol{\chi}_{\ell-1}\right\|^2 + \delta_{\ell-1}^2} d\vec{x}. \tag{2.47}$$

Here, $V = \int_{\mathcal{D}} d\vec{x}$, and $\delta_{\ell-1}^2$ are introduced for restoring the differentiability of the TV factor [45]. The value of $\delta_{\ell-1}^2$ is chosen to be large in the beginning of the optimization and small towards the end, which is given by

$$\delta_{\ell-1}^2 = C_{\mathrm{CSI},\ell-1/2}^{\boldsymbol{\chi}} \Delta^2, \tag{2.48}$$

where, Δ denotes the mesh size of the discretized domain $\mathcal{D}$. More details of MR-CSI can be found in [45, 86, 105].

2.3.2 LINEAR SAMPLING METHOD

LINEAR SAMPLING METHOD

Far field LSM transforms the nonlinear inverse scattering problem to a linear one. It was originally proposed in [96], and has recently received considerable attention in dealing with inverse scattering problems [13, 106]. LSM avoids incorrect model assumptions, however it requires more measurement data than the iterative methods. Now we define the far field operator $\mathcal{F} : L^2[0,2\pi] \to L^2[0,2\pi]$ by (see Fig. 2.11)

$$\left(\mathcal{F}\boldsymbol{\phi}_z\right)\left(\vec{s}_s\right) := \int_{\mathbb{S}^2} \vec{E}_\infty\left(\vec{s}_s, \vec{d}\right)\boldsymbol{\phi}_z\left(\vec{d}\right) d\vec{s}_d = \vec{E}_{e,\infty}\left(\vec{s}_s, \vec{z}, \vec{q}\right), \quad \vec{s}_s \in \mathbb{S}^2, \tag{2.49}$$

where, $\mathbb{S}^2$ is the unit circle in $\mathbb{R}^3$, $\vec{z} \in \mathbb{R}^3$ denotes a sampling grid, $\vec{d} \in \mathbb{S}^2$ represents all possible directions of the incident plane waves, $\vec{E}_\infty\left(\vec{s}_s, \vec{d}\right)$ is the far field pattern of the

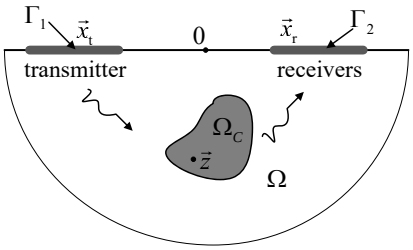

Figure 2.12: Geometry of the near-field LSM.

scattered field, $\vec{E}_{e,\infty}(\vec{x},\vec{z},\vec{q})$ is the far field pattern of an electric dipole, of which the electric field is as follows

$$\vec{E}_e(\vec{x},\vec{z},\vec{q}) := \frac{i}{k}\nabla_x \times \nabla_x \times \vec{q}\,\Phi(\vec{x},\vec{z}), \tag{2.50}$$

where, $\vec{q}$ is the polarization of the electric dipole placed at $\vec{z}$, and $\Phi(\vec{x},\vec{z})$ is the fundamental point solution to Maxwell's equations. Explicitly, for a 3-D homogeneous space with the wave number $k>0$ and the time factor $\exp(i\omega t)$, we have

$$\Phi(\vec{x},\vec{z}) = \frac{1}{4\pi}\frac{\exp(-ik\|\vec{x}-\vec{z}\|_2)}{\|\vec{x}-\vec{z}\|_2}, \quad \vec{x}\in\mathbb{R}^3, \tag{2.51}$$

and

$$\vec{E}_{e,\infty}(\vec{s}_s,\vec{z},\vec{q}) = \frac{-ik}{4\pi}(\vec{s}_s\times\vec{q})\times\vec{s}_s e^{ik\vec{s}_s\cdot\vec{z}}. \tag{2.52}$$

Near field Subsequently, Fata and Guzina generalized LSM to near field for solving the near-field inverse problems in elastodynamics [98]. Analysis of LSM in EM near field can be found in [107]. Now we give an introduction to LSM based on a near field operator. Assume the incident field is radiated from sources located on a bounded planar domain, Γ_1, and the scattered field is measured on a bounded planar sub-domain, Γ_2 (see Fig. 2.12). The inverse scattering problem is to determine Ω_c from the knowledge of the tangential components $\vec{v}\times\vec{E}(\cdot,\vec{x}_t,\vec{p})$ and $\vec{v}\times\vec{H}(\cdot,\vec{x}_t,\vec{p})$ measured on the surface Γ_2 for all the point sources at $\vec{x}_t\in\Gamma_1$ and two linearly independent polarizations $\vec{p}$ tangent to Γ_1. Here $\vec{v}(\vec{x}_r)$ is the outward unit normal vector of the measurement surface, Γ_2. The near-field operator, $\mathcal{N}: L_2(\Gamma_1)\to L_2(\Gamma_2)$, is defined as follows

$$\begin{aligned}(\mathcal{N}\boldsymbol{\phi}_z)(\vec{x}_r) &:= \int_{\Gamma_1}\vec{v}(\vec{x}_r)\times\left(\vec{E}^{sct}(\vec{x}_r,\vec{x}_t)\boldsymbol{\phi}_z(\vec{x}_t) - \vec{E}^{sct}_{bg}(\vec{x}_r,\vec{x}_t)\boldsymbol{\phi}_z(\vec{x}_t)\right)d\vec{x}_t \\ &= \vec{v}(\vec{x}_r)\times\overline{\overline{G}}(\vec{x}_r,\vec{z})\vec{q}, \quad \vec{x}_t\in\Gamma_2,\end{aligned} \tag{2.53}$$

where, $\overline{\overline{G}}(\vec{x}_r,\vec{z})$ is the Green's tensor with respect to a source point $\vec{z}$, $\vec{E}^{sct}_{bg}(\vec{x}_r,\vec{x}_t,\boldsymbol{\phi}_z(\vec{x}_t))$ is the scattered electric field due to the background medium in the absence of scatterer

Ω_c, and $\vec{q}$ is the polarization of the electric dipole placed at $\vec{z} \in \Omega$. The scattered field is observed at $\vec{x}_r \in \Gamma_2$, and $\boldsymbol{\phi}_z(\vec{x}_t)$ is a tangential field at $\vec{x}_t \in \Gamma_1$ with $\vec{v} \cdot \boldsymbol{\phi}_z(\vec{x}_t) = 0$ corresponding to the sampling grid $\vec{z}$. LSM is based on numerically determining $\boldsymbol{\phi}_z$ and hence the scattering object according to [107, Theorems 3.1 and 3.2], which is as follows:

1. Select a grid of "sampling points" in a region Ω known to contain the scattering objects.
2. Use regularization methods to compute an approximate solution, $\boldsymbol{\phi}_z(\cdot)$, to the near field equation (2.53) for each sampling grid, $\vec{z}$.
3. Plotting the indicator function $I_q(\vec{z}) = 1 \Big/ \left\| \boldsymbol{\phi}_z(\cdot) \right\|_{L_2(\Gamma_1)}$ for all $\vec{z} \in \Omega$.

As pointed out by [108], a generalized indicator function considering different polarizations can be defined as

$$I(\vec{z}) = \frac{\sum_{\vec{q}} \frac{1}{\|\boldsymbol{\phi}_z(\cdot)\|_{L_2(\Gamma_1)}}}{\max\left(\sum_{\vec{q}} \frac{1}{\|\boldsymbol{\phi}_z(\cdot)\|_{L_2(\Gamma_1)}}\right)}. \tag{2.54}$$

LSM INVERSION VIA "VIRTUAL EXPERIMENTS"

Now let us take a look at the basic principle of LSM as a way of quantitative inversion based on the concept of "virtual experiments". For the sake of simplicity, we consider a scalar field instead, i.e., the Transverse Magnetic (TM) polarization, and the linear sampling equation can be simply written to the form of

$$G(\vec{x}_s, \vec{x}_r) = \int_{\Gamma_1} \boldsymbol{\phi}(\vec{x}_t | \vec{x}_s) E^{sct}(\vec{x}_r, \vec{x}_t) \, d\vec{x}_t. \tag{2.55}$$

The scattered field can be formulated as follows

$$E^{sct}(\vec{x}_r, \vec{x}_t) = \int_{\mathcal{D}} G(\vec{x}_r, \vec{x}) E^{tot}(\vec{x}, \vec{x}_t) \chi(\vec{x}) \, d\vec{x}. \tag{2.56}$$

Substitution of Eq. (2.56) into Eq. (2.55) and swap of the two integrals yield

$$\begin{aligned} G(\vec{x}_s, \vec{x}_r) &= \int_{\mathcal{D}} G(\vec{x}_r, \vec{x}) \left\{ \int_{\Gamma_1} \boldsymbol{\phi}(\vec{x}_t | \vec{x}_s) E^{tot}(\vec{x}, \vec{x}_t) \, d\vec{x}_t \right\} \chi(\vec{x}) \, d\vec{x} \\ &= \int_{\mathcal{D}} G(\vec{x}_r, \vec{x}) \left\{ \int_{\Gamma_1} \boldsymbol{\phi}(\vec{x}_t | \vec{x}_s) E^{inc}(\vec{x}, \vec{x}_t) \, d\vec{x}_t + G(\vec{x}_s, \vec{x}) \right\} \chi(\vec{x}) \, d\vec{x}. \end{aligned} \tag{2.57}$$

If P sampling points at $\vec{x}_s$, can be selected to well indicate the profile of the scatterer, then each term

$$\int_{\Gamma_1} \boldsymbol{\phi}(\vec{x}_t | \vec{x}_s) E^{inc}(\vec{x}, \vec{x}_t) \, d\vec{x}_t + G(\vec{x}_s, \vec{x})$$

with respect to the sampling point at $\vec{x}_s$, can be viewed as one "virtual experiment". The contrast, $\chi(\vec{x})$, is then estimated by solving the P "virtual experiments" as a least-square problem or by the Singular Value Decomposition (SVD) method [13].

As the optimization techniques discussed above belong to local optimization methods, all of them are prone to the occurrence of false solutions [27]. *A priori* information of the scatterers, such as a good initial guess, the position and the quantity of the scatterers, etc., is normally required for ensuring the inversion performance. Hybrid inversion methods [104, 109–111] were also proposed, in which the support of the scatterers is first determined by qualitative inversion methods and then used as *a priori* information for quantitative inversion.

2.4 CONCLUSIONS

In this chapter, the EM direct scattering problem is formulated by means of the FDFD scheme, and the computing accuracy of a solver package, "MaxwellFDFD", and its companion C program, "FD3D", is tested numerically with 2-D and 3-D benchmark problems. Based on the FDFD scheme, the EM inverse scattering problem is formulated and introduced. Finally, a review of the challenges and the state-of-the-art of inversion techniques is presented. The fundamentals presented in this chapter are important for introducing the following chapters.

3

Cross-Correlated Contrast Source Inversion

In iterative inversion methods, the cost functional to be minimized generally consists of two additive terms: the data error term and the state error term [37]. On one hand, the data error term ensures that the model fits the measurements; On the other hand, the state error term ensures that the model satisfies Maxwell's equations. For iterative inversion methods, a good initial guess is required such that the iterative inversion process departs on the right track leading to the global optimal solution. In classical nonlinear iterative inversion algorithms, the contrast is sought by minimizing not only the data error but also the state error. In doing so, the estimated solution is monitored by Maxwell's equations in the field domain during the whole inversion process. However, the state error still needs to be monitored in the measurement domain. Otherwise, the mapping of the state error to the measurement domain may run out of control. Inspired by this fact, a so-called cross-correlated error term is proposed in this chapter. The name comes from the fact that it is an interrelation between the state error term and the data error term. By introducing this novel error term to the cost functional, the state error and the data error are cross-correlated, leading to a more robust inversion method, the Cross-Correlated Contrast Source Inversion (CC-CSI) method.

The remainder of this chapter is organized as follows: this cross-correlated error term and the novel inversion method are introduced in Section 3.1, from which one can see how the gradient of the new cost functional is calculated without significantly increasing the computational complexity. The performance of the proposed method is investigated based on a 2-Dimensional (2-D) benchmark problem excited by both Transverse Magnetic (TM)- and Transverse Electric (TE)-polarized waves. The proposed CC-CSI method turns out to be more robust, and it is also of higher inversion accuracy

Parts of this chapter have been published in [112] and submitted to [113].

compared to both classical Contrast Source Inversion (CSI) and Multiplicative Regularized Contrast Source Inversion (MR-CSI). In Section 3.2, a multi-frequency version of CC-CSI, referred to as Multi-Frequency Cross-Correlated Contrast Source Inversion (MF-CC-CSI), is proposed, which exploits the frequency diversity by inverting multi-frequency data simultaneously. A numerical simulation is presented in Section 3.2.2, and an example of the experimental data inversion is given in Section 3.2.3. It is demonstrated that the advantage brought by the new error term is still significant in the multi-frequency cases. As Maxwell's equations are formulated with a 3-Dimensional (3-D) Finite Difference Frequency Domain (FDFD) formulation, it can be straightforwardly applied to the reconstruct 3-D scattering objects.

3.1 CROSS-CORRELATED ERROR AND CC-CSI

3.1.1 MOTIVATION

As mentioned before, a good initial guess is critical for the iterative methods to successfully converge to the global optimal solution. This can be explained firstly by the fact that there are two unknown variables — the contrast and the contrast sources. Secondly, although classical CSI is able to minimize the data error by constraining the state error at the meantime, a global optimal solution is still not guaranteed because of the severe ill-posedness. For simplicity, let us first define the measurement matrix as $\boldsymbol{\Phi}_p := \boldsymbol{M}_{\mathcal{S},p}\boldsymbol{A}^{-1}$. The condition number of matrix $\boldsymbol{\Phi}_p$ is further defined as

$$\kappa(\boldsymbol{\Phi}_p) := \sigma_{\max}\left(\boldsymbol{\Phi}_p\right)/\sigma_{\min}\left(\boldsymbol{\Phi}_p\right), \tag{3.1}$$

where, $\sigma_{\max}\left(\boldsymbol{\Phi}_p\right)$ and $\sigma_{\min}\left(\boldsymbol{\Phi}_p\right)$ are maximal and minimal singular values of $\boldsymbol{\Phi}_p$, respectively. As discussed in Subsection 3.1.4, the measurement matrix has a large condition number, which means a minor state error in the field space, $L^2(\mathcal{D})$, may cause a large error in the measurement space, $L^2(\mathcal{S})$. This potential mismatch is neglected in the classical formulation of the cost functional. Inspired by the above analysis, a cross-correlated error term is proposed in the following. By introducing it to the cost functional, a novel inversion scheme, CC-CSI, is developed.

3.1.2 CROSS-CORRELATED ERROR

Recall Eq. (2.35) in Chapter 2, Eq. (2.36a) is the data equation in the measurement domain and Eq. (2.35b) is the state equation in the field domain. Eq. (2.35b) is used to monitor the behavior of the solution in the field domain and check if it satisfies Maxwell's equations. Since Eq. (2.35b) is always not perfectly satisfied, the "=" is supposed to be a "≈". Note that the solution is monitored only in the field domain, the mismatch in the field domain should also be monitored back in the measurement domain. Otherwise, the inversion scheme is not complete. In order to fill this gap, we define a new equation in the measurement domain as follows

$$\boldsymbol{y}_p = \boldsymbol{\Phi}_p\left(\boldsymbol{\chi}^{\text{iso}}\boldsymbol{e}_p^{\text{inc}} + \boldsymbol{\chi}^{\text{iso}}\boldsymbol{A}^{-1}\boldsymbol{j}_p\right). \tag{3.2}$$

In doing so, the solution is monitored not only in the field domain by the state error term but also in the measurement domain by the new equation, Eq. (3.2), which is actually a nonlinear data equation. Subsequently, the new error equation is formulated as follows

$$\boldsymbol{\xi}_p = \boldsymbol{y}_p - \boldsymbol{\Phi}_p \left(\boldsymbol{\chi}^{\text{iso}} \boldsymbol{e}_p^{\text{inc}} + \boldsymbol{\chi}^{\text{iso}} \boldsymbol{A}^{-1} \boldsymbol{j}_p \right). \tag{3.3}$$

And the new error term is defined as

$$\eta^{\mathcal{S}} \sum_{p=1}^{P} \left\| \boldsymbol{\xi}_p \right\|_{\mathcal{S}}^2, \tag{3.4}$$

where, $\eta^{\mathcal{S}}$ is a normalization factor given by Eq. (2.38). We refer to this novel error term as the cross-correlated error.

3.1.3 FORMULATION OF CC-CSI

FORMULATION OF THE COST FUNCTIONAL

By introducing this error term to the cost functional, a novel inversion method, CC-CSI, is proposed. Specifically, the cross-correlated error equation for reconstructing the contrast sources is defined as follows

$$\boldsymbol{\xi}_{p,\ell-1/2} = \boldsymbol{y}_p - \boldsymbol{\Phi}_p \left(\boldsymbol{\chi}_{\ell-1}^{\text{iso}} \boldsymbol{e}_p^{\text{inc}} + \boldsymbol{\chi}_{\ell-1}^{\text{iso}} \boldsymbol{A}^{-1} \boldsymbol{j}_{p,\ell-1} \right). \tag{3.5}$$

Note that if the state error is zero, then theoretically we have $\boldsymbol{\rho}_p = \boldsymbol{\xi}_p$. Sufficiently minimizing the cost function of Eq. (2.37) does not necessarily mean that the cross-correlated error has been sufficiently minimized. Therefore, the cost functional for updating the contrast source is modified as a superposition of three error terms, i.e.,

$$\mathcal{C}_{\text{CC-CSI},\ell-1/2} = \eta^{\mathcal{S}} \sum_{p=1}^{P} \left\| \boldsymbol{\rho}_{p,\ell-1/2} \right\|_{\mathcal{S}}^2 + \eta_{\ell-1}^{\mathcal{D}} \sum_{p=1}^{P} \left\| \boldsymbol{\gamma}_{p,\ell-1/2} \right\|_{\mathcal{D}}^2 + \eta^{\mathcal{S}} \sum_{p=1}^{P} \left\| \boldsymbol{\xi}_{p,\ell-1/2} \right\|_{\mathcal{S}}^2, \tag{3.6}$$

where, $\boldsymbol{\rho}_{p,\ell-1/2}$ and $\boldsymbol{\gamma}_{p,\ell-1/2}$ are defined in Eq. (2.36a) and Eq. (2.36b), respectively.

UPDATING THE CONTRAST SOURCES

The gradient (Fréchet derivative) of the modified cost functional, $\mathcal{C}_{\text{CC-CSI},\ell-1/2}$, with respect to the contrast sources, $\boldsymbol{j}_p$, is

$$\begin{aligned} \boldsymbol{g}_p = &-2\eta^{\mathcal{S}} \boldsymbol{\Phi}_p^H \boldsymbol{\rho}_{p,\ell-1/2} + 2\eta_{\ell-1}^{\mathcal{D}} \left(\boldsymbol{\chi}_{\ell-1}^{\text{iso}} \boldsymbol{A}^{-1} - \boldsymbol{I} \right)^H \boldsymbol{\gamma}_{p,\ell-1/2} - \\ &2\eta^{\mathcal{S}} \left(\boldsymbol{\Phi}_p \boldsymbol{\chi}_{\ell-1}^{\text{iso}} \boldsymbol{A}^{-1} \right)^H \boldsymbol{\xi}_{p,\ell-1/2}. \end{aligned} \tag{3.7}$$

In the following part of the thesis, $\boldsymbol{I}$ represents the identity matrix, and $(\cdot)^H$ is the conjugate transpose operator. Now suppose $\boldsymbol{j}_{p,\ell-1}$ and $\boldsymbol{\chi}_{\ell-1}$ are known, then we update the contrast sources by

$$\boldsymbol{j}_{p,\ell} = \boldsymbol{j}_{p,\ell-1} + \alpha_{p,\ell} \boldsymbol{\nu}_{p,\ell}, \tag{3.8}$$

where, $\alpha_{p,\ell}$ is constant, and the update directions, $\boldsymbol{\nu}_{p,\ell}$, are the update directions chosen to be the Polak-Ribière conjugate gradient directions, given by

$$\boldsymbol{\nu}_{p,\ell} = \begin{cases} 0, & \ell = 0, \\ \boldsymbol{g}_{p,\ell} + \dfrac{\sum_{p'} \left\langle \boldsymbol{g}_{p',\ell}, \boldsymbol{g}_{p',\ell} - \boldsymbol{g}_{p',\ell-1} \right\rangle_{\mathcal{D}}}{\sum_{p'} \left\| \boldsymbol{g}_{p',\ell-1} \right\|_{\mathcal{D}}^2} \boldsymbol{\nu}_{p,\ell-1}, & \ell \geq 1, \end{cases} \tag{3.9}$$

where,

$$\boldsymbol{g}_{p,\ell} = \boldsymbol{g}_p \big|_{\boldsymbol{j}_p = \boldsymbol{j}_{p,\ell-1}}. \tag{3.10}$$

The step size, $\alpha_{p,\ell}$, can be explicitly found as

$$\arg\min_{\alpha_p} \quad \mathcal{C}_{\text{CC-CSI},\ell-1/2} \big|_{\boldsymbol{j}_p = \boldsymbol{j}_{p,\ell-1} + \alpha_p \boldsymbol{\nu}_{p,\ell}}. \tag{3.11}$$

See Appendix A.1 for its derivation.

UPDATING THE CONTRAST

Once the contrast sources are updated, we update the contrast by

$$\boldsymbol{\chi}_\ell^{\text{iso}} = \boldsymbol{\chi}_{\ell-1}^{\text{iso}} + \beta_\ell \boldsymbol{\nu}_\ell^{\text{iso}}, \tag{3.12}$$

where, β_ℓ is the step size and the update direction, $\boldsymbol{\nu}_\ell^{\text{iso}}$, is in the formulation of

$$\boldsymbol{\nu}_\ell^{\text{iso}} = \left[\boldsymbol{\nu}_\ell^{\chi\,T} \; \boldsymbol{\nu}_\ell^{\chi\,T} \; \boldsymbol{\nu}_\ell^{\chi\,T} \right]^T, \tag{3.13}$$

where, $(\cdot)^T$ represents the transpose operator, $\boldsymbol{\nu}_\ell^\chi$ are the Polak-Ribière conjugate gradient directions, given by

$$\boldsymbol{\nu}_\ell^\chi = \begin{cases} 0, & \ell = 0, \\ \boldsymbol{g}_\ell^\chi + \dfrac{\left\langle \boldsymbol{g}_\ell^\chi, \boldsymbol{g}_\ell^\chi - \boldsymbol{g}_{\ell-1}^\chi \right\rangle_{\mathcal{D}}}{\left\| \boldsymbol{g}_{\ell-1}^\chi \right\|_{\mathcal{D}}^2} \boldsymbol{\nu}_{\ell-1}^\chi, & \ell \geq 1, \end{cases} \tag{3.14}$$

where, $\boldsymbol{g}_\ell^\chi$ is the preconditioned gradient of the contrast cost functional

$$\mathcal{C}_{\text{CC-CSI},\ell} = \eta_{\ell-1}^{\mathcal{D}} \sum_{p=1}^{P} \left\| \boldsymbol{\gamma}_{p,\ell} \right\|_{\mathcal{D}}^2 + \eta^{\mathcal{S}} \sum_{p=1}^{P} \left\| \boldsymbol{\xi}_{p,\ell} \right\|_{\mathcal{S}}^2, \tag{3.15}$$

in which, $\boldsymbol{\gamma}_{p,\ell}$ is defined by Eq. (2.44), and $\boldsymbol{\xi}_{p,\ell}$ is defined as

$$\boldsymbol{\xi}_{p,\ell} = \boldsymbol{y}_p - \boldsymbol{\Phi}_p \left(\boldsymbol{\chi}_{\ell-1}^{\text{iso}} \boldsymbol{e}_p^{\text{inc}} + \boldsymbol{\chi}_{\ell-1}^{\text{iso}} \boldsymbol{A}^{-1} \boldsymbol{j}_{p,\ell} \right). \tag{3.16}$$

Specifically, $\boldsymbol{g}_\ell^\chi$ is found to be

$$\boldsymbol{g}_\ell^\chi = \left. \frac{2\eta_{\ell-1}^{\mathcal{D}} \sum_{p=1}^{P} \sum_\gamma \overline{\boldsymbol{e}_{p,\gamma,\ell}^{\text{tot}}} \boldsymbol{\gamma}_{p,\gamma,\ell} - 2\eta^{\mathcal{S}} \sum_{p=1}^{P} \sum_\gamma \overline{\boldsymbol{e}_{p,\gamma,\ell}^{\text{tot}}} \boldsymbol{\Phi}_p^H \boldsymbol{\xi}_{p,\gamma,\ell}}{\sum_{p=1}^{P} \sum_\gamma \boldsymbol{e}_{p,\gamma,\ell}^{\text{tot}} \overline{\boldsymbol{e}_{p,\gamma,\ell}^{\text{tot}}}} \right|_{\boldsymbol{\chi} = \boldsymbol{\chi}_{\ell-1}}. \tag{3.17}$$

The step size, β_ℓ, is determined by minimizing

$$\frac{\sum_{p=1}^{P}\left\|\left(\boldsymbol{\chi}_{\ell-1}^{\text{iso}}+\beta\boldsymbol{v}_{\ell}^{\text{iso}}\right)\boldsymbol{e}_{p,\ell}^{\text{tot}}-\boldsymbol{j}_{p,\ell}\right\|_{\mathcal{D}}^{2}}{\sum_{p=1}^{P}\left\|\left(\boldsymbol{\chi}_{\ell-1}^{\text{iso}}+\beta\boldsymbol{v}_{\ell}^{\text{iso}}\right)\boldsymbol{e}_{p}^{\text{inc}}\right\|_{\mathcal{D}}^{2}}+\eta^{\mathcal{S}}\sum_{p=1}^{P}\left\|\boldsymbol{y}_{p}-\boldsymbol{\Phi}_{p}\left(\boldsymbol{\chi}_{\ell-1}^{\text{iso}}+\beta\boldsymbol{v}_{\ell}^{\text{iso}}\right)\boldsymbol{e}_{p,\ell}^{\text{tot}}\right\|_{\mathcal{S}}^{2}. \tag{3.18}$$

This is a problem of finding the minimum of a single-variable function, and can be solved efficiently by the Brent's method [114, 115].

3

INITIALIZATION

If no *a priori* information is available, the contrast sources are initialized by (see [85, 116])

$$\boldsymbol{j}_{p,0}=\frac{\left\|\boldsymbol{\Phi}_{p}^{H}\boldsymbol{y}_{p}\right\|_{\mathcal{D}}^{2}}{\left\|\boldsymbol{\Phi}_{p}\boldsymbol{\Phi}_{p}^{H}\boldsymbol{y}_{p}\right\|_{\mathcal{S}}^{2}}\boldsymbol{\Phi}_{p}^{H}\boldsymbol{y}_{p}, \tag{3.19}$$

which are obtained by back-propagation, multiplied by a weight to ensure that the data error is minimized. The contrast is initialized by (see [45])

$$\boldsymbol{\chi}_{0}=\left(\sum_{p=1}^{P}\sum_{\gamma}\boldsymbol{j}_{p,\gamma,0}\overline{\boldsymbol{e}_{p,\gamma,0}^{\text{tot}}}\right)\oslash\left(\sum_{p=1}^{P}\sum_{\gamma}\boldsymbol{e}_{p,\gamma,0}^{\text{tot}}\overline{\boldsymbol{e}_{p,\gamma,0}^{\text{tot}}}\right), \tag{3.20}$$

with $\boldsymbol{e}_{p,0}^{\text{tot}}=\boldsymbol{e}_{p}^{\text{inc}}+\boldsymbol{A}^{-1}\boldsymbol{j}_{p,0}$. Note that "$\oslash$" represents the element-wise division in the following of this thesis.

The CC-CSI method is given in Algorithm 1, where $\Re\{\cdot\}$ represents the real part operator and, correspondingly, the imaginary part operator is represented by $\Im\{\cdot\}$. Since the objects are assumed to be isotropic, we average the two components of the contrast for TE cases, and the three components of the contrast for 3-D case, after each update of the contrast.

CONSTRUCTION OF THE SENSING MATRIX, $\boldsymbol{\Phi}_p$

In this subsection, we show that the CC-CSI method can be implemented without significantly increasing the computational complexity compared to the classical CSI method. Since the selecting matrix, $\boldsymbol{M}_{\mathcal{S},p}\in\mathbb{C}^{M\times N}$, has only $M<<N$ rows, the sensing matrix, $\boldsymbol{\Phi}_p$, can be calculated iteratively by solving M linear systems of equations,

$$\boldsymbol{A}^{T}\boldsymbol{\varphi}_{m,p}=\boldsymbol{M}_{\mathcal{S},p}^{m\ T},\quad m=1,2,3,\cdots,M, \tag{3.21}$$

where, $\boldsymbol{M}_{\mathcal{S},p}^{m}$ is the m-th row of the selecting matrix $\boldsymbol{M}_{\mathcal{S},p}$. The sensing matrix is then assembled by $\boldsymbol{\Phi}_p=\left[\boldsymbol{\varphi}_{1,p},\boldsymbol{\varphi}_{2,p},\cdots,\boldsymbol{\varphi}_{M,p}\right]^{T}$. Since $M<<N$, it is computationally much more efficient than the Lower Upper (LU) decomposition of the stiffness matrix $\boldsymbol{A}$ (if LU decomposition is used). This feature also makes it suitable to be computed and stored beforehand, which is of great importance for real applications, especially for 3-D inverse scattering problems. Although CC-CSI requires more matrix-vector multiplications, the extra computational cost is not significant as long as $M<<N$.

Algorithm 1: Cross-correlated Contrast Source Inversion.

Input : $\boldsymbol{A}$, $\boldsymbol{\Phi}_p$, $\boldsymbol{j}_p$, $\boldsymbol{e}_p^{\text{inc}}$

Output: $\boldsymbol{\chi}$

Initialize the contrast sources, $\boldsymbol{j}_p$;

Initialize the total fields by $\boldsymbol{e}_p^{\text{tot}} = \boldsymbol{e}_p^{\text{sct}} + \boldsymbol{e}_p^{\text{inc}}$, where $\boldsymbol{e}_p^{\text{sct}} = \boldsymbol{A}^{-1}\boldsymbol{j}_p$;

$\eta^S = \left(\sum_{p=1}^{P} \left\|\boldsymbol{y}_p\right\|_{\mathcal{S}}^2\right)^{-1}$, $\boldsymbol{g}^\chi = \boldsymbol{0}$, $\boldsymbol{v}_p = \boldsymbol{0}$, $\boldsymbol{v}_\chi = \boldsymbol{0}$;

Initialize the contrast, $\boldsymbol{\chi}$, by Eq. (3.20);

Set the maximum number of iterates, N_{max}, and set $\ell = 1$;

begin

  If $\ell > N_{\text{max}}$, **then** break;

  $\eta^{\mathcal{D}} \leftarrow \left(\sum_{p=1}^{P} \left\|\boldsymbol{\chi}^{\text{iso}}\boldsymbol{e}_p^{\text{inc}}\right\|_{\mathcal{D}}^2\right)^{-1}$;

  $\boldsymbol{\rho}_p \leftarrow \boldsymbol{y}_p - \boldsymbol{\Phi}_p\boldsymbol{j}_p$ ▷ compute the data error;

  $\boldsymbol{\xi}_p \leftarrow \boldsymbol{y}_p - \boldsymbol{\Phi}_p\boldsymbol{\chi}^{\text{iso}}\boldsymbol{e}_p^{\text{tot}}$ ▷ compute the cross-correlated error;

  $\boldsymbol{\gamma}_p \leftarrow \boldsymbol{\chi}^{\text{iso}}\boldsymbol{e}_p^{\text{tot}} - \boldsymbol{j}_p$ ▷ compute the state error;

  $\boldsymbol{g}_p^{\text{old}} \leftarrow \boldsymbol{g}_p$, and calculate the gradient $\boldsymbol{g}_p$ by Eq. (3.7);

  $\boldsymbol{v}_p \leftarrow \boldsymbol{g}_p + \frac{\sum_{p'}\left\langle \boldsymbol{g}_{p'}, \boldsymbol{g}_{p'} - \boldsymbol{g}_{p'}^{\text{old}}\right\rangle_{\mathcal{D}}}{\sum_{p'}\left\|\boldsymbol{g}_{p'}^{\text{old}}\right\|_{\mathcal{D}}^2}\boldsymbol{v}_p$ ▷ Polak-Ribière conjugate gradient;

  Compute the step sizes, α_p, by Eq. (A.22) ▷ compute the step size α_p;

  $\boldsymbol{j}_p \leftarrow \boldsymbol{j}_p + \alpha_p\boldsymbol{v}_p$ ▷ update the contrast sources;

  $\boldsymbol{e}_p^{\text{tot}} \leftarrow \boldsymbol{e}_p^{\text{tot}} + \alpha_p\boldsymbol{e}_p^{v}$, where $\boldsymbol{e}_p^{v} \leftarrow \boldsymbol{A}^{-1}\boldsymbol{v}_p$ ▷ update the total fields;

  $\boldsymbol{\gamma}_p \leftarrow \boldsymbol{\chi}^{\text{iso}}\boldsymbol{e}_p^{\text{tot}} - \boldsymbol{j}_p$ ▷ update the state error;

  $\boldsymbol{\xi}_p \leftarrow \boldsymbol{y}_p - \boldsymbol{\Phi}_p\boldsymbol{\chi}^{\text{iso}}\boldsymbol{e}_p^{\text{tot}}$ ▷ update the cross-correlated error;

  $\boldsymbol{g}_{\text{old}}^\chi \leftarrow \boldsymbol{g}^\chi$, and $\boldsymbol{g}^\chi$ is calculated by Eq. (3.17);

  $\boldsymbol{v}^\chi \leftarrow \boldsymbol{g}^\chi + \frac{\left\langle \boldsymbol{g}^\chi, \boldsymbol{g}^\chi - \boldsymbol{g}_{\text{old}}^\chi\right\rangle_{\mathcal{D}}}{\left\|\boldsymbol{g}_{\text{old}}^\chi\right\|_{\mathcal{D}}^2}\boldsymbol{v}^\chi$;

  The step size, β, is determined by minimizing Eq. (3.18) ▷ compute the step size β;

  $\boldsymbol{\chi} \leftarrow \boldsymbol{\chi} + \beta\boldsymbol{v}^\chi$ ▷ update the contrast;

  $\ell \leftarrow \ell + 1$;

end

return $\boldsymbol{\chi}$;

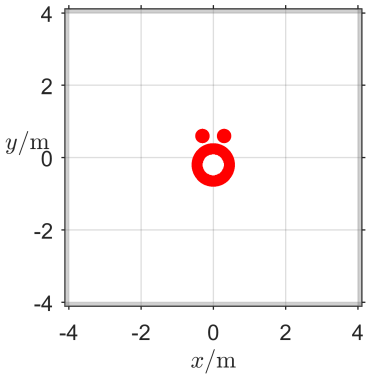

Figure 3.1: Original "Austria" profile contained in a region of $[-4, 4] \times [-4, 4]$ m^2. The boundaries of the four sides are terminated with PMLs. The two z-normal boundaries are subject to PBCs.

In a simple case where the background is homogeneous medium, the sensing matrices can be analytically given. Take the TM-polarization case as an example, $\mathbf{\Phi}_p$ is analytically formulated as follows

$$\mathbf{\Phi}_p[q,n] = \frac{\mathrm{i}\omega_i\mu_0}{4} H_0^{(1)}\left(-k\left\|\vec{x}_{p,q} - \vec{x}_n\right\|_2\right), \tag{3.22}$$

where, $\mathbf{\Phi}_p[q,n]$ is the entry in the q-th row and n-th column of matrix $\mathbf{\Phi}_p$; $H_0^{(1)}(\cdot)$ is the Hankel function of the first kind; $\vec{x}_{p,q}$ is the position vector of the q-th receiver corresponding to the p-th source; $\vec{x}_n$ is the n-th position vector in the discretized inversion domain. The construction of the sensing matrix in homogeneous background medium for the TE-polarization case and the 3-D case is given in Appendix B.

3.1.4 NUMERICAL SIMULATION

CONFIGURATION

In this section, the proposed algorithm is tested with a 2-D benchmark problem — the "Austria" profile, which was also used in [105, 117–119]. Based on the benchmark problem, the performance of CC-CSI is analyzed in comparison to classical CSI and MR-CSI. Specifically, the objects to be inverted consist of two disks and one ring. Let us first establish our coordinate system such that the z-axis is parallel to the axis of the objects. The disks of radius 0.2 m are centred at $(-0.3, 0.6)$ m and $(0.3, 0.6)$ m. The ring is centred at $(0, -0.2)$ m, and it has an exterior radius of 0.6 m and an inner radius of 0.3 m. The geometry of the "Austria" profile is shown in Fig. 3.1.

The ElectroMagnetic (EM) direct scattering problem is solved by a MATLAB-based 3-D FDFD package "MaxwellFDFD" [30]. The x- and y-normal boundaries are covered by Perfectly Matched Layers (PMLs) to simulate the anechoic chamber environment (see the gray layers of Fig. 3.1 at the boundaries of the test domain), while the two

z-normal boundaries are subject to Periodic Boundary Conditions (PBCs) to simulate the 2-D configuration. Line sources parallel to the z-axis are used to generate TM-polarized and TE-polarized incident waves. Non-uniform meshes are used to generate the scattered data, which means the testing domain is discretized with different mesh sizes determined by the distribution of the permittivity, viz., coarse meshes for low permittivity and fine meshes for high permittivity. The accuracy of the FDFD scheme is ensured by the following criterion [35]

$$\Delta \leq \frac{\lambda_0}{15\sqrt{\varepsilon_r}}, \tag{3.23}$$

where, λ_0 is the wavelength in the free space. Non-uniform meshes greatly reduce the computational burden for solving the direct scattering problem. In contrast, uniform meshes are used to invert the scattered data, since the distribution of the permittivity is unknown beforehand. A criterion to guarantee the inverting accuracy is

$$\Delta \leq \frac{\lambda_0}{15\sqrt{\max\{\varepsilon_r\}}}. \tag{3.24}$$

In our simulation, the electric line source (TM polarization) and the magnetic line source (TE polarization) are considered simultaneously since there are no interactions with each other. The three components of the incident fields (in the absence of the scatterers) and the total fields (in the presence of the scatterers) are collected at the positions of the receivers. The x- and y-components correspond to the TE polarization and the z-component corresponds to the TM polarization. The measurement data of the scattered fields are obtained by subtracting the incident fields from the total fields.

Belkebir and Tijhuis [117] and Litman et al. [118] have used 64 sources and 65 receivers on a circle of radius 3 m centred at (0, 0), while the inverting domain was discretized into 30 × 30 cells. Van den Berg et al. [105, 119] have taken 48 source/receiver stations, while the inverting domain was discretized into 64 × 64 cells. In our simulation, we considered a 2-D bistatic measurement configuration similar to the one used in the experiments of the Fresnel datasets [31, 32]. For a fair comparison, the contrast sources are initialized by Eq. (3.19), and the contrast is initialized by Eq. (3.20) for all the three algorithms. Two examples in a free space with different measurement configurations are considered. The positivity of the real part of the contrast and the negativity of the imaginary part of the contrast are enforced in the inversion by setting the negative real part and the positive imaginary part zero.

EXAMPLE 1

The measurement configuration of the first example is shown in Fig. 3.2. One transmitter and one receiver are positioned on a circle of radius 3 m centred at the origin (0, 0). For the sake of simplicity, let us consider the polar coordinate system. Let ϕ_T and ϕ_R represent the angular components of the transmitter position vector and the receiver position vector, respectively. In the first round of measurement, $\phi_T = 0°$ and the receiver rotates such that ϕ_R varies from 60° to 300° in steps of 5°. In the second round of measurement, $\phi_T = 30°$ and the receiver rotates such that ϕ_R varies from 90° to 330°

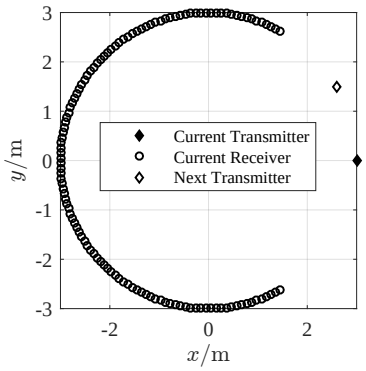

Figure 3.2: Measurement configuration of Example 1.

Table 3.1: Condition numbers of the sensing matrices of TM/TE-polarization at 300 MHz and 400 MHz.

$\kappa(\boldsymbol{\Phi}_p)$ Frequency / Polarization	300 MHz	400 MHz
TM	3.49×10^{15}	2.04×10^{15}
TE	1.17×10^{16}	7.58×10^{15}

in steps of 5°. In this way, the transmitter rotates from 0° to 330° in steps of 30°, and 12 rounds of measurements are carried out in total.

In this example, lossy scatterers are tested. The conductivity of the three cylinders is 10 mS/m, and the relative permittivity is 3.0. The measurements are carried out at two operating frequencies, 300 MHz and 400 MHz. The corresponding values of the contrast are $\chi = 2.0 - 0.6\mathrm{i}$ at 300 MHz and $\chi = 2.0 - 0.45\mathrm{i}$ at 400 MHz. The inversion domain is restricted to the region $[-1.5, 1.5] \times [-1.5, 1.5]$ m^2. The dimension of the mesh grid is 30 $\times$ 30 mm^2. As the receiver rotates along a circle, there are 72 different receiving positions, and we have a sensing matrix $\boldsymbol{\Phi}_p \in \mathbb{C}^{49\times 10000}$ for TM polarization, and $\boldsymbol{\Phi}_p \in \mathbb{C}^{98\times 20000}$ for TE polarization. The positions on the arc where the receiver does not work are not considered in the inversion by the three methods. The condition numbers of the sensing matrices of the two polarization at 300 MHz and 400 MHz are listed in Table 3.1. As one can see the condition numbers of the sensing matrices for both TM and TE polarization are of large values, indicating that an error in the contrast sources, $\boldsymbol{j}_p$, may cause an increased error in the measurement data, $\boldsymbol{y}_p$. It is worth noting that in the formulation of TE scattering problems, the operators involved have the same form, but one spatial dimension lower, compared to full 3-D scattering problems. Hence, the performance gain with CC-CSI in future 3-D inversion problems can be compared to the performance gain in TE cases.

To simulate the inevitable measurement error in real experiments, additive Gaussian

random noise, $\boldsymbol{n}_p$, is added directly to the scattered field data. The power of the scattered field data matrix is measured before adding noise. In addition, the noise is also added to the total field data and the incident field data by $\boldsymbol{y}_p^{\text{tot}} + \boldsymbol{n}_p/2$ and $\boldsymbol{y}_p^{\text{inc}} - \boldsymbol{n}_p/2$, respectively. In doing so, the disturbance of the noise is reflected not only in the scattered field data but also in the modelling of the incident fields, which better approaches the real situation. To appraise the inversion performance (inversion accuracy and rate of convergence) quantitatively, let us define the reconstruction errors as follows

$$err_\chi = \|\boldsymbol{\chi} - \hat{\boldsymbol{\chi}}\|_{\mathcal{D}} / \|\boldsymbol{\chi}\|_{\mathcal{D}}\,, \tag{3.25a}$$

$$err_\varepsilon = \|\Re\{\boldsymbol{\chi} - \hat{\boldsymbol{\chi}}\}\|_{\mathcal{D}} / \|\Re\{\boldsymbol{\chi}\}\|_{\mathcal{D}}\,, \tag{3.25b}$$

$$err_\sigma = \|\Im\{\boldsymbol{\chi} - \hat{\boldsymbol{\chi}}\}\|_{\mathcal{D}} / \|\Im\{\boldsymbol{\chi}\}\|_{\mathcal{D}}\,, \tag{3.25c}$$

where, $\boldsymbol{\chi}$ and $\hat{\boldsymbol{\chi}}$ are the true contrast and the inverted contrast, respectively; err_χ, err_ε, and err_σ are respectively the complex contrast error, the permittivity error and the conductivity error. Three of the errors enable us to appraise the inversion accuracy from different perspectives.

TM-polarized data Let us first consider the inversion of the TM data. Since the incident fields in the Region Of Interest (ROI) is not available in real applications, we consider the modelling of the incident fields, although actually the numerical solutions of the incident fields are known in our simulations. We use the approach reported in [120] to model the incident fields. Specifically, the transmitting antenna is approximated by line source parallel to the cylindrical objects. The amplitude and phase are calibrated by multiplying a complex ratio which is calculated using only the value of the field when the transmitting and the receiving antennas are in opposite directions. For each frequency and each source position, one complex calibration factor is determined. The incident field measurement data and the modelling data are shown in Fig. 3.3 for comparison with disturbance of different Signal to Noise Ratios (SNRs), 30 dB (a, b) and 10 dB (c-d), respectively.

From Fig. 3.3 (a) we observe that, in the inversion of the 300 MHz TM data, the three methods obtain approximately an equal complex contrast error (about 0.4) after 2048 iterations. Classical CSI and CC-CSI have similar complex contrast error curves, while the one of MR-CSI decreases faster in the first 1000 iterations, indicating the Total Variation (TV) regularization indeed speeds up the rate of convergence in this case. However, when the SNR of the 300 MHz data decreases to 10 dB, the complex contrast error curve of MR-CSI does not decrease anymore. In addition, we can also see from Fig. 3.3 (a) that, in the inversion of the 10 dB SNR data, the complex contrast error curves of classical CSI and CC-CSI start to increase after about 700 iterations, which tells us that a good termination condition is required for both classical CSI and CC-CSI, otherwise, the inversion accuracy may deteriorate after a mount of iterations when the disturbance of noise to the measurement data is not negligible. Now let us switch further to 400 MHz. From Fig. 3.3 (b) we observe that, for both 30 dB SNR data and 10 dB SNR data, the complex contrast error curves of both MR-CSI and classical CSI do not decrease either, while the one of CC-CSI is still going down although with a slower rate of convergence compared to the 300 MHz case and finally reaches a complex contrast error around

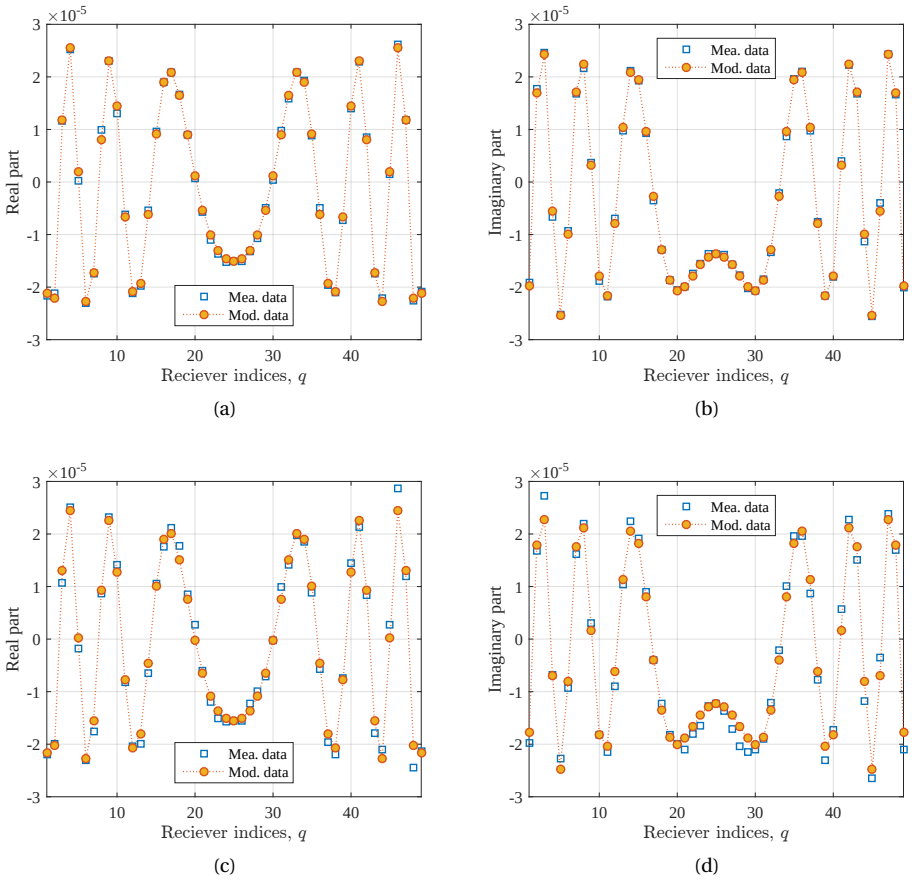

Figure 3.3: Comparison of the measurement data collected without scatterer and the data obtained by modelling the incident fields in the TM case. (a) Real part, 300 MHz; (b) Imaginary part, 300 MHz; (c) Real part, 400 MHz; (d) Imaginary part, 400 MHz.

0.7. From Figs. 3.3 (c) and 3.3 (d) we observe the same phenomena as Figs. 3.3 (a) and 3.3 (b), because the permittivity dominates the contrast in this example. From Fig. 3.3 (e) we observe that 1) the reconstruction of the conductivity is not as good as that of the permittivity; 2) classical CSI and CC-CSI arrive at an approximately equal conductivity error around 0.7; 3) the TV regularization further reduces the conductivity error by about 0.2 in the 300 MHz case; 4) all the methods fail to obtain a reasonable conductivity error in the 400 MHz.

As a summary of the above results, we first analyze the reason for the unstable performance of MR-CSI. As is well known, the TV regularization was originally proposed for the noise removal in digital image processing [121]. Obviously, the feasibility condition for applying the TV regularization is that one must first have an image which is suitable for processing. This is apparently not the case in classical CSI, because the

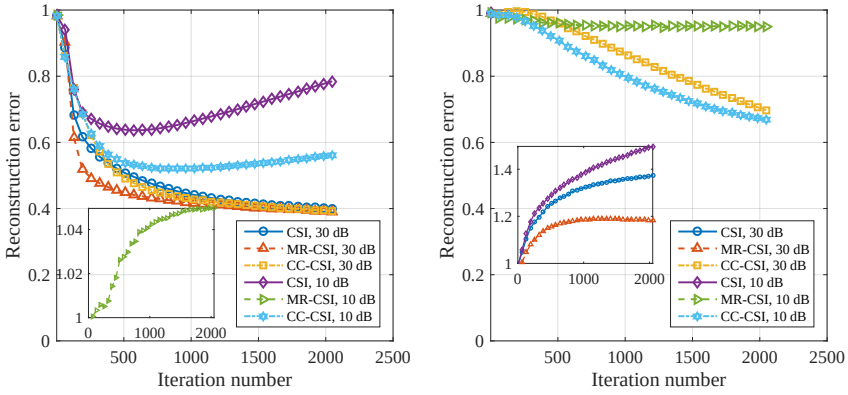

(a) Contrast error, 300 MHz (b) Contrast error, 400 MHz

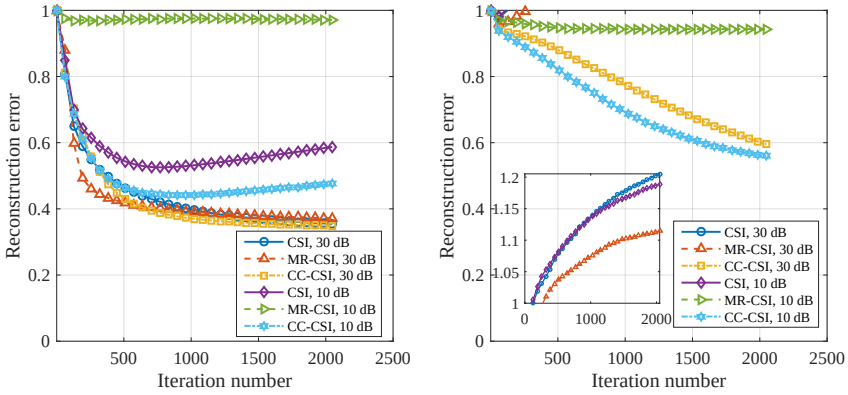

(c) Permittivity error, 300 MHz (d) Permittivity error, 400 MHz

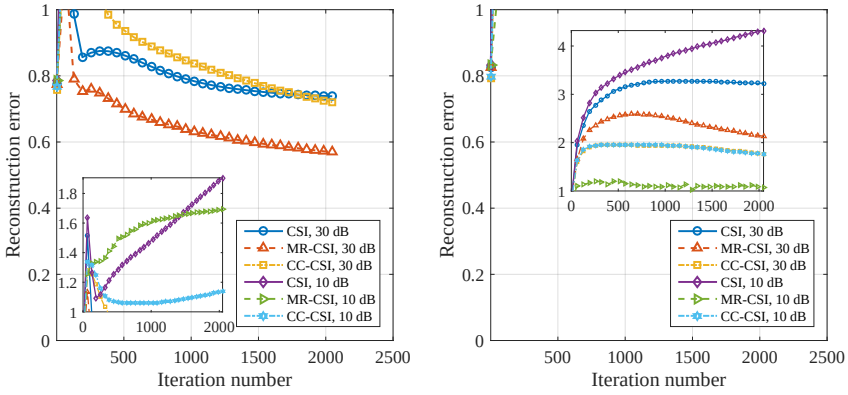

(e) Conductivity error, 300 MHz (f) Conductivity error, 400 MHz

Figure 3.4: Reconstruction error curves of classical CSI, MR-CSI, and CC-CSI in the TM case of Example 1. Left: 300 MHz; Right: 400 MHz. (a), (b): complex contrast error, err_χ; (c), (d): permittivity error, err_ε; (e), (f): conductivity error, err_σ;

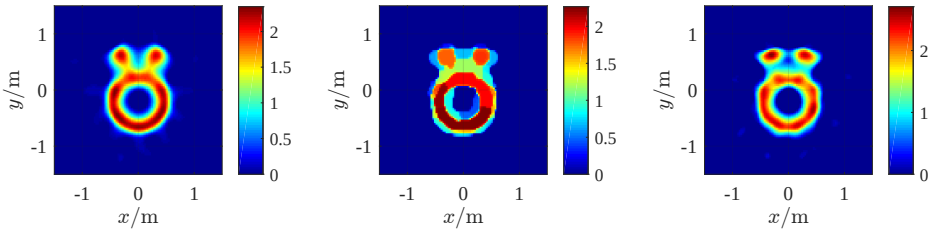

(a) $\varepsilon_{r,con}$, CC-CSI, 300 MHz (b) $\varepsilon_{r,con}$, MR-CSI, 300 MHz (c) $\varepsilon_{r,con}$, CSI, 300 MHz

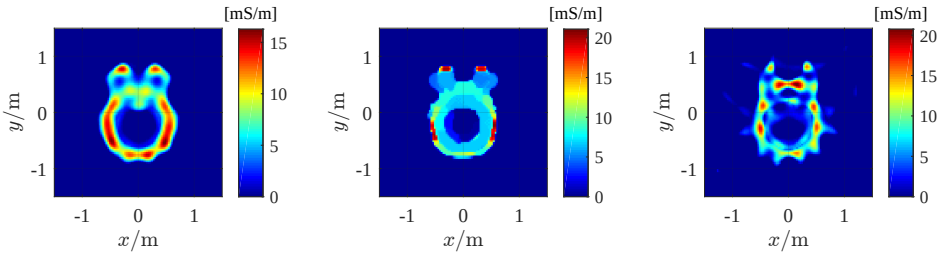

(d) σ_{con}, CC-CSI, 300 MHz (e) σ_{con}, MR-CSI, 300 MHz (f) σ_{con}, CSI, 300 MHz

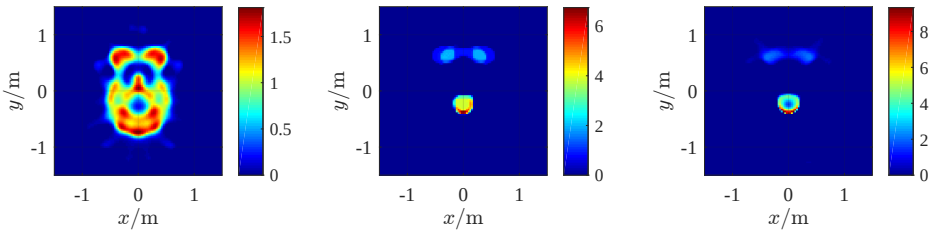

(g) $\varepsilon_{r,con}$, CC-CSI, 400 MHz (h) $\varepsilon_{r,con}$, MR-CSI, 400 MHz (i) $\varepsilon_{r,con}$, CSI, 400 MHz

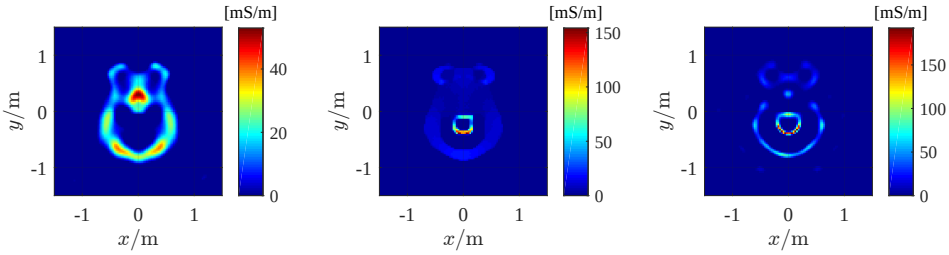

(j) σ_{con}, CC-CSI, 400 MHz (k) σ_{con}, MR-CSI, 400 MHz (l) σ_{con}, CSI, 400 MHz

Figure 3.5: Reconstructed relative permittivity, $\varepsilon_{r,con}$, and conductivity, σ_{con}, in Example 1 with 2048 iterations. SNR= 30dB. TM-polarization data.

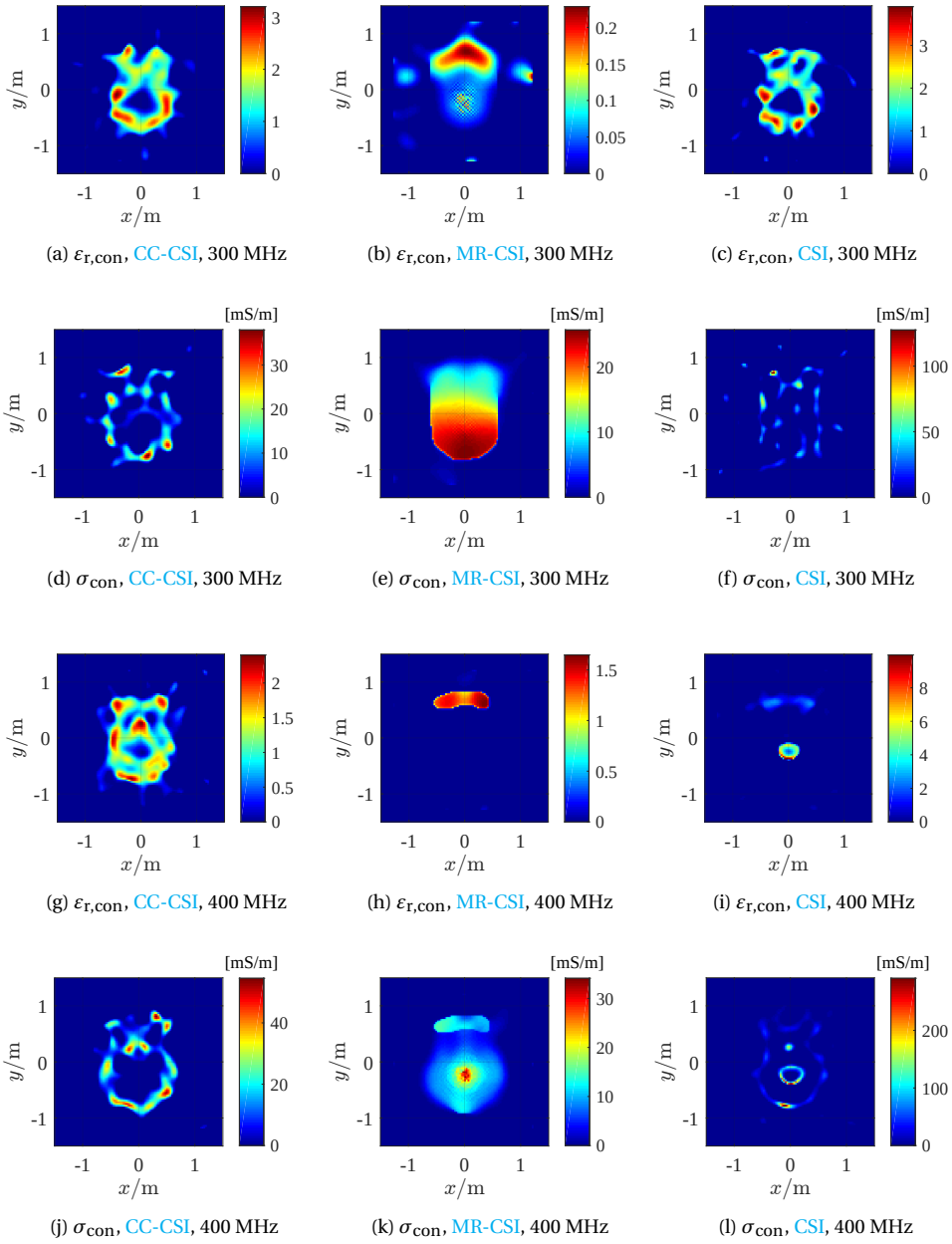

(a) $\varepsilon_{r,con}$, CC-CSI, 300 MHz (b) $\varepsilon_{r,con}$, MR-CSI, 300 MHz (c) $\varepsilon_{r,con}$, CSI, 300 MHz

(d) σ_{con}, CC-CSI, 300 MHz (e) σ_{con}, MR-CSI, 300 MHz (f) σ_{con}, CSI, 300 MHz

(g) $\varepsilon_{r,con}$, CC-CSI, 400 MHz (h) $\varepsilon_{r,con}$, MR-CSI, 400 MHz (i) $\varepsilon_{r,con}$, CSI, 400 MHz

(j) σ_{con}, CC-CSI, 400 MHz (k) σ_{con}, MR-CSI, 400 MHz (l) σ_{con}, CSI, 400 MHz

Figure 3.6: Reconstructed relative permittivity, $\varepsilon_{r,con}$, and conductivity, σ_{con}, in Example 1 with 2048 iterations. SNR= 10dB. TM-polarization data.

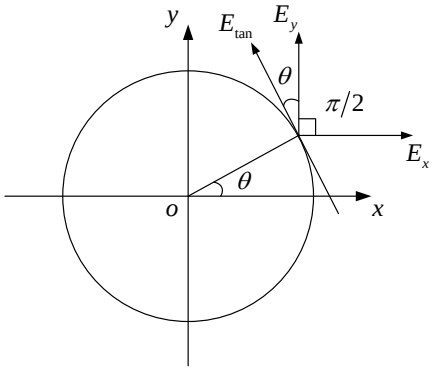

Figure 3.7: Geometric illustration of the tangential component of the electric field in TE cases.

contrast image in classical CSI is optimized iteratively. In the beginning of MR-CSI, the TV constraint is applied to an image that may have nothing to do with the true image. Therefore, it may mislead and degrade the optimization process. Benefits can be possibly obtained from MR-CSI only if the contrast can be reliably reconstructed without using the TV constraint. In other words, benefits from MR-CSI cannot be guaranteed in general situations.

The inversion results get worse when switching to a higher frequency because a high frequency means more complicated unknown total fields to estimate and more local minima the algorithms may encounter. There are at least two reasons for the higher conductivity error in comparison to the permittivity error: 1) The real part of the contrast is larger than the imaginary part, which means the permittivity dominates the contrast; 2) The existence of a conductivity suppresses the propagation of the EM wave. If the total field attenuates in the interior of the objects, its estimation gets more difficult.

The reconstructed permittivity and conductivity images are also given in Fig. 3.5 (SNR= 30 dB) and Fig. 3.6 (SNR= 10 dB) for a better view of the inverted results.

TE-polarized data In the TE case, the modelling of the incident fields is realized in the same way. Since there are two components involved — the x- and y-components, the complex calibration factor is determined using the tangential component of the incident field data, E_{tan}. As illustrated in Fig. 3.7, the calculation formula of E_{tan} is

$$E_{\text{tan}} = E_x \cos(\theta + \pi/2) + E_y \sin(\theta + \pi/2)\,. \tag{3.26}$$

Figs. 3.8 (a-b) and 3.8 (c-d) show the tangential components of the measurement data and the modelling data at 300 MHz and 400 MHz, respectively, for comparison.

Fig. 3.9 gives the comparison of the three reconstruction errors, from which one can get the same conclusions as for the TM case. By comparison of the TM results and the TE results, we can see that it is slightly more reliable to invert the TE data than inverting the TM data. The reason is due to the reduced degree of non-linearity for TE cases as compared to TM cases. We refer to [122] for more discussion about this problem.

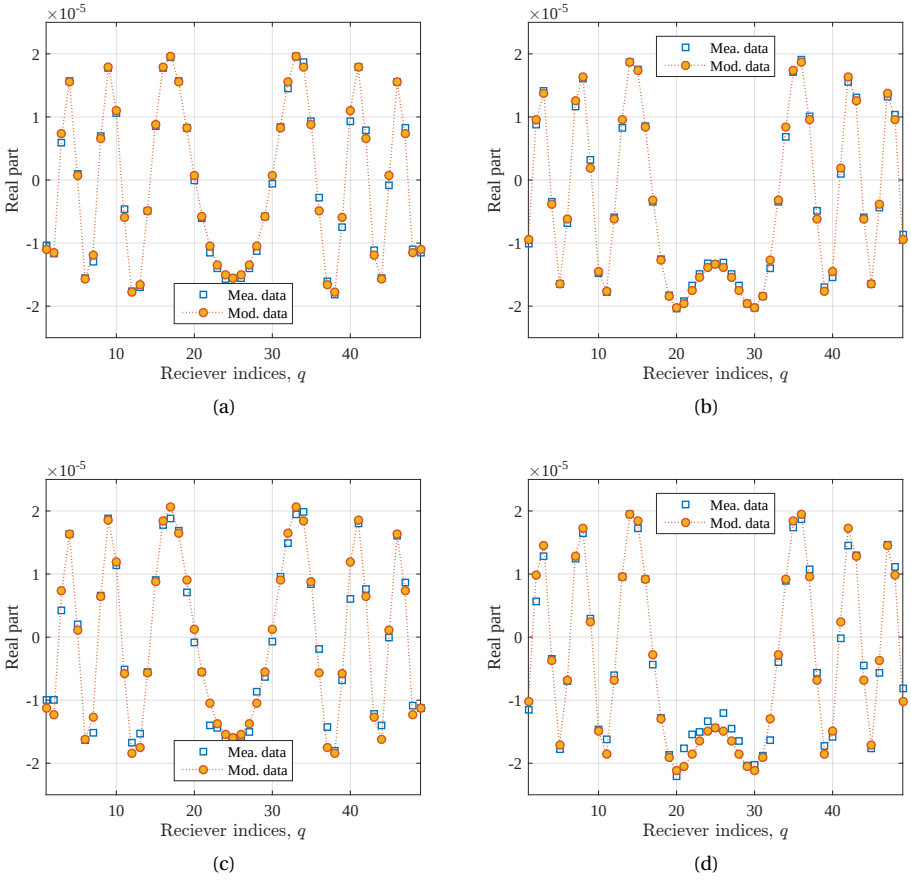

Figure 3.8: Comparison of the tangential component of the measurement data collected without scatterer and the one obtained by modelling the incident fields in the TE case. (a) Real part, 300 MHz; (b) Imaginary part, 300 MHz; (c) Real part, 400 MHz; (d) Imaginary part, 400 MHz.

Fig. 3.10 and Fig. 3.11 give the inverted permittivity and conductivity images by inverting the 30 dB SNR and 10 dB SNR TE-polarized data, respectively.

EXAMPLE 2

In the second example, let us consider the objects having the same geometry as in Example 1. The three cylinders are made of dielectric material ($\varepsilon_r = 3.0$, $\sigma = 0$ mS/m). The difference is that the interior of the ring is now filled with dielectric material ($\varepsilon_r = 1.5$, $\sigma = 0$ mS/m). The measurement configuration is shown in Fig. 3.12, which is similar to that of Example 1, except for the rotation steps of the transmitter and the receiver. Specifically, in the first round of measurement, $\phi_T = 0°$ and the receiver rotates such that ϕ_R varies from 60° to 300° in steps of 3°. In the second round of measurement, $\phi_T = 30°$ and the receiver rotates such that ϕ_R varies from 90° to 330° in steps of 3°. In this way,

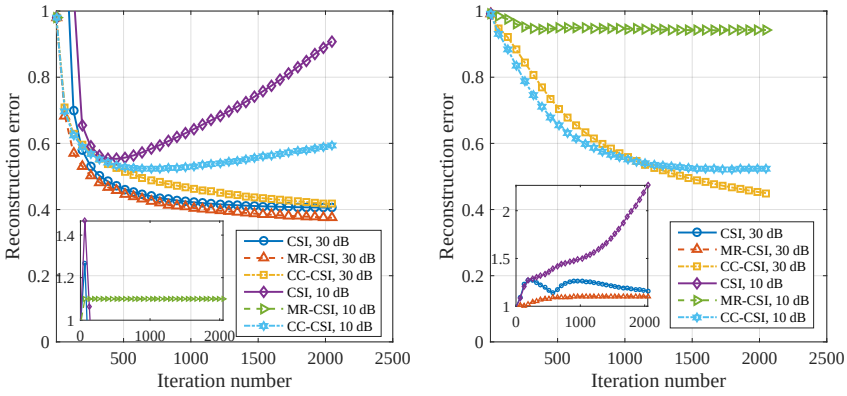

(a) Contrast error, 300 MHz (b) Contrast error, 400 MHz

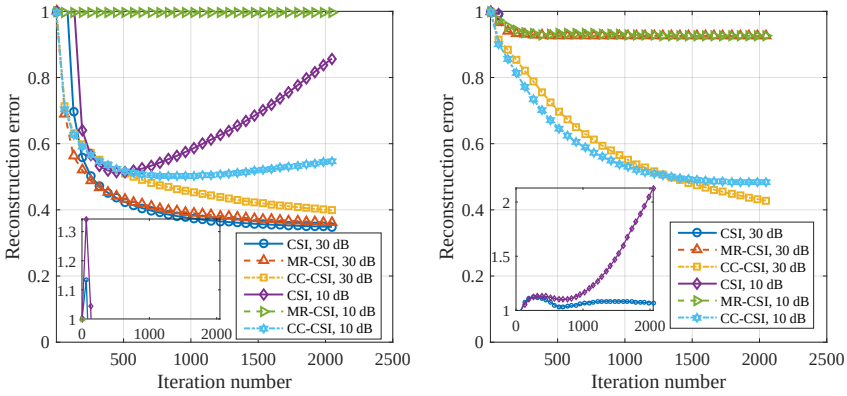

(c) Permittivity error, 300 MHz (d) Permittivity error, 400 MHz

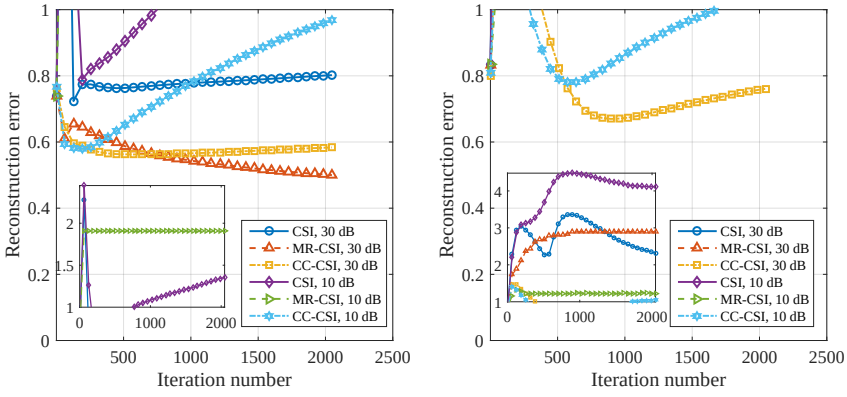

(e) Conductivity error, 300 MHz (f) Conductivity error, 400 MHz

Figure 3.9: Reconstruction error curves of classical CSI, MR-CSI, and CC-CSI in the TE case of Example 1. Left: 300 MHz; Right: 400 MHz. (a), (b): complex contrast error, err_χ; (c), (d): permittivity error, err_ε; (e), (f): conductivity error, err_σ;

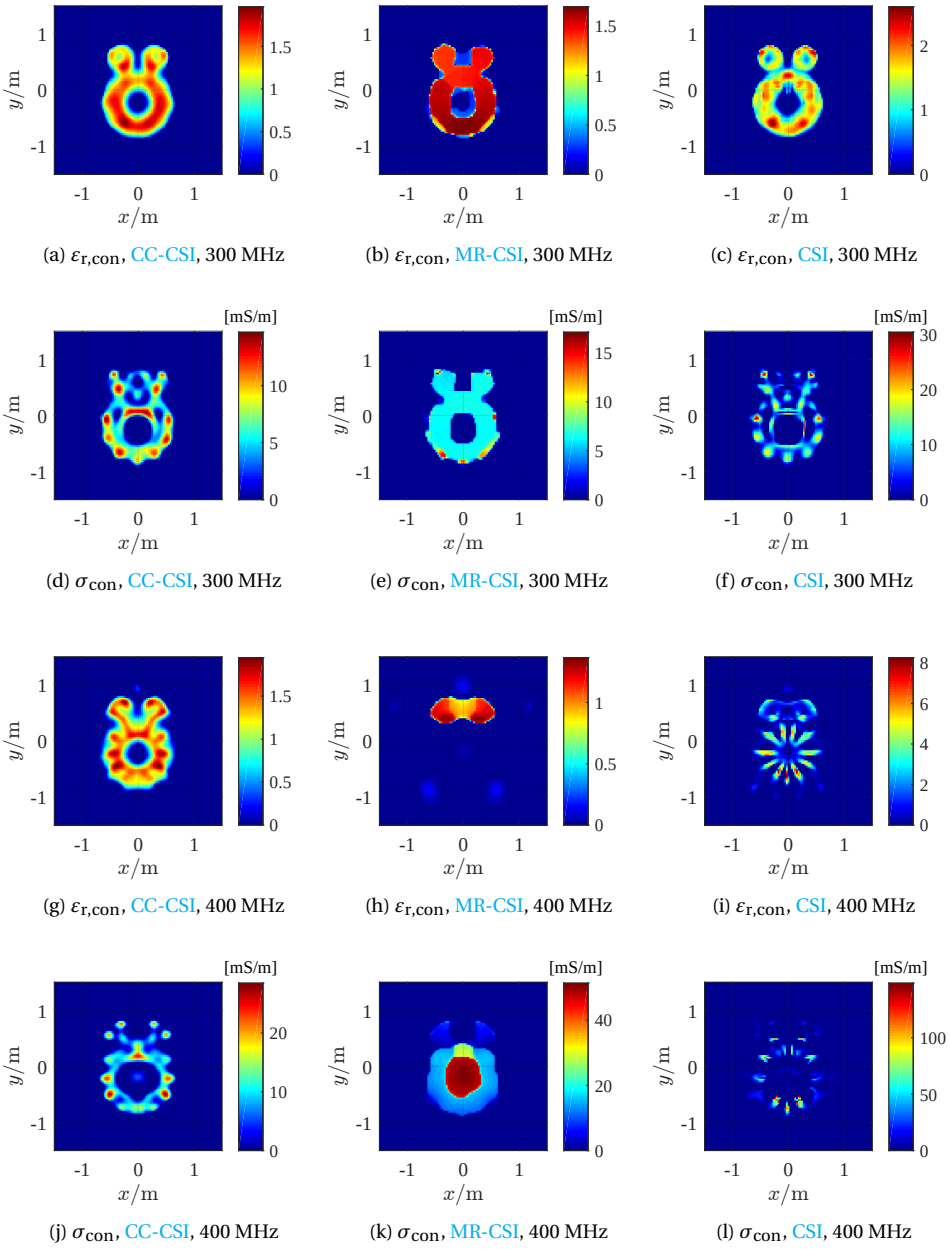

(a) $\varepsilon_{r,con}$, CC-CSI, 300 MHz (b) $\varepsilon_{r,con}$, MR-CSI, 300 MHz (c) $\varepsilon_{r,con}$, CSI, 300 MHz

(d) σ_{con}, CC-CSI, 300 MHz (e) σ_{con}, MR-CSI, 300 MHz (f) σ_{con}, CSI, 300 MHz

(g) $\varepsilon_{r,con}$, CC-CSI, 400 MHz (h) $\varepsilon_{r,con}$, MR-CSI, 400 MHz (i) $\varepsilon_{r,con}$, CSI, 400 MHz

(j) σ_{con}, CC-CSI, 400 MHz (k) σ_{con}, MR-CSI, 400 MHz (l) σ_{con}, CSI, 400 MHz

Figure 3.10: Reconstructed relative permittivity, $\varepsilon_{r,con}$, and conductivity, σ_{con}, in Example 1 with 2048 iterations. SNR= 30dB. TE-polarization data.

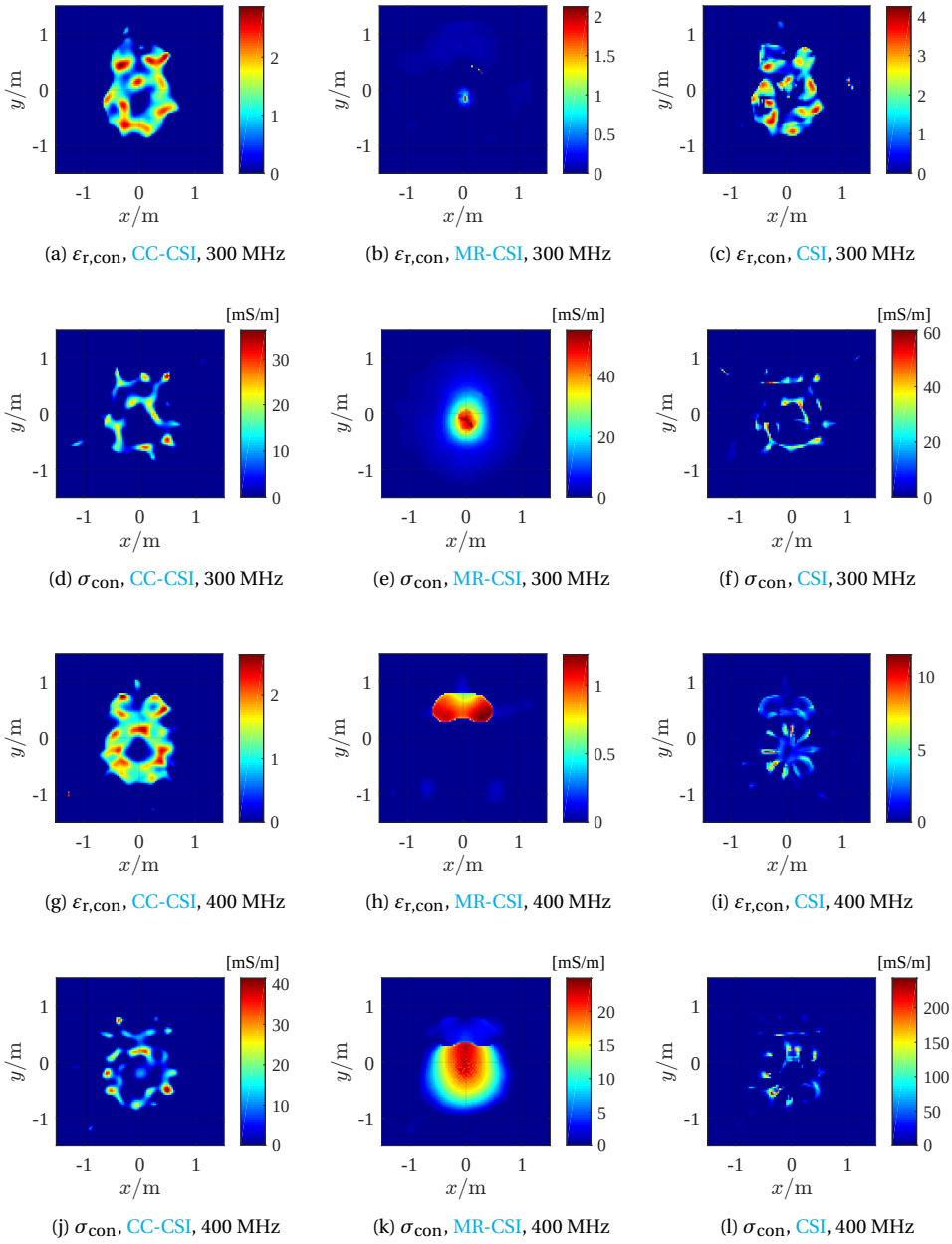

(a) $\varepsilon_{r,con}$, CC-CSI, 300 MHz (b) $\varepsilon_{r,con}$, MR-CSI, 300 MHz (c) $\varepsilon_{r,con}$, CSI, 300 MHz

(d) σ_{con}, CC-CSI, 300 MHz (e) σ_{con}, MR-CSI, 300 MHz (f) σ_{con}, CSI, 300 MHz

(g) $\varepsilon_{r,con}$, CC-CSI, 400 MHz (h) $\varepsilon_{r,con}$, MR-CSI, 400 MHz (i) $\varepsilon_{r,con}$, CSI, 400 MHz

(j) σ_{con}, CC-CSI, 400 MHz (k) σ_{con}, MR-CSI, 400 MHz (l) σ_{con}, CSI, 400 MHz

Figure 3.11: Reconstructed relative permittivity, $\varepsilon_{r,con}$, and conductivity, σ_{con}, in Example 1 with 2048 iterations. SNR= 10dB. TE-polarization data.

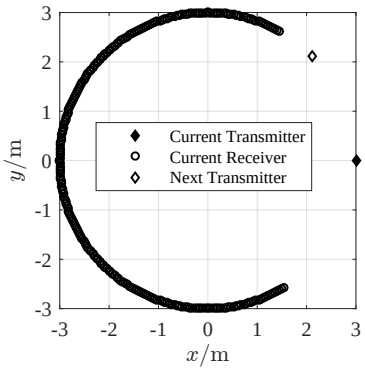

Figure 3.12: Measurement configuration of Example 2.

the transmitter rotates from 0° to 330° in steps of 30°, and 12 rounds of measurements are performed in total.

The incident fields are modeled using the aforementioned approach, and the TM- and TE-polarized data at both 300 MHz and 400 MHz are inverted by CC-CSI, MR-CSI, and classical CSI, respectively, with 2048 iterations. The permittivity error curves are given in Fig. 3.13, and the conductivity error curves are not given because the objects are dielectric. The reconstructed relative permittivity and conductivity images by inverting the 30 dB SNR 300 MHz TM-polarized data and the 10 dB SNR 400 MHz TE-polarized data are shown in Fig. 3.14 and Fig. 3.15, respectively. Figs. 3.13 (a) and 3.13 (d) demonstrate that CC-CSI is of better robustness in comparison to MR-CSI and classical CSI. Fig. 3.13 (c) shows that CC-CSI also fails in the inversion of the 400 MHz TM-polarized data, because 1) the hollow cylinder is filled with dielectric material in this example, which is more complicated than that in Example 1; 2) CC-CSI still belongs to the local optimization algorithms and the convergence to the optimal solution can still not be guaranteed. However, from Fig. 3.13 (d) we observe that by using the TE-polarized data of a 30 dB SNR and a 10 dB SNR, CC-CSI successfully converges to a good result, which can be observed from Fig. 3.15 as well. The reason is due to the reduced degree of non-linearity for TE cases as compared to TM cases [122]. We remark in the end that one can also benefit from the use of both TM and TE polarization in a cascade algorithm or simultaneously. We refer to [123–125] for more discussion about these ideas.

3.2 MULTI-FREQUENCY CC-CSI

3.2.1 FORMULATION

The multi-frequency inversion problem discussed in this section is assumed to be non-dispersive, i.e., the contrast to be inverted is independent of frequency. Let us use the subscript i to represent the i-th frequency. In the update of the contrast sources, the

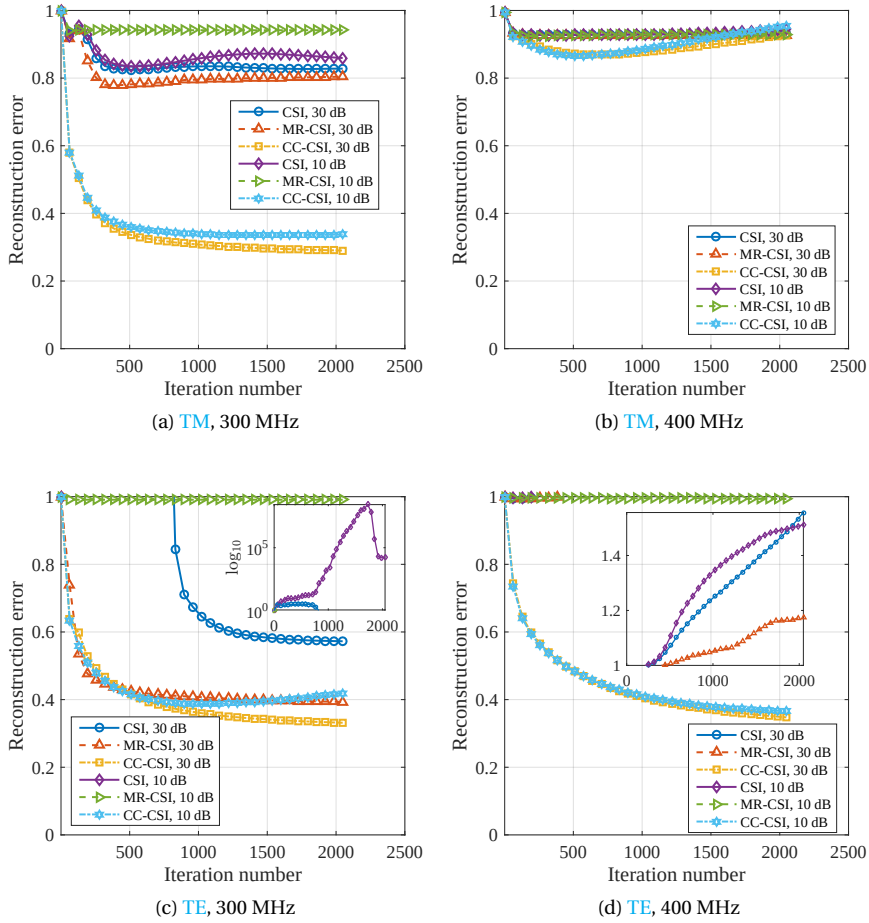

(a) TM, 300 MHz (b) TM, 400 MHz

(c) TE, 300 MHz (d) TE, 400 MHz

Figure 3.13: Permittivity error curves of classical CSI, MR-CSI, and CC-CSI in the TE case of Example 2. (a) TM, 300 MHz; (b) TE, 300 MHz; (c) TM, 400 MHz; (b) TE, 400 MHz.

data error equation, the state error equation and the cross-correlated error equation corresponding to the p-th source are defined respectively as follows

$$\boldsymbol{\rho}_{p,i,\ell-1/2} = \boldsymbol{y}_{p,i} - \boldsymbol{\Phi}_{p,i}\boldsymbol{j}_{p,i}, \tag{3.27}$$

$$\boldsymbol{\gamma}_{p,i,\ell-1/2} = \boldsymbol{\chi}^{\text{iso}}_{i,\ell}\boldsymbol{e}^{\text{inc}}_{p,i} + \boldsymbol{\chi}^{\text{iso}}_{i,\ell}\boldsymbol{A}_i^{-1}\boldsymbol{j}_{p,i} - \boldsymbol{j}_{p,i}, \tag{3.28}$$

$$\boldsymbol{\xi}_{p,i,\ell-1/2} = \boldsymbol{y}_{p,i} - \boldsymbol{\Phi}_{p,i}\left(\boldsymbol{\chi}^{\text{iso}}_{i,\ell}\boldsymbol{e}^{\text{inc}}_{p,i} + \boldsymbol{\chi}^{\text{iso}}_{i,\ell}\boldsymbol{A}_i^{-1}\boldsymbol{j}_{p,i}\right), \tag{3.29}$$

with $p = 1,2,3,\cdots,P$, $i = 1,2,3,\cdots,I$, where

$$\boldsymbol{A}_i = \mu_0^{-1}\boldsymbol{C}_h^{\text{sc}}\boldsymbol{C}_e^{\text{sc}} - \omega_i^2\boldsymbol{D}_{\epsilon_{\text{bg}}}. \tag{3.30}$$

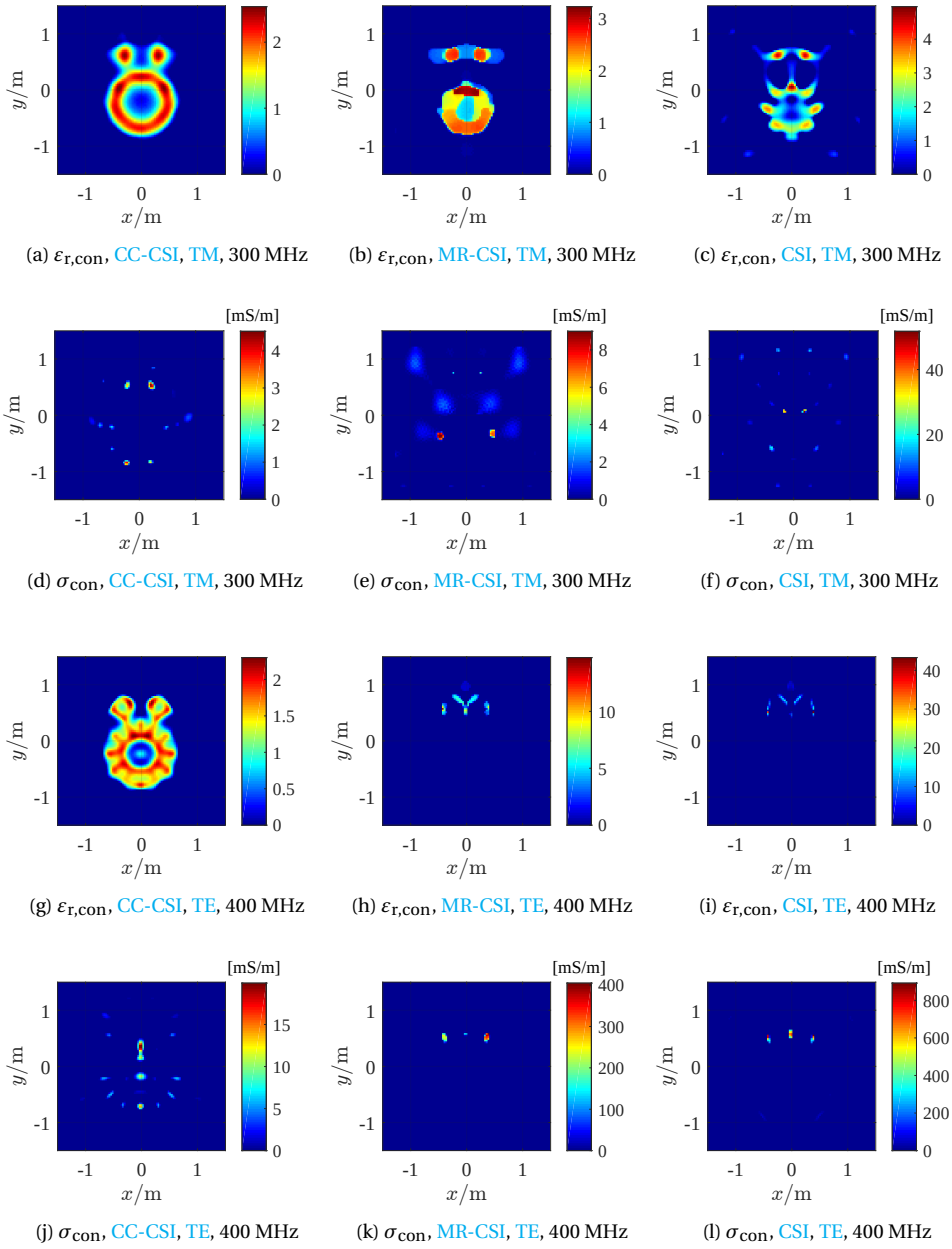

(a) $\varepsilon_{\mathrm{r,con}}$, CC-CSI, TM, 300 MHz (b) $\varepsilon_{\mathrm{r,con}}$, MR-CSI, TM, 300 MHz (c) $\varepsilon_{\mathrm{r,con}}$, CSI, TM, 300 MHz

(d) σ_{con}, CC-CSI, TM, 300 MHz (e) σ_{con}, MR-CSI, TM, 300 MHz (f) σ_{con}, CSI, TM, 300 MHz

(g) $\varepsilon_{\mathrm{r,con}}$, CC-CSI, TE, 400 MHz (h) $\varepsilon_{\mathrm{r,con}}$, MR-CSI, TE, 400 MHz (i) $\varepsilon_{\mathrm{r,con}}$, CSI, TE, 400 MHz

(j) σ_{con}, CC-CSI, TE, 400 MHz (k) σ_{con}, MR-CSI, TE, 400 MHz (l) σ_{con}, CSI, TE, 400 MHz

Figure 3.14: Reconstructed relative permittivity, $\varepsilon_{\mathrm{r,con}}$, and conductivity, σ_{con}, in Example 2 with 2048 iterations. SNR= 30dB. (a-f) correspond to Fig. 3.13 (a); (g-l) correspond to Fig. 3.13 (d).

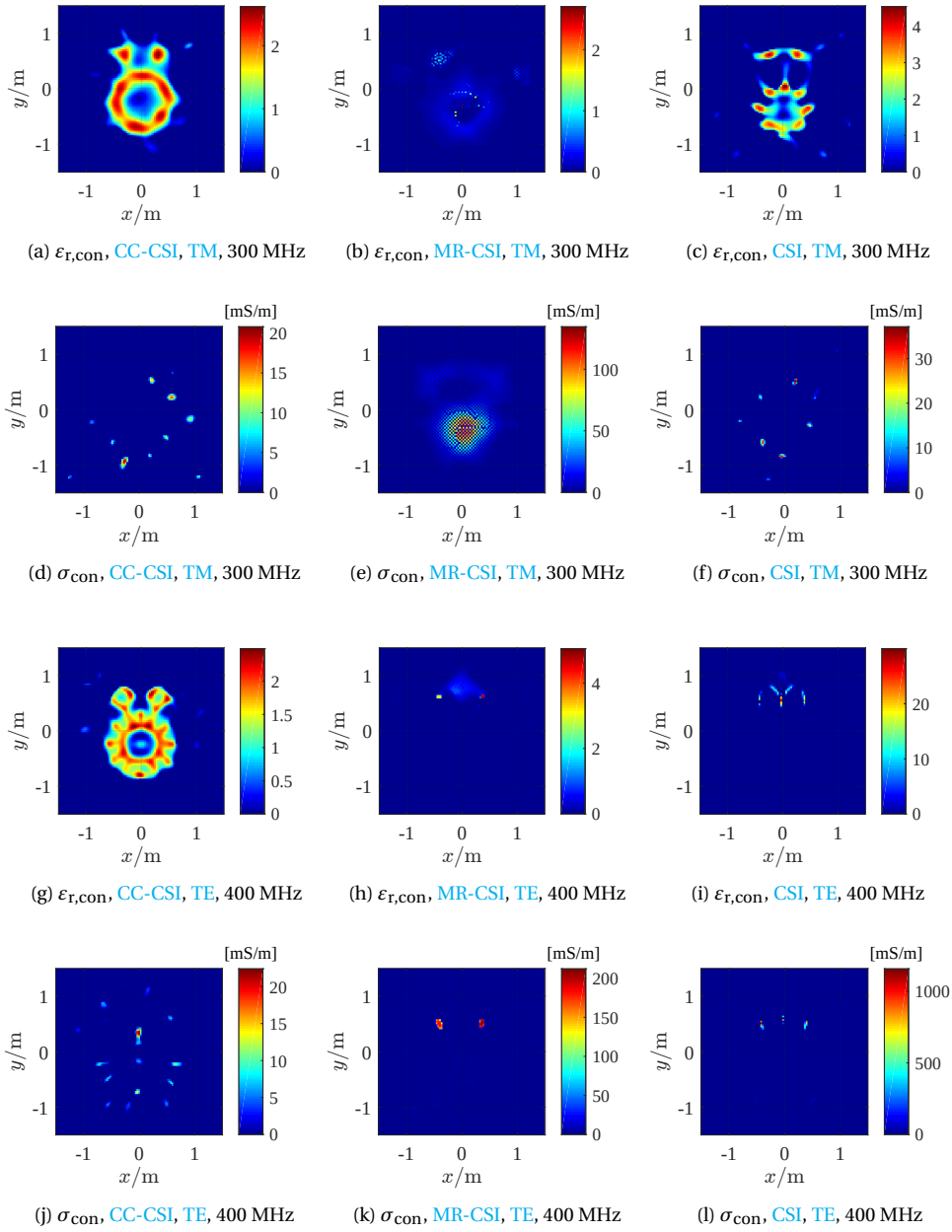

(a) $\varepsilon_{r,con}$, CC-CSI, TM, 300 MHz (b) $\varepsilon_{r,con}$, MR-CSI, TM, 300 MHz (c) $\varepsilon_{r,con}$, CSI, TM, 300 MHz

(d) σ_{con}, CC-CSI, TM, 300 MHz (e) σ_{con}, MR-CSI, TM, 300 MHz (f) σ_{con}, CSI, TM, 300 MHz

(g) $\varepsilon_{r,con}$, CC-CSI, TE, 400 MHz (h) $\varepsilon_{r,con}$, MR-CSI, TE, 400 MHz (i) $\varepsilon_{r,con}$, CSI, TE, 400 MHz

(j) σ_{con}, CC-CSI, TE, 400 MHz (k) σ_{con}, MR-CSI, TE, 400 MHz (l) σ_{con}, CSI, TE, 400 MHz

Figure 3.15: Reconstructed relative permittivity, $\varepsilon_{r,con}$, and conductivity, σ_{con}, in Example 2 with 2048 iterations. SNR= 10dB. (a-f) correspond to Fig. 3.13 (a); (g-l) correspond to Fig. 3.13 (d).

Here, ω_i represents the i-th angular frequency. The cost functional for updating the contrast sources is defined as follows

$$\begin{aligned}\mathcal{C}_{\text{MF-CC-CSI},\ell-1/2} = &\sum_{i=1}^{I}\eta_i^{\mathcal{S}}\sum_{p=1}^{P}\left\|\boldsymbol{\rho}_{p,i,\ell-1/2}\right\|_{\mathcal{S}}^2 + \sum_{i=1}^{I}\eta_{i,\ell-1}^{\mathcal{D}}\sum_{p=1}^{P}\left\|\boldsymbol{\gamma}_{p,i,\ell-1/2}\right\|_{\mathcal{D}}^2 + \\ &\sum_{i=1}^{I}\eta_i^{\mathcal{S}}\sum_{p=1}^{P}\left\|\boldsymbol{\xi}_{p,i,\ell-1/2}\right\|_{\mathcal{S}}^2,\end{aligned} \tag{3.31}$$

where, $\eta_i^{\mathcal{S}}$ and $\eta_{i,\ell}^{\mathcal{D}}$ are defined as

$$\eta_i^{\mathcal{S}} = \sum_{p=1}^{P}\left\|\boldsymbol{y}_{p,i}\right\|_{\mathcal{S}}^2, \quad \eta_{i,\ell}^{\mathcal{D}} = \sum_{p=1}^{P}\left\|\boldsymbol{\chi}_{i,\ell}^{\text{iso}}\boldsymbol{e}_{p,i}^{\text{inc}}\right\|_{\mathcal{D}}^2,$$

respectively.

UPDATING THE CONTRAST SOURCES

The gradient (Fréchet derivative) of the modified cost functional with respect to the contrast sources is

$$\begin{aligned}\boldsymbol{g}_{p,i} = &-2\eta_i^{\mathcal{S}}\boldsymbol{\Phi}_{p,i}^{H}\boldsymbol{\rho}_{p,i,\ell-1} + 2\eta_{i,\ell-1}^{\mathcal{D}}\left(\boldsymbol{\chi}_{i,\ell-1}^{\text{iso}}\boldsymbol{A}_i^{-1} - \boldsymbol{I}\right)^{H}\boldsymbol{\gamma}_{p,i,\ell-1} - \\ &2\eta_i^{\mathcal{S}}\left(\boldsymbol{\Phi}_{p,i}\boldsymbol{\chi}_{i,\ell-1}^{\text{iso}}\boldsymbol{A}_i^{-1}\right)^{H}\boldsymbol{\xi}_{p,i,\ell-1}.\end{aligned} \tag{3.32}$$

Now suppose $\boldsymbol{j}_{p,i,\ell-1}$ and $\boldsymbol{\chi}_{i,\ell-1}$ are known, then we update the contrast sources, $\boldsymbol{j}_{p,i,\ell-1}$, by

$$\boldsymbol{j}_{p,i,\ell} = \boldsymbol{j}_{p,i,\ell-1} + \alpha_{p,i,\ell}\boldsymbol{\nu}_{p,i,\ell}, \tag{3.33}$$

where, $\alpha_{p,i,\ell}$ are the step sizes, and the update directions, $\boldsymbol{\nu}_{p,i,\ell}$, are chosen as the Polak-Ribière conjugate gradient direction, which is given by

$$\boldsymbol{\nu}_{p,i,\ell} = \begin{cases} 0, & \ell = 0, \\ \boldsymbol{g}_{p,i,\ell} + \dfrac{\sum_{p'}\left\langle \boldsymbol{g}_{p',i,\ell}, \boldsymbol{g}_{p',i,\ell} - \boldsymbol{g}_{p',i,\ell-1}\right\rangle_{\mathcal{D}}}{\sum_{p'}\left\|\boldsymbol{g}_{p',i,\ell-1}\right\|_{\mathcal{D}}^2}\boldsymbol{\nu}_{p,i,\ell-1}, & \ell \geq 1. \end{cases} \tag{3.34}$$

where

$$\boldsymbol{g}_{p,i,\ell} = \boldsymbol{g}_{p,i}\big|_{\boldsymbol{j}_{p,i}=\boldsymbol{j}_{p,i,\ell-1}}. \tag{3.35}$$

The step sizes, $\alpha_{p,i,\ell}$, are the minimizers of the cost functional

$$\mathcal{C}_{\text{MF-CC-CSI},\ell-1/2}\big|_{\boldsymbol{j}_{p,i}=\boldsymbol{j}_{p,i,\ell-1}+\alpha_{p,i}\boldsymbol{\nu}_{p,i,\ell}}. \tag{3.36}$$

See Appendix A.2 for the derivation of $\alpha_{p,i,\ell}$.

UPDATING THE CONTRAST

Suppose $\boldsymbol{\chi}^{\text{iso}}_{i,\ell-1}$ is known and consider the relation

$$\boldsymbol{\chi}^{\text{iso}}_{1,\ell-1} = \Re\left\{\boldsymbol{\chi}^{\text{iso}}_{i,\ell-1}\right\} + \frac{\omega_1}{\omega_i}\Im\left\{\boldsymbol{\chi}^{\text{iso}}_{i,\ell-1}\right\}, \quad i = 1,2,3,\cdots,I, \tag{3.37}$$

we therefore define $\boldsymbol{\chi}^{\text{iso}} = \boldsymbol{\chi}^{\text{iso}}_1$. Once the contrast sources, $\boldsymbol{j}_{p,i,\ell}$, are determined, we update the contrast, $\boldsymbol{\chi}^{\text{iso}}_{\ell-1}$, by

$$\boldsymbol{\chi}^{\text{iso}}_{\ell} = \boldsymbol{\chi}^{\text{iso}}_{\ell-1} + \beta_\ell \boldsymbol{v}^{\text{iso}}_{\ell}, \tag{3.38}$$

where, β_ℓ is the step size and the update direction, $\boldsymbol{v}^{\text{iso}}_{\ell}$, is given by

$$\boldsymbol{v}^{\text{iso}}_{\ell} = \left[\boldsymbol{v}^{\chi\,T}_{\ell}\ \boldsymbol{v}^{\chi\,T}_{\ell}\ \boldsymbol{v}^{\chi\,T}_{\ell}\right]^T, \tag{3.39}$$

where, $\boldsymbol{v}^{\chi}_{\ell}$ is chosen to be the Polak-Ribière conjugate gradient directions, which is given by

$$\boldsymbol{v}^{\chi}_{\ell} = \begin{cases} 0, & n = 0, \\ \boldsymbol{g}^{\chi}_{\ell} + \dfrac{\left\langle \boldsymbol{g}^{\chi}_{\ell}, \boldsymbol{g}^{\chi}_{\ell} - \boldsymbol{g}^{\chi}_{\ell-1}\right\rangle_{\mathcal{D}}}{\left\|\boldsymbol{g}^{\chi}_{\ell-1}\right\|^2_{\mathcal{D}}}\boldsymbol{v}^{\chi}_{\ell-1}, & n \geq 1. \end{cases} \tag{3.40}$$

Here, $\boldsymbol{g}^{\chi}_{\ell}$ is the preconditioned gradient of the contrast cost functional

$$\mathcal{C}_{\text{MF-CC-CSI},\ell} = \sum_{i=1}^{I}\eta^{\mathcal{D}}_{i,\ell-1}\sum_{p=1}^{P}\left\|\boldsymbol{\gamma}_{p,i,\ell}\right\|^2_{\mathcal{D}} + \sum_{i=1}^{I}\eta^{\mathcal{S}}_{i}\sum_{p=1}^{P}\left\|\boldsymbol{\xi}_{p,i,\ell}\right\|^2_{\mathcal{S}}, \tag{3.41}$$

where,

$$\boldsymbol{\gamma}_{p,i,\ell} = \boldsymbol{\chi}^{\text{iso}}_{i,\ell-1}\boldsymbol{e}^{\text{inc}}_{p,i} + \boldsymbol{\chi}^{\text{iso}}_{i,\ell-1}\boldsymbol{A}^{-1}_i\boldsymbol{j}_{p,i,\ell} - \boldsymbol{j}_{p,i,\ell}, \tag{3.42}$$

$$\boldsymbol{\xi}_{p,i,\ell} = \boldsymbol{y}_{p,i} - \boldsymbol{\Phi}_{p,i}\left(\boldsymbol{\chi}^{\text{iso}}_{i,\ell-1}\boldsymbol{e}^{\text{inc}}_{p,i} + \boldsymbol{\chi}^{\text{iso}}_{i,\ell-1}\boldsymbol{A}^{-1}_i\boldsymbol{j}_{p,i,\ell}\right). \tag{3.43}$$

Specifically, $\boldsymbol{g}^{\chi}_{\ell}$ is given by

$$\boldsymbol{g}^{\chi}_{\ell} = \frac{2\Re\left\{\sum_{i=1}^{I}\boldsymbol{g}^{\chi}_{i,\ell}\right\}}{\sum_{i=1}^{I}\sum_{p=1}^{P}\sum_{\gamma}\boldsymbol{e}^{\text{tot}}_{p,i,\gamma,\ell}\overline{\boldsymbol{e}^{\text{tot}}_{p,i,\gamma,\ell}}} + \mathrm{i}\frac{2\Im\left\{\sum_{i=1}^{I}\frac{\omega_1}{\omega_i}\boldsymbol{g}^{\chi}_{i,\ell}\right\}}{\sum_{i=1}^{I}\left(\frac{\omega_1}{\omega_i}\right)^2\sum_{p=1}^{P}\sum_{\gamma}\boldsymbol{e}^{\text{tot}}_{p,i,\gamma,\ell}\overline{\boldsymbol{e}^{\text{tot}}_{p,i,\gamma,\ell}}}, \tag{3.44}$$

where,

$$\boldsymbol{g}^{\chi}_{i,\ell} = \eta^{\mathcal{D}}_{i,\ell-1}\sum_{p=1}^{P}\sum_{\gamma}\overline{\boldsymbol{e}^{\text{tot}}_{p,i,\gamma,\ell}}\boldsymbol{\gamma}_{p,i,\gamma,\ell} - \eta^{\mathcal{S}}_{i}\sum_{p=1}^{P}\sum_{\gamma}\overline{\boldsymbol{e}^{\text{tot}}_{p,i,\gamma,\ell}}\boldsymbol{\Phi}^{H}_{p,i}\boldsymbol{\xi}_{p,i,\gamma,\ell}. \tag{3.45}$$

The step size, β_ℓ, is determined by minimizing the updated cost function in the formulation of

$$\sum_{i=1}^{I}\frac{\sum_{p=1}^{P}\left\|\left(\boldsymbol{\chi}^{\text{iso}}_{i,\ell-1} + \beta\boldsymbol{\chi}^{\text{iso}}_{i,\ell}\right)\boldsymbol{e}^{\text{tot}}_{p,i,\ell} - \boldsymbol{j}_{p,i,\ell}\right\|^2_{\mathcal{D}}}{\sum_{p=1}^{P}\left\|\left(\boldsymbol{\chi}^{\text{iso}}_{i,\ell-1} + \beta\boldsymbol{\chi}^{\text{iso}}_{i,\ell}\right)\boldsymbol{e}^{\text{inc}}_{p,i}\right\|^2_{\mathcal{D}}} + \sum_{i=1}^{I}\eta^{\mathcal{S}}_{i}\sum_{p=1}^{P}\left\|\boldsymbol{y}_{p,i} - \boldsymbol{\Phi}_{p,i}\left(\boldsymbol{\chi}^{\text{iso}}_{i,\ell-1} + \beta\boldsymbol{\chi}^{\text{iso}}_{i,\ell}\right)\boldsymbol{e}^{\text{tot}}_{p,i,\ell}\right\|^2_{\mathcal{S}}. \tag{3.46}$$

This is a problem of finding the minimum of a single-variable function, which can be solved efficiently by the Brent's method [114, 115].

INITIALIZATION

If no *a priori* information about the objects is available, the contrast source is initialized using the values obtained by back-propagation

$$\boldsymbol{j}_{p,i,0} = \frac{\left\| \boldsymbol{\Phi}_{p,i}^{H} \boldsymbol{y}_{p,i} \right\|_{\mathcal{D}}^{2}}{\left\| \boldsymbol{\Phi}_{p,i} \boldsymbol{\Phi}_{p,i}^{H} \boldsymbol{y}_{p,i} \right\|_{\mathcal{S}}^{2}} \boldsymbol{\Phi}_{p,i}^{H} \boldsymbol{y}_{p,i}, \tag{3.47}$$

and the starting value of the total field is

$$\boldsymbol{e}_{p,i,0}^{\mathrm{tot}} = \boldsymbol{e}_{p,i}^{\mathrm{inc}} + \boldsymbol{A}_{i}^{-1} \boldsymbol{j}_{p,i,0}. \tag{3.48}$$

The contrast is initialized by (see [120])

$$\boldsymbol{\chi}_{1,0} = \frac{\Re\left\{ \sum_{i=1}^{I} \sum_{p=1}^{P} \sum_{\gamma} \boldsymbol{j}_{p,i,\gamma,0} \overline{\boldsymbol{e}_{p,i,\gamma,0}^{\mathrm{tot}}} \right\}}{\sum_{i=1}^{I} \sum_{p=1}^{P} \sum_{\gamma} \boldsymbol{e}_{p,i,\gamma,0}^{\mathrm{tot}} \overline{\boldsymbol{e}_{p,i,\gamma,0}^{\mathrm{tot}}}} + \mathrm{i} \frac{\Im\left\{ \sum_{i=1}^{I} \frac{\omega_1}{\omega_i} \sum_{p=1}^{P} \sum_{\gamma} \boldsymbol{j}_{p,i,\gamma,0} \overline{\boldsymbol{e}_{p,i,\gamma,0}^{\mathrm{tot}}} \right\}}{\sum_{i=1}^{I} \left(\frac{\omega_1}{\omega_i} \right)^{2} \sum_{p=1}^{P} \sum_{\gamma} \boldsymbol{e}_{p,i,\gamma,0}^{\mathrm{tot}} \overline{\boldsymbol{e}_{p,i,\gamma,0}^{\mathrm{tot}}}}. \tag{3.49}$$

Since free space is considered in the following examples, the contrast must have non-negative real part and non-positive imaginary part. Such properties are enforced in the following examples by simply setting the negative real part and the positive imaginary part of the contrast to zero following each update of the contrast for both MF-CC-CSI and Multi-Frequency Multiplicative Regularized Contrast Source Inversion (MF-MR-CSI). In addition, the contrast sources and the contrast are initialized by Eq. (3.47) and Eq. (3.49), respectively, for fair comparison.

3.2.2 NUMERICAL SIMULATION

In this subsection, both MF-CC-CSI and MF-MR-CSI are tested for comparison with a 2-D benchmark problem — the "Austria" profile, which was also used in Subsection 3.1.4. The objects consist of two disks and one ring. Let us first establish our coordinate system such that the z-axis is parallel to the axis of the objects. The disks of radius 0.2 m are centred at $(-0.3, 0.6)$ m and $(0.3, 0.6)$ m. The ring is centred at $(0, -0.2)$ m, and it has an exterior radius of 0.6 m and an inner radius of 0.3 m. We assume that the three cylinders are made of same material. Two sets of dielectric parameters are considered, which are $\varepsilon_{\mathrm{r}} = 3$, $\sigma = 5$ mS/m, and $\varepsilon_{\mathrm{r}} = 10$, $\sigma = 10$ mS/m, respectively. Since we assume a free space environment, the contrast values are $\Delta\varepsilon_{\mathrm{r}} = 2$, $\Delta\sigma = 5$ mS/m, and $\Delta\varepsilon_{\mathrm{r}} = 9$, $\Delta\sigma = 10$ mS/m, respectively. The direct scattering problems are solved by a MATLAB-based "MaxwellFDFD" package [35] with a fine and non-uniform grid size of $\lambda/(45\sqrt{\varepsilon_{\mathrm{r}}})$.

MEASUREMENT CONFIGURATION

In order to approach the realistic situation, we selected a measurement configuration which is similar to the experiment conducted by the Remote Sensing and Microwave Experiments Team at the Institut Fresnel, France [31]. An emitter is fixed on the circular

rail, while a receiver is rotating with the arm around a vertical cylindrical target. The targets rotated from 0° to 330° in steps of 30°, and the receiver rotated from 60° to 300° in steps of 5°. The distance from the emitter/receiver to the origin is 3 m. Simulation is sequentially done in the absence/presence of the objects at five frequencies of 0.1 GHz, 0.2 GHz, 0.3 GHz, 0.4 GHz, and 0.5 GHz. Selection of the five frequencies considered the dimension of the targets and the wave number of the EM wave in the interior of the targets. Scattered field data are obtained by subtracting the incident field data, $\boldsymbol{y}_p^{\text{inc}}$, from the total field data, $\boldsymbol{y}_p^{\text{tot}}$.

Although the incident fields in the inversion domain can be easily obtained in numerical simulations, it is not available in real applications. Therefore, we consider the modelling of the incident fields using the collected incident field data. We select the approach reported in [120]. Specifically, the transmitting antenna is approximated by line source parallel to the cylindrical objects. The incident field by the line source is calibrated by multiplying a complex ratio which is calculated using only the value of the field when the transmitting and the receiving antenna are in opposite directions. For each frequency and source position, one complex calibration factor is determined. To simulate the inevitable measurement error in real experiments, additive Gaussian random noise, $\boldsymbol{n}_p$, is added directly to the scattered field data. The power of the scattered field data matrix is measured before adding noise. In addition, the noise is also added to the total field data and the incident field data by $\boldsymbol{y}_p^{\text{tot}} + \boldsymbol{n}_p/2$ and $\boldsymbol{y}_p^{\text{inc}} - \boldsymbol{n}_p/2$, respectively. In doing so, the disturbance of the noise is reflected not only in the scattered field data but also in the modelling of the incident fields. To appraise the inversion accuracy, let us define the reconstruction error as follows

$$err := \|\hat{\boldsymbol{\chi}} - \boldsymbol{\chi}\|_2 / \|\boldsymbol{\chi}\|_2 \,. \tag{3.50}$$

where, $\hat{\boldsymbol{\chi}}$ and $\boldsymbol{\chi}$ are the reconstructed contrast and the exact contrast, respectively. Since large values of frequency tolerates large reconstruction errors of the conductivity (see Subsection 3.2.3 for more discussion), $\hat{\boldsymbol{\chi}}$ and $\boldsymbol{\chi}$ in Eq. (3.50) correspond to the highest frequency to ensure that the imaginary part of the contrast error is not over amplified in the evaluation of the inversion accuracy. In the following two cases, the inversion domain is restricted to $[-1.20, 1.20] \times [-1.20, 1.20]$ m^2 and discretized into uniform grids with a size of 0.30×0.30 mm^2.

INVERSION RESULTS

Case 1: $\Delta\varepsilon_{\mathbf{r}} = 2$, $\Delta\sigma = 5$ mS/m Let us first consider the lower contrast case, i.e., $\Delta\varepsilon_{\text{r}} = 2$, $\Delta\sigma = 5$ mS/m. MF-CC-CSI and MF-MR-CSI are used to process the TM- and TE-polarized numerical data respectively with 2048 iterations. Different frequency bands of 0.1-0.5 GHz and 0.3-0.5 GHz and different SNRs of 30 dB and 10 dB are tested. Fig. 3.16 shows the reconstruction error curves in term of the iteration number, which indicates obviously that MF-CC-CSI shows smaller reconstruction errors compared to MF-MR-CSI. It is also easy to observe that noise indeed leads to a degradation of the inversion accuracy (see the error curves of MF-CC-CSI shown in Figs. 3.16 (b) and 3.16 (d) when processing the 10 dB SNR data). As the frequency increases up to 0.3-0.5 GHz, the reconstruction error of MF-MR-CSI remains close to 1, indicating that MF-MR-CSI completely fails to invert the data in this frequency band.

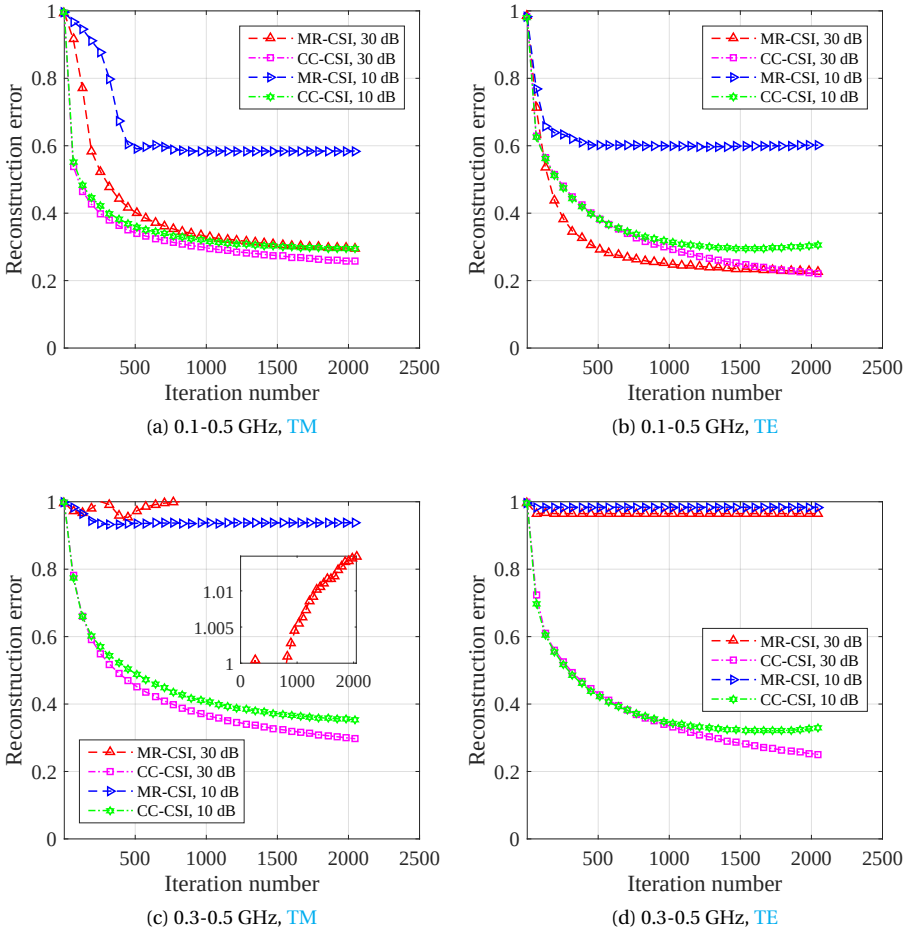

(a) 0.1-0.5 GHz, TM (b) 0.1-0.5 GHz, TE

(c) 0.3-0.5 GHz, TM (d) 0.3-0.5 GHz, TE

Figure 3.16: Inversion error curves of MF-CC-CSI and MF-MR-CSI in terms of iteration number in case 1 ($\Delta\varepsilon_{\mathbf{r}} = 2$, $\Delta\sigma = 5$ mS/m) by processing the TM-polarized (a, c) and TE-polarized (b, d) data. Different frequency bands of 0.1-0.5 GHz (a, b) and 0.3-0.5 GHz (c, d) and different SNRs of 30 dB and 10 dB are considered.

Case 2: $\Delta\varepsilon_{\mathbf{r}} = 9$, $\Delta\sigma = 10$ mS/m In this case, the contrast increases to $\Delta\varepsilon_{\mathbf{r}} = 9$, $\Delta\sigma = 10$ mS/m, which is supposed to be more challenging. We have also considered the frequency band 0.1-0.5 GHz, and from Fig. 3.17 we observe that both MF-CC-CSI and MF-MR-CSI show large reconstruction errors. However, the former obtained smaller and more smoothly decreasing reconstruction error curves than the latter. Now let us remove the high-frequency data and consider the frequency band 0.1-0.2 GHz, one can see from the bottom two subfigures of Fig. 3.17 that the inversion accuracy of MF-CC-CSI has been improved; The reconstruction error curve of MF-MR-CSI started to decrease when processing the 0.1-0.2 GHz 30 dB synthetic data. Both of the two cases demonstrate that MF-CC-CSI is a more reliable inversion method in comparison to MF-MR-CSI.

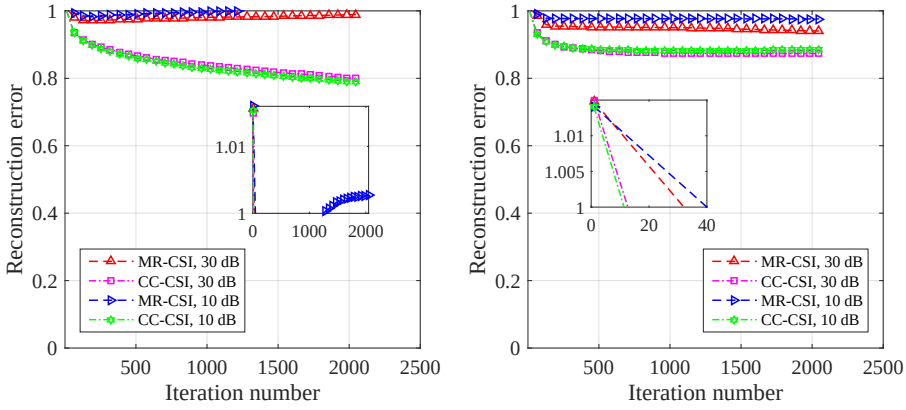

(a) 0.1-0.5 GHz, TM (b) 0.1-0.5 GHz, TE

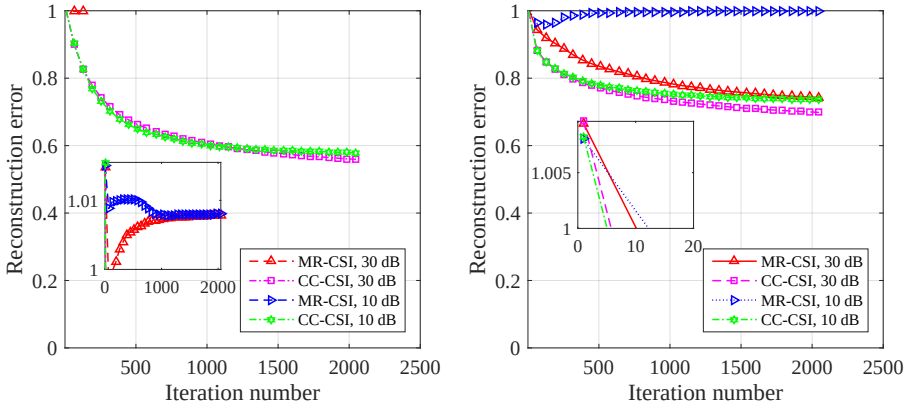

(c) 0.1-0.2 GHz, TM (d) 0.1-0.2 GHz, TE

Figure 3.17: Inversion error curves of MF-CC-CSI and MF-MR-CSI in terms of iteration number in case 2 ($\Delta\varepsilon_r$ = 9, $\Delta\sigma$ = 10 mS/m) by processing the TM-polarized (a, c) and TE-polarized (b, d) data. Different frequency bands of 0.1-0.5 GHz (a, b) and 0.1-0.2 GHz (c, d) and different SNRs of 30 dB and 10 dB are considered.

3.2.3 EXPERIMENTAL DATA

CONFIGURATION

In this section, we consider the experiment carried out by Institut Fresnel in the year of 2005 [32]. In this experiment, the receiver stays in the azimuthal plane (xoy) and rotates along two-thirds of a circle from 60° to 300° with the angular step being 1°. The source antenna stays at the fixed location (θ = 0°). The targets are rotated to obtain different illumination incidences. The distance from the transmitter and receiver to the centre of the target domain is 1.67 m.

To avoid the redundancy of our discussion, let us select the most complicated configuration that corresponds to the datasets *FoamTwinDielTM* and *FoamTwinDielTE*. The targets consist of one larger circular dielectric cylinder with a smaller one embedded insider and a smaller adjacent one outside (see Fig. 5 (c) in [32]). Two smaller circular dielectric cylinders have relative permittivity value of $\varepsilon_r = 3 \pm 0.3$ while the larger one is of a relative permittivity $\varepsilon_r = 1.45 \pm 0.15$. In this configuration, the targets are rotated from 0° to 340° in steps of 20°. 241 × 18 measurements are obtained at each frequency (in TE polarization, only the component orthogonal to both the invariance axis of the cylinder and the direction of illumination is measured). The measurement configuration is given in Fig. 1 of [32]. To increase the inversion difficulty, let us assume the data in the low-frequency band is not available anymore, and we only have the measurement data at 7 GHz, 8 GHz, 9 GHz, and 10 GHz.

INVERSION RESULTS

First, let us model the incident fields with the same approach as we did in the numerical simulation. To reduce the computational burden, we restrict the inversion domain to $[-82.5, 82.5] \times [-97.5, 67.5]$ mm^2. The inversion domain is discretized with a grid size of 1.5×1.5 mm^2. The multi-frequency datasets, *FoamTwinDielTM* and *FoamTwinDielTE*, at 7 GHz, 8 GHz, 9 GHz, and 10 GHz were processed by MF-CC-CSI and MF-MR-CSI, respectively. Both of them were terminated after 2048 iterations. In addition, we also did a simulation to generate the perfect data of the same targets in the same configuration. The only thing different is that the distance between antennas and the centre of the inversion domain was shortened from 1.67 m to 0.20 m. Otherwise, the scattering domain with the frequency up to 10 GHz is too huge for a standard desktop.

Fig. 3.18 (*FoamTwinDielTM*) and Fig. 3.19 (*FoamTwinDielTE*) show the inverted results by processing the multi-frequency datasets (Line 1: MF-CC-CSI; Line 2: MF-MR-CSI) and the noise-free synthetic data (Line 3: MF-CC-CSI; Line 4: MF-MR-CSI) at 7 GHz, 8 GHz, 9 GHz, and 10 GHz. One can see that MF-CC-CSI successfully reconstructed the three cylinders with a good reconstruction accuracy from both the experimental data and the noise-free perfect synthetic data, while MF-MR-CSI only obtained good inversion results from the noise-free perfect TE-polarized synthetic data. The artefacts of the inverted contrast conductivity (see the right figure in Line 3 of Fig. 3.18) is inevitable and so far can only be explained as a reconstruction error to the best of our knowledge. The higher the frequency is, the larger such artefacts will be. This is easy to understand by noting that $\chi_i = \Delta\varepsilon_r - \mathrm{i}\Delta\sigma/\omega_i$, i.e., a large value of the angular frequency, ω_i, tolerates a large reconstruction error of the contrast conductivity, $\Delta\sigma$. The synthetic data enables us to obtain the reconstruction error curves of both methods, which are shown in Fig. 3.20. The error curves show us the inversion performance of both methods during the whole inversion process, demonstrating again the advantage of MF-CC-CSI in more complicated scenarios. One can also see that the multiplicative regularization can improve the inversion accuracy indeed when the contrast can be reconstructed to a reasonable accuracy. The reason has been fully discussed in [112].

We finally remark that, for the multi-frequency data inversion, a good termination condition is required for MF-CC-CSI as well. Otherwise, the inversion accuracy may deteriorate after a number of iterations when the noise disturbance to the measurement data is not negligible.

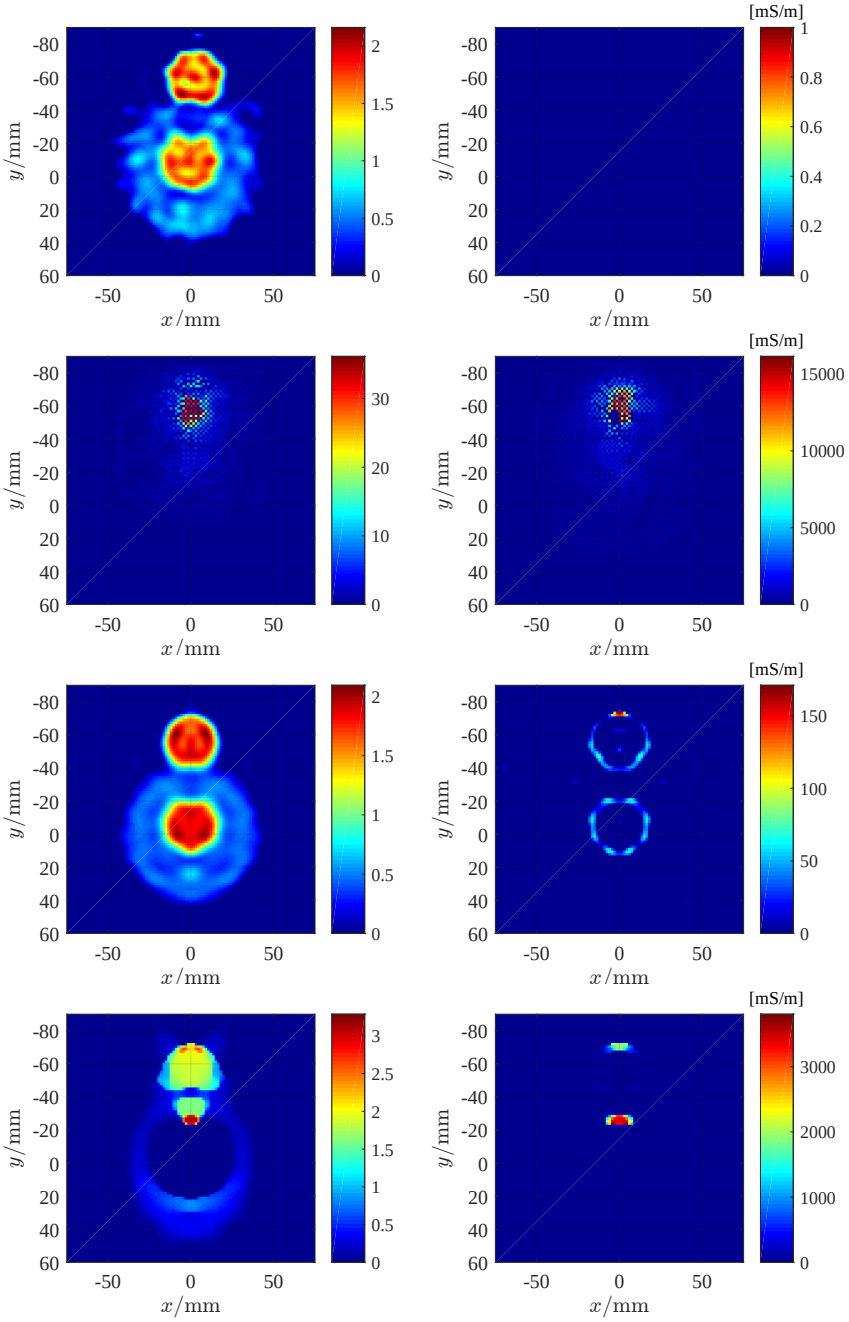

Figure 3.18: Relative permittivity (left) and conductivity (right) of the inverted contrast by processing the multi-frequency dataset *FoamTwinDielTM* (Line 1: MF-CC-CSI; Line 2: MF-MR-CSI) and its perfect synthetic data (Line 3: MF-CC-CSI; Line 4: MF-MR-CSI) at 7 GHz, 8 GHz, 9 GHz, and 10 GHz with 2048 iterations.

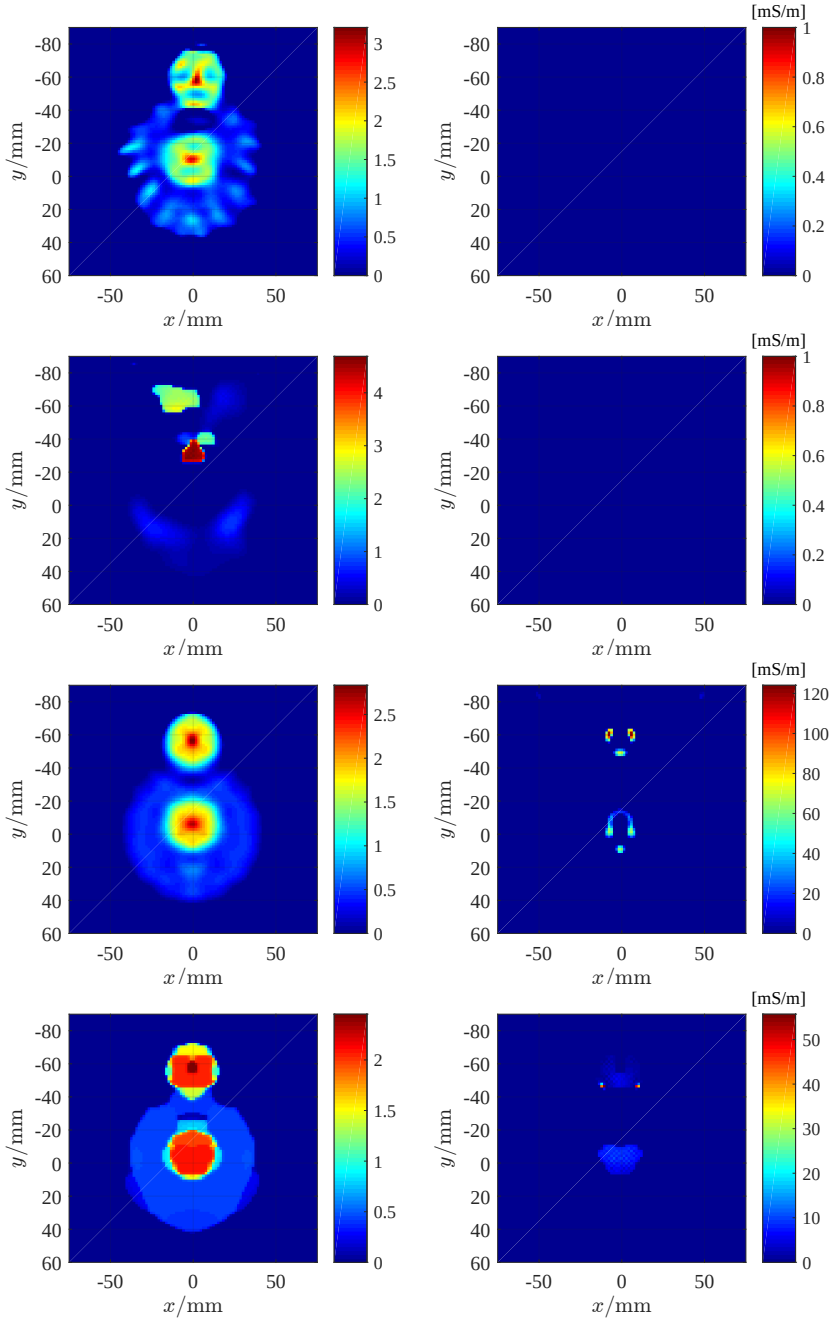

Figure 3.19: Relative permittivity (left) and conductivity (right) of the inverted contrast by processing the multi-frequency dataset *FoamTwinDielTE* (Line 1: MF-CC-CSI; Line 2: MF-MR-CSI) and its perfect synthetic data (Line 3: MF-CC-CSI; Line 4: MF-MR-CSI) at 7 GHz, 8 GHz, 9 GHz, and 10 GHz with 2048 iterations.

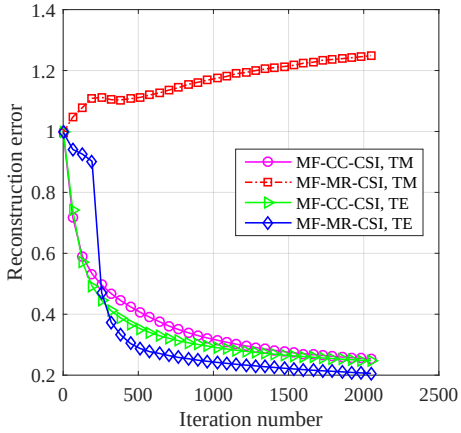

Figure 3.20: Inversion error curves of MF-CC-CSI and MF-MR-CSI in terms of iteration number in processing the multi-frequency perfect synthetic data of the Fresnel datasets, *FoamTwinDielTM* and *FoamTwinDielTE*, at 7 GHz, 8 GHz, 9 GHz, and 10 GHz.

3.3 CONCLUSIONS

In this chapter, a novel error term, the cross-correlated error, and a novel inversion method, the CC-CSI method, are proposed. The introduction of the novel error term interrelates the state error and the data error. It is shown that CC-CSI can be implemented without significantly increasing the computational burden. The proposed algorithm is tested with a 2-D benchmark problem. Numerical simulations with both TM-polarized wave and TE-polarized wave show that CC-CSI outperforms classical CSI and MR-CSI in the aspects of robustness and inversion accuracy. Subsequently, a multi-frequency version of CC-CSI, MF-CC-CSI, is proposed, which is able to process the multi-frequency data simultaneously. Numerical and experimental results show that it is more robust than the MF-MR-CSI method.

The proposed inversion approach is versatile, because 1) as Maxwell's equations are formulated within a 3-D FDFD scheme, it is straightforward to extend the proposed inversion scheme to future 3-D inverse scattering problems; 2) one can benefit from the cross-correlated error term as long as the classical cost functional is involved.

4

A Linear Model for Inverting Highly Conductive Scatterers

To overcome the ill-posedness of the inverse scattering problem, regularization constraints are always considered in the formulation of the cost functional. For instance, the state error cost functional in classical Contrast Source Inversion (CSI), the multiplicative Total Variation (TV) constraint in Multiplicative Regularized Contrast Source Inversion (MR-CSI), and the cross-correlated error cost functional in Cross-Correlated Contrast Source Inversion (CC-CSI). In this chapter, the highly conductive inverse scattering problem is considered and a linear model is proposed, which, to some extent, enables us to overcome the ill-posedness by exploiting the joint sparsity of the contrast sources. In comparison to non-linear iterative inversion methods, the proposed linear model is computationally more efficient since a solution to the direct scattering problem is not needed anymore. Specifically, the inverse scattering problem is first formulated by means of Finite Difference Frequency Domain (FDFD) [35]. The cost functional is formulated equivalently as the superposition of the data error and the sum-of-norm of the contrast sources. For the highly conductive scatterers, the induced currents excited by the incident fields only exist on the boundaries (the ElectroMagnetic (EM) field is almost zero in the interior), therefore, the contrast source shows sparsity. Consequently, the reconstruction methods in Compressive Sensing (CS) [126] can be used to solve the linear model. If incident fields illuminate from different angles, more than one contrast source is involved and more importantly the contrast sources are of joint sparsity, which can be exploited by reformulating the problem to a Multiple Measurement Vectors (MMV) [127] model (an extension of the Single Measurement Vector (SMV) model). A spectral projected gradient method, referred to as Spectral Projected Gradient for ℓ_1-norm minimization (SPGL1) [128, 129], is used to search the optimal solutions regarding

Parts of this chapter have been published in [42].

the sum-of-norm constraint. Sketching the superposition of the intensity of the contrast sources ends up with the profile of the targets.

In a nutshell, major differences of the proposed approach in comparison to other existing methods are as follows:

1. In comparison to linear methods with a linear model of weak scattering assumptions (such as Born/Rytov approximations), the proposed model is more applicable since no weak scattering approximation has been made.

2. In comparison to linear methods with a linear model of no weak scattering approximations (such as Linear Sampling Method (LSM)), the joint sparse structure of the contrast sources is enforced in the proposed approach by use of sum-of-norm regularization constraint, resulting in higher resolving ability.

3. In comparison to the linear iterative algebra of multiple levels with a non-linear model (such as CSI), calculation of the total fields for the proposed approach is not needed, resulting in higher imaging efficiency.

4. In comparison to super-resolution methods based on the pseudo-spectrum analysis (such as Time-reversal MUltiple SIgnal Classification (MUSIC)), the proposed approach does not need to estimate the scatterer number, nor does it need to care about how the imaging domain is discretized.

We verified the validity of the proposed method with both 2-Dimensional (2-D) synthetic data generated by a MATLAB-based "MaxwellFDFD" package [30], and the 2-D Fresnel experimental data of both Transverse Magnetic (TM) wave and Transverse Electric (TE) wave [31]. The remainder of the chapter is organized as follows: In Subsection 4.1.1, the proposed linear model is introduced; Subsection 4.1.2, 4.1.3, and 4.1.4 introduce the algorithms of solving the TM-polarized SMV model, the TM-polarized MMV model, and the TE-polarized MMV model, respectively; Subsection 4.1.5 introduces a termination criterion based on the Cross-Validation (CV) technique; The inverted results with synthetic data and experimental data are given in Section 4.2. Finally, Section 4.3 ends this chapter with conclusions.

4.1 MMV LINEAR INVERSION MODEL

4.1.1 FORMULATION

First, let us formulate the inverse problem following the vector form of the FDFD scheme in [35], and rewrite the data equations, Eqs. (2.35a) as follows

$$\boldsymbol{y}_p = \boldsymbol{\Phi}\boldsymbol{j}_p, \quad p = 1,2,3,\cdots,P, \tag{4.1}$$

where, $\boldsymbol{\Phi}$ is the sensing matrix. Note that, in this chapter, we assume the measurement configuration does not change for difference incident angles. In the numerical simulations and experimental data inversion, some measurement data close to the transmitting

antenna are omitted. However, the probing positions do not change and we represent the different measurements with the same sensing matrix and treat them with a specific trick in the inversion process. Normally, the state equations are also required which, for inverse scattering problems of highly conductive scatterers, can be written as

$$\boldsymbol{e}_p^{\text{inc}} = -\boldsymbol{A}^{-1}\omega^2 \boldsymbol{j}_p, \quad \vec{x} \in \partial\Gamma, \quad p = 1, 2, 3, \cdots, P. \tag{4.2}$$

One feasible approach to solving the inverse scattering problem of highly conductive scatterers is that one can first make an initial guess of $\partial\Gamma$, then find the contrast sources by solving the state equations, Eqs. (4.2). Substitute the contrast sources into the data equations, Eqs. (4.1), and the boundary $\partial\Gamma$ can be optimized with Gauss-Newton iteration method. A fast convergence can be achieved in this way. However, *a priori* information on the positions and quantity of the scatterers is required, which has a crucial influence on the inversion performance.

In the rest of this chapter, a simple linear model, referred to as the MMV linear inversion model, is constructed and solved by a sum-of-norm optimization method. In doing so, the nonlinear inverse scattering problem can be simplified and addressed linearly without considering the state equations. Specifically, in order to exploit the joint sparsity of the contrast sources, the linear data model, Eq. (4.1), is reformulated as a linear inverse source model, given by

$$\boldsymbol{Y} = \boldsymbol{\Phi}\boldsymbol{J} + \boldsymbol{U}, \tag{4.3}$$

where, $\boldsymbol{J} = \left[\boldsymbol{j}_1, \boldsymbol{j}_2, \cdots, \boldsymbol{j}_P\right]$ is the contrast source matrix, and $\boldsymbol{Y} = \left[\boldsymbol{y}_1, \boldsymbol{y}_2, \cdots, \boldsymbol{y}_P\right]$ is the measurement data matrix, and $\boldsymbol{U}$ represents the additive complex measurement noise matrix. It is referred to as an MMV model when $P > 1$. If there is only one source, i.e., $P = 1$, Eq. (4.3) reduces to a SMV model. In the following, a sum-of-norm of the contrast source matrix is considered as a constraint for solving the linear inversion model.

4.1.2 SOLVING THE SMV MODEL: TM CASE

First, consider the single source configuration illuminated by a TM-polarized wave. The inverse scattering problem is formulated as a Basis Pursuit Denoise ($\text{BP}_{\widetilde{\sigma}}$) problem [130]:

$$\text{SMV}_{\text{TM}}\ \text{BP}_{\widetilde{\sigma}}: \quad \text{minimize} \quad \left\|\boldsymbol{j}_p\right\|_1 \quad \text{subject to} \quad \left\|\boldsymbol{\Phi}\boldsymbol{j}_p - \boldsymbol{y}_p\right\|_2 \leq \widetilde{\sigma}. \tag{4.4}$$

where, $\widetilde{\sigma}$ represents the noise level, and the contrast source is regularized with the ℓ_1-norm constraint. Solving this problem means searching for a solution of $\boldsymbol{j}_p$ which is of the smallest ℓ_1-norm and meanwhile satisfies the inequality condition. Although the $\text{BP}_{\widetilde{\sigma}}$ problem is straightforward for understanding the inverse problem, it is not easy to solve directly even if we exactly know the value of $\widetilde{\sigma}$. An equivalent problem that is much simpler to solve is the Lasso (LS_τ) problem [131], which is formulated as

$$\text{SMV}_{\text{TM}}\ \text{LS}_\tau: \quad \text{minimize} \quad \left\|\boldsymbol{\Phi}\boldsymbol{j}_p - \boldsymbol{y}_p\right\|_2 \quad \text{subject to} \quad \left\|\boldsymbol{j}_p\right\|_1 \leq \tau. \tag{4.5}$$

The LS_τ problem can be solved using a Spectral Projected Gradient (SPG) method that is proposed based on convex optimization theory [132–134]. Details of the SPG method for

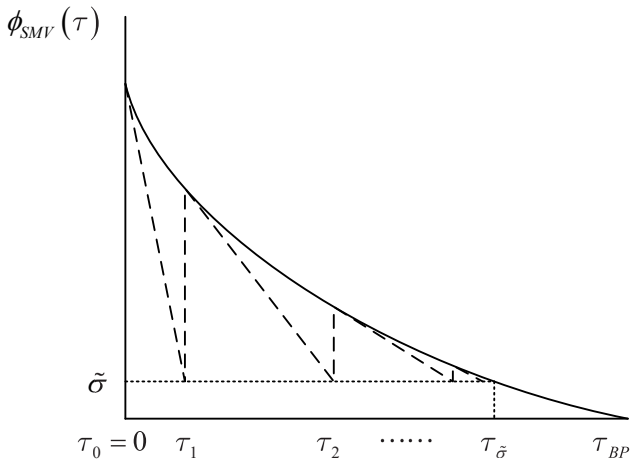

Figure 4.1: Probing the Pareto curve: the update of parameter τ.

solving the LS_τ problem (4.5) is given by [128, Algorithm 1], in which $\mathcal{P}_\tau[\cdot]$ is a projection operator defined as

$$\mathcal{P}_\tau\left[\boldsymbol{j}_p\right] := \left\{ \underset{\boldsymbol{x}}{\arg\min} \quad \left\|\boldsymbol{j}_p - \boldsymbol{x}\right\|_2 \quad \text{subject to} \quad \|\boldsymbol{x}\|_1 \leq \tau \right\}. \tag{4.6}$$

$\mathcal{P}_\tau[\cdot]$ gives the projection of a vector $\boldsymbol{j}_p$ onto the one-norm ball with radius τ.

In practice, τ is usually not available. For solving this problem, a Pareto curve is defined in SPGL1 algorithm [128] by

$$\phi_{\text{SMV}_{\text{TM}}}(\tau) = \left\|\boldsymbol{\Phi}\boldsymbol{j}_{p,\tau} - \boldsymbol{y}_p\right\|_2, \tag{4.7}$$

where, $\boldsymbol{j}_{p,\tau}$ is the optimal solution to the LS_τ problem. It is easy to find that the $\text{BP}_{\tilde{\sigma}}$ problem is equivalent to the LS_τ problem when $\phi_{\text{SMV}_{\text{TM}}}(\tau) = \tilde{\sigma}$ is satisfied. The Pareto curve is proved to be differentiable under some conditions, and the root of the nonlinear equation $\phi_{\text{SMV}_{\text{TM}}}(\tau) = \tilde{\sigma}$ can be reached by Newton iterations [128]

$$\tau_{h+1} = \tau_h + \frac{\tilde{\sigma} - \phi_{\text{SMV}_{\text{TM}}}(\tau_h)}{\phi'_{\text{SMV}_{\text{TM}}}(\tau_h)}, \tag{4.8}$$

where,

$$\phi'_{\text{SMV}_{\text{TM}}}(\tau_{h+1}) = -\frac{\left\|\boldsymbol{\Phi}^H \boldsymbol{r}_{p,\tau_h}\right\|_\infty}{\left\|\boldsymbol{r}_{p,\tau_h}\right\|_2}. \tag{4.9}$$

where, $\boldsymbol{r}_{p,\tau_h} = \boldsymbol{\Phi}\boldsymbol{j}_{p,\tau_h} - \boldsymbol{y}_p$ is the residual vector. The update of τ by probing the Pareto curve is illustrated in Fig. 4.1. This procedure requires computing successively more accurate solutions to LS_τ. The Newton root-finding framework for solving the SMV_{TM} $\text{BP}_{\tilde{\sigma}}$ problem is given in [129, Algorithm 1].

4.1.3 SOLVING THE MMV MODEL: TM CASE

Let us now first consider the 2-D multi-source configuration with TM-polarized illumination. As all the contrast sources are focused on the boundary of the scatterers, the contrast source matrix, $\boldsymbol{J}$, shows a row-sparsity. Therefore, the inverse scattering problem with multi-source configurations can be formulated as an MMV_{TM} $\text{BP}_{\widetilde{\sigma}}$ problem regularized by a sum-of-norm constraint

$$\text{MMV}_{\text{TM}}\,\text{BP}_{\widetilde{\sigma}}: \quad \text{minimize} \quad \kappa(\boldsymbol{J}) \quad \text{subject to} \quad \|\boldsymbol{\Phi}\boldsymbol{J}-\boldsymbol{Y}\|_F \le \widetilde{\sigma}, \tag{4.10}$$

where, $\kappa(\boldsymbol{J})$ is the mixed (α,β)-norm defined as

$$\|\boldsymbol{J}\|_{\alpha,\beta} := \left(\sum_{i=1}^{N}\left\|\boldsymbol{J}_{i,:}^T\right\|_\beta^\alpha\right)^{1/\alpha}, \tag{4.11}$$

with $\boldsymbol{J}_{i,:}$ denoting the i-th row of $\boldsymbol{J}$, and $\|\cdot\|_\beta$ the conventional β-norm. $\|\cdot\|_F$ is the Frobenius norm which is equivalent to the mixed (2,2)-norm $\|\cdot\|_{2,2}$. In this problem, we consider $\alpha=1$ and $\beta=2$, which is a sum-of-norm constraint. Accordingly, the MMV_{TM} LS_τ problem is reformulated as

$$\text{MMV}_{\text{TM}}\,\text{LS}_\tau: \quad \text{minimize} \quad \|\boldsymbol{\Phi}\boldsymbol{J}-\boldsymbol{Y}\|_F \quad \text{subject to} \quad \|\boldsymbol{J}\|_{1,2} \le \tau, \tag{4.12}$$

and the Pareto curve for the MMV model is defined as

$$\phi_{\text{MMV}_{\text{TM}}}(\tau) = \|\boldsymbol{\Phi}\boldsymbol{J}_\tau - \boldsymbol{Y}\|_F, \tag{4.13}$$

where, $\boldsymbol{J}_\tau$ is the optimal solution to the LS_τ problem (4.12).

According to [129, Theorem 2.2] and [135, Chapter 5], $\phi_{\text{MMV}_{\text{TM}}}(\tau)$ is continuously differentiable and

$$\phi'_{\text{MMV}_{\text{TM}}}(\tau_h) = -\frac{\left\|\boldsymbol{\Phi}^H\left(\boldsymbol{\Phi}\boldsymbol{J}_{\tau_h}-\boldsymbol{Y}\right)\right\|_{\infty,2}}{\left\|\boldsymbol{\Phi}\boldsymbol{J}_{\tau_h}-\boldsymbol{Y}\right\|_F}, \tag{4.14}$$

where, $\|\cdot\|_{\infty,2}$ is the dual norm of $\|\cdot\|_{1,2}$ [129, Corollary 6.2]. Similarly, the root of the nonlinear equation $\phi_{\text{MMV}_{\text{TM}}}(\tau)=\widetilde{\sigma}$ can also be reached by Newton iterations

$$\tau_{h+1} = \tau_h + \frac{\widetilde{\sigma}-\phi_{\text{MMV}_{\text{TM}}}(\tau_h)}{\phi'_{\text{MMV}_{\text{TM}}}(\tau_h)}. \tag{4.15}$$

The projection operator $\mathcal{P}_\tau[\cdot]$ is replaced with orthogonal projection onto $\|\cdot\|_{1,2}$ balls, $\mathcal{P}_{\tau,\text{MMV}_{\text{TM}}}[\cdot]$, which is defined as follows

$$\mathcal{P}_{\tau,\text{MMV}_{\text{TM}}}[\boldsymbol{J}] := \left\{\arg\min_{\boldsymbol{X}} \quad \|\boldsymbol{J}-\boldsymbol{X}\|_F \quad \text{subject to} \quad \|\boldsymbol{X}\|_{1,2} \le \tau\right\}. \tag{4.16}$$

We refer to [129, Theorem 6.3] for the implementation of the projection operator. The MMV_{TM} $\text{BP}_{\widetilde{\sigma}}$ problem is solved by Algorithm 2 and Algorithm 3 with the Pareto curve, $\phi_{\text{MMV}_{\text{TM}}}(\tau)$, its derivative with respective to τ, $\phi'_{\text{MMV}_{\text{TM}}}(\tau)$, and the projection operator, $\mathcal{P}_{\tau,\text{MMV}_{\text{TM}}}[\cdot]$, defined by Eq. (4.13), Eq. (4.14), and Eq. (4.16), respectively. Note that Tr represents the trace of a matrix.

Algorithm 2: Spectral projected gradient for MMV_{TM} LS_τ problem.

Input : $\boldsymbol{\Phi}$, $\boldsymbol{Y}$, $\boldsymbol{J}$, τ
Output: $\boldsymbol{J}_\tau$, $\boldsymbol{R}_\tau$

Set minimum and maximum step lengths $0 < \alpha_{\min} < \alpha_{\max}$;
Set initial step length $\alpha_0 \in [\alpha_{\min}, \alpha_{\max}]$ and sufficient descent parameter $\gamma \in (0, 0.5)$;
Set an integer line search history length $M \geq 1$;
$\boldsymbol{J}_0 = \mathcal{P}_{\tau,\text{MMV}_{\text{TM}}}[\boldsymbol{J}]$, $\boldsymbol{R}_0 = \boldsymbol{Y} - \boldsymbol{\Phi}\boldsymbol{J}_0$, $\boldsymbol{G}_0 = -\boldsymbol{\Phi}^H \boldsymbol{R}_0$, $\ell = 0$;
begin
  $\delta_\ell \leftarrow \left| \|\boldsymbol{R}_\ell\|_F - \frac{\text{Tr}\{\boldsymbol{Y}^H \boldsymbol{R}_\ell\} - \tau \|\boldsymbol{G}_\ell\|_{\infty,2}}{\|\boldsymbol{R}_\ell\|_F} \right|$ ▷ compute duality gap;
  If $\delta_\ell \leq \epsilon$, **then** break;
  $\alpha \leftarrow \alpha_\ell$ ▷ initial step length;
  begin
    $\overline{\boldsymbol{J}} \leftarrow \mathcal{P}_{\tau,\text{MMV}_{\text{TM}}}[\boldsymbol{J}_\ell - \alpha \boldsymbol{G}_\ell]$ ▷ projection;
    $\overline{\boldsymbol{R}} \leftarrow \boldsymbol{Y} - \boldsymbol{\Phi}\overline{\boldsymbol{J}}$ ▷ update the corresponding residual;
    if $\left\|\overline{\boldsymbol{R}}\right\|_F^2 \leq \max\limits_{h \in [0, \min\{\ell, M-1\}]} \|\boldsymbol{R}_{\ell-h}\|_F^2 + \gamma \Re\left\{\text{Tr}\left\{\left(\overline{\boldsymbol{J}} - \boldsymbol{J}_\ell\right)^H \boldsymbol{G}_{p,\ell}\right\}\right\}$ **then**
      break;
    else
      $\alpha \leftarrow \alpha/2$;
    end
  end
  $\boldsymbol{J}_{\ell+1} \leftarrow \overline{\boldsymbol{J}}$, $\boldsymbol{R}_{\ell+1} \leftarrow \overline{\boldsymbol{R}}$, $\boldsymbol{G}_{\ell+1} \leftarrow -\boldsymbol{\Phi}^H \boldsymbol{R}_{\ell+1}$ ▷ update iterates;
  $\Delta\boldsymbol{J} \leftarrow \boldsymbol{J}_{\ell+1} - \boldsymbol{J}_\ell$, $\Delta\boldsymbol{G} \leftarrow \boldsymbol{G}_{\ell+1} - \boldsymbol{G}_\ell$;
  if $\Re\{\text{Tr}\{\Delta\boldsymbol{J}^H \Delta\boldsymbol{G}\}\} \leq 0$ **then**
    $\alpha_{\ell+1} \leftarrow \alpha_{\max}$ ▷ update the Barzilai-Borwein step length;
  else
    $\alpha_{\ell+1} \leftarrow \min\left\{\alpha_{\max}, \max\left[\alpha_{\min}, \frac{\text{Tr}\{\Delta\boldsymbol{J}^H \Delta\boldsymbol{J}\}}{\Re\{\text{Tr}\{\Delta\boldsymbol{J}^H \Delta\boldsymbol{G}\}\}}\right]\right\}$;
  end
  $\ell \leftarrow \ell + 1$;
end
return $\boldsymbol{J}_\tau \leftarrow \boldsymbol{J}_\ell$, $\boldsymbol{R}_\tau \leftarrow \boldsymbol{R}_\ell$;

4.1.4 SOLVING THE MMV MODEL: TE CASE

For the TE polarization case, the electric field is not a scalar anymore. Care must be taken in the formulation of the MMV $\text{BP}_{\widetilde{\sigma}}$ problem. Considering the two components of electric field, E_x and E_y, the inverse scattering problem for the TE case can be formulated as

$$\text{MMV}_{\text{TE}}\ \text{BP}_{\widetilde{\sigma}}: \quad \text{minimize} \quad \kappa_{\text{TE}}(\boldsymbol{J}) \quad \text{subject to} \quad \rho(\boldsymbol{\Phi}\boldsymbol{J} - \boldsymbol{Y}) \leq \widetilde{\sigma}, \tag{4.17}$$

Algorithm 3: Newton root-finding framework.

Input : $\boldsymbol{\Phi}$, $\boldsymbol{Y}$, $\widetilde{\sigma}$
Output: $\boldsymbol{J}_{\widetilde{\sigma}}$

$\boldsymbol{J}_0 \leftarrow \boldsymbol{0}$, $\boldsymbol{R}_0 \leftarrow \boldsymbol{Y}$, $\tau_0 \leftarrow 0$, $h \leftarrow 0$;
begin
  If $|\|\boldsymbol{R}_h\|_F - \widetilde{\sigma}| \leq \epsilon$, **then** break;
  Solve the MMV_{TM} LS_τ problem for τ_h using Algorithm 2;
  $\boldsymbol{R}_h \leftarrow \boldsymbol{\Phi}\boldsymbol{J}_h - \boldsymbol{Y}$;
  $\tau_{h+1} \leftarrow \tau_h + \frac{\widetilde{\sigma} - \phi_{\text{MMV}_{\text{TM}}}(\tau_h)}{\phi'_{\text{MMV}_{\text{TM}}}(\tau_h)}$ ▷ Newton update;
  $h \leftarrow h + 1$;
end
return $\boldsymbol{J}_{\widetilde{\sigma}} \leftarrow \boldsymbol{J}_h$;

where,

$$\kappa_{\text{TE}}(\boldsymbol{J}) := \sum_{n=1}^{N} \left\| \left[\boldsymbol{J}_{2n-1,:} \; \boldsymbol{J}_{2n,:} \right]^T \right\|_2, \tag{4.18}$$

and

$$\rho(\cdot) := \|\cdot\|_F, \tag{4.19}$$

are gauge functions, since κ_{TE} and ρ satisfy the following properties [136]

1. κ_{TE} and ρ are nonnegative, $\kappa_{\text{TE}}(\boldsymbol{X}) \geq 0$, $\rho(\boldsymbol{X}) \geq 0$;
2. κ_{TE} and ρ are positive homogeneous, $\kappa_{\text{TE}}(\alpha\boldsymbol{X}) = \alpha\kappa_{\text{TE}}(\boldsymbol{X})$, $\rho(\alpha\boldsymbol{X}) = \alpha\rho(\boldsymbol{X})$;
3. κ_{TE} and ρ vanish at the origin, $\kappa_{\text{TE}}(\boldsymbol{0}) = 0$, $\rho(\boldsymbol{0}) = 0$;
4. κ_{TE} and ρ are convex.

The MMV_{TE} LS_τ problem is formulated accordingly as

$$\text{MMV}_{\text{TE}}\ \text{LS}_\tau: \quad \text{minimize} \quad \rho(\boldsymbol{\Phi}\boldsymbol{J} - \boldsymbol{Y}) \quad \text{subject to} \quad \kappa_{\text{TE}}(\boldsymbol{J}) \leq \tau. \tag{4.20}$$

Different from the TM case, the TE mixed-norm, $\kappa_{\text{TE}}(\boldsymbol{J})$, is defined by summing up the ℓ_2-norms of N vectors. The elements of each vector come from two adjacent rows of matrix $\boldsymbol{J}$. The two adjacent rows represent the two spatially orthogonal components, x and y, respectively, and each ℓ_2-norm is physically the square root of the power of all the contrast sources induced by multiple transmitters on one discretized grid. Before using Algorithm 2 and Algorithm 3 to solve the MMV_{TE} LS_τ problem, we must answer the following questions:

1. Is the Pareto curve, $\phi_{\text{MMV}_{\text{TE}}}(\tau)$, strictly decreasing and continuously differentiable?
2. If so, what is the explicit expression of the derivative?
3. How to implement the projection operator, $\mathcal{P}_{\tau,\text{MMV}_{\text{TE}}}[\cdot]$?

In the following, Questions 1 and 2 are answered in the derivation of the dual, $\mathcal{G}(\boldsymbol{Z},\lambda)$, and Question 3 is answered in the introduction of the projection operator, $\mathcal{P}_{\tau,\text{MMV}_{\text{TE}}}[\cdot]$.

Derivation of the dual Let us rewrite Eq. (4.20) in terms of $\boldsymbol{J}$ and an explicit residual term $\boldsymbol{R}$ as follows

$$\underset{\boldsymbol{J},\boldsymbol{R}}{\text{minimize}} \quad \rho(\boldsymbol{R}) \quad \text{subject to} \quad \boldsymbol{\Phi}\boldsymbol{J}+\boldsymbol{R}=\boldsymbol{Y}, \quad \kappa_{\text{TE}}(\boldsymbol{J}) \leq \tau. \tag{4.21}$$

The dual to this equivalent problem is given by [137, Chapter 5]

$$\underset{\boldsymbol{Z},\lambda}{\text{maximize}} \quad \mathcal{G}(\boldsymbol{Z},\lambda) \quad \text{subject to} \quad \lambda \geq 0, \tag{4.22}$$

where $\boldsymbol{Z} \in \mathbb{C}^{(2M)\times P}$ and $\lambda \in \mathbb{C}$ are dual variables, and $\mathcal{G}$ is the Lagrange dual function, given by

$$\mathcal{G}(\boldsymbol{Z},\lambda) := \inf_{\boldsymbol{J},\boldsymbol{R}} \left\{ \rho(\boldsymbol{R}) - \text{Tr}\left\{\boldsymbol{Z}^H(\boldsymbol{\Phi}\boldsymbol{J}+\boldsymbol{R}-\boldsymbol{Y})\right\} + \lambda\left(\kappa_{\text{TE}}(\boldsymbol{J})-\tau\right)\right\}. \tag{4.23}$$

By separability of the infimum over $\boldsymbol{J}$ and $\boldsymbol{R}$ we can rewrite $\mathcal{G}$ in terms of two separate suprema,

$$\mathcal{G}(\boldsymbol{Z},\lambda) = \text{Tr}\left\{\boldsymbol{Y}^H\boldsymbol{Z}\right\} - \tau\lambda - \sup_{\boldsymbol{R}}\left\{\text{Tr}\left\{\boldsymbol{Z}^H\boldsymbol{R}\right\} - \rho(\boldsymbol{R})\right\} - \sup_{\boldsymbol{J}}\left\{\text{Tr}\left\{\boldsymbol{Z}^H(\boldsymbol{\Phi}\boldsymbol{J})\right\} - \lambda\kappa_{\text{TE}}(\boldsymbol{J})\right\}. \tag{4.24}$$

It is easy to see that the first supremum is the conjugate function of ρ and the second supremum is the conjugate function of κ_{TE} [137, Chapter 3.3], by noting that

$$\text{Tr}\left\{\boldsymbol{Z}^H\boldsymbol{R}\right\} = \text{vec}\{\boldsymbol{Z}\}^H\text{vec}\{\boldsymbol{R}\}, \quad \rho(\boldsymbol{R}) = \rho(\text{vec}\{\boldsymbol{R}\}), \tag{4.25}$$

and

$$\text{Tr}\left\{\boldsymbol{Z}^H(\boldsymbol{\Phi}\boldsymbol{J})\right\} = \text{vec}\left\{\widetilde{\boldsymbol{Z}}\right\}^H\text{vec}\{\boldsymbol{J}\}, \quad \kappa_{\text{TE}}(\boldsymbol{J}) = \kappa_{\text{TE}}(\text{vec}\{\boldsymbol{J}\}), \tag{4.26}$$

respectively. Here, $\text{vec}\{\cdot\}$ is the vectorization of a matrix, $\widetilde{\boldsymbol{Z}} = \boldsymbol{\Phi}^H\boldsymbol{Z} \in \mathbb{C}^{(2N)\times P}$, and $\kappa_{\text{TE}}(\text{vec}\{\boldsymbol{J}\})$ is defined equivalently as $\kappa_{\text{TE}}(\boldsymbol{J})$ in Eq. (4.18). Therefore, we have

$$\text{Tr}\left\{\boldsymbol{Z}^H\boldsymbol{R}\right\} - \rho(\boldsymbol{R}) = \begin{cases} 0 & \rho^o(\boldsymbol{Z}) \leq 1 \\ \infty & \text{otherwise} \end{cases}, \tag{4.27}$$

and

$$\text{Tr}\left\{\boldsymbol{Z}^H(\boldsymbol{\Phi}\boldsymbol{J})\right\} - \lambda\kappa_{\text{TE}}(\boldsymbol{J}) = \begin{cases} 0 & \kappa^o_{\text{TE}}(\widetilde{\boldsymbol{Z}}) \leq \lambda \\ \infty & \text{otherwise} \end{cases}, \tag{4.28}$$

where, the polar of ρ and κ_{TE} are defined by

$$\rho^o(\boldsymbol{Z}) := \sup_{\boldsymbol{R}}\left\{\text{Tr}\left\{\boldsymbol{Z}^H\boldsymbol{R}\right\} \middle| \rho(\boldsymbol{R}) \leq 1\right\}, \tag{4.29}$$

and

$$\kappa^o_{\text{TE}}(\widetilde{\boldsymbol{Z}}) := \sup_{\boldsymbol{J}}\left\{\text{Tr}\left\{\boldsymbol{Z}^H(\boldsymbol{\Phi}\boldsymbol{J})\right\} \middle| \kappa_{\text{TE}}(\boldsymbol{J}) \leq \lambda\right\}, \tag{4.30}$$

respectively. If the gauge function is a norm, the polar reduces to the dual norm [137, Section 3.3.1], i.e., $\rho^o(\boldsymbol{Z}) = \|\boldsymbol{Z}\|_F$ and

$$\kappa^o_{\text{TE}}(\widetilde{\boldsymbol{Z}}) = \left(\sum_{n=1}^{N} \left\|\left[\widetilde{\boldsymbol{Z}}_{2n-1,:}\ \widetilde{\boldsymbol{Z}}_{2n,:}\right]\right\|_2^{\infty}\right)^{1/\infty} = \max\left\{\left\|\left[\widetilde{\boldsymbol{Z}}_{2n-1,:}\ \widetilde{\boldsymbol{Z}}_{2n,:}\right]\right\|_2 \middle| n = 1,2,3,\cdots,N\right\} \tag{4.31}$$

(for more details see [129, Corollary 6.2]). Substitution of (4.27) and (4.28) into (4.24) yields

$$\underset{\boldsymbol{Z},\lambda}{\text{maximize}} \quad \text{Tr}\left\{\boldsymbol{Y}^H\boldsymbol{Z}\right\} - \tau\lambda \quad \text{subject to} \quad \rho^o(\boldsymbol{Z}) \le 1, \quad \kappa^o_{\text{TE}}(\widetilde{\boldsymbol{Z}}) \le \lambda. \tag{4.32}$$

In the case $\rho(\cdot) = \|\cdot\|_F$, the dual variable $\boldsymbol{Z}$ can be easily derived from

$$\sup_{\boldsymbol{R}} \quad \text{Tr}\left\{\boldsymbol{Z}^H\boldsymbol{R}\right\} - \|\boldsymbol{R}\|_F = 0, \quad \text{if } \|\boldsymbol{Z}\|_F \le 1, \tag{4.33}$$

which is $\boldsymbol{Z} = \frac{\boldsymbol{R}}{\|\boldsymbol{R}\|_F}$. To derive the optimal λ, we can observe from Eq. (4.32) that as long as $\tau > 0$, λ must be at its lower bound $\kappa^o_{\text{TE}}(\widetilde{\boldsymbol{Z}})$, otherwise one can increase the objective $\text{Tr}\left\{\boldsymbol{Y}^H\boldsymbol{Z}\right\} - \tau\lambda$. Therefore, we obtain

$$\lambda = \frac{\kappa^o_{\text{TE}}\left(\boldsymbol{\Phi}^H\boldsymbol{R}\right)}{\|\boldsymbol{R}\|_F}. \tag{4.34}$$

According to [135, Theorem 5.2], we know that, on the open interval $\tau \in (0, \tau_0)$, where

$$\tau_0 = \min\left\{\tau \ge 0 \,\middle|\, \phi_{\text{MMV}_{\text{TE}}}(\tau) = \min_{\boldsymbol{J}} \rho(\boldsymbol{R})\right\},$$

the Pareto curve,

$$\phi_{\text{MMV}_{\text{TE}}}(\tau) = \rho(\boldsymbol{R})\big|_{\boldsymbol{J}=\boldsymbol{J}_\tau}, \tag{4.35}$$

is strictly decreasing and continuously differentiable with the derivative given by

$$\phi'_{\text{MMV}_{\text{TE}}}(\tau) = -\lambda = -\frac{\kappa^o_{\text{TE}}\left(\boldsymbol{\Phi}^H\boldsymbol{R}\right)}{\|\boldsymbol{R}\|_F}. \tag{4.36}$$

Projection operator The projection operator $\mathcal{P}_\tau[\cdot]$ is replaced with orthogonal projection onto $\kappa_{\text{TE}}(\cdot)$ balls, $\mathcal{P}_{\tau,\text{MMV}_{\text{TE}}}[\cdot]$, which is defined as follows

$$\mathcal{P}_{\tau,\text{MMV}_{\text{TE}}}[\boldsymbol{J}] := \left\{\underset{\boldsymbol{X}}{\text{argmin}} \quad \|\boldsymbol{J}-\boldsymbol{X}\|_F \quad \text{subject to} \quad \kappa_{\text{TE}}(\boldsymbol{X}) \le \tau\right\}. \tag{4.37}$$

With a simple matrix transformation of $\overline{\boldsymbol{J}}_{n,:} = \left[\boldsymbol{J}_{2n-1,:}\ \boldsymbol{J}_{2n,:}\right]$ and $\overline{\boldsymbol{X}}_{n,:} = \left[\boldsymbol{X}_{2n-1,:}\ \boldsymbol{X}_{2n,:}\right]$, we can rewrite Eq. (4.37) as follows

$$\left\{\underset{\overline{\boldsymbol{X}}}{\text{argmin}} \quad \left\|\overline{\boldsymbol{J}}-\overline{\boldsymbol{X}}\right\|_F \quad \text{subject to} \quad \left\|\overline{\boldsymbol{X}}\right\|_{1,2} \le \tau\right\} = \mathcal{P}_{\tau,\text{MMV}_{\text{TM}}}\left[\overline{\boldsymbol{J}}\right]. \tag{4.38}$$

In doing so, the projection operator in TE case satisfies [129, Theorem 6.3].

Now the MMV_{TE} $\text{BP}_{\widetilde{\sigma}}$ problem can be solved by Algorithm 2 and Algorithm 3 with the Pareto curve, $\phi_{\text{MMV}_{\text{TE}}}(\tau)$, its derivative with respective to τ, $\phi'_{\text{MMV}_{\text{TE}}}(\tau)$, and the projection operator, $\mathcal{P}_{\tau,\text{MMV}_{\text{TE}}}[\cdot]$, defined by Eq. (4.35), Eq. (4.36), and Eq. (4.38), respectively.

4.1.5 CV-BASED MODIFIED SPGL1

In real applications, the noise level, i.e., the parameter $\widetilde{\sigma}$, is generally unknown, which means the termination condition, $\phi_{\mathrm{MMV}}(\tau)=\widetilde{\sigma}$, does not work anymore. In order to deal with this problem, we modified the SPGL1 method based on the CV technique [138, 139], in which $\widetilde{\sigma}$ is set 0 and the iteration is terminated using the CV technique. In doing so, the problem of estimating the noise level, i.e., the parameter $\widetilde{\sigma}$, can be well circumvented.

CV is a statistical technique that separates a data-set into a training (estimation) set and a testing (CV) set. The training set is used to construct the model and the testing set is used to adjust the model order so that the noise is not over-fitted. The basic idea behind this technique is to sacrifice a small number of measurements in exchange for prior knowledge. Specifically, when CV is utilized in SPGL1 method, we separate the original scattering matrix to a reconstruction matrix, $\boldsymbol{\Phi}_{p,\mathrm{rec}}\in\mathbb{C}^{Q_{\mathrm{rec}}\times N}$, and a CV matrix, $\boldsymbol{\Phi}_{p,\mathrm{CV}}\in\mathbb{C}^{Q_{\mathrm{CV}}\times N}$ with $Q=Q_{\mathrm{rec}}+Q_{\mathrm{CV}}$. The measurement vectors, $\boldsymbol{y}_p$, are also separated accordingly to a group of reconstruction measurement vectors, $\boldsymbol{y}_{p,\mathrm{rec}}\in\mathbb{C}^{Q_{\mathrm{rec}}}$, and a group of CV measurement vectors, $\boldsymbol{y}_{p,\mathrm{CV}}\in\mathbb{C}^{Q_{\mathrm{CV}}}$. The reconstruction residual and the CV residual are defined as

$$r_{\mathrm{rec}}=\left(\sum_{p=1}^{P}\left\|\boldsymbol{y}_{p,\mathrm{rec}}-\boldsymbol{\Phi}_{p,\mathrm{rec}}\boldsymbol{j}_p\right\|_2^2\right)^{1/2} \tag{4.39}$$

and

$$r_{\mathrm{CV}}=\left(\sum_{p=1}^{P}\left\|\boldsymbol{y}_{p,\mathrm{CV}}-\boldsymbol{\Phi}_{p,\mathrm{CV}}\boldsymbol{j}_p\right\|_2^2\right)^{1/2}, \tag{4.40}$$

respectively. In doing so, every iteration can be viewed as two separate parts: reconstructing the contrast sources by SPGL1 and evaluating the outcome by the CV technique. The trend of the CV residual in iteration behaves abruptly different (turns from decreasing to increasing) comparing to that of reconstruction residual, as soon as the reconstructed signal starts to overfit the noise. The reconstructed contrast sources are selected as the output corresponding to the smallest CV residual. To find the smallest CV residual, we consider an alternative termination condition which is given by

$$N_{\mathrm{Iter}}>N_{\mathrm{opt}}+\Delta N, \tag{4.41}$$

where, N_{Iter} is the current iteration number, N_{opt} is the iteration index corresponding to the smallest CV residual — the optimal solution. The idea behind this criterion is that the CV residual is identified as the smallest one if the CV residual keeps increasing monotonously for ΔN iterations. In the following experimental examples, this termination condition works well with $\Delta N=30$.

Once the normalized contrast sources are obtained, one can achieve the shape of the scatterers defined as

$$\boldsymbol{\gamma}_{\mathrm{MMV_{TM}},n}=\sum_{p=1}^{P}\left|\boldsymbol{j}_{p,n}\right|^2,\quad n=1,2,3,\cdots,N, \tag{4.42}$$

or

$$\boldsymbol{\gamma}_{\mathrm{MMV_{TE}},n}=\sum_{p=1}^{P}\left(\left|\boldsymbol{j}_{p,2n-1}\right|^2+\left|\boldsymbol{j}_{p,2n}\right|^2\right),\quad n=1,2,3,\cdots,N, \tag{4.43}$$

where $\boldsymbol{j}_{p,n}$, $\boldsymbol{\gamma}_{\mathrm{MMV_{TM}},n}$, and $\boldsymbol{\gamma}_{\mathrm{MMV_{TE}},n}$ represent the n-th element of the vectors $\boldsymbol{j}_p$, $\boldsymbol{\gamma}_{\mathrm{MMV_{TM}}}$, and $\boldsymbol{\gamma}_{\mathrm{MMV_{TE}}}$, respectively.

4.2 SYNTHETIC AND EXPERIMENTAL DATA INVERSION

In this section, the proposed method is tested with both synthetic data and experimental data. In the meanwhile, we have also processed the same data using LSM for comparison. Since the background of the experiments is free space, LSM consists in solving the integral equations of the indicator functions (see Fig. 2.12)

$$\int_{\Gamma_1} E_3\left(\vec{x}_\mathrm{r}, \vec{x}_\mathrm{t}\right) g_3\left(\vec{x}_\mathrm{t} \middle| \vec{z}\right) d\vec{x}_\mathrm{t} = E_{3,3}\left(\vec{x}_\mathrm{r} \middle| \vec{z}\right), \tag{4.44}$$

and

$$\int_{\Gamma_1} \begin{bmatrix} E_1 & 0 \\ 0 & E_2 \end{bmatrix} \left(\vec{x}_\mathrm{r}, \vec{x}_\mathrm{t}\right) \begin{bmatrix} g_{1,1} & g_{1,2} \\ g_{2,1} & g_{2,2} \end{bmatrix} \left(\vec{x}_\mathrm{t} \middle| \vec{z}\right) d\vec{x}_\mathrm{t} = \begin{bmatrix} E_{1,1} & E_{1,2} \\ E_{2,1} & E_{2,2} \end{bmatrix} \left(\vec{x}_\mathrm{r} \middle| \vec{z}\right), \tag{4.45}$$

for the TM and TE cases, respectively, where, $E_1\left(\vec{x}_\mathrm{r}, \vec{x}_\mathrm{t}\right)$, $E_2\left(\vec{x}_\mathrm{r}, \vec{x}_\mathrm{t}\right)$, and $E_3\left(\vec{x}_\mathrm{r}, \vec{x}_\mathrm{t}\right)$ represent x-, y-, and z-components of the scattered field probed at $\vec{x}_\mathrm{r}$ corresponding to the transmitter at $\vec{x}_\mathrm{t}$, respectively; $\vec{z}$ is the sampling point in the inversion domain; $E_{i,j}\left(\vec{x}_\mathrm{r} \middle| \vec{z}\right)$ is i-th component of the electric field at $\vec{x}_\mathrm{r}$ generated by an ideal electric dipole located at $\vec{z}$ with the polarization vector parallel to x_j-axis, which are given by

$$E_{3,3} = \frac{1}{4}\omega\mu_0 H_0^{(1)}(-kR), \tag{4.46a}$$

$$E_{1,1} = \frac{-k}{4\omega\varepsilon_0}\left(\frac{H_1^{(1)}(-kR)}{R} + \frac{kx_2^2}{R^2}H_2^{(1)}(-kR)\right), \tag{4.46b}$$

$$E_{1,2} = \frac{k^2 x_1 x_2}{4\omega\varepsilon_0 R^2} H_2^{(1)}(-kR), \tag{4.46c}$$

$$E_{2,1} = \frac{k^2 x_1 x_2}{4\omega\varepsilon_0 R^2} H_2^{(1)}(-kR), \tag{4.46d}$$

$$E_{2,2} = \frac{-k}{4\omega\varepsilon_0}\left(\frac{H_1^{(1)}(-kR)}{R} + \frac{kx_1^2}{R^2}H_2^{(1)}(-kR)\right), \tag{4.46e}$$

where, $R = \left\|\vec{z} - \vec{x}_\mathrm{r}\right\|_2$ (See Appendix B for the derivation). Eq. (4.44) and Eq. (4.45) can be reformulated as a set of linear systems of equations

$$\boldsymbol{Y}\boldsymbol{g}_{\vec{z}} = \boldsymbol{f}_{\vec{z}}, \tag{4.47}$$

where, $\boldsymbol{Y}$ is the measurement data matrix, $\boldsymbol{g}_{\vec{z}}$ is the indicator function of the sampling point $\vec{z}$ in the form of a column vector, $\boldsymbol{f}_{\vec{z}}$ is the right side of Eq. (4.44) in the form of a column vector. Following the same approach to solving Eq. (4.47) in [13, 140], the shape of the scatterers is defined by

$$\boldsymbol{\gamma}_{\mathrm{LSM}}(\vec{z}) = 1 \Big/ \left\|\boldsymbol{g}_{\vec{z}}\right\|^2, \tag{4.48}$$

4

where, $\left\|\boldsymbol{g}_{\vec{z}}\right\|^2$ is given by

$$\|\boldsymbol{g}_{\vec{z}}\|^2 = \sum_{d=1}^{D}\left(\frac{s_d}{s_d^2+a^2}\right)^2\left|\boldsymbol{u}_d^H\boldsymbol{f}_{\vec{z}}\right|^2, \tag{4.49}$$

where, s_d represents the singular value of the data matrix, $\boldsymbol{Y}$, corresponding to the singular vector $\boldsymbol{u}_d$, $D=\min\{P,Q\}$, and $a=0.01\times\max_d\{s_d\}$.

We have also considered, in the TM cases, the improved LSM proposed in [106] in the comparison of the proposed method and LSM. The indicator function of the improved LSM is defined as

$$\boldsymbol{\gamma}_{\mathrm{LSM},I}(\vec{z}) = \left(\prod_{i=1}^{I}\frac{\left\|\boldsymbol{g}^x_{i,\vec{z}}\right\|^2}{\left\|\boldsymbol{g}_{\vec{z}}\right\|^2}\frac{\left\|\boldsymbol{g}^y_{i,\vec{z}}\right\|^2}{\left\|\boldsymbol{g}_{\vec{z}}\right\|^2}\right)^{\frac{1}{2I}}, \quad I=ka, \tag{4.50}$$

where, a is the radius of the smallest ball that covers the targets, the power $\frac{1}{2I}$ is a normalization factor, and $\boldsymbol{g}^x_{i,\vec{z}}$ and $\boldsymbol{g}^y_{i,\vec{z}}$ are obtained by replacing $E_{3,3}\left(\vec{z},\vec{x}_{\mathrm{r}}\right)$ in Eq. (4.44) with $\varphi_i^x\left(\vec{z},\vec{x}_{\mathrm{r}}\right)$ and $\varphi_i^y\left(\vec{z},\vec{x}_{\mathrm{r}}\right)$, respectively, the formulae of which are

$$\varphi_i^x = \frac{1}{4}\omega\mu_0 H_i^{(1)}(-kR)\cos\left(i(\phi_{\mathrm{r}}-\phi_{\mathrm{s}})\right), \tag{4.51a}$$

$$\varphi_i^y = \frac{1}{4}\omega\mu_0 H_i^{(1)}(-kR)\sin\left(i(\phi_{\mathrm{r}}-\phi_{\mathrm{s}})\right), \tag{4.51b}$$

where, ϕ_{r} and ϕ_{s} are the angular components of the polar coordinates of $\vec{z}$ and $\vec{x}_{\mathrm{r}}$, respectively. It is worth mentioning that both the contrast sources, $\boldsymbol{j}_p$, and the indicator function, $\boldsymbol{g}_{\vec{x}}$, are proportional to the amplitude of the electric field. According to the definition in Eq. (4.42), Eq. (4.43), and Eq. (4.48), $\boldsymbol{\gamma}_{\mathrm{MMV}}$ and $\boldsymbol{\gamma}_{\mathrm{LSM}}$ are proportional and inversely proportional to the power of the electric field, respectively. Therefore, the dB scaling used in the following examples is defined as

$$\boldsymbol{\gamma}_{\mathrm{dB}} = 10\times\log_{10}\left(\frac{\boldsymbol{\gamma}}{\max\{\boldsymbol{\gamma}\}}\right). \tag{4.52}$$

4.2.1 SYNTHETIC DATA IMAGING

In this subsection, the proposed method is first tested using synthetic data. The transmitting antenna is simulated for simplicity with an ideal electric dipole (TM-polarization case) and an ideal magnetic dipole (TE-polarization case). Coordinate system is established such that the dielectric parameters are variable along the x- and y-axes, but invariable along z-axis. The transmitting antenna rotates with a step of 10° on a circular orbit of 3 m radius centring at the origin (0,0). The receiving positions are taken on the same orbit with a step of 5° without any position close than 30° from the transmitting antenna. The measurement configuration of Simulation 1 and 2 is shown in Fig. 4.2, in which the selection of CV measurements and reconstruction measurements is illustrated. Empirically, an arc length $\geq\lambda/3$ is a good selection. The number of the CV

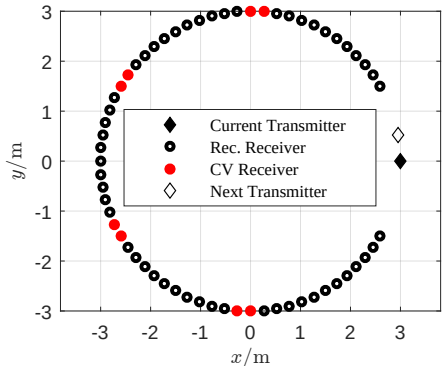

Figure 4.2: Measurement configuration of Simulations 1 and 2.

receivers on each arc depends on the density of the receiver positions, and the total CV receiver number is around 20% of the total measurement number [139]. The operating frequency is 500 MHz for both configurations. Two configurations of different objects are considered. One is combined with two circular metallic cylinders and the other one is a metallic cylinder with a "crescent-shaped" cross section. The radius of the circular cross section is 0.2 m ($= \lambda/3$), and the centres of the two circles are $(-0.45, 0.6)$ and $(0.45, 0.6)$, respectively. The crescent is the subtraction of two circles of radius 0.6 m ($= \lambda$) centring at (0, 0) and (0.4, 0), respectively. See Fig. 4.3 (a) and Fig. 4.5 (a) for their true geometry. The EM direct scattering problem is solved by a MATLAB-based 3-Dimensional (3-D) FDFD package "MaxwellFDFD" [30]. The technique of non-uniform staggered grids is used to reduce the computational burden, while for inverting the measurement data, we consider uniform discretization such that an inverse crime is circumvented. In the forward solver, we consider a coarse grid size of $\lambda/(15\sqrt{\epsilon_r})$ and the computational error brought by the coarse discretization plays the role of the noise disturbance. The data for inversion is obtained by subtracting the incident field from the total field. Periodic Boundary Conditions (PBCs) are imposed on the design of the FDFD stiffness matrix in order to simulate the 2-D configuration. Perfectly Matched Layers (PMLs) are used to simulate an anechoic chamber environment.

SIMULATION 1

In the first simulation, two identical circular metallic cylinders are considered. The radius of the circular cross section is 0.2 m ($= \lambda/3$), and the centres of the two circles are $(-0.45, 0.6)$ and $(0.45, 0.6)$, respectively. The true size and positions are shown in Fig. 4.3 (a). To reduce the computational cost, we restrict the inversion domain to $[-1.0, 1.0] \times [-0.4, 1.6]$ m^2. The inversion domain is uniformly discretized with a grid size of 0.01 m ($= \lambda/60$). Let us first consider the TM-polarized data. The residual curves are shown in Fig. 4.4 (a). The trend of the residual curves is like staircases, and each step corresponds to one update of the parameter τ. The CV residual starts to increase after 38 iterations, and $\Delta N = 30$ more iterations are performed before termination. The solution of the minimum CV residual is the optimal solution. The scatterer shape reconstructed

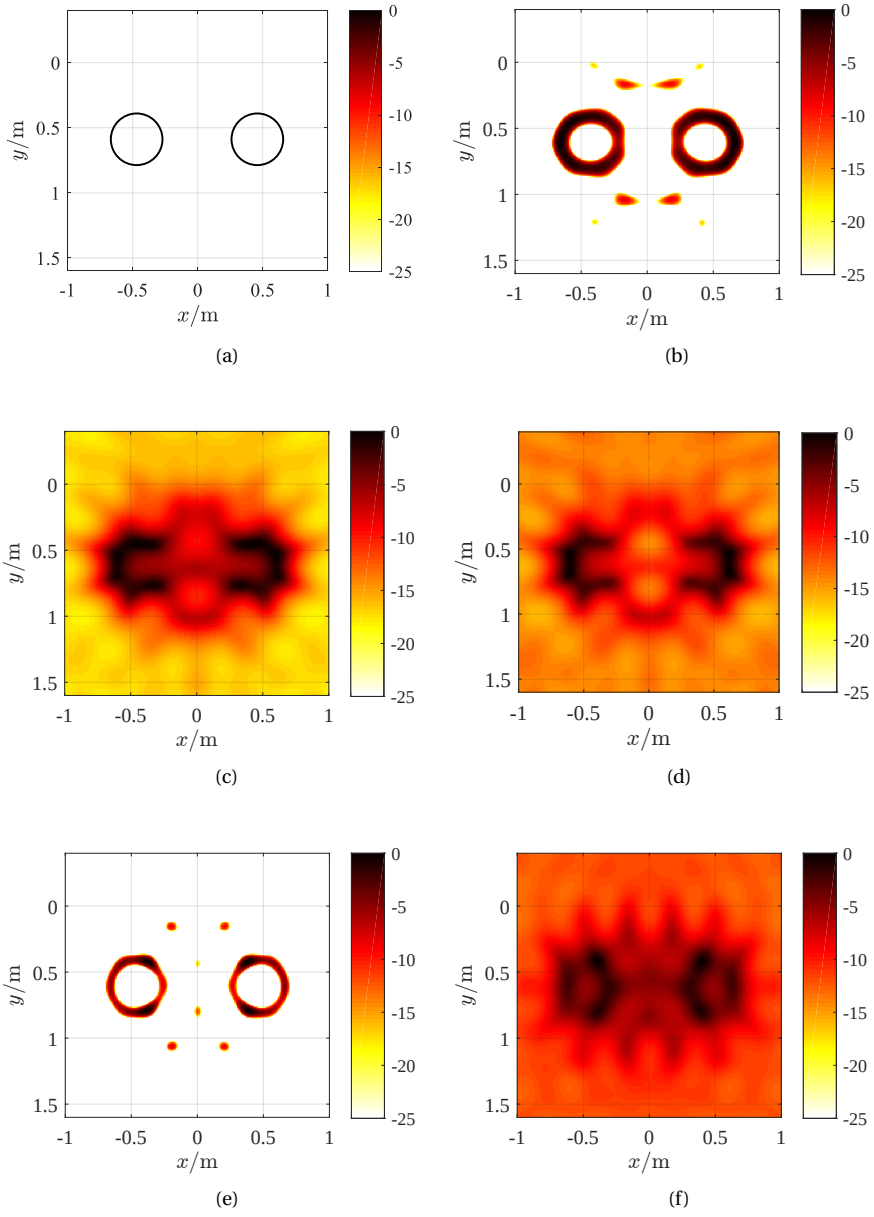

Figure 4.3: Scatterer geometry and its reconstructed shapes in Simulation 1. (a) Scatterer geometry; Reconstructed shape by processing the TM-polarized data with MMV (b), LSM (c), and the improved LSM with $I = 7$ (d), respectively. Reconstructed shape by processing the TE-polarized data with MMV (e) and LSM (f), respectively.

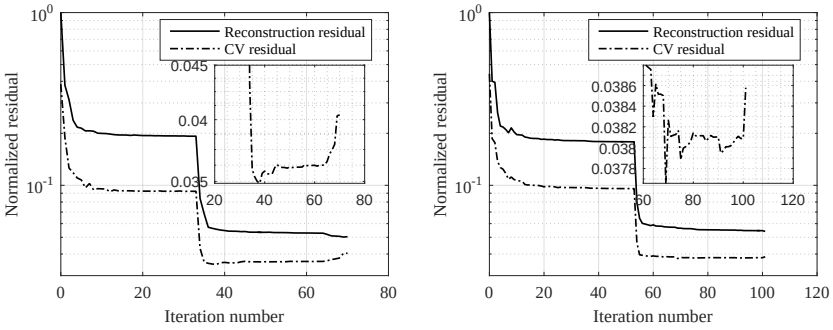

Figure 4.4: Reconstruction residual and CV residual curves of Simulation 1. (a) TM-polarized data; (b) TE-polarized data.

by MMV, LSM, and the improved LSM with $I = 6$ is shown in Figs. 4.3 (b), 4.3 (c) and 4.3 (d), respectively. By comparison of Figs. 4.3 (c) and 4.3 (d), it is observed that the artefacts between the two circular cylinders are suppressed by the improved LSM. However, the average amplitude of the sidelobes in the region of no targets increases from −20 dB to −15 dB. From Fig. 4.3 (b) we observe that the reconstructed boundary of the two identical circular cylinders shows higher resolution and lower sidelobes in comparison to 4.3(c) and (d), indicating that the resolving ability of the proposed method is better than LSM. Now let us process the TE-polarized data. Fig. 4.4 (b) gives the residual curves, and Figs. 4.3 (e) and 4.3 (f) show the scatterer shape reconstructed by MMV and LSM, respectively, from which we demonstrate again that in the aspect of resolving ability the proposed method outperforms both LSM and the improved LSM.

SIMULATION 2

To further test the inversion performance of the proposed method, we consider in the second simulation a metallic cylinder with a "crescent-shaped" cross section. The exact scatterer geometry is shown in Fig. 4.5 (a). We restrict the inversion domain to $[-1.0, 1.0] \times [-1.0, 1.0]$ m^2, in which the target is fully covered. The inversion domain is uniformly discretized with a grid size of 0.01 m ($= \lambda/60$). First, we process the TM-polarized data by MMV and LSM, respectively. Figs. 4.5 (b), 4.5 (c), and 4.5 (d) show the reconstructed shape by MMV, LSM, and the improved LSM, respectively, from which we can see the boundary at the left side is well reconstructed by the three methods, while the arc at the right side shows more artefacts in both Fig. 4.5 (b) and Fig. 4.5 (c), because the arc at the right side is concave and therefore the multi-path scattering is more serious than the boundary at the left side which is convex. Comparison of Figs. 4.5 (c) and 4.5 (d) demonstrates again the suppression to artefacts brought by the improved LSM is at the cost of increasing the average level of image noise. The scatterer shape reconstructed by processing the TE-polarized data with MMV and LSM is shown in Figs. 4.5 (e) and 4.5 (f), respectively, from which we see the same phenomenon in the discussion of Figs. 4.3 (e) and 4.3 (f). From the results, we demonstrate again that the proposed method shows

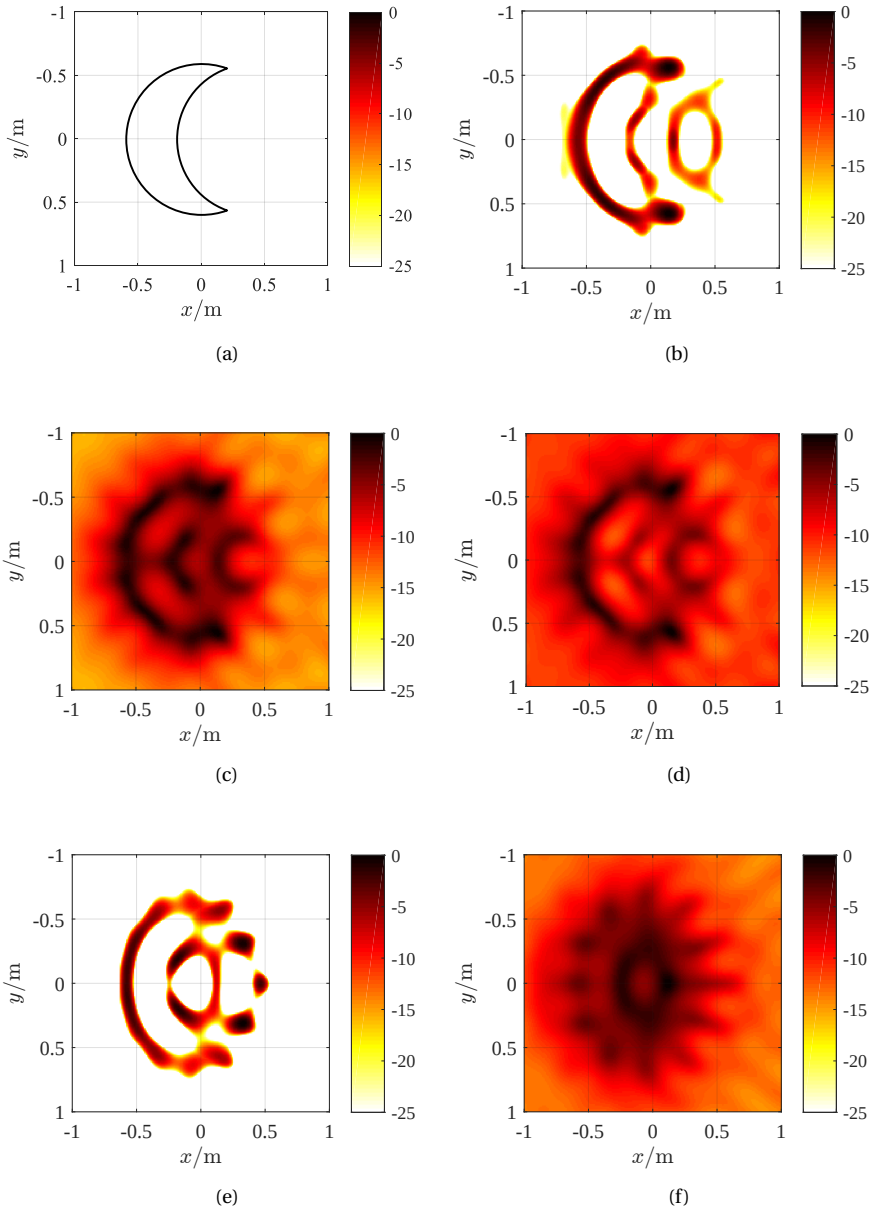

Figure 4.5: Scatterer geometry and its reconstructed shapes in Simulation 2. (a) Scatterer geometry; Reconstructed shape by processing the TM-polarized data with MMV (b), LSM (c), and the improved LSM with $I = 6$ (d), respectively. Reconstructed shape by processing the TE-polarized data with MMV (e) and LSM (f), respectively.

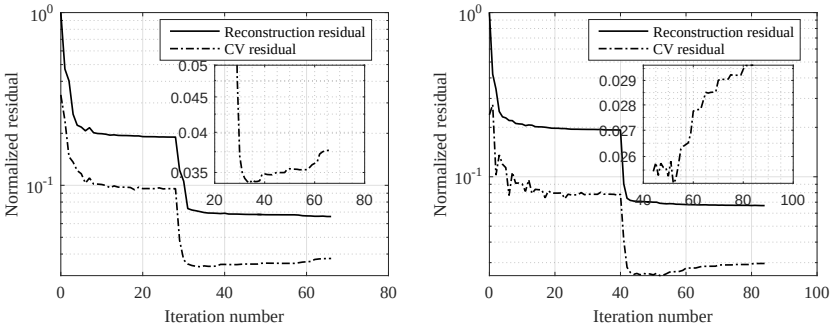

Figure 4.6: Reconstruction residual and CV residual curves of Simulation 2. (a) TM-polarized data; (b) TE-polarized data.

Table 4.1: Running times of the two numerical examples.

Example	Polarization	MMV [s]	LSM [s]	Improved LSM [s]
1	TM	16.1	0.0404	0.6900
	TE	80.1	0.0999	/
2	TM	14.7	0.0429	1.2583
	TE	59.2	0.0877	/

a higher resolving ability than both LSM and the improved LSM. The corresponding residual curves of the TM and TE cases are given in Figs. 4.6 (a) and 4.6 (b), respectively.

COMPUTATION TIME

Since the sensing matrices can be computed (or analytically given for a homogeneous background) and stored beforehand, the MMV-based linear method only involves a number of matrix-vector multiplications. The codes for reconstructing the contrast sources are written in MATLAB language. We ran the codes on a desktop with one Intel(R) Core(TM) i5-3470 CPU @ 3.20 GHz, and we did not use parallel computing. Table 4.1 lists the running times of the proposed method, LSM, and the improved LSM in the two simulations. As one can see that the computation time of the proposed method is hundreds of times longer than that of LSM and tens of times longer than the improved LSM. The most time-consuming part of the proposed method is the matrix-vector multiplication in each iteration, while LSM only calls Singular Value Decomposition (SVD) to the measurement data matrix for once. However, the running times of the proposed method are still acceptable in view of the gain of resolving ability.

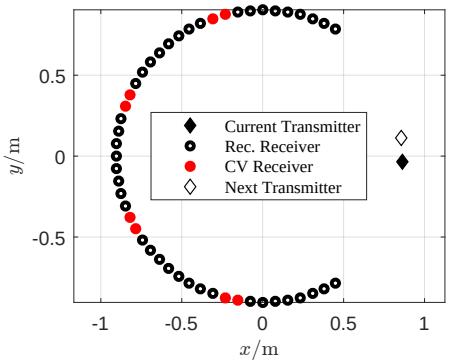

Figure 4.7: Measurement configuration of the Fresnel data-sets: *rectTM_cent*, *uTM_shaped*, and *rectTE_8f*.

4.2.2 EXPERIMENTAL DATA IMAGING

In this subsection, we applied our method to the experimental data provided by the Remote Sensing and Microwave Experiments Team at the Institut Fresnel, France, using an HP8530 network analyzer [31]. The experimental setup consists of a large anechoic chamber, 14.50 m long, 6.50 m wide and 6.50 m high, with a set of three positioners to adjust antennas or target positions. Fig. 4.7 gives the measurement configuration, in which the selection of CV measurements and reconstruction measurements is illustrated. The time dependence in this experiment is $\exp(\mathrm{i}\omega t)$. Therefore, after subtracting the incident field from the total field, the measurement data can be directly used for inversion. The targets we consider here are a rectangular metallic cylinder and a "U-shaped" metallic cylinder, which are shown in Figs. 4.8 (a) and 4.8 (b). Three data-sets are processed: *rectTM_cent*, *uTM_shaped*, and *rectTE_8f*.

First, let us process the TM-polarized data-set: *rectTM_cent* at 16 GHz. The inversion domain for imaging the rectangular metallic cylinder is restricted to $[-50, 50] \times [-50, 50]$ mm^2, and the inversion domain is uniformly discretized with a grid size of 0.5 mm ($= \lambda/37.5$). Figs. 4.9 (a), 4.9 (b), and 4.9 (c) show the scatterer shape reconstructed by MMV, LSM, and the improved LSM, respectively, from which we observe that Fig. 4.9 (a) shows a higher resolution and less artefacts than Figs. 4.9 (b) and 4.9 (c). Now let us consider the "U-shaped" metallic cylinder. The inversion domain is restricted to $[-100, 100] \times [-100, 100]$ mm^2, and the inversion domain is uniformly discretized with a grid size of 1 mm ($= \lambda/37.5$). Figs. 4.10 (a), 4.10 (b), and 4.10 (c) give the scatterer shape reconstructed by MMV, LSM, and the improved LSM, respectively. In this experiment, the artefacts inside the "U-shaped" cylinder is better suppressed by the improved LSM, while the increase of the noise level is obvious as well (from -18 dB of Fig. 4.10 (b) to -13 dB of Fig. 4.10 (c)). The boundary of the "U-shaped" cylinder is well reconstructed by the proposed method, while the occurrence of artefacts is inevitable in this case. Finally, let us process the TE-polarized data-set: *rectTE_8f* at 16 GHz. The scatterer shape reconstructed by MMV and LSM is shown in Figs. 4.11 (a) and 4.11 (b), respectively. It is easy to see that the boundary of the rectangular metallic cylinder is not distinguishable in Fig. 4.11 (b), while

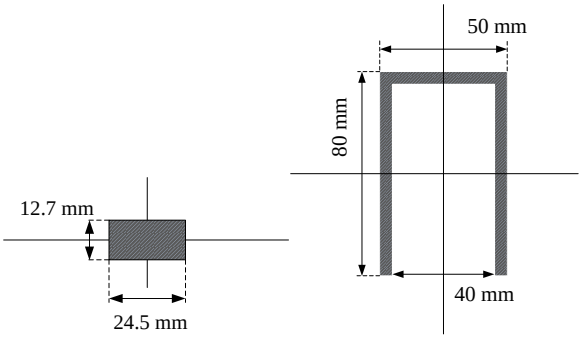

Figure 4.8: (a) The rectangular highly conductive cylinder; (b) The "U-shaped" highly conductive cylinder; (c) The dielectric object combined by two identical circular cylinders.

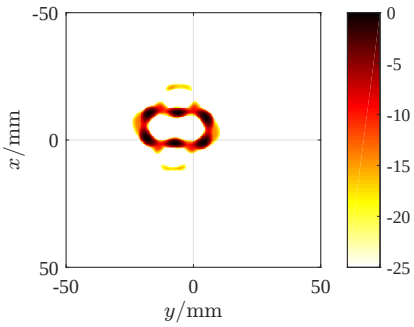

(a)

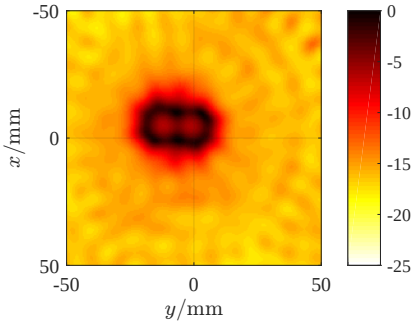

(b)

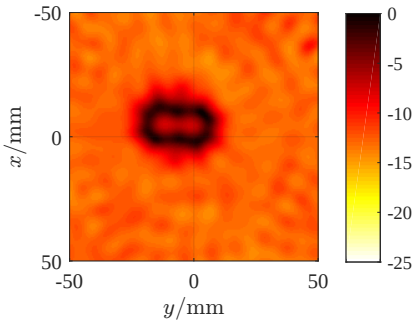

(c)

Figure 4.9: Scatterer shape reconstructed by processing the TM-polarized data-set: *rectTM_cent* at 16 GHz with MMV (a), LSM (b), and the improved LSM with $I = 9$ (c), respectively.

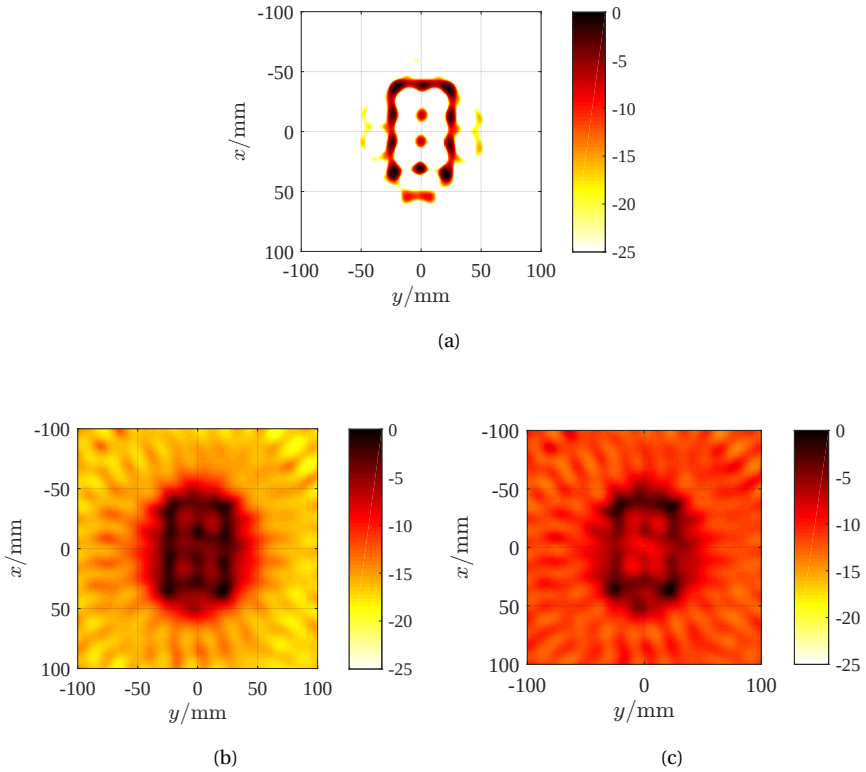

Figure 4.10: Scatterer shape reconstructed by processing the TM-polarized data-set: *uTM_shaped* at 8 GHz with MMV (a), LSM (b), and the improved LSM with $I = 8$ (c), respectively.

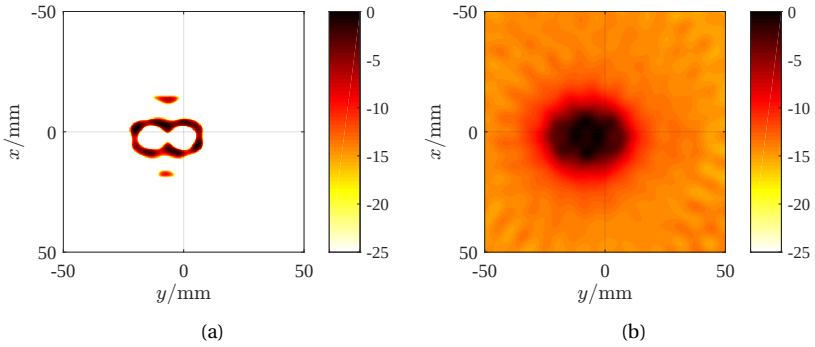

Figure 4.11: Scatterer shape reconstructed by processing the TE-polarized data-set: *rectTE_8f* at 16 GHz with MMV (a) and LSM (b), respectively.

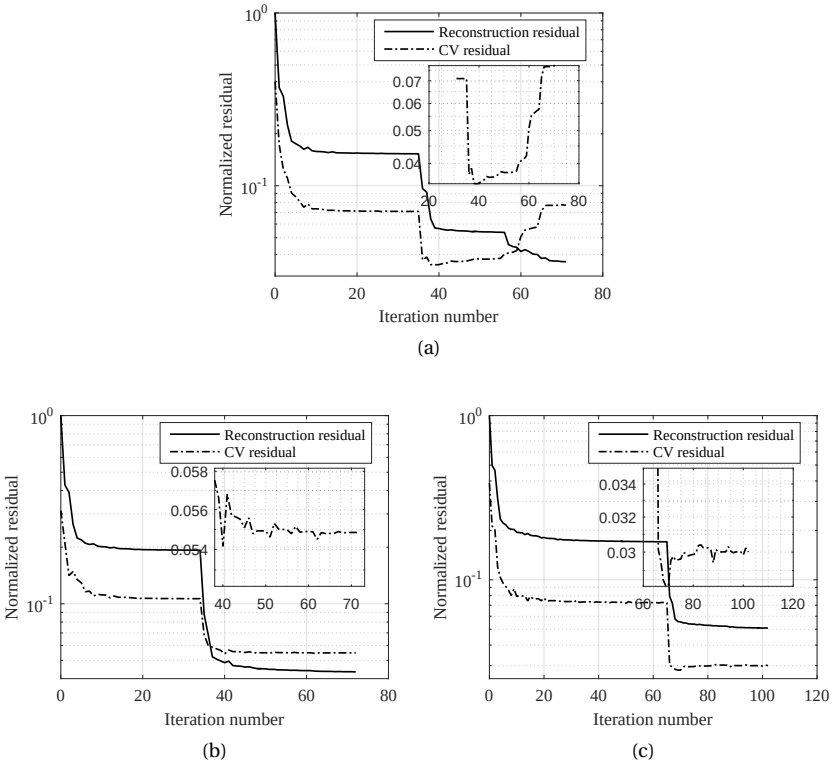

Figure 4.12: Reconstruction residual curve and CV residual curve of the Fresnel data-sets: *rectTM_cent* (a), *uTM_shaped* (b), and *rectTE_8f* (c), at 16 GHz, 8 GHz, and 16 GHz, respectively.

in Fig. 4.11 (a) the rectangular boundary can be well distinguished, demonstrating the higher resolving ability of our method in comparison to LSM. Figs. 4.12 (a), 4.12 (b), and 4.12 (c) show the residual curves of the proposed method in the three experiments.

4.3 CONCLUSIONS

In this chapter, a linear model based on the MMV model is proposed for addressing the nonlinear inverse scattering problem of highly conductive objects. The sum-of-norm of the contrast source matrix is used for the first time as a regularization constraint. A CV-based modified SPGL1 method is proposed for solving the proposed model, which circumvents the noise level estimation. Numerical results and experimental results demonstrate that the proposed method is able to reconstruct the boundary of the highly conductively targets with a higher resolution than both LSM and the improved LSM, even in some cases where the latter two methods fail to reconstruct the correct shape. The running time of the proposed method is hundreds of times longer than LSM and

tens of times longer than the improved LSM, but it is still acceptable and promising in view of the gain of resolving performance and the linear relationship between the computational complexity and the size of the inversion domain. A drawback of the proposed method is that it might fail in the presence of not conductive scatterers. One way of overcoming this limitation will be discussed later in Chapter 6.

5

LINEARIZED 3-D CONTRAST SOURCE INVERSION

Although the 3-Dimensional (3-D) inverse scattering problem is the most close-to-life model, it generally requires a huge amount of computational resources to achieve a valuable solution. In this chapter, a linearized 3-D ElectroMagnetic (EM) contrast source inversion method is proposed and successfully applied to two typical half-space configurations: 1) Ground Penetrating Radar (GPR) imaging and 2) Through-the-Wall Imaging (TWI). Specifically, the linear method proposed in Chapter 4 is extended to 3-D configuration. Then the total fields are calculated with the estimated contrast sources. Finally, an estimation of the contrast can be obtained by minimizing a cost functional which is a superposition of the data error and the state error. The contrast is estimated as the least square solution to the state equations, and the range constraints on the real part and imaginary part of the contrast are considered as *a priori* information.

The proposed method is capable to reconstruct not only the shape but also a coarse estimation of the dielectric parameters of the objects. Since the total fields in the inversion domain are updated only once, it is far more efficient than the nonlinear iterative inversion methods, e.g., Contrast Source Inversion (CSI) and Born Iterative Method (BIM). We have applied the proposed method to two typical half-space configurations: GPR imaging and TWI, and successfully obtained a coarse estimation of the contrast. The EM direct scattering problems are solved by a 3-D Finite Difference Frequency Domain (FDFD) solver — "MaxwellFDFD", and its companion C program — "FD3D" [30]. Moreover, we have also discussed the performance of the proposed linearized inversion method when the dielectric parameters of the background are not exactly known. It is worth noting that a similar strategy was considered by Caorsi et al. [142–144]. The limitations of this strategy were discussed by Chew, Bolomey et al. [145]. However,

Parts of this chapter have been published in [141].

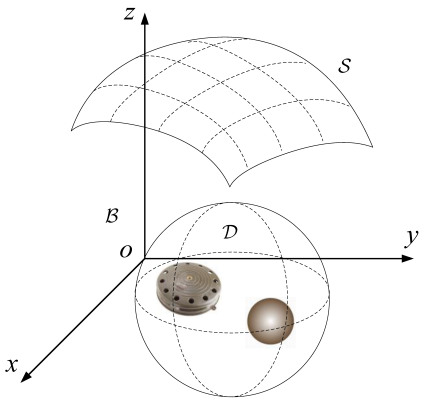

Figure 5.1: General geometry of 3-D inverse scattering problems. Sources and receivers are located on the surface $\mathcal{S}$. Objects are located in the inversion region $\mathcal{D}$.

the exploitation of the joint information of the equivalent currents via the sum-of-norm constraint term distinguishes our method from their strategy.

This chapter is organized as follows: In Section 5.1, the Multiple Measurement Vectors (MMV) linear method proposed in Chapter 4 is extended to 3-D inverse problems. The inversion of the contrast is introduced in Section 5.2. The inverted results of the numerical experiments of GPR imaging and TWI are given in Section 5.3 with the exact and an inexact background model. Finally, Section 5.4 summarizes this chapter.

5.1 EXTENSION OF THE MMV LINEAR METHOD TO 3-D CASES

5.1.1 FORMULATION

We consider a scattering configuration as depicted in Fig. 5.1, in which sources and receivers are located on the surface $\mathcal{S}$, and the objects are located in the background medium $\mathcal{B} \subset \mathbb{R}^3$. The region $\mathcal{D} \subset \mathcal{B}$ is the imaging domain which contains the objects. The sources are denoted by the subscript p in which $p \in \{1,2,3...,P\}$, and the receivers are denoted by the subscript q in which $q \in \{1,2,3,...,Q\}$. The electric field corresponding to each source is measured by all the receivers.

Considering a constant permeability μ_0, we can write the electric field equation in frequency-domain based on Maxwell's equations. By recalling Eq. (4.17), the formulation of the inverse scattering problem for the 3-D case can be formulated to a $\text{MMV}_{3\text{D}}$ Basis Pursuit Denoise ($\text{BP}_{\tilde{\sigma}}$) problem as follows

$$\text{MMV}_{3\text{D}}\ \text{BP}_{\tilde{\sigma}}: \quad \text{minimize} \quad \kappa_{3\text{D}}(\boldsymbol{J}) \quad \text{subject to} \quad \rho\left(\boldsymbol{\Phi}\cdot\boldsymbol{J}-\boldsymbol{Y}\right) \leq \tilde{\sigma}, \tag{5.1}$$

where,

$$\kappa_{3\text{D}}(\boldsymbol{J}) := \sum_{n=1}^{N} \left\| \left[\boldsymbol{J}_{2n-2,:}\ \boldsymbol{J}_{2n-1,:}\ \boldsymbol{J}_{2n,:}\right]^T \right\|_2. \tag{5.2}$$

The equivalent $\text{MMV}_{3\text{D}}$ Lasso (LS_τ) problem is formulated accordingly as follows

$$\text{MMV}_{3\text{D}}\ \text{LS}_\tau: \quad \text{minimize} \quad \rho\left(\boldsymbol{\Phi}\cdot\boldsymbol{J}-\boldsymbol{Y}\right) \quad \text{subject to} \quad \kappa_{3\text{D}}(\boldsymbol{J})\le\tau. \tag{5.3}$$

5.1.2 DERIVATION OF THE DUAL

To avoid redundancy, we refer to Subsection 4.1.4 for most of the derivation of the dual of the 3-D inverse problem. The polar of $\kappa_{3\text{D}}$ is given as follows

$$\begin{aligned}\kappa^o_{3\text{D}}(\widetilde{\boldsymbol{Z}}) &= \left(\sum_{n=1}^{N}\left\|\left[\widetilde{\boldsymbol{Z}}_{2n-2,:}\ \widetilde{\boldsymbol{Z}}_{2n-1,:}\ \widetilde{\boldsymbol{Z}}_{2n,:}\right]\right\|_2^{\infty}\right)^{1/\infty}\\ &= \max\left\{\left\|\left[\widetilde{\boldsymbol{Z}}_{2n-2,:}\ \widetilde{\boldsymbol{Z}}_{2n-1,:}\ \widetilde{\boldsymbol{Z}}_{2n,:}\right]\right\|_2 \middle| \, n=1,2,3,\cdots,N\right\}.\end{aligned} \tag{5.4}$$

The derivative of the Pareto curve is

$$\phi'_{\text{MMV}_{3\text{D}}}(\tau) = -\frac{\kappa^o_{3\text{D}}\left(\boldsymbol{\Phi}^H\cdot\boldsymbol{R}\right)}{\|\boldsymbol{R}\|_F}. \tag{5.5}$$

5.1.3 PROJECTION OPERATOR

The projection operator $\mathcal{P}_\tau[\cdot]$ is replaced with orthogonal projection onto $\kappa_{3\text{D}}(\cdot)$ balls, $\mathcal{P}_{\tau,\text{MMV}_{3\text{D}}}[\cdot]$, which is defined as follows

$$\mathcal{P}_{\tau,\text{MMV}_{3\text{D}}}[\boldsymbol{J}] := \left\{\underset{\boldsymbol{X}}{\text{argmin}} \quad \|\boldsymbol{J}-\boldsymbol{X}\|_F \quad \text{subject to} \quad \kappa_{3\text{D}}(\boldsymbol{X})\le\tau\right\}. \tag{5.6}$$

With a simple matrix transformation of

$$\overline{\boldsymbol{J}}_{n,:} = \left[\boldsymbol{J}_{2n-2,:}\ \boldsymbol{J}_{2n-1,:}\ \boldsymbol{J}_{2n,:}\right]$$

and

$$\overline{\boldsymbol{X}}_{n,:} = \left[\boldsymbol{X}_{2n-2,:}\ \boldsymbol{X}_{2n-1,:}\ \boldsymbol{X}_{2n,:}\right],$$

we can rewrite Eq. (5.6) as follows

$$\left\{\underset{\overline{\boldsymbol{X}}}{\text{argmin}} \quad \left\|\overline{\boldsymbol{J}}-\overline{\boldsymbol{X}}\right\|_F \quad \text{subject to} \quad \left\|\overline{\boldsymbol{X}}\right\|_{1,2}\le\tau\right\} = \mathcal{P}_{\tau,\text{MMV}_{\text{TM}}}\left[\overline{\boldsymbol{J}}\right]. \tag{5.7}$$

In doing so, the projection operator in 3-D case satisfies [129, Theorem 6.3].

5.2 INVERTING THE CONTRAST

Assuming we have reconstructed the contrast sources, the scattered fields can be calculated. Then if we know the incident fields, it is easy to obtain the total fields. In

order to solve the contrast, we define the data equations and the state equations as follows

$$\boldsymbol{f}_p = \boldsymbol{\Phi}_p \hat{\boldsymbol{e}}_p^{\text{tot}} \boldsymbol{\chi}, \quad p = 1,2,3,\cdots,P; \tag{5.8a}$$

$$\hat{\boldsymbol{j}}_p = \hat{\boldsymbol{e}}_p^{\text{tot}} \boldsymbol{\chi}, \quad p = 1,2,3,\cdots,P. \tag{5.8b}$$

The contrast can be obtained by iteratively minimizing a cost functional, $\mathcal{C}(\boldsymbol{\chi})$, which is defined as the sum of the data error and the state error

$$\underset{\boldsymbol{\chi}}{\text{minimize}} \quad \mathcal{C}(\boldsymbol{\chi}) := \frac{\left\|\boldsymbol{f} - \boldsymbol{\Psi}\boldsymbol{\chi}\right\|_2^2}{\left\|\boldsymbol{f}\right\|_2^2} + \frac{\left\|\hat{\boldsymbol{j}} - \hat{\boldsymbol{e}}_p^{\text{tot}}\boldsymbol{\chi}\right\|_2^2}{\left\|\hat{\boldsymbol{e}}_p^{\text{inc}}\boldsymbol{\chi}\right\|_2^2}, \tag{5.9}$$

where

$$\boldsymbol{f} = \begin{bmatrix} \boldsymbol{f}_1^T & \boldsymbol{f}_2^T & \cdots & \boldsymbol{f}_P^T \end{bmatrix}^T, \tag{5.10}$$

$$\boldsymbol{j} = \begin{bmatrix} \boldsymbol{j}_1^T & \boldsymbol{j}_2^T & \cdots & \boldsymbol{j}_P^T \end{bmatrix}^T, \tag{5.11}$$

and

$$\boldsymbol{\Psi} = \begin{bmatrix} \boldsymbol{\Phi}_1 \boldsymbol{D}_{\hat{\boldsymbol{e}}_1^{\text{tot}}} \\ \boldsymbol{\Phi}_2 \boldsymbol{D}_{\hat{\boldsymbol{e}}_2^{\text{tot}}} \\ \vdots \\ \boldsymbol{\Phi}_P \boldsymbol{D}_{\hat{\boldsymbol{e}}_P^{\text{tot}}} \end{bmatrix}. \tag{5.12}$$

Specifically, the contrast is updated via

$$\boldsymbol{\chi}_\ell = \boldsymbol{\chi}_{\ell-1} + \alpha_\ell \boldsymbol{v}_{\boldsymbol{\chi},\ell}, \tag{5.13}$$

where, α_n is a constant, and the update directions, $\boldsymbol{v}_{\boldsymbol{\chi},\ell}$, are chosen to be the Polak-Ribière conjugate gradient directions given by

$$\begin{aligned} &\boldsymbol{v}_{\boldsymbol{\chi},0} = 0 \\ &\boldsymbol{v}_{\boldsymbol{\chi},\ell} = \boldsymbol{g}_{\boldsymbol{\chi},\ell} + \frac{\left\langle \boldsymbol{g}_{\boldsymbol{\chi},\ell}, \boldsymbol{g}_{\boldsymbol{\chi},\ell} - \boldsymbol{g}_{\boldsymbol{\chi},\ell-1} \right\rangle_2}{\left\|\boldsymbol{g}_{\boldsymbol{\chi},\ell-1}\right\|_2^2} \boldsymbol{v}_{\boldsymbol{\chi},\ell-1} \ \ell \geq 1, \end{aligned} \tag{5.14}$$

where, $\boldsymbol{g}_{\boldsymbol{\chi},\ell}$ is the gradient of the contrast cost functional $\mathcal{C}(\boldsymbol{\chi})$ given by

$$\boldsymbol{g}_{\boldsymbol{\chi},\ell} = \frac{-2\boldsymbol{\Psi}^H\left(\boldsymbol{f} - \boldsymbol{\Psi}\boldsymbol{\chi}_{\ell-1}\right)}{\left\|\boldsymbol{f}\right\|_2^2} + \frac{-2\overline{\hat{\boldsymbol{e}}_p^{\text{tot}}}\left(\hat{\boldsymbol{j}} - \hat{\boldsymbol{e}}_p^{\text{tot}}\boldsymbol{\chi}_{\ell-1}\right)}{\left\|\hat{\boldsymbol{e}}_p^{\text{inc}}\boldsymbol{\chi}_{\ell-1}\right\|_2^2}. \tag{5.15}$$

Here, $\langle\cdot,\cdot\rangle_2$ represents the inner product of two vectors, $(\cdot)^H$ represents the conjugate transpose of a matrix. The step size α_n is determined by minimizing the cost function as follows

$$\mathcal{C}_\ell(\alpha_\ell) = \frac{\left\|\boldsymbol{f} - \boldsymbol{\Psi}\left(\boldsymbol{\chi}_{\ell-1} + \alpha_\ell \boldsymbol{v}_{\boldsymbol{\chi},\ell}\right)\right\|_2^2}{\left\|\boldsymbol{f}\right\|_2^2} + \frac{\left\|\hat{\boldsymbol{j}} - \hat{\boldsymbol{e}}_p^{\text{tot}}\left(\boldsymbol{\chi}_{\ell-1} + \alpha_\ell \boldsymbol{v}_{\boldsymbol{\chi},\ell}\right)\right\|_2^2}{\left\|\hat{\boldsymbol{e}}_p^{\text{inc}}\left(\boldsymbol{\chi}_{\ell-1} + \alpha_\ell \boldsymbol{v}_{\boldsymbol{\chi},\ell}\right)\right\|_2^2}, \tag{5.16}$$

which is a problem of finding the minimum of a single-variable function, and can be solved efficiently by using the Brent's method [114, 115].

The contrast is initialized using the least square solution to the state equations Eq. (5.8b), i.e.,

$$\boldsymbol{\chi}_0 = \left(\hat{\boldsymbol{e}}_p^{\text{tot}} \boldsymbol{j}\right) \oslash \left(\hat{\boldsymbol{e}}_p^{\text{tot}} \overline{\hat{\boldsymbol{e}}_p^{\text{tot}}}\right), \tag{5.17}$$

where, $\oslash$ represents the element-wise division.

By considering the relation, $\boldsymbol{\chi} = \boldsymbol{\epsilon} - \boldsymbol{\epsilon}_{\text{bg}}$, where $\boldsymbol{\epsilon}$ and $\boldsymbol{\epsilon}_{\text{bg}}$ are the complex permittivity of the test domain and the background, and noting the fact that

$$\Re\{\boldsymbol{\epsilon}\} \succeq 1, \quad \Im\{\boldsymbol{\epsilon}\} \preceq 0, \tag{5.18}$$

we can simply obtain

$$\Re\{\boldsymbol{\chi}\} \succeq 1 - \Re\{\boldsymbol{\epsilon}_{\text{bg}}\}, \quad \Im\{\boldsymbol{\chi}\} \preceq -\Im\{\boldsymbol{\epsilon}_{\text{bg}}\}. \tag{5.19}$$

Here, $\Re\{\cdot\}$ and $\Im\{\cdot\}$ represent the real part and imaginary part of a scalar/vector/matrix; "$\succeq$" and "$\preceq$" represent the component-wise inequality between the elements of a vector and a constant. Therefore, range constraints are considered in the iterations as a priori information, which is done by setting the real part to $1 - \Re\{\boldsymbol{\epsilon}_{\text{bg}}\}$ whenever $\Re\{\boldsymbol{\chi}_\ell\} < 1 - \Re\{\boldsymbol{\epsilon}_{\text{bg}}\}$, and setting the imaginary part to $-\Im\{\boldsymbol{\epsilon}_{\text{bg}}\}$ whenever $\Im\{\boldsymbol{\chi}_\ell\} > -\Im\{\boldsymbol{\epsilon}_{\text{bg}}\}$. In our experiments, the contrast is assumed to be isotropic, i.e., $\chi_{3n-2} = \chi_{3n-1} = \chi_{3n}$. Therefore, we use the mean of the three components as the final estimation of the contrast.

5.3 NUMERICAL EXPERIMENTS

5.3.1 CONFIGURATION

In this section, the proposed linearized 3-D contrast source inversion method is applied to two typical 3-D half-space inverse problems — GPR imaging and TWI. The EM direct scattering problem is solved by a MATLAB-based 3-D FDFD package 'MaxwellFDFD' and its companion C program "FD3D" [30]. Considering a 3-D Cartesian coordinate system, the x-, y-, and z-normal boundaries of a rectangular region are covered by Perfectly Matched Layers (PMLs) to simulate the anechoic chamber environment. Non-uniform meshes are used to generate the scattered data, which means the testing domain is discretized with different mesh sizes according to the distribution of the permittivity, viz., coarse meshes for low permittivity and fine meshes for high permittivity. The accuracy of the FDFD scheme is ensured by the following criterion [35]

$$\Delta \leq \frac{\lambda_0}{15\sqrt{\varepsilon_{\text{r}}}}, \tag{5.20}$$

where, λ_0 is the wavelength in free space, and ε_{r} is the relative permittivity of the testing domain. Non-uniform meshes greatly reduce the computational burden for solving the direct scattering problem. In contrast, uniform meshes are used to invert the scattered

data since the distribution of the permittivity is unknown beforehand. In order to guarantee the inversion accuracy, we make sure the following condition is satisfied

$$\Delta \leq \frac{\lambda_0}{15\sqrt{\max\{\varepsilon_r\}}}. \tag{5.21}$$

The source used in the numerical experiments consists of an x-polarized electric dipole and a y-polarized one. A circularly polarized wave is generated at 200 MHz by introducing a $\pi/2$ phase shift between the two dipoles. The x- and y-components of the electric fields are measured at several positions simultaneously. For the two half-space configurations, 6 × 6 sources are uniformly distributed on the xoy plane ([−3.0, 3.0], [−3.0, 3.0], z) m, and 9 × 9 receivers are uniformly distributed in the same region. The distance between the receivers both along the x- and y-axis is $\lambda_0/2 = 0.75$ m. Here, λ_0 is the wavelength of the generated wave in free space.

The measurement data used for inversion consist of the scattered fields obtained by subtracting the incident fields from the probed total fields. Random white noise is added to the measurement data following the similar procedure in [119],

$$\boldsymbol{f}_{p,noise} = \boldsymbol{f}_p + \zeta \times \max_m\{|f_{p,m}|\}(\boldsymbol{n}_1 + \mathrm{i}\boldsymbol{n}_2), \quad p = 1,2,3,\cdots,P,\ m = 1,2,3,\cdots,M, \tag{5.22}$$

where, $\boldsymbol{n}_1$ and $\boldsymbol{n}_2$ are two vectors consisting of random numbers varying from -1 up to 1, ζ representing the amount of noise, and $\max_m\{|f_{p,m}|\}$ represents the largest value among the amplitudes of the M measurement data, which means the noise is scaled by the largest amplitude of the measurement data. In the following examples, the measurement data are disturbed according to Eq. (5.22) with $\zeta = 0.05$.

5.3.2 GPR IMAGING: LOSSY OBJECTS

In this subsection, we consider the inversion of two lossy objects, a sphere ($\varepsilon_r = 2$, $\sigma = 0.05$ S/m) of radius 0.3 m and a cube ($\varepsilon_r = 6$, $\sigma = 0.01$ S/m) of side length 0.6 m, buried in soil ($\varepsilon_r = 3$, $\sigma = 0.001$ S/m, corresponding to a dry sandy soil). The testing domain is ([−3.5, 3.5], [−3.5, 3.5], [−2.5, 1.0]) m. Sources and receivers are uniformly located on the square plane ([−3, 3], [−3, 3], 0.5) m, and the half space -2.5 m $< z < 0$ m is filled with soil. The sphere is centred at ([0.7, −0.7, −1.0]) m, and the cube is in the region ([−1.0, −0.4], [0.4, 1.0], [−1.3, −0.7]) m. Fig. 5.2 gives the geometry of this experiment, in which the 9 × 9 receivers are shown with different colours — 69 receivers in green colour and 12 receivers in red colour. The green ones represent the reconstruction measurements and the red ones represent the Cross-Validation (CV) measurements for estimating the contrast sources.

For creating the sensing matrix, we discretize the test domain with uniform mesh resolution determined by Eq. (5.21), and assemble it with the vectors $\boldsymbol{\varphi}_m$ obtained by solving the M linear system of equations, Eqs. (3.21). In order to decrease the computational burden, we constrain the inversion domain in the region ([−2.0, 2.0], [−2.0, 2.0], [−2.5, 0.0]) m. As a matter of fact, more meshes are used due to the introduction of the PMLs. In our simulations, iterative solvers are used in solving the 3-D direct scattering problems and the scattering matrix. The computation was accelerated by parallel computing programming with 16 cores.

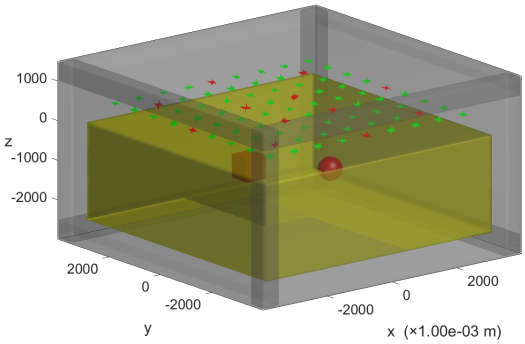

Figure 5.2: Geometry of the GPR imaging experiment. Soil: $\epsilon_r = 3$, $\sigma = 0.001$ S/m. Sphere: $\epsilon_r = 2$, $\sigma = 0.05$ S/m. Cube: $\epsilon_r = 6$, $\sigma = 0.01$ S/m. 6×6 sources and 9×9 receivers are uniformly distributed on the square plane $([-3, 3], [-3, 3], 0.5)$ m. The 12 red receivers correspond to the CV measurements, and the 69 green ones correspond to the measurements used for reconstructing the contrast sources.

Fig. 5.3 (a) gives the reconstruction residual and the CV residual in the iterative process of estimating the contrast sources, from which we can see that the reconstruction residual curve and the CV residual curve have a stair-like shape. As a matter of fact, the i-th stair corresponds to the LS_τ problem with the parameter τ_i. See [128] for more details about the updating criterion of the parameter τ. From the sub view in Fig. 5.3 (a), we can see that the CV residual starts to increase at the 179-th iteration, while the reconstruction residual can still be minimized further. This indicates that the iteration process starts to overfit the noise. Therefore, the contrast sources are supposed to be chosen as the approximate solution corresponding to the smallest CV residual. Fig. 5.3 (b) shows the data error curve and the state error curve. From Fig. 5.3 (b) we can see a relatively large state error 22% has been preserved and cannot be minimized after 40 iterations due to the inexact estimation of the contrast sources, while, in this experiment, the data error has been minimized to a relatively small one 9%.

The shape of the reconstructed results is given in Fig. 5.4. Since the contrast is assumed to be isotropic, the shape of the original contrast is defined as

$$I_n = \left| \frac{\chi_{3n-2} + \chi_{3n-1} + \chi_{3n}}{3} \right|, \quad n = 1, 2, 3, \cdots, N, \tag{5.23}$$

and is shown in Fig. 5.4 (a). The shape of the contrast sources is defined as

$$I_n = \sum_{p=1}^{P} \sqrt{\left|\boldsymbol{j}_{p,3n-2}\right|^2 + \left|\boldsymbol{j}_{p,3n-1}\right|^2 + \left|\boldsymbol{j}_{p,3n}\right|^2}, \quad n = 1, 2, 3, \cdots, N, \tag{5.24}$$

and shown in Fig. 5.4 (b), from which we can see that the 3-D image of the contrast sources is elongated along the z-axis, indicating a good resolution along x- and y-axis and a poor resolution along z-axis. This can be explained by the planar distribution of the sources and receivers. Due to the limited aperture in the half-space configurations, the nonuniqueness of the inverse problem gets worse. Thus, it is extremely difficult to achieve an exact reconstruction. Figs. 5.4 (c) and (d) show the shape of the reconstructed

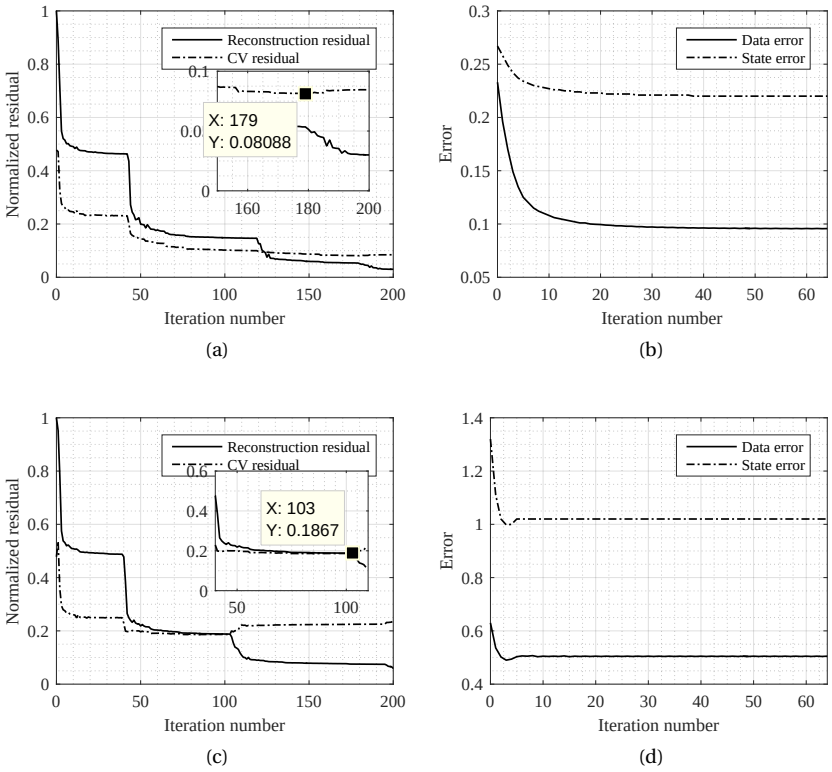

Figure 5.3: Residual curves of the GPR imaging experiment. Reconstruction residual and CV residual curves for estimating the contrast sources using the exact background model (a) and an inexact background model ($1.25\epsilon_{\mathrm{bg}}$) (c). Data error and state error curves for reconstructing of the contrast using the exact background model (b) and an inexact background model ($1.25\epsilon_{\mathrm{bg}}$) (d).

contrast permittivity and the reconstructed contrast conductivity, from which we can see that the location and the basic shape of the buried objects can be well distinguished.

To study the estimation accuracy of the dielectric parameters, Fig. 5.5 shows the cross sections ($x = 0.7$ m, $y = 0.7$ m, and $z = -1.15$ m) of the reconstructed contrast permittivity and conductivity, together with those of the real ones. By comparing Fig. 5.5 (a) and Fig. 5.5 (c), we see that the reconstructed contrast permittivity has negative values down to -1.7 (the real on is -2) in the top region of the sphere, while the one for the cube has positive values up to 2.4 (the real one is 3). Although the estimation of the dielectric parameters is not very accurate, it consists well with the real situation. From Fig. 5.5 (b) we see that the sphere has larger conductivity than the cube, this is well presented in the reconstructed results shown in Fig. 5.5 (d), and the maximum value of the estimated contrast conductivity is 0.04 S/m which is very close to the real value 0.05 S/m.

In order to study the influence of the background mismatch to the inversion per-

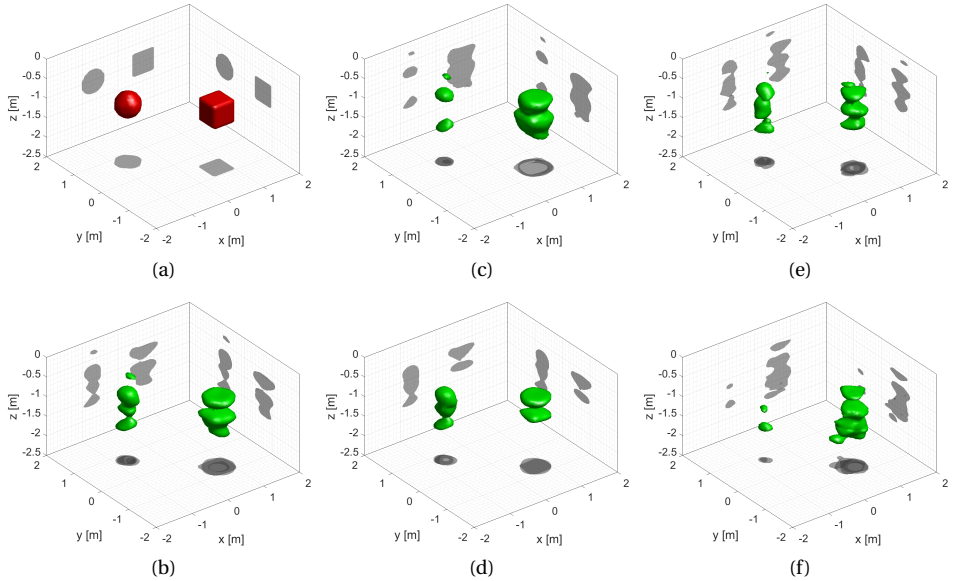

Figure 5.4: 3-D shape of the reconstructed results in the GPR imaging experiment at 200 MHz. 5% random white noise is added. (a): True objects. (b): Reconstructed contrast sources. Reconstructed contrast permittivity (c) and contrast conductivity (d) using the exact background model. Reconstructed contrast permittivity (e) and contrast conductivity (f) using an inexact background model ($1.25\epsilon_{bg}$).

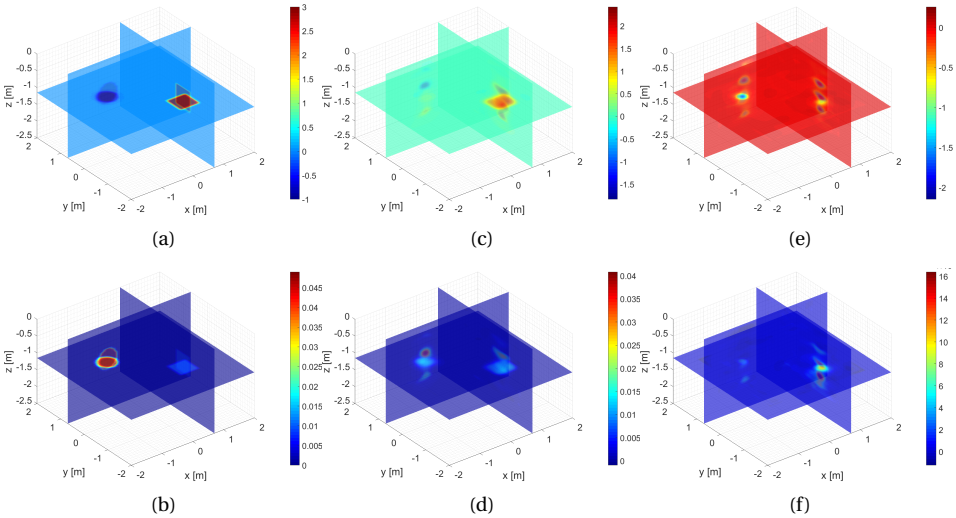

Figure 5.5: Cross sections of the reconstructed dielectric parameters in the GPR imaging experiment at 200 MHz. 5% random white noise is added. The unit of the conductivity is S/m. (a): True contrast permittivity. (b): True contrast conductivity. Reconstructed contrast permittivity (c) and contrast conductivity (d) using the exact background model. Reconstructed contrast permittivity (e) and contrast conductivity (f) using an inexact background model ($1.25\epsilon_{bg}$).

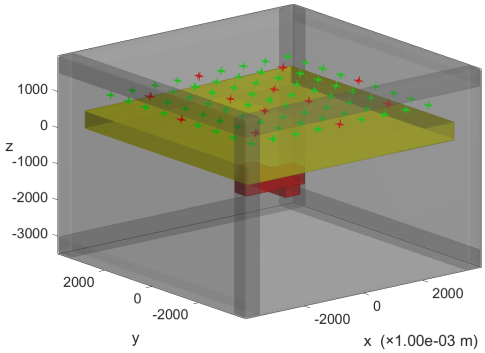

Figure 5.6: Geometry of the TWI experiment. Wall: $\epsilon_r = 4$, $\sigma = 0.01$ S/m. Object: $\epsilon_r = 2$, $\sigma = 0.001$ S/m and highly conductive material $\epsilon_r = 1$, $\sigma = 1$ S/m. The wall is in the region ([−3.5, 3.5], [−3.5, 3.5], [0, 0.5]). 6 × 6 sources and 9 × 9 receivers are uniformly distributed on the square plane ([−3, 3]; [−3, 3]; 1.0) m. The 12 red dots represent the CV measurements, and the 69 green dots are the reconstruction measurements.

5

formance of the proposed method, we process the same measurement data with an inexact background model. Specifically, we assume the geometry of the ground is exactly known, but the dielectric parameters of the soil are estimated higher than the exact value by 25%. It is worth noting that the incident fields, as well as the sensing matrix, $\boldsymbol{\Phi}_p$, need to be recalculated according to the inexact background model. In addition, the contrast must be restricted according to the newly estimated dielectric parameters of the soil. Figs. 5.4 (e) and 5.4 (f) give the shape of the inverted results obtained by processing the same measurement data with the inexact dielectric parameters of the soil ($1.25 \times \boldsymbol{\epsilon}_{\text{bg}}$). From Figs. 5.4 (e) and 5.4 (f) we can see that more artefacts are reconstructed due to the mismatch of the background model. The resolution in the x- and y-dimension is still acceptable, but the resolution in the z-dimension gets worse. Figs. 5.5 (e) and 5.5 (f) give the cross sections ($x = 0.7$ m, $y = 0.7$ m, and $z = -1.15$ m) of the reconstructed contrast permittivity and conductivity, from which we can see that the mismatch seriously degrades the reconstruction accuracy of the dielectric parameters of the objects.

5.3.3 THROUGH-THE-WALL IMAGING

In this subsection, we consider the inversion of a cross object placed behind a wall ($\varepsilon_r = 4$, $\sigma = 0.01$ S/m). The testing domain is ([−3.5, 3.5], [−3.5, 3.5], [−3.0, 1.5]) m. 6 × 6 sources and 9 × 9 receivers are uniformly located on the square plane ([−3, 3], [−3, 3], 1.0) m, and the wall is in the region ([−3.5, 3.5], [−3.5, 3.5], [0, 0.5]) m. The cross object is combined with two rectangular blocks in the region ([−1.0, 1.0], [−0.25, 0.25], [−1.5, −1.0]) m and ([−0.25, 0.25], [−1.0, 1.0], [−1.5, −1.0]) m. The geometry of the TWI experiment is shown in Fig. 5.6. The receivers are shown with different colours, of which the green ones represent the reconstruction measurements and the red ones represent the CV measurements. The inversion domain is constrained in the region ([−2.0, 2.0], [−2.0, 2.0], [−2.5, 0.0]) m.

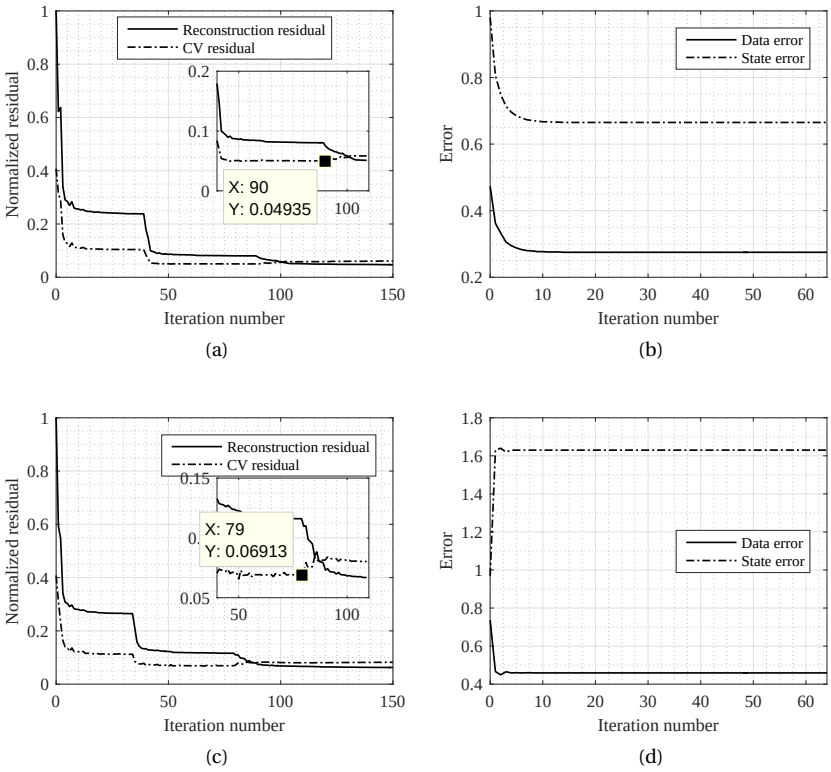

Figure 5.7: Residual curves of the TWI experiment with an EM penetrable object. Reconstruction residual curves and CV residual curves for estimating the contrast sources using the exact background model (a) and an inexact background model ($0.75\epsilon_{\mathrm{bg}}$) (c). Data error and state error curves for reconstructing the contrast using the exact background model (b) and an inexact background model ($0.75\epsilon_{\mathrm{bg}}$) (d).

In this TWI experiment, we investigate the inversion performance of the proposed method not only to the EM penetrable object but also to the highly conductive object. For the latter, the morphological information is of more interest. The exact and inexact wall models are all considered for calculating the sensing matrix, $\boldsymbol{\Phi}_p$, and modelling the incident fields.

PENETRABLE OBJECT

Let us first use the cross object whose relative permittivity $\varepsilon_{\mathrm{r}} = 2$ and conductivity $\sigma = 0.001$ S/m. The TWI measurement data was disturbed by 5% random white noise according to Eq. (5.22), and was then inverted with the incident fields and the sensing matrix calculated with the exact wall model. Fig. 5.7 (a) shows the reconstruction residual curve and the CV residual curve for recovering the contrast sources. The CV residual reaches the smallest value at the 90-th iteration where we obtain the optimal solution of the contrast sources. Fig. 5.7 (b) shows the data error curve and the state error

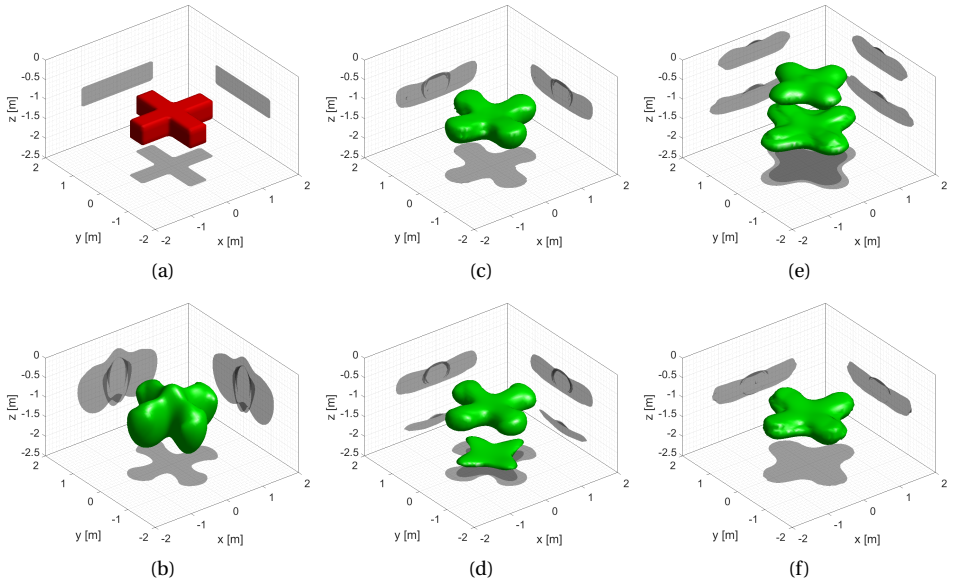

Figure 5.8: 3-D shape of the reconstructed results in the TWI experiment at 200 MHz. 5% random white noise is added. (a): True objects. (b): Reconstructed contrast sources. Reconstructed contrast permittivity (c) and contrast conductivity (d) using the exact background model. Reconstructed contrast permittivity (e) and contrast conductivity (f) using an inexact background model ($0.75\epsilon_{\text{bg}}$).

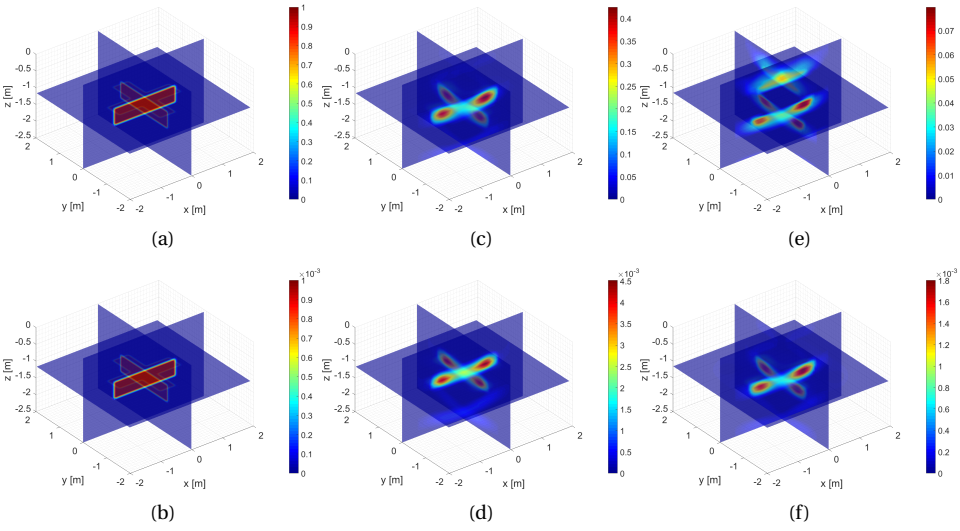

Figure 5.9: Cross sections of the reconstructed dielectric parameters in the TWI experiment at 200 MHz. 5% random white noise is added. The unit of the contrast conductivity is S/m. (a): True contrast permittivity. (b): True contrast conductivity. Reconstructed contrast permittivity (c) and contrast conductivity (d) using the exact background model. Reconstructed contrast permittivity (e) and contrast conductivity (f) using an inexact background model ($0.75\epsilon_{\text{bg}}$).

curve for reconstructing the contrast. The iterative process converges after 10 iterations, however, there is a relatively large data error of 0.27 and a state error of 0.67 that cannot be minimized anymore. This is due to the inexact estimation of the contrast sources which can be obviously seen from Figs. 5.8 (a) and 5.8 (b) in which the shape of the real object and the reconstructed contrast sources are shown.

As a matter of fact, due to the limited amount of independent measurement data, a good inversion can hardly be achieved with just the back-scattered fields. In our method, the contrast sources and the total fields are fixed while reconstructing the contrast, such that the iterative process can be prevented from converging to a local optimal solution that might be far away from the real solution. Figs. 5.8 (c) and 5.8 (d) give the shape of the reconstructed contrast permittivity and the reconstructed contrast conductivity, and the corresponding cross sections ($x = 0$ m, $y = 0$ m, and $z = -1.15$ m) are shown in Figs. 5.9 (c) and 5.9 (d). For better comparison, the cross sections of the exact parameters are given as well in Figs. 5.9 (a) and 5.9 (b). We can see from Figs. 5.8 (a), 5.8 (c) and 5.8 (d) that the shape of the cross is nicely reconstructed. The shown artefacts in the reconstructed contrast conductivity are actually very weak compared to the reconstructed object, which can be seen from Fig. 5.9 (d). If we average the reconstructed parameters in the cross region, then we have a coarse estimation of the contrast $\Delta\hat{\varepsilon}_r \approx 0.2$ and $\Delta\hat{\sigma} \approx 0.002$ S/m.

Assume that the dielectric parameters of the wall are underestimated by 25%, the incident fields and the sensing matrix need to be recalculated correspondingly. However, since the object is surrounded by free space, the range constraints given by Eq. (5.19) keep the same. We do inversion to the same disturbed measurement data. Fig. 5.7 (c) shows the reconstruction residual curve and the CV residual curve for recovering the contrast sources. Fig. 5.7 (d) shows the data error curve and the state error curve for reconstructing the contrast. The CV residual starts to increase at the 79-th iteration where we obtain the optimal solution of the contrast sources. By comparison of Figs. 5.7 (b) and 5.7 (d) we can see that the inexact wall model results in larger data error (0.45) and state error (1.65) compared to those with the exact background model. The shape of the reconstructed contrast permittivity and the contrast conductivity with the inexact wall model is shown in Figs. 5.8 (e) and 5.8 (f), respectively. And the corresponding cross sections are given in Figs. 5.9 (e) and 5.9 (f). An obvious cross ghost above the real object can be observed in the reconstructed contrast permittivity, while the reconstructed contrast conductivity is still good enough to identify the object. By comparison of Figs. 5.9 (c) and 5.9 (d) and Figs. 5.9 (e) and 5.9 (f), we see that after introducing the background model error, the reconstructed contrast conductivity stays at the same order of magnitude, while the reconstructed contrast conductivity is lower than the exact value by around one order of the magnitude.

HIGHLY CONDUCTIVE OBJECT

To study the performance of the proposed method for the inversion of highly conductive objects, let us now test a cross object of the same size but made of a highly conductive material ($\varepsilon_r = 1$, $\sigma = 10^5$ S/m). Firstly, let us process the measurement data using the exact background model. Namely, we do the same thing as that of the previous cross object, but just replacing the measurement data. Figs. 5.10 (a) and 5.10 (b) give the residual curves of recovering both the contrast sources and the contrast. We can see

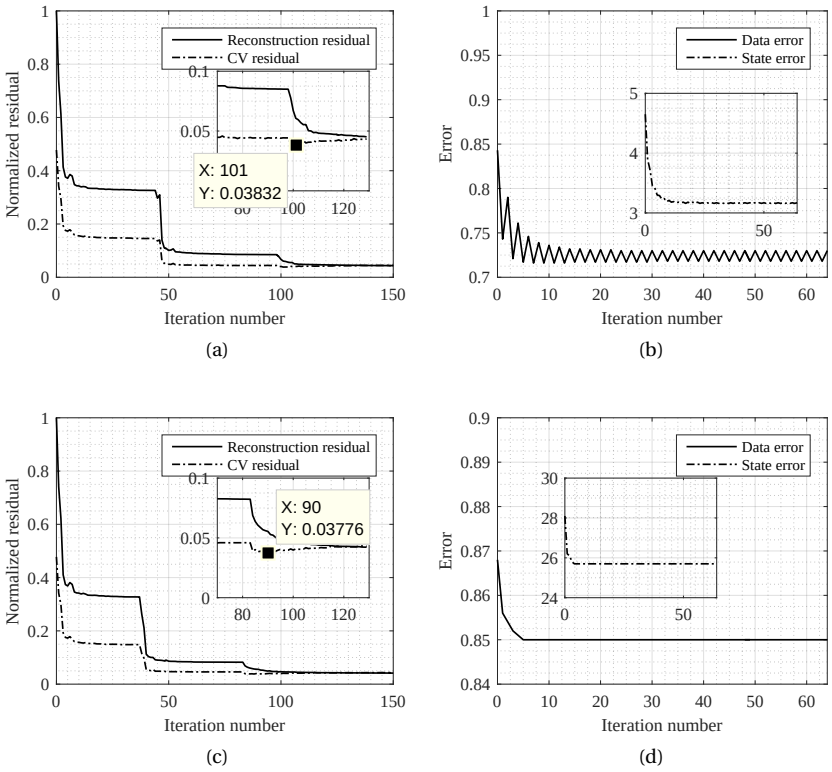

Figure 5.10: Residual curves of the TWI experiment with highly conductive object. Reconstruction residual and CV residual curves for estimating the contrast sources using the exact background model (a) and an inexact background model (a wall of 0.75 m thickness) (c). Data error and state error curves for reconstructing the contrast using the exact background model (b) and an inexact background model (a wall of 0.75 m thickness) (d).

that the data error and the state error are larger than those of inverting the penetrable cross object, indicating that the contrast sources are reconstructed with a larger error. Figs. 5.11 (a) and 5.11 (b) show the shape of the real cross object and the shape of the inverted contrast sources, from which we can see that the contrast sources have a basic cross-like shape extending along the z-axis from $z_1 = -0.5$ m to $z_2 = -1.5$ m. As a matter of fact, for highly conductive objects, the contrast sources are supposed to distribute on the top surface of the object, and the EM fields in the interior are zero due to the serious attenuation of the electric fields. This nicely explains why the middle of the contrast sources is exactly the top surface of the real object, i.e., $(z_1 + z_2)/2 = -1$ m. The reconstructed contrast permittivity and contrast conductivity are shown in Figs. 5.11 (c) and 5.11 (d), and the corresponding cross sections are shown in Figs. 5.12 (c) and 5.12 (d). We can see a ghost of the contrast permittivity with a maximum value of 1, and the reconstructed contrast conductivity is more focused on the top surface of the cross

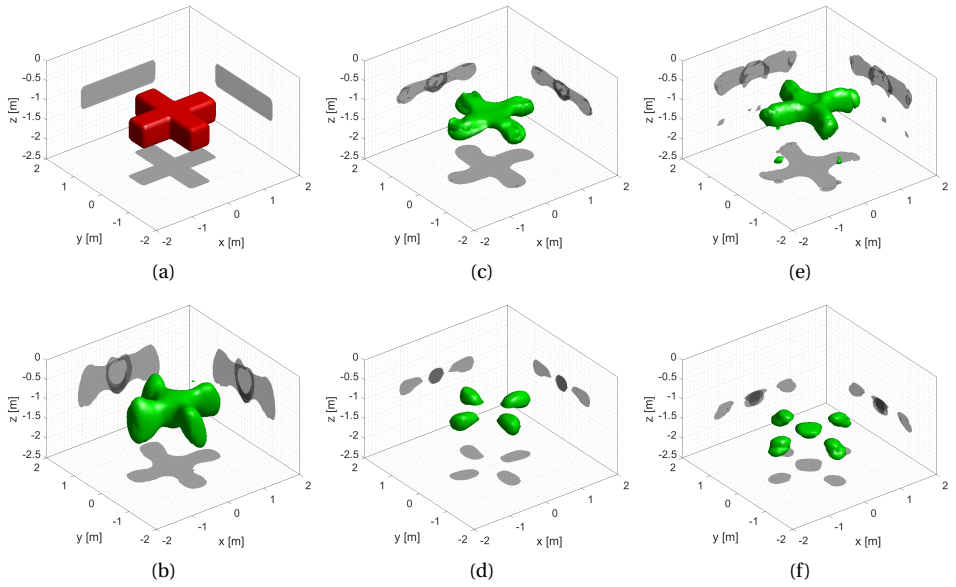

Figure 5.11: 3-D shape of the reconstructed results in the TWI experiment at 200 MHz. 5% random white noise is added. (a): Real objects. (b): Reconstructed contrast sources. Reconstructed contrast permittivity (c) and contrast conductivity (d) using the exact background model. Reconstructed contrast permittivity (e) and contrast conductivity (f) using an inexact background model (a wall of 0.75 m thickness).

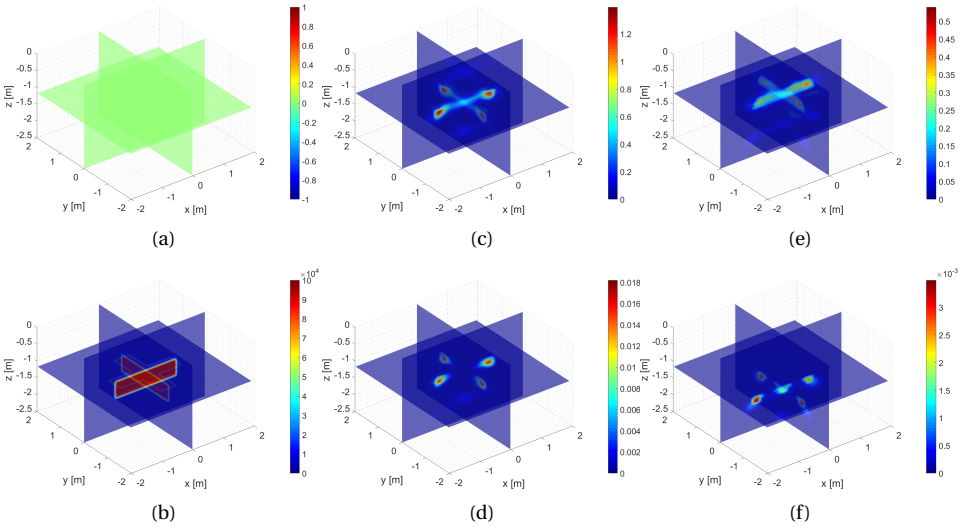

Figure 5.12: Cross sections of the reconstructed dielectric parameters in the TWI experiment at 200 MHz. 5% random white noise is added. The unit of the contrast conductivity is S/m. (a): True contrast permittivity. (b): True contrast conductivity. Reconstructed contrast permittivity (c) and contrast conductivity (d) using the exact background model. Reconstructed contrast permittivity (e) and contrast conductivity (f) using an inexact background model (a wall of 0.75 m thickness).

object due to the higher conductivity compared to the penetrable cross object. Although the estimation of the dielectric parameters is not accurate in the inversion of highly conductive objects, we get the basic morphological information of the objects, which is of more importance in real applications.

In the inversion with an inexact wall model, we changed the thickness of the wall to 0.75 m while using the exact dielectric parameters. The residual curves are shown in Figs. 5.10 (c) and 5.10 (d). Obviously, the data error and the state error are larger than those of the inversion using the exact wall model (see Figs. 5.10 (a) and 5.10 (b)). The corresponding inverted results are given in Figs. 5.11 (e) and 5.11 (f) and Figs. 5.12 (e) and 5.12 (f), from which we can see that the 3-D image of the contrast permittivity is lifted up by 0.25 m, and the one of the contrast conductivity is lowered by 0.5 m. This is a very interesting phenomenon because the mismatch of the background model is reflected by the mismatch of the 3-D images of the contrast permittivity and the contrast conductivity.

5.3.4 PERFORMANCE ANALYSIS

To summarize this section, we remark that the linearized 3-D inversion method gives good inverted results for the inversion of a lossy object in GPR imaging and an EM penetrable object in TWI. It is also able to provide the morphological information of highly conductive objects. The quality of the background estimation is critical for ensuring the accuracy of the inverted results. This method leaves a large data error and a large state error for solving the 3-D half-space inverse scattering problems. However, it helps to prevent the iterative process from converging to a totally false local optimal solution in the cases where only back-scattered fields are available.

In the numerical experiments, the program for reconstructing the contrast sources and the contrast is realized by MATLAB codes. We ran the codes on a desktop with one Intel(R) Core(TM) i5-3470 CPU @ 3.20 GHz, and we did not use parallel computing. The running time of each iteration is 3.1 s and 2.0 s respectively for the GPR case, and 3.5 s and 2.2 s respectively for the TWI case. The codes of solving the total fields are written with C language and PETSc. We run the codes on a server with two Intel(R) Xeon(R) CPUs E5-2650 v2 @ 2.60GHz containing 16 cores totally. Parallel computing was used with 16 cores. The running time of solving the total field for each source is 48 s for the GPR case and 25 s for the TWI case. In the GPR case, we ran 200 iterations for recovering the contrast sources and 20 iterations for recovering the contrast, the total running time is about 40 min. $((200\times 3.1+20\times 2.0+36\times 48)/60)$. In the TWI case, we ran 150 iterations for recovering the contrast sources and 20 iterations for recovering the contrast, the total running time is about 27.4 min. $((150\times 3.5+20\times 2.2+36\times 25)/60)$. If we implement the MATLAB codes using parallel computing technique with 16 cores, the running time can be reduced by at least 8 times. In doing so, the total running time can be further reduced to 30 min and 16.5 min, respectively. For conventional iterative inversion methods, such as CSI and BIM, the update of the total fields in each iteration requires at least 57.6 min. $((2\times 36\times 48)/60)$ and 30 min. $((2\times 36\times 25)/60)$, respectively. The total running times are at least a multiple of the above times, where the multiple is determined by the required iteration number. Obviously, the proposed method is more

efficient in comparison to conventional iterative inversion methods.

5.4 CONCLUSIONS

In this chapter, it has been proposed that the 3-D inverse scattering problem of half-space configuration can be transferred to a cascade of a sum-of-norm regularized linear inverse source problem and a linear optimization problem. The regularized solutions of the contrast sources are sought by solving a linear sum-of-norm optimization problem, with which the total fields are calculated and the contrast is estimated. The proposed method is tested successfully in a GPR configuration and a TWI configuration. The inversion quality with both exact and inexact background models is discussed and its sensitivity to the accuracy of the background modelling is shown as well. Results show that this method is not only efficient but also robust with respect to the reconstruction quality when the amount of the retrievable data is limited by the one-side probing configuration. In the cases where the scattering objects extend over a large region, the influence of the regularization constraint becomes less significant. However, this problem can be, to a very large extent, overcome by a multi-frequency version of the proposed method.

6

GMMV-BASED LINEAR INVERSION

In this chapter, the Multiple Measurement Vectors (MMV) linear method proposed in Chapter 4 is extended to process the multi-frequency data based on the Generalized Multiple Measurement Vectors (GMMV) model [127, 147]. In our method, the sum-of-norm of the contrast sources is used as a regularization constraint to address the ill-posedness. Finite Difference Frequency Domain (FDFD) [35] is used to construct the scattering operator which enables a simple incorporation of the complicated background medium, and the Spectral Projected Gradient for ℓ_1-norm minimization (SPGL1) method [128, 129], is selected to estimate the contrast sources by solving a sum-of-norm minimization problem. In the literature, sparse scatterer imaging has been studied in [40], in which Single Measurement Vector (SMV) model was used, but the joint structure of the contrast source matrix was not considered. The application of joint sparsity in the field of medical imaging has been reported in [148], which is actually a hybridization of Compressive Sensing (CS) [126] and the MUltiple SIgnal Classification (MUSIC) method based on a generalized MUSIC criterion. In the aforementioned work, sparse targets (original or equivalently transformed) and their sparsest solutions are considered, and the problems of defining the best discretization grid and estimating the target number are critical for ensuring that the level of sparsity is recoverable. In [41], equivalence principles were considered for reconstructing the boundary of dielectric scatterers. In this chapter, we demonstrate that, by exploiting the frequency diversity, a regularized solution of the contrast sources obtained by solving the GMMV model is sufficient to indicate the spatial profile of the non-sparse targets of both metallic material and dielectric material.

The remainder of this chapter is organized as follows: The problem statement is given in Section 6.1; The GMMV-based linear method is introduced in Section 6.2; The validity of the proposed method is demonstrated with experimental data in Section 6.3,

Parts of this chapter have been submitted to [146].

in which three configurations: dielectric scatterers, metallic scatterers and hybrid scatterers, are considered; In Section 6.4, the difference and relationship between GMMV and Linear Sampling Method (LSM) is discussed; Finally, we ends this chapter with the conclusions given in Section 6.5.

6.1 PROBLEM STATEMENT

For the sake of simplicity, we consider the 2-Dimensional (2-D) Transverse Magnetic (TM)-polarized ElectroMagnetic (EM) inverse scattering problem. A bounded, simply connected, homogeneous/inhomogeneous background domain $\mathcal{D}$ contains unknown objects. The domain $\mathcal{S}$ contains the sources and receivers. The sources are denoted by the subscript p in which $p \in \{1,2,3,\cdots,P\}$, and the receivers are denoted by the subscript q in which $q \in \{1,2,3,\cdots,Q\}$. We use a right-handed coordinate system and the unit vector in the invariant direction points out of the paper.

Assume the background is known, and the permeability of the background and unknown objects is constant, denoted by μ_0. The contrast corresponding to the i-th frequency is defined as $\chi_i = \epsilon_i - \epsilon_{\mathrm{bg},i}$, where $\epsilon_i = \varepsilon - \mathrm{i}\sigma/\omega_i$ and $\epsilon_{\mathrm{bg},i} = \varepsilon_{\mathrm{bg}} - \mathrm{i}\sigma_{\mathrm{bg}}/\omega_i$ are the complex permittivity of the inversion domain in the presence/absence of the targets respectively. Here, ε and $\varepsilon_{\mathrm{bg}}$ are the permittivity of the inversion domain in the presence/absence of the targets respectively, σ and σ_{bg} are the conductivity of the inversion domain in the presence/absence of the targets respectively; ω_i is the i-th angular frequency, and i represents the imaginary unit. The time factor is $\exp(\mathrm{i}\omega_i t)$. For the 2-D TM-polarized scattering problem, the electric field is a scalar and the scattering wave equation with respect to the scattered field can be easily derived from Maxwell's equations, which is given by

$$-\nabla^2 E^{\mathrm{sct}}_{p,i} - k_i^2 E^{\mathrm{sct}}_{p,i} = \omega_i^2 \mu_0 J_{p,i}, \quad p = 1,2,3,\cdots,P, \quad i = 1,2,3,\cdots,I, \tag{6.1}$$

where, ∇^2 is the Laplace operator, $k_i = \omega_i \sqrt{\epsilon_{\mathrm{bg}}\mu_0}$ is the i-th wavenumber, $J_{p,i} = \chi_i E^{\mathrm{tot}}_{p,i}$ is the contrast source corresponding to the p-th source and the i-th frequency, $E^{\mathrm{sct}}_{p,i}$ and $E^{\mathrm{tot}}_{p,i}$ are the scattered electric field and the total electric field at the i-th frequency, respectively. The inverse scattering problem discussed in this chapter is to retrieve the geometrical features of the scatterers from a set of measured scattered fields.

6.2 THE GMMV-BASED LINEAR METHOD

6.2.1 THE GMMV FORMULATION

Following the vector form of the FDFD scheme in [35], we discretize the 2-D inversion space with N grids and recast the scattering wave equation, Eq. (6.1), into the following matrix formalism

$$\boldsymbol{A}_i \boldsymbol{e}^{\mathrm{sct}}_{p,i} = \omega_i^2 \boldsymbol{j}_{p,i}, \quad p = 1,2,3,\cdots,P, \quad i = 1,2,3,\cdots,I, \tag{6.2}$$

where $\boldsymbol{A}_i \in \mathbb{C}^{N\times N}$ is the FDFD stiffness matrix of the i-th frequency, which is highly sparse; $\boldsymbol{e}^{\text{sct}}_{p,i} \in \mathbb{C}^N$ and $\boldsymbol{j}_{p,i} \in \mathbb{C}^N$ are the scattered electric fields and the contrast sources in the form of a column vector, respectively. Obviously, the solution to Eq. (6.2) can be obtained by inverting the stiffness matrix $\boldsymbol{A}_i$, which yields $\boldsymbol{e}^{\text{sct}}_{p,i} = \boldsymbol{A}_i^{-1}\omega_i^2 \boldsymbol{j}_{p,i}$. In the inverse scattering problem, the scattered fields are measured with a number of receivers at specified positions, yielding the data equations given by

$$\boldsymbol{y}_{p,i} = \boldsymbol{\Phi}_{p,i}\boldsymbol{j}^{\text{ic}}_{p,i}, \quad p = 1,2,3,\cdots,P, \quad i = 1,2,3,\cdots,I, \tag{6.3}$$

where, $\boldsymbol{\Phi}_{p,i} = \mathcal{M}_p^{\mathcal{S}}\boldsymbol{A}_i^{-1}\omega_i \in \mathbb{C}^{Q\times N}$ is the sensing matrix for the measurement $\boldsymbol{y}_{p,i}$, $\boldsymbol{j}^{\text{ic}}_{p,i} = \omega_i \boldsymbol{j}_{p,i}$ is the normalized contrast source proportional to the induced current $\mathrm{i}\omega_i\mu_0\boldsymbol{j}_{p,i}$. Here, $\mathcal{M}_p^{\mathcal{S}}$ is a measurement matrix selecting the values of the p-th scattered field at the positions of the receivers.

In the rest of this subsection, a GMMV model [147] is constructed and solved by exploiting the joint sparsity of the normalized contrast sources. In doing so, the contrast sources can be well estimated by solving a sum-of-norm minimization problem, and the solution can be consequently used to indicate the shape of the scatterers. To do so, we reformulated the data equations Eq. (6.3) as

$$\boldsymbol{Y} = \boldsymbol{\Phi}\cdot\boldsymbol{J} + \boldsymbol{U}, \tag{6.4}$$

where

$$\boldsymbol{Y} = \begin{bmatrix}\boldsymbol{y}_{1,1} & \boldsymbol{y}_{2,1} & \cdots & \boldsymbol{y}_{P,1} & \boldsymbol{y}_{1,2} & \cdots & \boldsymbol{y}_{P,I}\end{bmatrix}, \tag{6.5}$$

$$\boldsymbol{J} = \begin{bmatrix}\boldsymbol{j}^{\text{ic}}_{1,1} & \boldsymbol{j}^{\text{ic}}_{2,1} & \cdots & \boldsymbol{j}^{\text{ic}}_{P,1} & \boldsymbol{j}^{\text{ic}}_{1,2} & \cdots & \boldsymbol{j}^{\text{ic}}_{P,I}\end{bmatrix}, \tag{6.6}$$

and $\boldsymbol{\Phi}\cdot\boldsymbol{J}$ is defined by

$$\boldsymbol{\Phi}\cdot\boldsymbol{J} = \begin{bmatrix}\boldsymbol{\Phi}_{1,1}\boldsymbol{j}^{\text{ic}}_{1,1} & \boldsymbol{\Phi}_{2,1}\boldsymbol{j}^{\text{ic}}_{2,1} & \cdots & \boldsymbol{\Phi}_{P,I}\boldsymbol{j}^{\text{ic}}_{P,I}\end{bmatrix}, \tag{6.7}$$

and correspondingly, $\boldsymbol{\Phi}^H\cdot\boldsymbol{Y}$ is defined as

$$\boldsymbol{\Phi}^H\cdot\boldsymbol{Y} = \begin{bmatrix}\boldsymbol{\Phi}^H_{1,1}\boldsymbol{y}^{\text{ic}}_{1,1} & \boldsymbol{\Phi}^H_{2,1}\boldsymbol{y}^{\text{ic}}_{2,1} & \cdots & \boldsymbol{\Phi}^H_{P,I}\boldsymbol{y}^{\text{ic}}_{P,I}\end{bmatrix}. \tag{6.8}$$

Here, $\boldsymbol{Y} \in \mathbb{C}^{Q\times PI}$ is the measurement data matrix, and the columns of $\boldsymbol{J} \in \mathbb{C}^{N\times PI}$ are the multiple vectors to be solved. $\boldsymbol{U} \in \mathbb{C}^{Q\times PI}$ represents the complex additive noises satisfying certain probability distribution. It is worth noting that for a single frequency inverse scattering problem, if the positions of the receivers are fixed, i.e., $\boldsymbol{\Phi}_{1,1} = \boldsymbol{\Phi}_{2,1} = \cdots = \boldsymbol{\Phi}_{Q,1}$, Eq. (6.4) reduces to the standard MMV model [127].

6.2.2 GUIDELINE OF THE MEASUREMENT CONFIGURATION

Although the joint sparsity is used here as a regularization constraint instead of for an exact recovery, an investigation on the uniqueness condition is still of much importance at least for two reasons: 1) It is of interest to know how much we could benefit from the joint recovery; 2) It provides us with a guideline of designing the measurement configuration that can make the most of the joint processing.

According to the work of Chen and Huo [149] and Davies and Eldar [150], a necessary and sufficient condition for the measurements, $\boldsymbol{Y} = \boldsymbol{\Phi}\boldsymbol{J}$, to uniquely determine the row sparse matrix $\boldsymbol{J}$ is that

$$\left|\text{supp}(\boldsymbol{J})\right| < \frac{\text{spark}(\boldsymbol{\Phi}) - 1 + \text{rank}(\boldsymbol{Y})}{2}, \tag{6.9}$$

where, $\text{supp}(\boldsymbol{J})$ denotes the index set corresponding to non-zero rows of matrix $\boldsymbol{J}$, $\left|\text{supp}(\boldsymbol{J})\right|$ denotes the cardinality of $\text{supp}(\boldsymbol{J})$, the spark of a given matrix is defined as the smallest number of the columns that are linearly dependent. Thereafter, Heckel and Bölcskei have studied the GMMV problem and showed that having different measurement matrices can lead to performance improvement over the standard MMV case [147]. The above work about the uniqueness condition implies specifically in our method that in order to make the most of the joint processing, the column number of matrix $\boldsymbol{Y} \in \mathbb{C}^{Q\times(P\times I)}$ is supposed to be no less than the number of receivers, i.e., $P \times I \geq Q$. Moreover, with the same measurement configuration, the inversion performance can be further improved by exploiting the frequency diversity even for the case of $P > Q$. The latter is further demonstrated in Subsection 6.3.1.

The determination of the receiver number depends not only on the measurement geometry but also on the spatial bandwidth of the scattered field. We refer to [4] for a theoretical analysis of the retrievable information and the measurement strategies of the EM inverse scattering problems by considering very particular canonical cases and applying the Nyquist sampling criterion. This provides us with a lower bound of the essential measurements, however, more measurements are normally needed for at least two reasons: 1) the scattered fields are much more complicated and unpredictable in real-life applications; 2) extra measurements are needed for the Cross-Validation (CV) technique (see Chapter 4 and the following subsection).

6.2.3 SOLVING THE GMMV MODEL

GMMV BASIS PURSUIT DENOISE PROBLEM

Suppose the noise level is known beforehand, the approach to find the multiple vectors is based on solving the convex optimization problem referred to as GMMV Basis Pursuit Denoise ($\text{BP}_{\tilde{\sigma}}$) problem

$$\text{minimize} \quad \kappa(\boldsymbol{J}) \quad \text{subject to} \quad \|\boldsymbol{\Phi}\cdot\boldsymbol{J} - \boldsymbol{Y}\|_F \leq \tilde{\sigma}, \tag{6.10}$$

where, $\tilde{\sigma}$ represents the noise level; $\kappa(\boldsymbol{J})$ is the mixed (α,β)-norm defined as

$$\|\boldsymbol{J}\|_{\alpha,\beta} := \left(\sum_{n=1}^{N} \left\|\boldsymbol{J}_{n,:}^T\right\|_\beta^\alpha\right)^{1/\alpha}, \tag{6.11}$$

where, $\boldsymbol{J}_{n,:}$ denotes the n-th row of $\boldsymbol{J}$; $\|\cdot\|_\beta$ is the conventional β-norm; $(\cdot)^T$ is the transpose operator; $\|\cdot\|_F$ is the Frobenius norm which is equivalent to the mixed (2,2)-norm $\|\cdot\|_{2,2}$. Here, we select the mixed norm $\|\cdot\|_{1,2}$ as a regularized constraint. Although $\|\cdot\|_{1,2}$ tends to enforce the row-sparsity of the matrix $\boldsymbol{J}$, sparsity is not a premise for

this approach. The key point is the utilization of the joint structure of the contrast source matrix for improving the focusing ability. As demonstrated in the following experiments, this approach is able to image objects which are not sparse by exploitation of the frequency diversity.

MULTIPLE GMMV LASSO PROBLEMS

Since it is not straightforward to solve the GMMV BP$_{\tilde{\sigma}}$ problem, we consider the GMMV Lasso (LS$_\tau$) problem formulated as [128]

$$\text{minimize} \quad \|\boldsymbol{\Phi}\cdot\boldsymbol{J}-\boldsymbol{Y}\|_F \quad \text{subject to} \quad \|\boldsymbol{J}\|_{1,2}\le\tau. \tag{6.12}$$

The GMMV LS$_\tau$ problem is equivalent to the GMMV BP$_{\tilde{\sigma}}$ problem when $\tau=\tau_{\tilde{\sigma}}$. As the exact value of $\tau_{\tilde{\sigma}}$ is not available, a series of GMMV LS$_\tau$ problems with different values of τ must be solved. Now let us first introduce the Pareto curve defined as

$$\phi_{\text{GMMV}}(\tau)=\left\|\boldsymbol{\Phi}\cdot\boldsymbol{J}_\tau^{\text{opt}}-\boldsymbol{Y}\right\|_F, \tag{6.13}$$

where, $\boldsymbol{J}_\tau^{\text{opt}}$ is the optimal solution to the LS$_\tau$ problem given by Eq. (6.12). When the optimal solution $\boldsymbol{J}_{\tau_h}^{\text{opt}}$ to the GMMV LS$_\tau$ problem is found, τ_h is updated to τ_{h+1} by probing the Pareto curve. The searching procedure is terminated when $\phi_{\text{GMMV}}(\tau)=\tilde{\sigma}$. At the meantime, τ reaches $\tau_{\tilde{\sigma}}$.

UPDATING THE PARAMETER, τ

As the Pareto curve is proven to be a non-increasing convex function, Newton iteration is used for updating the parameter, τ. Specifically, τ is updated by

$$\tau_{h+1}=\tau_h+\frac{\tilde{\sigma}-\phi_{\text{GMMV}}(\tau_h)}{\phi'_{\text{GMMV}}(\tau_h)}, \tag{6.14}$$

where,

$$\phi'_{\text{GMMV}}(\tau_h)=-\frac{\left\|\boldsymbol{\Phi}^H\cdot\left(\boldsymbol{\Phi}\cdot\boldsymbol{J}_{\tau_h}^{\text{opt}}-\boldsymbol{Y}\right)\right\|_{\infty,2}}{\left\|\boldsymbol{\Phi}\cdot\boldsymbol{J}_{\tau_h}^{\text{opt}}-\boldsymbol{Y}\right\|_F}. \tag{6.15}$$

Here, $\|\cdot\|_{\infty,2}$ is the dual norm of $\|\cdot\|_{1,2}$. The searching procedure is illustrated in Fig. 4.1. Unless a good estimate of $\tau_{\tilde{\sigma}}$ can be obtained, we choose $\tau_{\tilde{\sigma}}=0$, yielding $\phi(0)=\|\boldsymbol{Y}\|_F$ and $\phi'(0)=\left\|\boldsymbol{\Phi}^H\cdot\boldsymbol{Y}\right\|_{\infty,2}$. With Eq. (6.14), it holds immediately that the next Newton iteration is

$$\tau_1=\frac{\tilde{\sigma}-\|\boldsymbol{Y}\|_F}{\left\|\boldsymbol{\Phi}^H\cdot\boldsymbol{Y}\right\|_{\infty,2}}. \tag{6.16}$$

Since the extension of the projection operator to the GMMV problem is straightforward, we refer to [128, 129] and Chapter 4 for more details of the derivation of the dual and the algorithm for solving the GMMV problem by SPGL1.

6.2.4 CV-BASED MODIFIED SPGL1

In real applications, the termination condition, $\phi_{\mathrm{GMMV}}(\tau)=\tilde{\sigma}$, is not applicable, because the noise level, i.e., the parameter, $\tilde{\sigma}$, is unknown in general. In order to deal with this problem, we modified the SPGL1 method based on the CV technique [138, 139], in which $\tilde{\sigma}$ is set 0 and the iteration is terminated using CV technique. In doing so, the problem of estimating the noise level, i.e., the parameter, $\tilde{\sigma}$, can be well circumvented.

Specifically, when CV is utilized in the SPGL1 method, we separate the original scattering matrix to a reconstruction matrix, $\boldsymbol{\Phi}_{p,i,\mathrm{rec}}\in\mathbb{C}^{Q_{\mathrm{rec}}\times N}$, and a CV matrix, $\boldsymbol{\Phi}_{p,i,\mathrm{CV}}\in\mathbb{C}^{Q_{\mathrm{CV}}\times N}$ with $Q=Q_{\mathrm{rec}}+Q_{\mathrm{CV}}$. The measurement vectors, $\boldsymbol{y}_{p,i}$, are also separated accordingly, to a group of reconstruction measurement vector, $\boldsymbol{y}_{p,i,\mathrm{rec}}\in\mathbb{C}^{Q_{\mathrm{rec}}}$, and a group of CV measurement vectors, $\boldsymbol{y}_{p,i,\mathrm{CV}}\in\mathbb{C}^{Q_{\mathrm{CV}}}$. The reconstruction residual and the CV residual are defined as

$$r_{\mathrm{rec}}=\left(\sum_{i=1}^{I}\sum_{p=1}^{P}\left\|\boldsymbol{y}_{p,i,\mathrm{rec}}-\boldsymbol{\Phi}_{p,i,\mathrm{rec}}\boldsymbol{j}_{p,i}\right\|_2^2\right)^{1/2} \tag{6.17}$$

and

$$r_{\mathrm{CV}}=\left(\sum_{i=1}^{I}\sum_{p=1}^{P}\left\|\boldsymbol{y}_{p,i,\mathrm{CV}}-\boldsymbol{\Phi}_{p,i,\mathrm{CV}}\boldsymbol{j}_{p,i}\right\|_2^2\right)^{1/2}, \tag{6.18}$$

respectively. In doing so, every iteration can be viewed as two separate parts: reconstructing the contrast sources by SPGL1 and evaluating the outcome by the CV technique. The CV residual curve turns to increase when the reconstructed signal starts to overfit the noise. The reconstructed contrast sources are selected as the output on the criterion that its CV residual is the least one. To find the least CV residual, we initialize $\tilde{\sigma}$ as 0 and terminate the iteration when

$$N_{\mathrm{Iter}}>N_{\mathrm{opt}}+\Delta N, \tag{6.19}$$

is satisfied, Here, N_{Iter} is the current iteration number, N_{opt} is the iteration index corresponding to the least CV residual — the optimal solution. Namely, the CV residual is identified as the least one if the CV residual keeps increasing monotonously for ΔN iteration. In the following experimental examples, this termination condition works well with $\Delta N=30$.

Once the normalized contrast sources are obtained, one can achieve the shape of the scatterers defined as

$$\boldsymbol{\gamma}_{\mathrm{GMMV},n}=\sum_{i=1}^{I}\sum_{p=1}^{P}\left|\boldsymbol{j}_{p,i,n}^{\mathrm{ic}}\right|^2,\quad n=1,2,3,\cdots,N, \tag{6.20}$$

where $\boldsymbol{j}_{p,i,n}^{\mathrm{ic}}$ and $\boldsymbol{\gamma}_{\mathrm{GMMV},n}$ represent the n-th element of the vectors $\boldsymbol{j}_{p,i}^{\mathrm{ic}}$ and $\boldsymbol{\gamma}_{\mathrm{GMMV}}$, respectively.

6.3 VALIDATION WITH EXPERIMENTAL DATA

In order to validate the proposed GMMV-based linear method, we have applied it to the experimental database provided by the Remote Sensing and Microwave Experiments Team at the Institut Fresnel, France, in the year 2001 [31] and 2005 [32], respectively. Three different cases of dielectric scatterers, metallic scatterers (convex and nonconvex), and hybrid ones of both are considered, respectively. To guarantee the accuracy of the FDFD scheme, the inversion domain is discretized with a grid size Δ^2 satisfying

$$\Delta \leq \frac{\min\{\lambda_i\}}{15}, \quad i = 1,2,3,\cdots,I, \tag{6.21}$$

where λ_i is the wavelength of the i-th frequency.

We have also processed the same data by LSM for comparison. Since the background of the experiments is free space and only TM wave is considered, the LSM method consists in solving the integral equation of the indicator function $g_i\left(\vec{x}_{\mathrm{t}}\middle|\vec{z}\right)$ at the i-th frequency (see Fig. 2.12)

$$\int_{\Gamma_1} E_i^{\mathrm{sct}}\left(\vec{x}_{\mathrm{r}},\vec{x}_{\mathrm{t}}\right) g_i\left(\vec{x}_{\mathrm{t}}\middle|\vec{z}\right) d\vec{x}_{\mathrm{t}} = \frac{\omega_i \mu_0}{4} H_0^{(1)}\left(-k_i \left\|\vec{z}-\vec{x}_{\mathrm{r}}\right\|_2\right), \tag{6.22}$$

where, $E_i^{\mathrm{sct}}\left(\vec{x}_{\mathrm{r}},\vec{x}_{\mathrm{t}}\right)$ is the scattered field probed at $\vec{x}_{\mathrm{r}}$ corresponding to the transmitter at $\vec{x}_{\mathrm{t}}$ and the i-th frequency, $\vec{z}$ is the sampling point in the inversion domain, $H_0^{(1)}(\cdot)$ is the Hankel function of the first kind, k_i is the wavenumber of the i-th frequency. Eq. (6.22) can be reformulated as a set of linear systems of equations

$$\boldsymbol{Y}_i \boldsymbol{g}_{i,\vec{z}} = \boldsymbol{f}_{i,\vec{z}}, \quad i = 1,2,3,\cdots,I, \tag{6.23}$$

where, $\boldsymbol{Y}_i$ is the measurement data matrix, $\boldsymbol{g}_{i,\vec{z}}$ is the indicator function of the sampling point $\vec{z}$ in the form of a column vector, $\boldsymbol{f}_{i,\vec{z}}$ is the right side of Eq. (6.22) in the form of a column vector, the index i represents the i-th frequency. Following the same approach to solving Eq. (6.23) in [13, 140], the indicator function $\boldsymbol{g}_{i,\vec{z}}$ is sought to be

$$\left\|\boldsymbol{g}_{i,\vec{z}}\right\|_2^2 = \sum_{d=1}^{D}\left(\frac{s_{i,d}}{s_{i,d}^2 + a_i^2}\right)^2 \left|\boldsymbol{u}_d^H \boldsymbol{f}_{i,\vec{z}}\right|^2, \tag{6.24}$$

where, $s_{i,d}$ represents the singular value of matrix $\boldsymbol{Y}_i$ corresponding to the singular vector $\boldsymbol{u}_d$, $(\cdot)^H$ is the conjugate transpose operator, $D = \min\{P,Q\}$, and $a_i = 0.01 \times \max_d\{s_{i,d}\}$. The shape of the scatterers is defined by

$$\boldsymbol{\gamma}_{\mathrm{LSM}}\left(\vec{z}\right) = \frac{1}{\left\|\boldsymbol{g}_{\vec{z}}^{\mathrm{MF}}\right\|_2^2}, \tag{6.25}$$

where, $\left\|\boldsymbol{g}_{\vec{z}}^{\mathrm{MF}}\right\|_2^2$ is a multi-frequency modified indicator defined as the average of the normalized modified ones computed at each frequency [151]

$$\left\|\boldsymbol{g}_{\vec{z}}^{\mathrm{MF}}\right\|^2 = \frac{1}{I}\sum_{i=1}^{I}\frac{\left\|\boldsymbol{g}_{i,\vec{z}}\right\|_2^2}{\max\limits_{\vec{z}\in\mathcal{D}}\left(\left\|\boldsymbol{g}_{i,\vec{z}}\right\|_2^2\right)}. \tag{6.26}$$

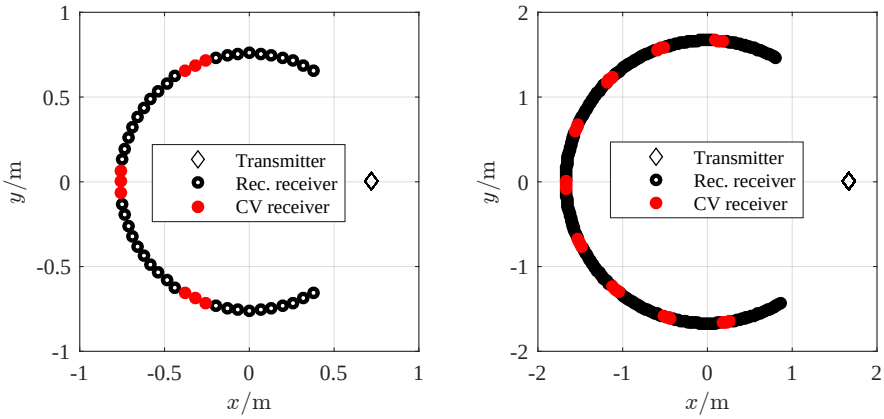

Figure 6.1: Measurement configuration of the data-sets: *twodielTM_8f*, *rectTM_dece*, and *uTM_shaped* (a) and the data-sets: *FoamDieIntTM* and *FoamMetExtTM* (b).

It is worth mentioning that the absolute value of the normalized contrast sources and the ℓ_2-norm of the indicator functions are proportional and inversely proportional to the amplitude of the electric field, respectively. According to the definition in Eq. (6.20) and Eq. (6.25), both $\boldsymbol{\gamma}_{\mathrm{GMMV}}$ and $\boldsymbol{\gamma}_{\mathrm{LSM}}$ are proportional to the power of the electric field respectively. Therefore, the dB scaling shown in the following examples is defined as

$$\boldsymbol{\gamma}_{\mathrm{dB}} = 10 \times \log_{10}\left(\frac{\boldsymbol{\gamma}}{\max\{\boldsymbol{\gamma}\}}\right). \tag{6.27}$$

6.3.1 DIELECTRIC SCATTERERS

EXAMPLE 1

In the first example, we consider the *twodielTM_8f* data-set provided in the first opus of the Institut Fresnel's database [31]. The targets consist of two identical circular cylinders, which are shown in Fig. 6.3 (a). All the cylinders have a radius of 1.5 cm and relative permittivity 3 ± 0.3. The emitter is placed at a fixed position on the circular rail, while a receiver is rotating around the centre of the vertical cylindrical target. The targets rotated from 0° to 350° in steps of 10° with a radius of 720 ± 3 mm, and the receiver rotated from 60° to 300° in steps of 5° with a radius of 760 ± 3 mm. Namely, we have 49×36 measurement data at each frequency when all the measurements are finished. The measurement configuration is shown in Fig. 6.1 (a), from which we can see 9 red dots representing the CV measurements and 40 circles representing the reconstruction measurements. The inversion domain is restricted to $[-75, 75] \times [-75, 75]$ mm^2, and the discretization grid size is 2.5×2.5 mm^2.

Let us first process the single frequency data at 4 GHz by the GMMV-based linear method and the LSM method. The data matrix, $\boldsymbol{Y}_i$, for LSM is a 72×36 matrix in which the data entries that are not available are replaced with zeros. The reconstruction residual curve and the CV residual curve are shown in Fig. 6.2 (a), from which we see the

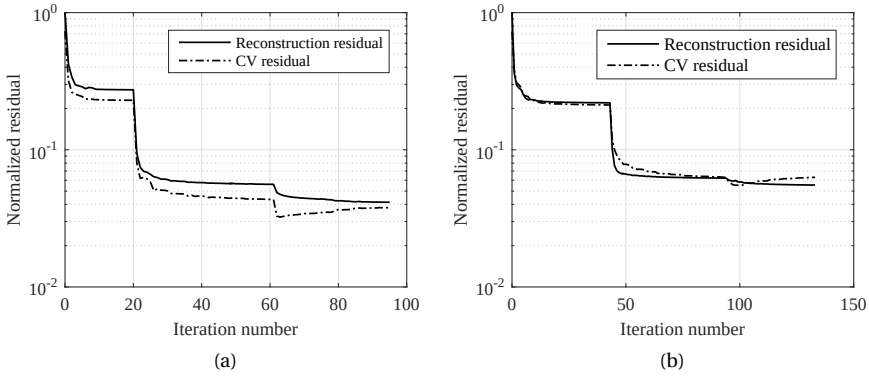

Figure 6.2: Normalized reconstruction residual curve and CV residual curve in Example 1, Subsection 6.3.1. (a): Reconstruction with single frequency at 4 GHz; (b): Reconstruction with multiple frequencies at 2 GHz, 4 GHz, 6 GHz, and 8 GHz.

CV residual decreases in the first 52 iterations and increases thereafter. The solutions at the turning point correspond to the optimal ones. In addition, the reconstruction residual corresponding to the turning point gives an estimation of the noise level $\tilde{\sigma} \approx 0.05\|\boldsymbol{Y}\|_F$. Figs. 6.3 (b) and 6.3 (c) show the images achieved by the two methods at 4 GHz with a dynamic range of 25 dB. As we can see the GMMV image is more clear than the LSM image. However, there is obvious shape distortion in the former one. Note that $Q = 49$, $P = 36$ and $I = 1$, we have $P \times I < Q$. Recalling the guideline of the measurement configuration discussed in Subsection 6.2.2, the reconstruction performance can be further improved via exploiting the frequency diversity. An obvious mismatch on the positions of the true objects and the reconstructed result can be observed. The reason is very likely to be the minor displacement and tilt occurred in the placement of the objects while doing this measurement, because the same phenomenon can be observed from the inverted results reported in [120] as well.

Now let us process the data at 2 GHz, 4 GHz, 6 GHz, and 8 GHz, simultaneously. The residual curves are shown in Fig. 6.2 (b) and the reconstructed images are shown in Figs. 6.3 (d) and 6.3 (e). By comparison of Figs. 6.3 (b) and 6.3 (d), one can see the reconstruction performance of the proposed GMMV-based linear method is improved by exploiting the frequency diversity. One can also observe that the GMMV-based linear method achieves lower sidelobes than the LSM method in the case of dielectric scatterers.

EXAMPLE 2

In the second example, we consider the *FoamDieIntTM* data-set provided in the second opus of the Institut Fresnel's database. The targets consist of a circular dielectric cylinder with a diameter of 30 mm embedded in another circular dielectric cylinder with a diameter of 80 mm. The smaller cylinder has a relative permittivity value of $\varepsilon_r = 3 \pm 0.3$, while the larger cylinder has a relative permittivity value of $\varepsilon_r = 1.45 \pm 0.15$. Fig. 6.5 (a) shows the true objects, and we refer to [32] for more description of the targets. The

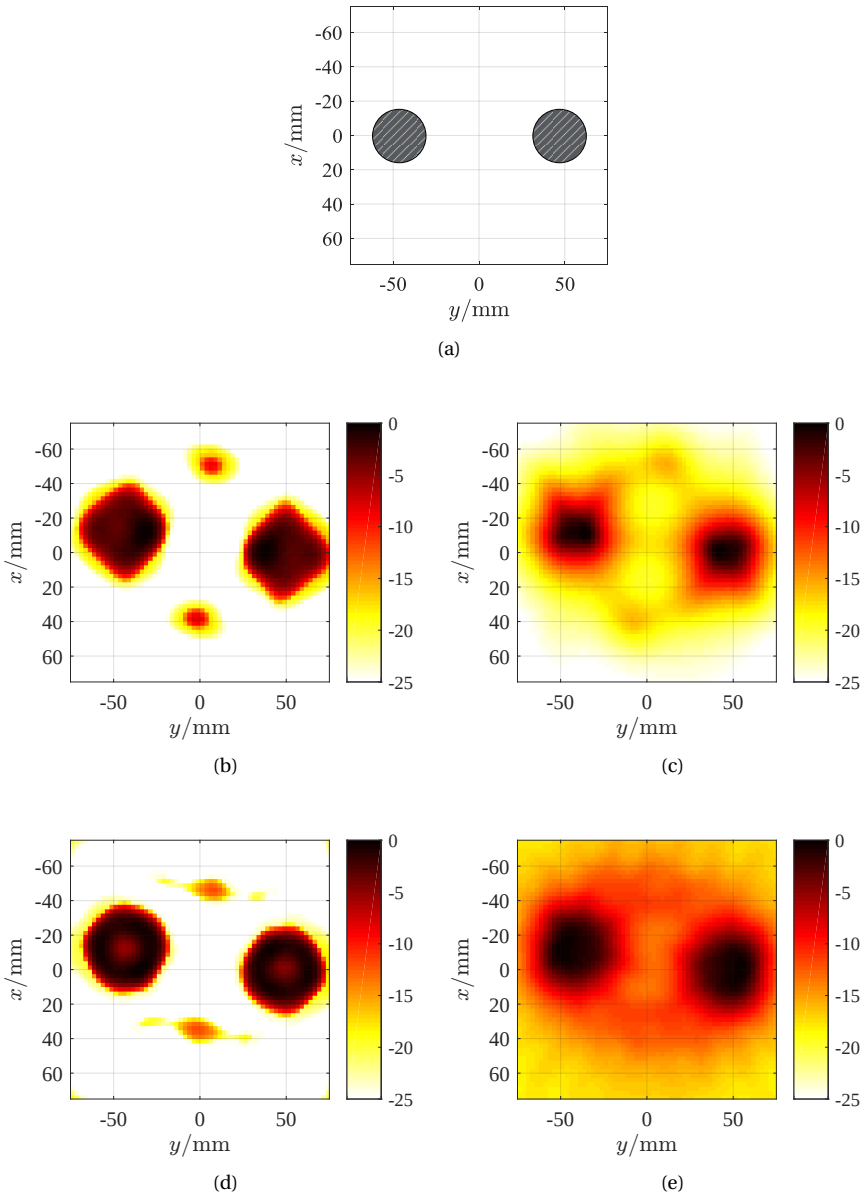

Figure 6.3: Scatterer geometry (a) of Example 1 in Subsection 6.3.1, its GMMV image (b), and LSM image (c) by processing the 4GHz data, and its GMMV image (d) and LSM image (e) by processing the multiple frequency data at 2 GHz, 4 GHz, 6 GHz, and 8 GHz.

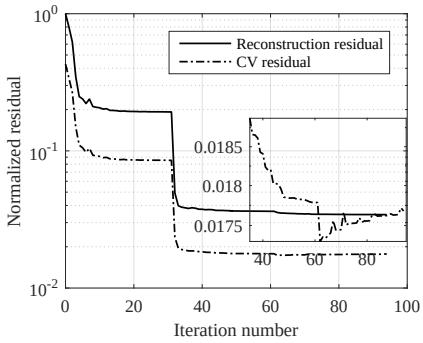

Figure 6.4: Normalized reconstruction residual curve and CV residual curve of Example 2 in Subsection 6.3.1. The multi-frequency data-set *FoamDieIntTM* at 2 GHz, 4 GHz, 6 GHz, 8 GHz, and 10 GHz are jointly processed.

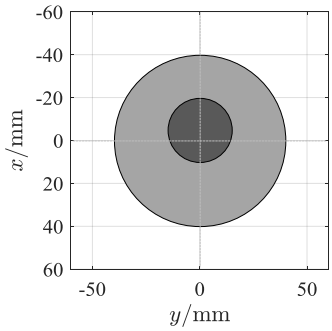

(a)

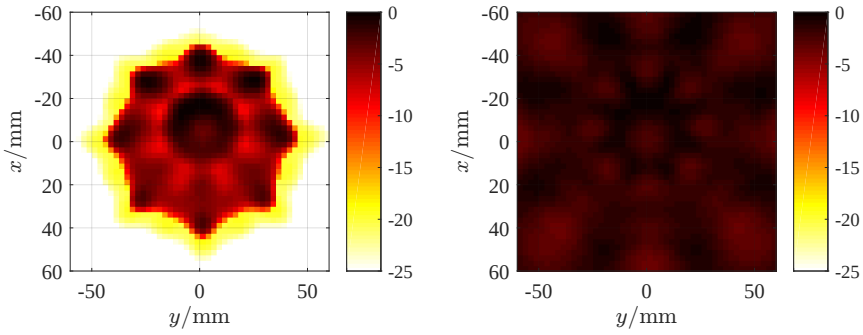

(b) (c)

Figure 6.5: Scatterer geometry (a) and its reconstructed shapes of the multi-frequency data-set: *FoamDieIntTM* at 2 GHz, 4 GHz, 6 GHz, 8 GHz, and 10 GHz, processed by GMMV (b) and LSM (c).

.

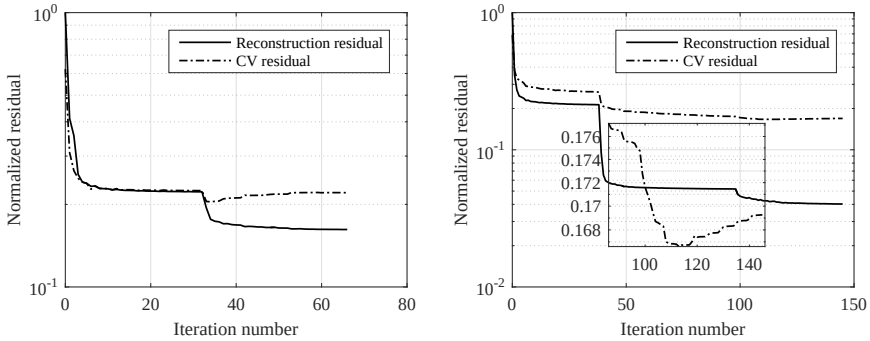

Figure 6.6: Normalized reconstruction residual curve and the CV residual curve in Subsection 6.3.2. (a): The rectangular metallic cylinder at 10 GHz, 12 GHz, 14 GHz, and 16 GHz; (b): The "U-shaped" metallic cylinder at 4 GHz, 8 GHz, 12 GHz, and 16 GHz.

experiment was carried out in 2005, in which the receiver stays in the azimuthal plane (xoy) and is rotated along two-thirds of a circle from 60° to 300° with the angular step being 1°. The source antenna stays at the fixed location ($\theta = 0°$), and the object is rotated to obtain different illumination incidences from 0° to 315° in steps of 45°. Namely, we have 241 × 8 measurements at each frequency. The distance from the transmitter or receiver to the centre of the target was increased to 1.67 m. The measurement configuration is shown in Fig. 6.1 (b), in which the diamond represents the emitter, the 4 × 9 red dots are the CV measurements, and the black circles are the reconstruction measurements.

The inversion domain is restricted to $[-60, 60] \times [-60, 60]$ mm^2, and the discretization grid size is 2.5 × 2.5 mm^2. Let us process the multi-frequency data at 2 GHz, 4 GHz, 6 GHz, 8 GHz, and 10 GHz simultaneously by the GMMV-based linear method and the LSM method, respectively. The data matrix, $\boldsymbol{Y}_i$, for LSM is a 360 × 8 matrix in which the data entries that are not available are replaced with zeros. The reconstruction residual curve and the CV residual curve are shown in Fig. 6.4, from which we see the CV residual decreases in the first 62 iterations and increases thereafter. Figs. 6.5 (b) and 6.5 (c) show the reconstructed images by the GMMV-based linear method and LSM, respectively. One can observe that the profile of the objects is reconstructed by the proposed method with a high resolution, while in the LSM image the objects cannot be distinguished at all.

6.3.2 METALLIC SCATTERERS

In this subsection, we applied the proposed method to the *rectTM_dece* and *uTM_shaped* data-sets in the first opus of the Institut Fresnel's database [31], which correspond to a convex scatterer — a rectangular metallic cylinder, and a non-convex scatterer — a "U-shaped" metallic cylinder, respectively. The dimensions of the rectangular cross section are 24.5 × 12.7 mm^2, while those of the "U-shaped" cylinder are about 80 × 50 mm^2. The

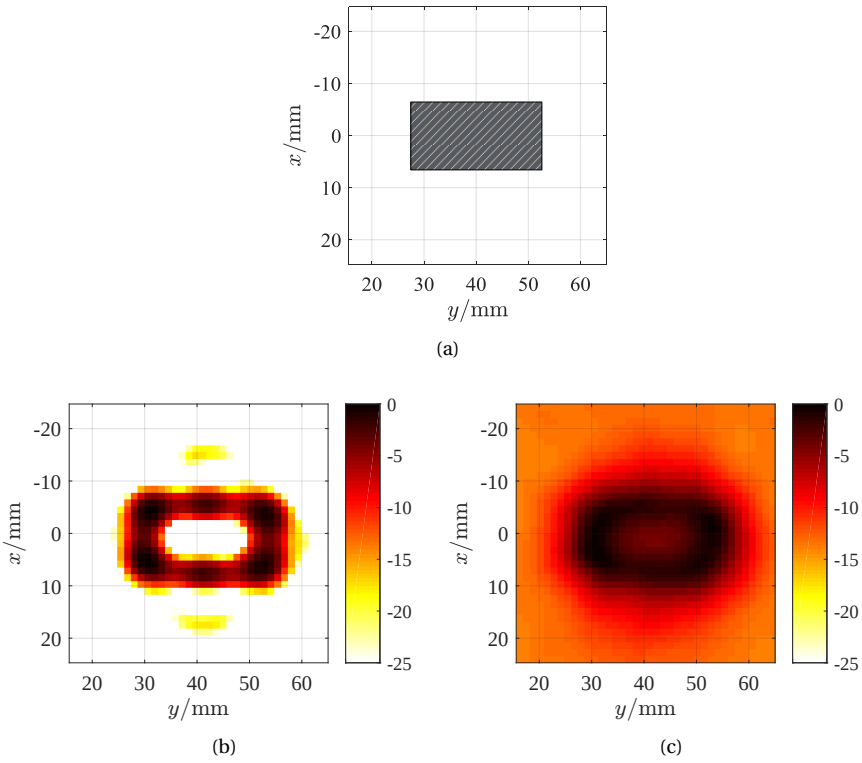

Figure 6.7: Scatterer geometry (a) of the rectangular metallic cylinder and its GMMV image (b) and LSM image (c) obtained by processing the multiple frequency data at 10 GHz, 12 GHz, 14 GHz, and 16 GHz.

.

measurement configuration is same as that in Subsection 6.3.1. More details about the description of the targets can be found in [31].

For the rectangular cylinder, the inversion domain is restricted to $[-25, 25] \times [15, 65]$ mm^2 and the multiple frequency data at 10 GHz, 12 GHz, 14 GHz, and 16 GHz are processed simultaneously. While for the larger "U-shaped" cylinder, the inversion domain is restricted to $[-70, 70] \times [-70, 70]$ mm^2 and the multiple frequency data at 4 GHz, 8 GHz, 12 GHz, and 16 GHz are processed simultaneously. The discretization grid size is 1.3×1.3 mm^2. Figs. 6.6 (a) and 6.6 (b) give the residual curves and the reconstructed images are shown in Fig. 6.7 and Fig. 6.8, respectively, from which we can see that the focusing performance of LSM is poor in the rectangular cylinder case and it is even worse in retrieving the shape of the non-convex "U-shaped" cylinder, while the rectangular shape and the "U" shape are well reconstructed by the proposed GMMV-based linear method, indicating that the latter shows higher resolving ability than the former in both the convex metallic target case and the non-convex metallic target case.

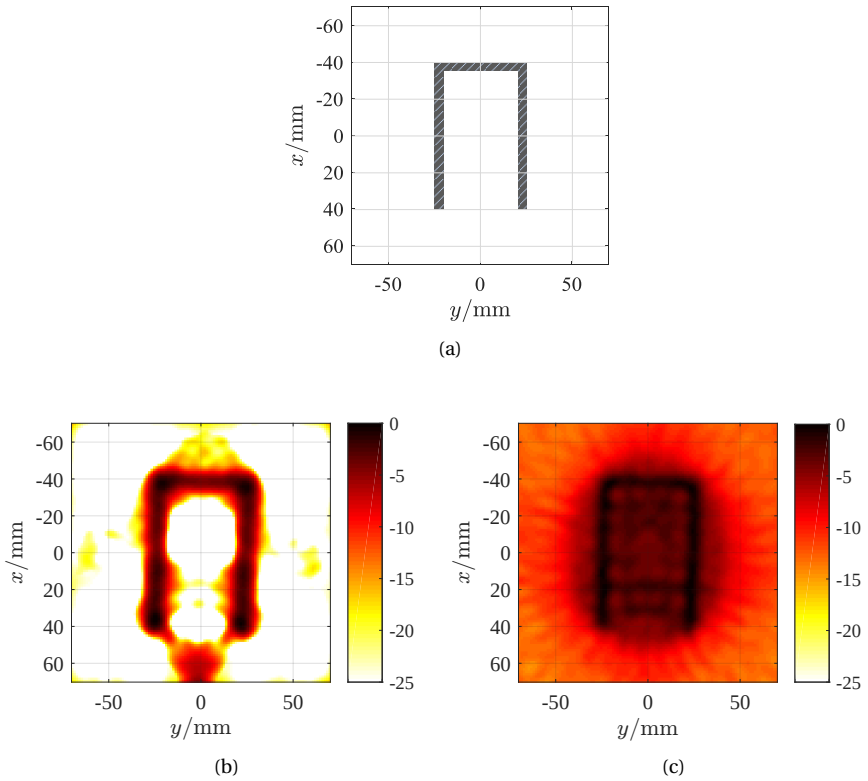

Figure 6.8: Scatterer geometry (a) of the "U-shaped" metallic cylinder and its GMMV image (b) and LSM image (c) by processing the multiple frequency data at 4 GHz, 8 GHz, 12 GHz, and 16 GHz.

.

6.3.3 HYBRID SCATTERERS

In this subsection, we applied the proposed method to hybrid scatterers consisting of a foam circular cylinder (diameter = 80 mm, $\varepsilon_r = 1.45 \pm 0.15$) and a copper tube (diameter = 28.5 mm, thickness = 2 mm), which was considered in the *FoamMetExtTM* data-set provided in the second opus of the Institut Fresnel's database. We refer to [32] for more description of the targets. The measurement configuration is shown in Fig. 6.1 (b). In contrast to the *FoamDieIntTM* data-set, this data-set is obtained using 18 transmitters, while other settings are kept the same. Specifically, the source antenna stays at the fixed location ($\theta = 0°$), and the object is rotated to obtain different illumination incidences from 0° to 340° in steps of 20°.

Let us first restrict the inversion domain to $[-90, 60] \times [-75, 75]$ mm^2 and discretize this domain with a grid size of 2.5 × 2.5 mm^2. The data at 7 frequencies, 2 GHz, 3 GHz, $\cdots$, and 8 GHz, are jointly processed. The data matrix, $\boldsymbol{Y}_i$, for LSM is a 360 × 18 matrix in which the data entries that are not available are replaced with zeros. Fig. 6.9 gives the

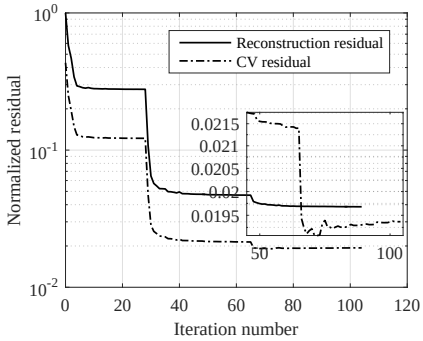

Figure 6.9: Normalized reconstruction residual curve and the CV residual curve in Subsection 6.3.3. The dataset *FoamMetExtTM* at 2 GHz, 3 GHz, ⋯, 8 GHz is processed.

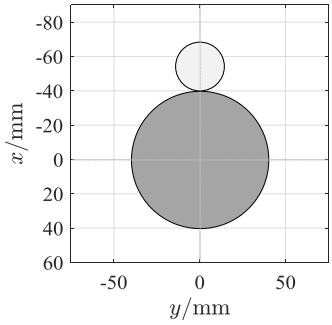

(a)

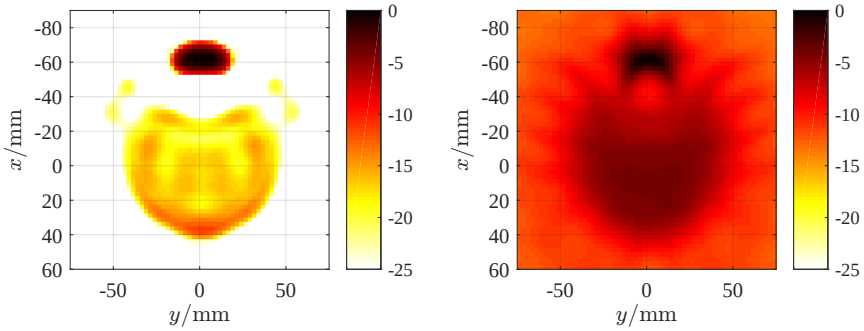

(b) (c)

Figure 6.10: Scatterer geometry (a) of the hybrid scatterers and their GMMV image (b) and LSM image (c) obtained by processing the multiple frequency data at 2 GHz, 3GHz, ⋯, 8 GHz.

Table 6.1: Running times of the experimental examples.

Data-set	Frequency number	GMMV /s	LSM /s
twodielTM_8f	1	2.5	0.0145
twodielTM_8f	4	12.7	0.0270
FoamDieIntTM	5	3.8	0.0693
rectTM_dece	4	2.7	0.0225
uTM_shaped	4	41.0	0.0498
FoamMetExtTM	7	15.6	0.0911

normalized residual curves of the GMMV-based linear method, and the reconstructed images by both methods are shown in Fig. 6.10. As we can see both the metallic cube and the circular foam cylinder can be well reconstructed by the GMMV-based linear method with a high resolution, but for a slight part lost in between. In addition, one can also see from the GMMV image that the metallic cube obviously has larger intensity than the foam cylinder, showing a potential ability to distinguish dielectric objects and metallic objects. In contrast, LSM shows a poor focusing ability in the hybrid scatterer case, indicating once again that the proposed GMMV-based linear method is able to achieve higher resolution images than the LSM method.

6.3.4 COMPUTATION TIME

In this subsection, we discuss the computational complexity of the GMMV-based linear imaging method. Since the sensing matrices can be computed (or analytically given for the experiments in homogeneous backgrounds) and stored beforehand, the GMMV-based linear method only involves a number of matrix-vector multiplications. The program was realized with MATLAB. We ran the program on a desktop with one Intel(R) Core(TM) i5-3470 CPU @ 3.20 GHz, and we did not use parallel computing. The running times of the GMMV-based linear method and LSM are listed in Table 6.1, from which we see that, on one hand, all the reconstructions by the GMMV-based linear method require less than 1 minute (or even a couple of seconds for some examples); on the other hand, LSM shows overwhelmingly higher efficiency in comparison to the GMMV-based linear method, because Singular Value Decomposition (SVD) in LSM is done once for all, and all of the indicator functions can be obtained simultaneously by several matrix-matrix multiplications. However, in view of the higher resolving ability of the proposed method, the extra computational cost is worth to pay. It is also worth mentioning that the proposed method is faster than the iterative shape reconstruction methods for which the direct scattering problem is solved in each iteration. In addition, parallel computing can be straightforwardly applied to the proposed method for acceleration.

6.4 DIFFERENCE AND RELATIONSHIP BETWEEN GMMV AND LSM

In this section, let us have a discussion on the difference and relationship between GMMV and LSM from the perspective of theoretical analysis. For conciseness, let us formulate both the GMMV-based linear inversion method and LSM with the FDFD scheme as follows

$$\boldsymbol{\Phi J} = \boldsymbol{Y}, \tag{6.28a}$$

$$\boldsymbol{\Phi} = \boldsymbol{YG}, \tag{6.28b}$$

where, $\boldsymbol{G}$ is the indicator function matrix given by

$$\boldsymbol{G} = \begin{bmatrix} \boldsymbol{g}_{1,1} & \boldsymbol{g}_{1,2} & \cdots & \boldsymbol{g}_{N,I} \end{bmatrix}, \tag{6.29}$$

and other notations remain consistent with the previous sections. Note that Eq. (6.28) applies to both the scalar waves and the vectorial waves. Obviously, Eq. (6.28a) is a direct formulation of the wave propagation, while Eq. (6.28b) is another formulation with the contrast source matrix removed from the left side and the measurement data matrix right multiplied by an indicator function matrix. Both of them share the merit that there is no weak scattering restriction. However, in the GMMV-based method, the sum-of-norm of matrix $\boldsymbol{J}$ is used as a regularized constraint, which means that the unknown vectors, $\boldsymbol{j}_{p,i}$, with respect to both different incident angles and different frequencies are estimated jointly. Therefore, the joint row-structure of the contrast source vectors is exploited, which suppresses the level of the artefacts especially for the high-frequency solutions. In other words, it plays a supplementary but also important role in its focusing ability. In the contrary, LSM conducts the estimation of the indicator functions separately. This explains the better resolving ability of the GMMV method. Since the SVD of the measurement matrix is done once for all in LSM, the indicator functions are calculated through several matrix-matrix multiplications. Compared to the iterative process in the GMMV method, LSM is more efficient.

6.5 CONCLUSIONS

In this chapter, a novel linear method for shape reconstruction based on the GMMV model is proposed. The sum-of-norm of the contrast sources is exploited as a regularization constraint in solving inverse scattering problems. We applied this method to process 2-D TM experimental data, and the results demonstrate that an estimated solution of the contrast sources regularized by the sum-of-norm constraint is sufficient to recover the spatial profile of the non-sparse targets. By comparison to LSM, it is demonstrated that the GMMV-based linear method outperforms LSM in the cases of dielectric scatterers, convex and non-convex metallic scatterers, and hybrid scatterers when the shape reconstruction quality and the level of the sidelobes are concerned. In view of the resolving ability and computational efficiency, the proposed method

looks very promising in the application to 3-Dimensional (3-D) imaging problems. In addition, the output of the GMMV-based linear method — the contrast sources, can be directly used for quantitative imaging when the incident fields are known or can be modelled with a reasonable accuracy.

In the future work, there are at least two limitations of the proposed method worth of studying: 1) For the dielectric scatterers with complicated geometries and strong scattering in their interior, although the basic profiles can be reconstructed, the details, such as the concave corners and the voids, are not distinguished well; 2) For 3-D inverse problems with lots of transmitters and receivers, the contrast source matrix demands huge memory resources.

7

CONCLUSIONS AND RECOMMENDATIONS FOR FUTURE WORK

This chapter gives the conclusions of the thesis and the recommendations for future work.

7.1 CONCLUSIONS

The major results of the thesis are the following

- The state-of-the-art of the contrast source inversion method is the Multiplicative Regularized Contrast Source Inversion (MR-CSI) method using a Total Variation (TV) constraint. In this thesis, it is demonstrated that, in some challenging situations of high contrasts and poor initial guesses, this method shows poor performance and even fails. Subsequently, a new error term is proposed which cross-correlates the mismatch between the data error and the state error. Based upon this new error term, a Cross-Correlated Contrast Source Inversion (CC-CSI) method has been developed, in which the novel cost functional is designed to interrelate the state error and the data error. We have also shown that CC-CSI can be implemented without significantly increasing the computational burden. The proposed algorithm is tested with a 2-Dimensional (2-D) benchmark problem. Numerical simulations with both Transverse Magnetic (TM)-polarized wave and Transverse Electric (TE)-polarized wave show that CC-CSI outperforms classical Contrast Source Inversion (CSI) and MR-CSI in the aspects of robustness and inversion accuracy. As Maxwell's equations are formulated within a 3-Dimensional

(3-D) Finite Difference Frequency Domain (FDFD) scheme, it is straightforward to extend the proposed inversion scheme to future 3-D inverse scattering problems. Finally, a multi-frequency version of CC-CSI is proposed, which is able to process multi-frequency data simultaneously. Numerical and experimental results show that it is more robust than the multi-frequency version of MR-CSI.

- A linear model is proposed for addressing the nonlinear inverse scattering problem of highly conductive objects. The Multiple Measurement Vectors (MMV) model is exploited and a sum-of-norm of the contrast source matrix is used as a regularization constraint. The intensity of the estimated contrast sources is able to indicate the position and profile of the highly conductive scatterers. In the reconstruction scheme, the Cross-Validation (CV) technique is used to circumvent the estimation of the noise level. Numerical results and experimental results demonstrate that the proposed method is able to reconstruct the boundary of the highly conductive targets with a higher resolution than both Linear Sampling Method (LSM) and the improved LSM, even in some cases where the latter two methods fail to reconstruct the correct shape. The running time of the proposed method is hundreds of times longer than LSM and tens of times longer than the improved LSM, but it is still acceptable and promising in view of the gain in the imaging resolution and the linear relationship between the computational complexity and the number of unknowns. In comparison to nonlinear iterative methods, it is very efficient because the solution to the direct scattering problem is not needed anymore.

- The linear model has been further considered in solving the 3-D inverse scattering problem in a half-space configuration. By solving a cascade of a group of inverse source problems and a linear optimization problem, lots of computation time has been saved in comparison to the nonlinear iterative methods. The fact is that an object in 3-D space shows higher sparsity than its projection onto a 2-D space. The proposed linear contrast source inversion method is able to circumvent the occurrence of false local optimal solutions when only partial measurement data are available. The proposed method is tested successfully in a Ground Penetrating Radar (GPR) configuration and a Through-the-Wall Imaging (TWI) configuration. The inversion quality with both an exact and an inexact background model is discussed and its sensitivity to the background estimation accuracy is shown as well. Results show that this method is not only efficient but also robust with respect to the reconstruction quality when the measurement data amount is limited by the one-side probing configuration. In the cases where the scattering objects extend over a large region, the influence of the regularization constraint becomes less significant. However, this problem can be, to a very large extent, overcome by a multi-frequency version of the proposed method.

- A multi-frequency version of the MMV-based linear shape reconstruction method has been proposed based on the Generalized Multiple Measurement Vectors (GMMV) model. By exploiting the frequency diversity, the proposed GMMV-based linear inversion method shows a good inversion performance for a variety of scatterers, including dielectric, lossy, and metallic scatterers. The exploitation

of the sum-of-norm constraint brings a supplementary focusing effect and leads to a higher resolving ability in comparison to the existing shape reconstruction methods, such as LSM. In view of the resolving ability and the computational efficiency, the proposed method looks very promising in the application to 3-D imaging problems. Besides, the output of the GMMV-based linear method — the estimation of the contrast sources, can be directly used for quantitative imaging if the incident fields are known or can be modelled with a reasonable accuracy.

7.2 RECOMMENDATIONS FOR FUTURE WORK

The work presented in this thesis can be continued or considered in some interesting topics and directions worth of studying in future work:

- The modelling of transmitting/receiving antenna radiating pattern. On one hand, for reconstructing the dielectric parameters, the exact values of the electric fields must be probed. Therefore, the measurement data are supposed to be interpreted to the field values. The exact interpretation depends on the modelling of the receiving antenna radiating pattern; On the other hand, seeking for the dielectric parameters requires the knowledge of the incident fields. It is safe to say that the inversion accuracy is closely related to the modelling quality of the transmitting antenna radiating pattern.

- The estimation of the average dielectric properties of the background medium. In an ideal homogeneous background medium, the measurement matrices (equivalently, the Green function) can be analytically given. However, in some real applications, the background is inhomogeneous and its dielectric properties are not exactly known. Therefore, the measurement matrix must be calculated numerically. A feasible approach is to estimate the average dielectric properties of the background. It is also interesting to consider the idea of using self-adaptive measurement matrices during the inversion process.

- Untangling the non-linearity of the inverse scattering problem in the data domain. Most of the research is focused on untangling the non-linearity of the inverse scattering problem in the inversion approaches. It is an interesting idea to think about this problem inversely, which is to untangle the non-linearity in the data domain. Some research work has been done [152], which shows promising results and deserves more attention in the future.

- The sparse representation of the targets. In this thesis, we have considered the sum-of-norm of the contrast source matrix as a regularization constraint. Since this norm tends to generate a sparse solution, if we can find a sparser representation of the solution in another domain, a better inversion performance can be expected.

- The extension of the proposed methods to other approaches and applications. For example, it is interesting to modify the already existing methods that are based on

the “data error + state error” cost functional by considering the newly-proposed cross-correlated error term. Or one can also apply the proposed methods to the acoustic inverse scattering problems and test the feasibility with more real measurement data.

- The development of a fast inversion approach. Inverting the dielectric properties of the targets involves the calculation of the total fields, which is computationally expensive. To promote the application of inversion techniques to solve the real inverse scattering problems, efficient inversion algorithms need to be developed without sacrificing too much inversion accuracy.

A

THE DERIVATION OF THE STEP SIZE IN CC-CSI

A.1 SINGLE FREQUENCY CC-CSI

First, let us rewrite the cost function $\mathcal{C}_{\text{CC-CSI},\ell-1/2}\big|_{\boldsymbol{j}_p=\boldsymbol{j}_{p,\ell-1}+\alpha_p\boldsymbol{\nu}_{p,\ell}}$ as follows

$$\begin{aligned}\mathcal{C}_{\text{CC-CSI},\ell-1/2}\big|_{\boldsymbol{j}_p=\boldsymbol{j}_{p,\ell-1}+\alpha_p\boldsymbol{\nu}_{p,\ell}} = \eta^{\mathcal{S}}\sum_{p=1}^{P}\left\|\boldsymbol{\rho}_{p,\ell-1/2}-\alpha_p\boldsymbol{\Phi}\boldsymbol{\nu}_{p,\ell}\right\|^2+\\ \eta_{n-1}^{\mathcal{D}}\sum_{p=1}^{P}\left\|\boldsymbol{\gamma}_{p,\ell-1/2}+\alpha_p\left(\boldsymbol{\chi}_{\ell-1}^{\text{iso}}\mathcal{M}_{\mathcal{D}}\boldsymbol{A}^{-1}-\boldsymbol{I}\right)\boldsymbol{\nu}_{p,\ell}\right\|^2+\\ \eta^{\mathcal{S}}\sum_{p=1}^{P}\left\|\boldsymbol{\xi}_{p,\ell-1/2}-\alpha_p\boldsymbol{\Phi}\boldsymbol{\chi}_{\ell-1}^{\text{iso}}\mathcal{M}_{\mathcal{D}}\boldsymbol{A}^{-1}\boldsymbol{\nu}_{p,\ell}\right\|^2\Bigg|_{\boldsymbol{j}_p=\boldsymbol{j}_{p,\ell-1}+\alpha_p\boldsymbol{\nu}_{p,\ell}}.\end{aligned} \tag{A.1}$$

Obviously, it can be further simplified in the form of

$$\mathcal{C}_{\text{CC-CSI},\ell-1/2}\big|_{\boldsymbol{j}_p=\boldsymbol{j}_{p,\ell-1}+\alpha_p\boldsymbol{\nu}_{p,\ell}} = \sum_{j=0}^{2}\left(a_{p,j}+b_{p,j}+c_{p,j}\right)\alpha_p^j. \tag{A.2}$$

Therefore, we have

$$\alpha_{p,\ell} = \arg\max_{\alpha_p}\left\{\mathcal{C}_{\text{CC-CSI},\ell-1/2}\big|_{\boldsymbol{j}_p=\boldsymbol{j}_{p,\ell-1}+\alpha_p\boldsymbol{\nu}_{p,\ell}}\right\} = -\frac{1}{2}\frac{a_{p,1}+b_{p,1}+c_{p,1}}{a_{p,2}+b_{p,2}+c_{p,2}}. \tag{A.3}$$

Note that

$$a_{p,2} = \eta^{\mathcal{S}}\left\|\boldsymbol{\Phi}\boldsymbol{\nu}_{p,\ell}\right\|_{\mathcal{S}}^2, \tag{A.4}$$

$$a_{p,1} = -2\eta^{\mathcal{S}}\Re\left\{\boldsymbol{\nu}_{p,\ell}^H\boldsymbol{\Phi}^H\boldsymbol{\rho}_{p,\ell-1/2}\right\}\Big|_{\boldsymbol{j}_p=\boldsymbol{j}_{p,\ell-1}}, \tag{A.5}$$

A

$$b_{p,2} = \eta_{n-1}^{\mathcal{D}} \left\| \boldsymbol{v}_{p,\ell} - \boldsymbol{\chi} \mathcal{M}_{\mathcal{D}} \boldsymbol{A}^{-1} \boldsymbol{v}_{p,\ell} \right\|_{\mathcal{D}}^2, \tag{A.6}$$

$$b_{p,1} = 2\eta_{n-1}^{\mathcal{D}} \Re \left\{ \boldsymbol{v}_{p,\ell}^H \left(\boldsymbol{\chi} \mathcal{M}_{\mathcal{D}} \boldsymbol{A}^{-1} - \boldsymbol{I} \right)^H \boldsymbol{\gamma}_{p,\ell-1/2} \right\} \Big|_{\boldsymbol{j}_p = \boldsymbol{j}_{p,\ell-1}}, \tag{A.7}$$

$$c_{p,2} = \eta^{\mathcal{S}} \left\| \boldsymbol{\Phi} \boldsymbol{\chi} \mathcal{M}_{\mathcal{D}} \boldsymbol{A}^{-1} \boldsymbol{v}_{p,\ell} \right\|_{\mathcal{S}}^2, \tag{A.8}$$

$$c_{p,1} = -2\eta^{\mathcal{S}} \Re \left\{ \boldsymbol{v}_{p,\ell}^H \left(\boldsymbol{\Phi} \boldsymbol{\chi} \mathcal{M}_{\mathcal{D}} \boldsymbol{A}^{-1} \right)^H \boldsymbol{\xi}_{p,\ell-1/2} \right\} \Big|_{\boldsymbol{j}_p = \boldsymbol{j}_{p,\ell-1}}, \tag{A.9}$$

and

$$\begin{aligned} \boldsymbol{g}_{p,\ell} = &-2\eta^{\mathcal{S}} \boldsymbol{\Phi}^H \boldsymbol{\rho}_{p,\ell-1/2} + 2\eta_{n-1}^{\mathcal{D}} \left(\boldsymbol{\chi}_{\ell-1}^{\text{iso}} \mathcal{M}_{\mathcal{D}} \boldsymbol{A}^{-1} - \boldsymbol{I} \right)^H \boldsymbol{\gamma}_{p,\ell-1/2} - \\ &2\eta^{\mathcal{S}} \left(\boldsymbol{\Phi} \boldsymbol{\chi}_{\ell-1}^{\text{iso}} \mathcal{M}_{\mathcal{D}} \boldsymbol{A}^{-1} \right)^H \boldsymbol{\xi}_{p,\ell-1/2} \Big|_{\boldsymbol{j}_p = \boldsymbol{j}_{p,\ell-1}}, \end{aligned} \tag{A.10}$$

it is easy to obtain

$$\alpha_{p,\ell} = -\frac{\Re \left\{ \left\langle \boldsymbol{g}_{p,\ell}, \boldsymbol{v}_{p,\ell} \right\rangle_{\mathcal{D}} \right\}}{2 \left(a_{p,2} + b_{p,2} + c_{p,2} \right)}, \tag{A.11}$$

where, $a_{p,2}$, $b_{p,2}$, and $c_{p,2}$ are given by Eq. (A.4), Eq. (A.6), and Eq. (A.8), respectively.

A.2 MULTI-FREQUENCY CC-CSI

First, let us rewrite the cost function $\mathcal{C}_{\text{MF-CC-CSI},\ell-1/2} \big|_{\boldsymbol{j}_{p,i} = \boldsymbol{j}_{p,i,\ell-1} + \alpha_{p,i} \boldsymbol{v}_{p,i,\ell}}$ as follows

$$\begin{aligned} \mathcal{C}_{\text{MF-CC-CSI},\ell-1/2} \big|_{\boldsymbol{j}_{p,i} = \boldsymbol{j}_{p,i,\ell-1} + \alpha_{p,i} \boldsymbol{v}_{p,i,\ell}} = &\sum_{i=1}^{I} \eta_i^{\mathcal{S}} \sum_{p=1}^{P} \left\| \boldsymbol{\rho}_{p,i,\ell-1/2} - \alpha_{p,i} \boldsymbol{\Phi}_i \boldsymbol{v}_{p,i,\ell} \right\|^2 + \\ &\sum_{i=1}^{I} \eta_{i,\ell-1}^{\mathcal{D}} \sum_{p=1}^{P} \left\| \boldsymbol{\gamma}_{p,i,\ell-1/2} + \alpha_{p,i} \left(\boldsymbol{\chi}_{\ell-1}^{\text{iso}} \mathcal{M}_{\mathcal{D}} \boldsymbol{A}_i^{-1} - \boldsymbol{I} \right) \boldsymbol{v}_{p,i,\ell} \right\|^2 + \\ &\sum_{i=1}^{I} \eta_i^{\mathcal{S}} \sum_{p=1}^{P} \left\| \boldsymbol{\xi}_{p,i,\ell-1/2} - \alpha_{p,i} \boldsymbol{\Phi}_i \boldsymbol{\chi}_{\ell-1}^{\text{iso}} \mathcal{M}_{\mathcal{D}} \boldsymbol{A}_i^{-1} \boldsymbol{v}_{p,i,\ell} \right\|^2 \Big|_{\boldsymbol{j}_{p,i} = \boldsymbol{j}_{p,i,\ell-1} + \alpha_{p,i} \boldsymbol{v}_{p,i,\ell}}. \end{aligned} \tag{A.12}$$

Obviously, it can be further simplified in the form of

$$\mathcal{C}_{\text{MF-CC-CSI},\ell-1/2} \big|_{\boldsymbol{j}_{p,i} = \boldsymbol{j}_{p,i,\ell-1} + \alpha_{p,i} \boldsymbol{v}_{p,i,\ell}} = \sum_{j=0}^{2} \sum_{i=1}^{I} \left(a_{p,i,j} + b_{p,i,j} + c_{p,i,j} \right) \alpha_{p,i}^j. \tag{A.13}$$

Therefore, we have

$$\begin{aligned} \alpha_{p,i,\ell} &= \arg\max_{\alpha_{p,i}} \left\{ \mathcal{C}_{\text{MF-CC-CSI},\ell-1/2} \big|_{\boldsymbol{j}_{p,i} = \boldsymbol{j}_{p,i,\ell-1} + \alpha_{p,i} \boldsymbol{v}_{p,i,\ell}} \right\} \\ &= -\frac{1}{2} \frac{a_{p,i,1} + b_{p,i,1} + c_{p,i,1}}{a_{p,i,2} + b_{p,i,2} + c_{p,i,2}}. \end{aligned} \tag{A.14}$$

Note that

$$a_{p,i,2} = \eta_i^{\mathcal{S}} \left\| \boldsymbol{\Phi}_i \boldsymbol{\nu}_{p,i,\ell} \right\|_{\mathcal{S}}^2, \tag{A.15}$$

$$a_{p,i,1} = -2\eta_i^{\mathcal{S}} \Re \left\{ \boldsymbol{\nu}_{p,i,\ell}^H \boldsymbol{\Phi}_i^H \boldsymbol{\rho}_{p,i,\ell-1/2} \right\} \Big|_{\boldsymbol{j}_{p,i}=\boldsymbol{j}_{p,i,\ell-1}}, \tag{A.16}$$

$$b_{p,i,2} = \eta_{i,\ell-1}^{\mathcal{D}} \| \boldsymbol{\nu}_{p,i,\ell} - \boldsymbol{\chi} \mathcal{M}_{\mathcal{D}} \boldsymbol{A}_i^{-1} \boldsymbol{\nu}_{p,i,\ell} \|_{\mathcal{D}}^2, \tag{A.17}$$

$$b_{p,i,1} = 2\eta_{i,\ell-1}^{\mathcal{D}} \Re \left\{ \boldsymbol{\nu}_{p,i,\ell}^H \left(\boldsymbol{\chi} \mathcal{M}_{\mathcal{D}} \boldsymbol{A}_i^{-1} - \boldsymbol{I} \right)^H \boldsymbol{\gamma}_{p,i,\ell-1/2} \right\} \Big|_{\boldsymbol{j}_{p,i}=\boldsymbol{j}_{p,i,\ell-1}}, \tag{A.18}$$

$$c_{p,i,2} = \eta_i^{\mathcal{S}} \left\| \boldsymbol{\Phi}_i \boldsymbol{\chi} \mathcal{M}_{\mathcal{D}} \boldsymbol{A}_i^{-1} \boldsymbol{\nu}_{p,i,\ell} \right\|_{\mathcal{S}}^2, \tag{A.19}$$

$$c_{p,i,1} = -2\eta_i^{\mathcal{S}} \Re \left\{ \boldsymbol{\nu}_{p,i,\ell}^H \left(\boldsymbol{\Phi}_i \boldsymbol{\chi} \mathcal{M}_{\mathcal{D}} \boldsymbol{A}_i^{-1} \right)^H \boldsymbol{\xi}_{p,i,\ell-1/2} \right\} \Big|_{\boldsymbol{j}_{p,i}=\boldsymbol{j}_{p,i,\ell-1}}, \tag{A.20}$$

and

$$\begin{aligned} \boldsymbol{g}_{p,i,\ell} = &-2\eta_i^{\mathcal{S}} \boldsymbol{\Phi}_i^H \boldsymbol{\rho}_{p,i,\ell-1/2} + 2\eta_{i,\ell-1}^{\mathcal{D}} \left(\boldsymbol{\chi}_{\ell-1}^{\text{iso}} \mathcal{M}_{\mathcal{D}} \boldsymbol{A}_i^{-1} - \boldsymbol{I} \right)^H \boldsymbol{\gamma}_{p,i,\ell-1/2} - \\ &2\eta_i^{\mathcal{S}} \left(\boldsymbol{\Phi}_i \boldsymbol{\chi}_{\ell-1}^{\text{iso}} \mathcal{M}_{\mathcal{D}} \boldsymbol{A}_i^{-1} \right)^H \boldsymbol{\xi}_{p,i,\ell-1/2} \Big|_{\boldsymbol{j}_{p,i}=\boldsymbol{j}_{p,i,\ell-1}}, \end{aligned} \tag{A.21}$$

it is easy to obtain

$$\alpha_{p,i,\ell} = -\frac{\Re \left\{ \left\langle \boldsymbol{g}_{p,i,\ell}, \boldsymbol{\nu}_{p,i,\ell} \right\rangle_{\mathcal{D}} \right\}}{2 \left(a_{p,i,2} + b_{p,i,2} + c_{p,i,2} \right)}, \tag{A.22}$$

where, $a_{p,i,2}$, $b_{p,i,2}$, and $c_{p,i,2}$ are given by Eq. (A.15), Eq. (A.17), and Eq. (A.19), respectively.

B

THE SENSING MATRIX IN FREE SPACE

B.1 2-D FREE SPACE

In a 2-Dimensional (2-D) space, the partial Maxwell's equations can be simplified as

$$\partial_{x_2} E_{x_3} = -\mathrm{i}\omega\mu H_{x_1}, \tag{B.1a}$$
$$-\partial_{x_1} E_{x_3} = -\mathrm{i}\omega\mu H_{x_2}, \tag{B.1b}$$
$$\partial_{x_1} E_{x_2} - \partial_{x_2} E_{x_1} = -\mathrm{i}\omega\mu H_{x_3}, \tag{B.1c}$$

and

$$\partial_{x_2} H_{x_3} = \mathrm{i}\omega\epsilon E_{x_1} + J_{x_1}, \tag{B.2a}$$
$$-\partial_{x_1} H_{x_3} = \mathrm{i}\omega\epsilon E_{x_2} + J_{x_2}, \tag{B.2b}$$
$$\partial_{x_1} H_{x_2} - \partial_{x_2} H_{x_1} = \mathrm{i}\omega\epsilon E_{x_3} + J_{x_3}. \tag{B.2c}$$

Here, the magnetic current is not considered.

B.1.1 TM POLARIZATION

Let us first suppose $J_{x_3} = \delta\left(\vec{x} - \vec{y}\right)$, $J_{x_1} = J_{x_2} = 0$, then we have $E_{x_1} = E_{x_2} = H_{x_3} = 0$, and

$$\nabla^2 E_{x_3} + k^2 E_{x_3} = \mathrm{i}\omega\mu_0 \delta\left(\vec{x} - \vec{y}\right), \tag{B.3}$$

where, $k^2 = \omega^2\epsilon\mu$.

Note that the 3-Dimensional (3-D) and 2-D solutions to the equation

$$\nabla^2 U + k^2 U = -\delta\left(\vec{x} - \vec{y}\right) \tag{B.4}$$

are

$$\begin{aligned} U_{[3]}\left(\vec{x},\vec{y},k\right) &= \mathcal{F}\left\{\frac{1}{4\pi}\frac{\delta(\tau-r/c)}{r}\right\} \\ &= \frac{\exp\left(-\mathrm{i}kr\right)}{4\pi r}, \end{aligned} \tag{B.5}$$

and

$$\begin{aligned} U_{[2]}\left(\vec{X},\vec{Y},k\right) &= \int_{-\infty}^{+\infty} U_{[3]}\left(\vec{x},\vec{y},k\right)|_{x_3=0}\,dy_3 \\ &= \int_{-\infty}^{+\infty} \frac{1}{4\pi\sqrt{R^2+y_3^2}}\exp\left(-\mathrm{i}k\sqrt{R^2+y_3^2}\right)dy_3 \\ &= \frac{1}{4\pi}\int_{-\infty}^{+\infty}\exp\left(-\mathrm{i}kR\cosh t\right)dt \quad \left(y_3 = R\sinh t\right) \\ &= \frac{\mathrm{i}}{4}H_0^{(1)}\left(-kR\right), \end{aligned} \tag{B.6}$$

respectively, where $r = \left\|\vec{x}-\vec{y}\right\|_2$, $\vec{X} = (x_1, x_2)$, $\vec{Y} = \left(y_1, y_2\right)$, and $R = \left\|\vec{X}-\vec{Y}\right\|_2$. Then we can simply obtain the 2-D solutions to Eq. (B.3) as follows

$$E_{x_3,[2]}\left(\vec{X},\vec{Y},k\right) = \frac{1}{4}\omega\mu_0 H_0^{(1)}\left(-kR\right). \tag{B.7}$$

B.1.2 TE POLARIZATION

Now let us suppose $J_{x_3} = 0$, we have $H_{x_1} = H_{x_2} = E_{x_3} = 0$, and

$$\left(\partial_{x_1}^2 + \partial_{x_2}^2\right)H_{x_3} + k^2 H_{x_3} = -\partial_{x_1}J_{x_2} + \partial_{x_2}J_{x_1}, \tag{B.8}$$

where, $k^2 = \omega^2\epsilon\mu$.

For the specific case $J_{x_1} = \delta\left(\vec{x}-\vec{y}\right)$, $J_{x_2} = J_{x_3} = 0$, we have

$$\left(\partial_{x_1}^2 + \partial_{x_2}^2\right)H_{x_3} + k^2 H_{x_3} = \partial_{x_2}J_{x_1}, \tag{B.9}$$

Using the following formula

$$\frac{dH_n^{(1)}(z)}{dz} = \frac{nH_n^{(1)}(z)}{z} - H_{n+1}^{(1)}(z), \tag{B.10}$$

we can simply obtain the 2-D solution to Eq. (B.9) as follows

$$\begin{aligned} H_{x_3,[2]}\left(\vec{X},\vec{Y},k\right) &= -\frac{\mathrm{i}}{4}\partial_{x_2}H_0^{(1)}\left(-kR\right) \\ &= -\frac{\mathrm{i}}{4}\left(-H_1^{(1)}\left(-kR\right)\frac{-kx_2}{R}\right) \\ &= -\frac{\mathrm{i}kx_2}{4R}H_1^{(1)}\left(-kR\right). \end{aligned} \tag{B.11}$$

Then, the 2-D solution of the electric field can be obtained according to the following equations

$$\begin{aligned} E_{x_1,[2]}\left(\vec{X},\vec{Y},k\right) &= (\mathrm{i}\omega\varepsilon_0)^{-1}\partial_{x_2}H_{x_3,[2]} \\ &= \frac{-k}{4\omega\varepsilon_0}\partial_{x_2}\frac{x_2}{R}H_1^{(1)}(-kR) \\ &= \frac{-k}{4\omega\varepsilon_0}\left(\frac{x_1^2}{R^3}H_1^{(1)}(-kR)+\frac{-kx_2^2}{R^2}\left(\frac{H_1^{(1)}(-kR)}{-kR}-H_2^{(1)}(-kR)\right)\right) \\ &= \frac{-k}{4\omega\varepsilon_0}\left(\frac{H_1^{(1)}(-kR)}{R}+\frac{kx_2^2}{R^2}H_2^{(1)}(-kR)\right), \end{aligned} \tag{B.12}$$

$$\begin{aligned} E_{x_2,[2]}\left(\vec{X},\vec{Y},k\right) &= -(\mathrm{i}\omega\varepsilon_0)^{-1}\partial_{x_1}H_{x_3,[2]} \\ &= \frac{kx_2}{4\omega\varepsilon_0}\partial_{x_1}\frac{1}{R}H_1^{(1)}(-kR) \\ &= \frac{kx_2}{4\omega\varepsilon_0}\left(\frac{-x_1}{R^3}H_1^{(1)}(-kR)+\frac{-kx_1}{R^2}\left(\frac{H_1^{(1)}(-kR)}{-kR}-H_2^{(1)}(-kR)\right)\right) \\ &= \frac{k^2x_1x_2}{4\omega\varepsilon_0R^2}H_2^{(1)}(-kR). \end{aligned} \tag{B.13}$$

Correspondingly, if $J_{x_2}=\delta\left(\vec{x}-\vec{y}\right)$, $J_{x_1}=J_{x_3}=0$, we have

$$\begin{aligned} H_{x_3,[2]}\left(\vec{X},\vec{Y},k\right) &= \frac{\mathrm{i}}{4}\partial_{x_1}H_0^{(1)}(-kR) \\ &= \frac{\mathrm{i}}{4}\left(-H_1^{(1)}(-kR)\frac{-kx_1}{R}\right) \\ &= \frac{\mathrm{i}kx_1}{4R}H_1^{(1)}(-kR), \end{aligned} \tag{B.14}$$

$$\begin{aligned} E_{x_1,[2]}\left(\vec{X},\vec{Y},k\right) &= (\mathrm{i}\omega\varepsilon_0)^{-1}\partial_{x_2}H_{x_3,[2]} \\ &= \frac{kx_1}{4\omega\varepsilon_0}\partial_{x_2}\frac{1}{R}H_1^{(1)}(-kR) \\ &= \frac{k^2x_1x_2}{4\omega\varepsilon_0R^2}H_2^{(1)}(-kR), \end{aligned} \tag{B.15}$$

$$\begin{aligned} E_{x_2,[2]}\left(\vec{X},\vec{Y},k\right) &= -(\mathrm{i}\omega\varepsilon_0)^{-1}\partial_{x_1}H_{x_3,[2]} \\ &= \frac{-k}{4\omega\varepsilon_0}\partial_{x_1}\frac{x_1}{R}H_1^{(1)}(-kR) \\ &= \frac{-k}{4\omega\varepsilon_0}\left(\frac{H_1^{(1)}(-kR)}{R}+\frac{kx_1^2}{R^2}H_2^{(1)}(-kR)\right). \end{aligned} \tag{B.16}$$

B.2 3-D FREE SPACE

First, we choose the time factor $\exp(\mathrm{i}\omega t)$, then we have

$$\vec{E}\left(\vec{x},\vec{y},\vec{q}\right) = -\frac{\mathrm{i}}{k}\nabla_{\vec{x}}\times\nabla_{\vec{x}}\times\vec{q}\,\Phi\left(\vec{x},\vec{y}\right), \tag{B.17}$$

where, $\vec{q}$ is the polarization of the electric dipole placed at the location $\vec{y}$, and $\Phi\left(\vec{x},\vec{y}\right)$ is the fundamental point solution to Maxwell's equations, Explicitly, for a 3-D homogeneous space with the wave number $k>0$, we have

$$\Phi\left(\vec{x},\vec{y}\right) = \frac{1}{4\pi}\frac{\exp(-\mathrm{i}kr)}{r}, \quad \vec{x}\in\mathbb{R}^3, \tag{B.18}$$

where $r = \left\|\vec{x}-\vec{y}\right\|_2$.

For simplicity, we assume $\vec{q} = \vec{q}_1 = (1,0,0)$ (for other orientations, the solutions can be easily obtained by the rotation operation), then substitution of Eq. (B.18) into Eq. (B.17) yields

$$\begin{aligned}
\vec{E}(\vec{x},\vec{y},\vec{q}_1) &= -\frac{\mathrm{i}}{4\pi k}\nabla_{\vec{x}}\times\nabla_{\vec{x}}\times\begin{bmatrix}1\\0\\0\end{bmatrix}\frac{\exp(-\mathrm{i}kr)}{r}\\
&= -\frac{\mathrm{i}}{4\pi k}\nabla_{\vec{x}}\times\begin{bmatrix}0\\\frac{\partial}{\partial x_3}\\-\frac{\partial}{\partial x_2}\end{bmatrix}\frac{\exp(-\mathrm{i}kr)}{r}\\
&= -\frac{\mathrm{i}}{4\pi k}\begin{bmatrix}-\frac{\partial^2}{\partial x_2\partial x_2}-\frac{\partial^2}{\partial x_3\partial x_3}\\\frac{\partial^2}{\partial x_1\partial x_2}\\\frac{\partial}{\partial x_1\partial x_3}\end{bmatrix}\frac{\exp(-\mathrm{i}kr)}{r}.
\end{aligned} \tag{B.19}$$

Further assuming $\vec{y} = (0,0,0)$ (for other locations, the solutions can be easily obtained by the shift operation), we have

$$\frac{\partial}{\partial x_2}\frac{\exp(-\mathrm{i}kr)}{r} = \exp(-\mathrm{i}kr)\left(-\frac{\mathrm{i}kx_2}{r^2}-\frac{x_2}{r^3}\right), \tag{B.20}$$

$$\frac{\partial}{\partial x_3}\frac{\exp(-\mathrm{i}kr)}{r} = \exp(-\mathrm{i}kr)\left(-\frac{\mathrm{i}kx_3}{r^2}-\frac{x_3}{r^3}\right), \tag{B.21}$$

$$\frac{\partial^2}{\partial x_1\partial x_2}\frac{\exp(-\mathrm{i}kr)}{r} = \exp(-\mathrm{i}kr)\left(-\frac{k^2x_1x_2}{r^3}+\frac{3\mathrm{i}kx_1x_2}{r^4}+\frac{3x_1x_2}{r^5}\right), \tag{B.22}$$

$$\frac{\partial^2}{\partial x_1\partial x_3}\frac{\exp(-\mathrm{i}kr)}{r} = \exp(-\mathrm{i}kr)\left(-\frac{k^2x_1x_3}{r^3}+\frac{3\mathrm{i}kx_1x_3}{r^4}+\frac{3x_1x_3}{r^5}\right), \tag{B.23}$$

$$\frac{\partial^2}{\partial x_2\partial x_2}\frac{\exp(-\mathrm{i}kr)}{r} = \exp(-\mathrm{i}kr)\left(-\frac{\mathrm{i}k}{r^2}-\frac{k^2x_2^2+1}{r^3}+\frac{3\mathrm{i}kx_2^2}{r^4}+\frac{3x_2^2}{r^5}\right), \tag{B.24}$$

$$\frac{\partial^2}{\partial x_3 \partial x_3}\frac{\exp(-\mathrm{i}kr)}{r} = \exp(-\mathrm{i}kr)\left(-\frac{\mathrm{i}k}{r^2} - \frac{k^2x_3^2+1}{r^3} + \frac{3\mathrm{i}kx_3^2}{r^4} + \frac{3x_3^2}{r^5}\right). \tag{B.25}$$

Substitution of Eq. (B.22), Eq. (B.23), Eq. (B.24), and Eq. (B.25) into Eq. (B.19) yields

$$\vec{E}(\vec{x},\vec{0},\vec{q}_1) = -\frac{\mathrm{i}\exp(-\mathrm{i}kr)}{4\pi k}\begin{bmatrix} \frac{2\mathrm{i}k}{r^2} + \frac{k^2(x_2^2+x_3^2)+2}{r^3} - \frac{3\mathrm{i}k(x_2^2+x_3^2)}{r^4} - \frac{3x_2^2+3x_3^2}{r^5} \\ -\frac{k^2x_1x_2}{r^3} + \frac{3\mathrm{i}kx_1x_2}{r^4} + \frac{3x_1x_2}{r^5} \\ -\frac{k^2x_1x_3}{r^3} + \frac{3\mathrm{i}kx_1x_3}{r^4} + \frac{3x_1x_3}{r^5} \end{bmatrix}. \tag{B.26}$$

Correspondingly, for $\vec{q}_2 = (0,1,0)$ and $\vec{q}_3 = (0,0,1)$, we have

$$\vec{E}(\vec{x},\vec{0},\vec{q}_2) = -\frac{\mathrm{i}\exp(-\mathrm{i}kr)}{4\pi k}\begin{bmatrix} -\frac{k^2x_2x_1}{r^3} + \frac{3\mathrm{i}kx_2x_1}{r^4} + \frac{3x_2x_1}{r^5} \\ \frac{2\mathrm{i}k}{r^2} + \frac{k^2(x_1^2+x_3^2)+2}{r^3} - \frac{3\mathrm{i}k(x_1^2+x_3^2)}{r^4} - \frac{3x_1^2+3x_3^2}{r^5} \\ -\frac{k^2x_2x_3}{r^3} + \frac{3\mathrm{i}kx_2x_3}{r^4} + \frac{3x_2x_3}{r^5} \end{bmatrix}, \tag{B.27}$$

and

$$\vec{E}(\vec{x},\vec{0},\vec{q}_3) = -\frac{\mathrm{i}\exp(-\mathrm{i}kr)}{4\pi k}\begin{bmatrix} -\frac{k^2x_3x_1}{r^3} + \frac{3\mathrm{i}kx_3x_1}{r^4} + \frac{3x_3x_1}{r^5} \\ -\frac{k^2x_3x_2}{r^3} + \frac{3\mathrm{i}kx_3x_2}{r^4} + \frac{3x_3x_2}{r^5} \\ \frac{2\mathrm{i}k}{r^2} + \frac{k^2(x_1^2+x_2^2)+2}{r^3} - \frac{3\mathrm{i}k(x_1^2+x_2^2)}{r^4} - \frac{3x_1^2+3x_2^2}{r^5} \end{bmatrix}, \tag{B.28}$$

respectively.

BIBLIOGRAPHY

[1] P. Zwamborn and P. Van den Berg, "A weak form of the conjugate gradient FFT method for two-dimensional TE scattering problems," *IEEE Transactions on Microwave Theory and Techniques*, vol. 39, no. 6, pp. 953–960, 1991.

[2] J. D. Taylor, *Introduction to ultra-wideband radar systems*. Boca Raton, Florida, USA: CRC press, 1995.

[3] J. Hadamard, *Lectures on Cauchy's problem in linear partial differential equations*. Mineola, New York: Dover Publications, Inc., 2014.

[4] O. Bucci and T. Isernia, "Electromagnetic inverse scattering: Retrievable information and measurement strategies," *Radio Science*, vol. 32, no. 6, pp. 2123–2137, 1997.

[5] D. J. Daniels, *Ground penetrating radar*. London, UK: Wiley Online Library, 2005.

[6] M. G. Amin, *Through-the-wall radar imaging*. Boca Raton, FL, USA: CRC press, 2011.

[7] S. Kuroda, M. Takeuchi, and H. J. Kim, "Full-waveform inversion algorithm for interpreting crosshole radar data: A theoretical approach," *Geosciences Journal*, vol. 11, no. 3, pp. 211–217, 2007.

[8] J. R. Ernst, H. Maurer, A. G. Green, and K. Holliger, "Full-waveform inversion of crosshole radar data based on 2-D finite-difference time-domain solutions of Maxwell's equations," *IEEE Transactions on Geoscience and Remote Sensing*, vol. 45, no. 9, pp. 2807–2828, 2007.

[9] J. Virieux and S. Operto, "An overview of full-waveform inversion in exploration geophysics," *Geophysics*, vol. 74, no. 6, pp. WCC1–WCC26, 2009.

[10] N. Bleistein, J. K. Cohen, W. John Jr, *et al.*, *Mathematics of multidimensional seismic imaging, migration, and inversion*, vol. 13. New York, USA: Springer Science & Business Media, 2013.

[11] A. E. Hooper and H. N. Hambric, "Unexploded ordinance (UXO): The problem," in *Detection and identification of visually obscured targets*, Philadelphia: Taylor and Francis, 1999.

[12] F. Di Benedetto, C. Estatico, J. G. Nagy, and M. Pastorino, "Numerical linear algebra for nonlinear microwave imaging," *Electronic Transactions on Numerical Analysis*, vol. 33, pp. 105–125, Oct. 2009.

[13] L. Crocco, I. Catapano, L. Di Donato, and T. Isernia, "The linear sampling method as a way to quantitative inverse scattering," *IEEE Transactions on Antennas and Propagation*, vol. 60, no. 4, pp. 1844–1853, 2012.

[14] M. T. Bevacqua, L. Crocco, L. Di Donato, and T. Isernia, "An algebraic solution method for nonlinear inverse scattering," *IEEE Transactions on Antennas and Propagation*, vol. 63, no. 2, pp. 601–610, 2015.

[15] P. Chiappinelli, L. Crocco, T. Isernia, and V. Pascazio, "Multiresolution techniques in microwave tomography and subsurface sensing," in *International Geoscience and Remote Sensing Symposium*, vol. 5, pp. 2516–2518, IEEE, Aug. 1999.

[16] S. Caorsi, M. Donelli, D. Franceschini, and A. Massa, "A new methodology based on an iterative multiscaling for microwave imaging," *IEEE Transactions on Microwave Theory and Techniques*, vol. 51, no. 4, pp. 1162–1173, 2003.

[17] M. Donelli, G. Franceschini, A. Martini, and A. Massa, "An integrated multiscaling strategy based on a particle swarm algorithm for inverse scattering problems," *IEEE Transactions on Geoscience and Remote Sensing*, vol. 44, no. 2, pp. 298–312, 2006.

[18] M. Salucci, G. Oliveri, and A. Massa, "GPR prospecting through an inverse-scattering frequency-hopping multifocusing approach," *IEEE Transactions on Geoscience and Remote Sensing*, vol. 53, no. 12, pp. 6573–6592, 2015.

[19] M. Salucci, L. Poli, N. Anselmi, and A. Massa, "Multifrequency particle swarm optimization for enhanced multiresolution GPR microwave imaging," *IEEE Transactions on Geoscience and Remote Sensing*, vol. 55, no. 3, pp. 1305–1317, 2017.

[20] L. Li, H. Zheng, and F. Li, "Two-dimensional contrast source inversion method with phaseless data: TM case," *IEEE Transactions on Geoscience and Remote Sensing*, vol. 47, no. 6, pp. 1719–1736, 2009.

[21] M. Li, O. Semerci, and A. Abubakar, "A contrast source inversion method in the wavelet domain," *Inverse Problems*, vol. 29, no. 2, p. 025015 (19pp), 2013.

[22] M. T. Bevacqua, L. Crocco, L. Di Donato, and T. Isernia, "Non-linear inverse scattering via sparsity regularized contrast source inversion," *IEEE Transactions on Computational Imaging*, vol. 3, no. 2, pp. 296–304, 2017.

[23] E. A. Marengo, E. S. Galagarza, and R. Solimene, "Data-driven linearizing approach in inverse scattering," *Journal of the Optical Society of America A*, vol. 34, no. 9, pp. 1561–1576, 2017.

[24] M. Serhir, P. Besnier, and M. Drissi, "An accurate equivalent behavioral model of antenna radiation using a mode-matching technique based on spherical near field measurements," *IEEE Transactions on Antennas and Propagation*, vol. 56, no. 1, pp. 48–57, 2008.

[25] M. Serhir, J.-M. Geffrin, A. Litman, and P. Besnier, "Aperture antenna modeling by a finite number of elemental dipoles from spherical field measurements," *IEEE Transactions on Antennas and Propagation*, vol. 58, no. 4, pp. 1260–1268, 2010.

[26] S. Nounouh, C. Eyraud, A. Litman, and H. Tortel, "Quantitative imaging with incident field modeling from multistatic measurements on line segments," *Antennas and Wireless Propagation Letters, IEEE*, vol. 14, pp. 253–256, Sep. 2015.

[27] T. Isernia, V. Pascazio, and R. Pierri, "On the local minima in a tomographic imaging technique," *IEEE Transactions on Geoscience and Remote Sensing*, vol. 39, no. 7, pp. 1596–1607, 2001.

[28] S. Caorsi, A. Massa, and M. Pastorino, "A crack identification microwave procedure based on a genetic algorithm for nondestructive testing," *IEEE Transactions on Antennas and Propagation*, vol. 49, no. 12, pp. 1812–1820, 2001.

[29] P. Rocca, M. Benedetti, M. Donelli, D. Franceschini, and A. Massa, "Evolutionary optimization as applied to inverse scattering problems," *Inverse Problems*, vol. 25, no. 12, p. 123003 (41pp), 2009.

[30] W. Shin, "MaxwellFDFD Webpage," 2015. https://github.com/wsshin/maxwellfdfd.

[31] K. Belkebir and M. Saillard, "Special section: Testing inversion algorithms against experimental data," *Inverse Problems*, vol. 17, no. 6, pp. 1565–1571, 2001.

[32] J.-M. Geffrin, P. Sabouroux, and C. Eyraud, "Free space experimental scattering database continuation: experimental set-up and measurement precision," *Inverse Problems*, vol. 21, no. 6, pp. S117–S130, 2005.

[33] A. Taflove and S. C. Hagness, *Computational electrodynamics: The finite-difference time domain method*. Norwood, MA, USA: Artech House, 2005.

[34] P. Monk, *Finite element methods for Maxwell's equations*. Oxford, UK: Oxford University Press, 2003.

[35] W. Shin, *3D finite-difference frequency-domain method for plasmonics and nanophotonics*. PhD thesis, Stanford University, The Department of Electrical Engineering, USA, 2013.

[36] W. Shin, "FD3D Webpage," 2015. https://github.com/wsshin/fd3d.

[37] D. Colton and R. Kress, *Inverse acoustic and electromagnetic scattering theory*, vol. 93. New York, USA: Springer, 3 ed., 2013.

[38] A. N. Kolmogorov and S. V. Fomine, *Eléments de la théorie des fonctions et de l'analyse fonctionnelle*. Moscow, Russia: Éditions MIR, 1973.

[39] A. N. Tikhonov, A. S. Leonov, and A. G. Yagola, *Nonlinear ill-posed problems*. Applied Mathematical Sciences, London: Chapman & Hall, 1998.

[40] G. Oliveri, P. Rocca, and A. Massa, "A Bayesian-compressive-sampling-based inversion for imaging sparse scatterers," *IEEE Transactions on Geoscience and Remote Sensing*, vol. 49, no. 10, pp. 3993–4006, 2011.

[41] M. Bevacqua and T. Isernia, "Shape reconstruction via equivalence principles, constrained inverse source problems and sparsity promotion," *Progress In Electromagnetics Research*, vol. 158, pp. 37–48, Feb. 2017.

[42] S. Sun, B. J. Kooij, and A. G. Yarovoy, "A linear model for microwave imaging of highly conductive scatterers," *IEEE Transactions on Mcrowave Theorey and Techniques*, vol. PP, no. 99, pp. 1–16, 2017.

[43] P. Lobel, L. Blanc-Féraud, C. Pichot, and M. Barlaud, "A new regularization scheme for inverse scattering," *Inverse Problems*, vol. 13, no. 2, p. 403, 1997.

[44] C. Pichot, P. Lobel, C. Dourthe, L. Blanc-Féraud, and M. Barlaud, "Microwave inverse scattering: Quantitative reconstruction of complex permittivity for different applications," *IEICE Transactions on Electronics*, vol. 80, no. 11, pp. 1343–1348, 1997.

[45] P. M. van den Berg, A. Van Broekhoven, and A. Abubakar, "Extended contrast source inversion," *Inverse Problems*, vol. 15, no. 5, pp. 1325–1344, 1999.

[46] W. C. Chew, *Waves and fields in inhomogeneous media*, vol. 522. New York, USA: IEEE press, 1995.

[47] N. Bleistein, *Mathematical methods for wave phenomena*. New York, USA: Academic Press, 1984.

[48] A. J. Devaney, *Mathematical foundations of imaging, tomography and wavefield inversion*. New York, USA: Cambridge University Press, 2012.

[49] W. Imbriale and R. Mittra, "The two-dimensional inverse scattering problem," *IEEE Transactions on Antennas and Propagation*, vol. 18, no. 5, pp. 633–642, 1970.

[50] V. Weston and W. Boerner, "An inverse scattering technique for electromagnetic bistatic scattering," *Canadian Journal of Physics*, vol. 47, no. 11, pp. 1177–1184, 1969.

[51] A. Roger, "Newton-Kantorovitch algorithm applied to an electromagnetic inverse problem," *IEEE Transactions on Antennas and Propagation*, vol. 29, no. 2, pp. 232–238, 1981.

[52] T. Angell, D. Colton, and A. Kirsch, "The three dimensional inverse scattering problem for acoustic waves," *Journal of Differential Equations*, vol. 46, no. 1, pp. 46–58, 1982.

[53] T. Hohage, "Logarithmic convergence rates of the iteratively regularized Gauss-Newton method for an inverse potential and an inverse scattering problem," *Inverse Problems*, vol. 13, no. 5, pp. 1279–1299, 1997.

[54] F. Hettlich, "The Landweber iteration applied to inverse conductive scattering problems," *Inverse Problems*, vol. 14, no. 4, pp. 931–947, 1998.

[55] O. Ivanyshyn and R. Kress, "Nonlinear integral equations in inverse obstacle scattering," in *Mathematical methods in scattering theory and biomedical engineering*, Singapore: World Scientific, 2006.

[56] T. Johansson and B. D. Sleeman, "Reconstruction of an acoustically sound-soft obstacle from one incident field and the far-field pattern," *IMA Journal of Applied Mathematics*, vol. 72, no. 1, pp. 96–112, 2007.

[57] R. Kress and W. Rundell, "A quasi-Newton method in inverse obstacle scattering," *Inverse Problems*, vol. 10, no. 5, pp. 1145–1157, 1994.

[58] L. Mönch, "A Newton method for solving the inverse scattering problem for a sound-hard obstacle," *Inverse Problems*, vol. 12, no. 3, pp. 309–323, 1996.

[59] R. Potthast, "Fréchet differentiability of boundary integral operators in inverse acoustic scattering," *Inverse Problems*, vol. 10, no. 2, pp. 431–447, 1994.

[60] D. Colton and R. Kress, *Integral equation methods in scattering theory*. Philadelphia, PA, USA: Society for Industrial and Applied Mathematics, 2013.

[61] A. Kirsch and R. Kress, "On an integral equation of the first kind in inverse acoustic scattering," in *Inverse Problems*, pp. 93–102, Basel, Switzerland: Birkhäuser Verlag, 1986.

[62] D. Colton and P. Monk, "A novel method for solving the inverse scattering problem for time-harmonic acoustic waves in the resonance region," *SIAM Journal on Applied Mathematics*, vol. 45, no. 6, pp. 1039–1053, 1985.

[63] D. Colton and P. Monk, "A novel method for solving the inverse scattering problem for time-harmonic acoustic waves in the resonance region II," *SIAM Journal on Applied Mathematics*, vol. 46, no. 3, pp. 506–523, 1986.

[64] D. Colton and P. Monk, "The numerical solution of the three-dimensional inverse scattering problem for time harmonic acoustic waves," *SIAM Journal on Scientific and Statistical Computing*, vol. 8, no. 3, pp. 278–291, 1987.

[65] T. Angell, R. Kleinman, and G. Roach, "An inverse transmission problem for the Helmholtz equation," *Inverse Problems*, vol. 3, no. 2, pp. 149–180, 1987.

[66] R. Potthast, *Point sources and multipoles in inverse scattering theory*. London, UK: CRC Press, 2001.

[67] R. Kress, "Newton's method for inverse obstacle scattering meets the method of least squares," *Inverse Problems*, vol. 19, no. 6, pp. S91–S104, 2003.

[68] F. Cakoni, D. Colton, and P. Monk, *The linear sampling method in inverse electromagnetic scattering*. Newark, Delaware, USA: SIAM, 2011.

[69] L. Di Donato, M. T. Bevacqua, L. Crocco, and T. Isernia, "Inverse scattering via virtual experiments and contrast source regularization," *IEEE Transactions on Antennas and Propagation*, vol. 63, no. 4, pp. 1669–1677, 2015.

[70] L. Di Donato and L. Crocco, "Model-based quantitative cross-borehole GPR imaging via virtual experiments," *IEEE Transactions on Geoscience and Remote Sensing*, vol. 53, no. 8, pp. 4178–4185, 2015.

[71] L. Di Donato, R. Palmeri, G. Sorbello, T. Isernia, and L. Crocco, "A new linear distorted-wave inversion method for microwave imaging via virtual experiments," *IEEE Transactions on Microwave Theory and Techniques*, vol. 64, no. 8, pp. 2478–2488, 2016.

[72] R. Palmeri, M. T. Bevacqua, L. Crocco, T. Isernia, and L. Di Donato, "Microwave imaging via distorted iterated virtual experiments," *IEEE Transactions on Antennas and Propagation*, vol. 65, no. 2, pp. 829–838, 2017.

[73] N. Joachimowicz, C. Pichot, and J. P. Hugonin, "Inverse scattering: An iterative numerical method for electromagnetic imaging," *IEEE Transactions on Antennas and Propagation*, vol. 39, no. 12, pp. 1742–1753, 1991.

[74] K. Belkebir, J.-M. Elissalt, J.-M. Geffrin, and C. Pichot, "Newton-Kantorovich and modified gradient-inversion algorithms applied to Ipswich data," *IEEE Antennas and Propagation Magazine*, vol. 38, no. 3, p. 41, 1996.

[75] K. Belkebir, R. E. Kleinman, and C. Pichot, "Microwave imaging-Location and shape reconstruction from multifrequency scattering data," *IEEE Transactions on Microwave Theory and Techniques*, vol. 45, no. 4, pp. 469–476, 1997.

[76] P. Lobel, R. Kleinman, C. Pichot, L. Blanc-Féraud, and M. Barlaud, "Conjugate gradient method for solving inverse scattering with experimental data," *IEEE Antennas and Propagation Magazine*, vol. 38, no. 3, pp. 48–51, 1996.

[77] R. Kleinman and P. Van den Berg, "A modified gradient method for two-dimensional problems in tomography," *Journal of Computational and Applied Mathematics*, vol. 42, no. 1, pp. 17–35, 1992.

[78] R. E. Kleinman and P. den Berg, "An extended range-modified gradient technique for profile inversion," *Radio Science*, vol. 28, no. 5, pp. 877–884, 1993.

[79] R. Kleinman and P. den Berg, "Two-dimensional location and shape reconstruction," *Radio Science*, vol. 29, no. 4, pp. 1157–1169, 1994.

[80] Y. Wang and W. C. Chew, "An iterative solution of the two-dimensional electromagnetic inverse scattering problem," *International Journal of Imaging Systems and Technology*, vol. 1, no. 1, pp. 100–108, 1989.

[81] W. C. Chew and Y.-M. Wang, "Reconstruction of two-dimensional permittivity distribution using the distorted Born iterative method," *IEEE Transactions on Medical Imaging*, vol. 9, no. 2, pp. 218–225, 1990.

[82] F. Li, Q. H. Liu, and L. p. Song, "Three-dimensional reconstruction of objects buried in layered media using Born and distorted Born iterative methods," *IEEE Geoscience and Remote Sensing Letters*, vol. 1, no. 2, pp. 107–111, 2004.

[83] C. Gilmore, P. Mojabi, and J. LoVetri, "Comparison of an enhanced distorted Born iterative method and the multiplicative-regularized contrast source inversion method," *IEEE Transactions on Antennas and Propagation*, vol. 57, no. 8, pp. 2341–2351, 2009.

[84] T. Isernia, L. Crocco, and M. D'Urso, "New tools and series for forward and inverse scattering problems in lossy media," *IEEE Geoscience and Remote Sensing Letters*, vol. 1, no. 4, pp. 327–331, 2004.

[85] P. M. Van Den Berg and R. E. Kleinman, "A contrast source inversion method," *Inverse Problems*, vol. 13, no. 6, pp. 1607–1620, 1997.

[86] A. Abubakar, W. Hu, P. Van Den Berg, and T. Habashy, "A finite-difference contrast source inversion method," *Inverse Problems*, vol. 24, no. 6, p. 065004 (17pp), 2008.

[87] A. Zakaria, C. Gilmore, and J. LoVetri, "Finite-element contrast source inversion method for microwave imaging," *Inverse Problems*, vol. 26, no. 11, p. 115010 (21pp), 2010.

[88] D. Colton and P. Monk, "A new method for solving the inverse scattering problem for acoustic waves in an inhomogeneous medium," *Inverse Problems*, vol. 5, no. 6, pp. 1013–1026, 1989.

[89] D. Colton and P. Monk, "A new method for solving the inverse scattering problem for acoustic waves in an inhomogeneous medium: II," *Inverse Problems*, vol. 6, no. 6, pp. 935–947, 1990.

[90] D. Colton and P. Monk, "A comparison of two methods for solving the inverse scattering problem for acoustic waves in an inhomogeneous medium," *Journal of Computational and Applied Mathematics*, vol. 42, no. 1, pp. 5–16, 1992.

[91] C. David and P. Hähner, "Modified far field operators in inverse scattering theory," *SIAM Journal on Mathematical Analysis*, vol. 24, no. 2, pp. 365–389, 1993.

[92] D. Colton and P. Monk, "On a class of integral equations of the first kind in inverse scattering theory," *SIAM Journal on Applied Mathematics*, vol. 53, no. 3, pp. 847–860, 1993.

[93] D. Colton and P. Monk, "A modified dual space method for solving the electromagnetic inverse scattering problem for an infinite cylinder," *Inverse Problems*, vol. 10, no. 1, pp. 87–107, 1994.

[94] D. Colton and L. Päivärinta, "Far field patterns and the inverse scattering problem for electromagnetic waves in an inhomogeneous medium," in *Mathematical Proceedings of the Cambridge Philosophical Society*, vol. 103, pp. 561–575, Cambridge University Press, 1988.

[95] D. Colton and R. Kress, "Time harmonic electromagnetic waves in an inhomogeneous medium," *Proceedings of the Royal Society of Edinburgh: Section A Mathematics*, vol. 116, no. 3-4, pp. 279–293, 1990.

[96] D. Colton and A. Kirsch, "A simple method for solving inverse scattering problems in the resonance region," *Inverse Problems*, vol. 12, no. 4, pp. 383–393, 1996.

[97] D. Colton, M. Piana, and R. Potthast, "A simple method using Morozov's discrepancy principle for solving inverse scattering problems," *Inverse Problems*, vol. 13, no. 6, pp. 1477–1493, 1997.

[98] S. N. Fata and B. B. Guzina, "A linear sampling method for near-field inverse problems in elastodynamics," *Inverse Problems*, vol. 20, no. 3, pp. 713–736, 2004.

[99] I. Catapano, F. Soldovieri, and L. Crocco, "On the feasibility of the linear sampling method for 3D GPR surveys," *Progress In Electromagnetics Research*, vol. 118, pp. 185–203, Jul. 2011.

[100] A. Kirsch, "Characterization of the shape of a scattering obstacle using the spectral data of the far field operator," *Inverse Problems*, vol. 14, no. 6, pp. 1489–1512, 1998.

[101] A. Kirsch, "Factorization of the far-field operator for the inhomogeneous medium case and an application in inverse scattering theory," *Inverse Problems*, vol. 15, no. 2, pp. 413–429, 1999.

[102] R. Potthast, "Stability estimates and reconstructions in inverse acoustic scattering using singular sources," *Journal of Computational and Applied Mathematics*, vol. 114, no. 2, pp. 247–274, 2000.

[103] R. Potthast, "A new non-iterative singular sources method for the reconstruction of piecewise constant media," *Numerische Mathematik*, vol. 98, no. 4, pp. 703–730, 2004.

[104] M. Rabbani, A. Tavakoli, and M. Dehmollaian, "A hybrid quantitative method for inverse scattering of multiple dielectric objects," *IEEE Transactions on Antennas and Propagation*, vol. 64, no. 3, pp. 977–987, 2016.

[105] P. Van den Berg and A. Abubakar, "Contrast source inversion method: State of art," *Progress in Electromagnetics Research*, vol. 34, no. 11, pp. 189–218, 2001.

[106] L. Crocco, L. Di Donato, I. Catapano, and T. Isernia, "An improved simple method for imaging the shape of complex targets," *IEEE Transactions on Antennas and Propagation*, vol. 61, no. 2, pp. 843–851, 2013.

[107] F. Cakoni, H. Haddar, *et al.*, "Analysis of two linear sampling methods applied to electromagnetic imaging of buried objects," *Inverse Problems*, vol. 22, no. 3, pp. 845–867, 2006.

[108] M. Eskandari, R. Safian, and M. Dehmollaian, "Three-dimensional near-field microwave imaging using hybrid linear sampling and level set methods in a medium with compact support," *IEEE Transactions on Antennas and Propagation*, vol. 62, pp. 5117–5125, Oct. 2014.

[109] I. Catapano, L. Crocco, M. D'Urso, and T. Isernia, "On the effect of support estimation and of a new model in 2-D inverse scattering problems," *IEEE Transactions on Antennas and Propagation*, vol. 55, no. 6, pp. 1895–1899, 2007.

[110] M. Brignone, G. Bozza, A. Randazzo, M. Piana, and M. Pastorino, "A hybrid approach to 3D microwave imaging by using linear sampling and ACO," *IEEE Transactions on Antennas and Propagation*, vol. 56, no. 10, pp. 3224–3232, 2008.

[111] I. Catapano, L. Crocco, M. D'Urso, and T. Isernia, "3D microwave imaging via preliminary support reconstruction: Testing on the Fresnel 2008 database," *Inverse Problems*, vol. 25, no. 2, pp. 1–23, 2009.

[112] S. Sun, B. J. Kooij, T. Jin, and A. G. Yarovoy, "Cross-correlated contrast source inversion," *IEEE Transactions on Antennas and Propagation*, vol. 65, no. 5, pp. 2592–2603, 2017.

[113] S. Sun, B. J. Kooij, and A. G. Yarovoy, "Inversion of multi-frequency data with the cross-correlated contrast source inversion method," *Radio Science*, 2017. submitted.

[114] R. P. Brent, *Algorithms for minimization without derivatives*. New Jersey, USA: Englewood Cliffs, 1973.

[115] G. E. Forsythe, M. A. Malcolm, and C. B. Moler, *Computer methods for mathematical computations*. Englewood Cliffs, NJ, USA: Prentice-Hall, 1976.

[116] T. M. Habashy, M. L. Oristaglio, and A. T. Hoop, "Simultaneous nonlinear reconstruction of two-dimensional permittivity and conductivity," *Radio Science*, vol. 29, no. 4, pp. 1101–1118, 1994.

[117] K. Belkebir and A. Tijhuis, "Using multiple frequency information in the iterative solution of a two-dimensional nonlinear inverse problem," in *Proceedings Progress in Electromagnetics Research Symposium (PIERS)*, p. 353, University of Innsbruck, 1996.

[118] A. Litman, D. Lesselier, and F. Santosa, "Reconstruction of a two-dimensional binary obstacle by controlled evolution of a level-set," *Inverse Problems*, vol. 14, no. 3, pp. 685–706, 1998.

[119] P. M. van den Berg, A. Abubakar, and J. T. Fokkema, "Multiplicative regularization for contrast profile inversion," *Radio Science*, vol. 38, no. 2, pp. 1–10, 2003.

[120] R. F. Bloemenkamp, A. Abubakar, and P. M. Van Den Berg, "Inversion of experimental multi-frequency data using the contrast source inversion method," *Inverse Problems*, vol. 17, no. 6, pp. 1611–1622, 2001.

[121] L. I. Rudin, S. Osher, and E. Fatemi, "Nonlinear total variation based noise removal algorithms," *Physica D: Nonlinear Phenomena*, vol. 60, no. 1, pp. 259–268, 1992.

[122] O. M. Bucci, N. Cardace, L. Crocco, and T. Isernia, "2D inverse scattering: degree of nonlinearity, solution strategies, and polarization effects," in *Image Reconstruction from Incomplete Data*, vol. 4123, pp. 185–194, International Society for Optics and Photonics, Nov. 2000.

[123] E. Le Brusq, I. Aliferis, J. Dauvignac, and C. Pichot, "Iterative nonlinear reconstruction of isotropic and anisotropic 2D objects using TE and TM polarizations," in *International Symposium on Electromagnetic Theory, Pisa, Italy*, pp. 703–705, May. 2004.

[124] E. Le Brusq, J. Dauvignac, I. Aliferis, C. Pichot, and X. Derobert, "Experimental detection and theoretical reconstruction of cylindrical cross-section objects using TM, TE and cascaded TM-TE polarizations: Applications to pipes," *Progress in Electromagnetics Research Symposium (PIERS2004), Pisa, Italy*, p. 658, Mar. 2004.

[125] S. Sun, B. J. Kooij, T. Jin, and A. G. Yarovoy, "Simultaneous TE and TM polarization inversion based on FDFD and frequency hopping scheme in ground penetrating radar," in *8th International Workshop on Advanced Ground Penetrating Radar (IWAGPR)*, pp. 1–5, IEEE, Jul. 2015.

[126] E. J. Candès, J. Romberg, and T. Tao, "Robust uncertainty principles: Exact signal reconstruction from highly incomplete frequency information," *IEEE Transactions on Information Theory*, vol. 52, no. 2, pp. 489–509, 2006.

[127] E. Van Den Berg and M. P. Friedlander, "Theoretical and empirical results for recovery from multiple measurements," *IEEE Transactions on Information Theory*, vol. 56, no. 5, pp. 2516–2527, 2010.

[128] E. van den Berg and M. P. Friedlander, "Probing the Pareto frontier for basis pursuit solutions," *SIAM Journal on Scientific Computing*, vol. 31, no. 2, pp. 890–912, 2008.

[129] E. Van den Berg and M. P. Friedlander, "Sparse optimization with least-squares constraints," *SIAM Journal on Optimization*, vol. 21, no. 4, pp. 1201–1229, 2011.

[130] S. Sun, G. Zhu, and T. Jin, "Novel methods to accelerate CS radar imaging by NUFFT," *IEEE Transactions on Geoscience and Remote Sensing*, vol. 53, no. 1, pp. 557–566, 2015.

[131] R. Tibshirani, "Regression shrinkage and selection via the lasso," *Journal of the Royal Statistical Society, Series B (Methodological)*, vol. 58, no. 1, pp. 267–288, 1996.

[132] E. G. Birgin, J. M. Martínez, and M. Raydan, "Nonmonotone spectral projected gradient methods on convex sets," *SIAM Journal on Optimization*, vol. 10, no. 4, pp. 1196–1211, 2000.

[133] E. G. Birgin, J. M. Martínez, and M. Raydan, "Inexact spectral projected gradient methods on convex sets," *IMA Journal of Numerical Analysis*, vol. 23, no. 4, pp. 539–559, 2003.

[134] Y.-H. Dai and R. Fletcher, "Projected Barzilai-Borwein methods for large-scale box-constrained quadratic programming," *Numerische Mathematik*, vol. 100, no. 1, pp. 21–47, 2005.

[135] E. van den Berg, *Convex optimization for generalized sparse recovery*. PhD thesis, University of British Columbia, 2009.

[136] R. T. Rockafellar, *Convex analysis, volume 28 of Princeton mathematics series*. Princeton, NJ, USA: Princeton University Press, 1970.

[137] S. Boyd and L. Vandenberghe, *Convex optimization*. New York, USA: Cambridge University Press, 2004.

[138] R. Ward, "Compressed sensing with cross validation," *IEEE Transactions on Information Theory*, vol. 55, no. 12, pp. 5773–5782, 2009.

[139] J. Zhang, L. Chen, P. T. Boufounos, and Y. Gu, "Cross validation in compressive sensing and its application of OMP-CV algorithm," *arXiv preprint arXiv:1602.06373*, 2016.

[140] I. Catapano, L. Crocco, and T. Isernia, "On simple methods for shape reconstruction of unknown scatterers," *IEEE Transactions on Antennas and Propagation*, vol. 55, no. 5, pp. 1431–1436, 2007.

[141] S. Sun, B. J. Kooij, and A. G. Yarovoy, "Linearized three-dimensional electromagnetic contrast source inversion and its applications to half-space configurations," *IEEE Transactions on Geoscience and Remote Sensing*, vol. 55, no. 6, pp. 3475–3487, 2017.

[142] S. Caorsi, G. L. Gragnani, and M. Pastorino, "Two-dimensional microwave imaging by a numerical inverse scattering solution," *IEEE Transactions on Microwave Theory and Techniques*, vol. 38, no. 8, pp. 981–980, 1990.

[143] S. Caorsi, G. L. Gragnani, and M. Pastorino, "A multiview microwave imaging system for two-dimensional penetrable objects," *IEEE Transactions on Microwave Theory and Techniques*, vol. 39, no. 5, pp. 845–851, 1991.

[144] S. Caorsi, G. L. Gragnani, and M. Pastorino, "Numerical solution to three-dimensional inverse scattering for dielectric reconstruction purposes," *IEE Proceedings H - Microwaves, Antennas and Propagation*, vol. 139, no. 1, pp. 45–52, 1992.

[145] W. C. Chew, Y. M. Wang, G. Otto, D. Lesselier, and J. C. Bolomey, "On the inverse source method of solving inverse scattering problems," *Inverse Problems*, vol. 10, no. 3, pp. 547–553, 1994.

[146] S. Sun, B. J. Kooij, A. G. Yarovoy, and T. Jin, "A linear method for shape reconstruction based on the generalized multiple measurement vectors model," *IEEE Transactions on Antennas and Propagation*, 2017. (submitted).

[147] R. Heckel and H. Bölcskei, "Joint sparsity with different measurement matrices," in *50th Annual Allerton Conference on Communication, Control, and Computing (Allerton)*, pp. 698–702, IEEE, Oct. 2012.

[148] O. Lee, J. M. Kim, Y. Bresler, and J. C. Ye, "Compressive diffuse optical tomography: Noniterative exact reconstruction using joint sparsity," *IEEE Transactions on Medical Imaging*, vol. 30, no. 5, pp. 1129–1142, 2011.

[149] J. Chen and X. Huo, "Theoretical results on sparse representations of multiple-measurement vectors," *IEEE Transactions on Signal Processing*, vol. 54, no. 12, pp. 4634–4643, 2006.

[150] M. E. Davies and Y. C. Eldar, "Rank awareness in joint sparse recovery," *IEEE Transactions on Information Theory*, vol. 58, no. 2, pp. 1135–1146, 2012.

[151] I. Catapano, L. Crocco, and T. Isernia, "Improved sampling methods for shape reconstruction of 3-D buried targets," *IEEE Transactions on Geoscience and Remote Sensing*, vol. 46, no. 10, pp. 3265–3273, 2008.

[152] L. Borcea, V. Druskin, A. V. Mamonov, and M. Zaslavsky, "Untangling nonlinearity in inverse scattering with data-driven reduced order models," *arXiv preprint arXiv:1704.08375*, 2017.

[153] S. Sun, B. J. Kooij, and A. G. Yarovoy, "Solving the PEC inverse scattering problem with a linear model," in *URSI International Symposium on Electromagnetic Theory (EMTS)*, pp. 144–147, Aug. 2016.

[154] S. Sun, B. J. Kooij, and A. G. Yarovoy, "Processing the experimental Fresnel data by the GMMV-based shape reconstruction method," in *International Conference on Electromagnetics in Advanced Applications (ICEAA)*, pp. 1–4, Sep. 2017.

ACRONYMS

2-D	2-Dimensional.
3-D	3-Dimensional.
BIM	Born Iterative Method.
BP$_{\tilde{\sigma}}$	Basis Pursuit Denoise.
CC-CSI	Cross-Correlated Contrast Source Inversion.
CG	Conjugate Gradient.
CS	Compressive Sensing.
CS-EB	Contrast Source Extended Born.
CSI	Contrast Source Inversion.
CT	Computed Tomography.
CV	Cross-Validation.
CWD	Concealed Weapon Detection.
DBIM	Distorted Born Iterative Method.
EFIE	Electric Field Integral Equation.
EM	ElectroMagnetic.
FD	Finite Defference.
FDFD	Finite Difference Frequency Domain.
FE	Finite Element.
GMMV	Generalized Multiple Measurement Vectors.
GPR	Ground Penetrating Radar.
LS$_\tau$	Lasso.
LSM	Linear Sampling Method.
LU	Lower Upper.
MF-CC-CSI	Multi-Frequency Cross-Correlated Contrast Source Inversion.
MF-MR-CSI	Multi-Frequency Multiplicative Regularized Contrast Source Inversion.
MG	Modified Gradient.
MMV	Multiple Measurement Vectors.
MR-CSI	Multiplicative Regularized Contrast Source Inversion.

MRI Magnetic Resonance Imaging.
MUSIC MUltiple SIgnal Classification.

NK Newton-Kantorovich.

PBC Periodic Boundary Condition.
PML Perfectly Matched Layer.

ROI Region Of Interest.

SMV Single Measurement Vector.
SNR Signal to Noise Ratio.
SPG Spectral Projected Gradient.
SPGL1 Spectral Projected Gradient for ℓ_1-norm minimization.
SVD Singular Value Decomposition.

TE Transverse Electric.
TM Transverse Magnetic.
TV Total Variation.
TWI Through-the-Wall Imaging.

SUMMARY

The inverse scattering problem is inherently nonlinear and improperly posed. Relevant study, such as the existence and uniqueness of the solution, the completeness of the far field pattern, etc., involves an abstruse mathematical theory. In our daily life, the inversion techniques play a significant role in areas such as radar, sonar, geophysical exploration, medical imaging and nondestructive testing. This thesis is focused on the qualitative and quantitative reconstruction of shape and medium parameters of scattering objects in electromagnetic inverse scattering theory.

The major contributions of this thesis are 1) the proposal of a novel cross-correlated error term and 2) the proposal of the sum-of-norm regularized reconstruction algorithm. The significance of the former lies in the fact that the proposed error term fills up a gap hidden in the classical "state error + data error" cost functional. In the optimization approaches, the data error term tends to recover the unknown properties of the objects directly from the measurement data, while the state error term attempts to ensure that the recovered results satisfy Maxwell's equations in the field domain. In other words, the solution must behave well in both the measurement domain and the field domain. However, there is still a gap in between because the minor mismatch in the field domain is not monitored in the measurement domain. The proposed cross-correlated error is a constraint which tends to get the mismatch in the field domain under control in the measurement domain. Therefore, one can say that this novel error term revolutionizes the formulation of the minimization functional of inversion techniques based on optimization theory. The significance of the latter is that the proposed reconstruction scheme enables us to excavate the joint information hidden in the formulation of multiple inverse source problems, without any significant additional computational effort.

Although the sum-of-norm regularization is not necessarily the best regularization constraint for some complicated scatterers, it demonstrates at least two points: 1) for an inverse source problem, benefits can be obtained from use of different incident fields; 2) the sum-of-norm regularization brings better resolving ability due to the joint processing of the multiple contrast source vectors.

The research results in this thesis are also applicable to the acoustic inverse scattering problems. Application of the qualitative and quantitative reconstruction approaches developed in this thesis to the experimental data in different areas of wave-field inversion would be very interesting as future work.

SAMENVATTING

Het inverse verstrooiingsprobleem is inherent niet-lineair en onvolledig gesteld. Relevante studie, zoals het bestaan en de uniciteit van de oplossing, de volledigheid van het verre veldpatroon, enz., behelst een ingewikkelde onderliggende wiskundige theorie. In ons dagelijks leven spelen inversietechnieken een belangrijke rol op gebieden zoals radar, sonar, geofysische exploratie, medische beeldvorming en niet-destructief testen. Dit proefschrift richt zich op de kwalitatieve en kwantitatieve reconstructie van de geometrische vorm en medium parameters van verstrooiings-objecten in de elektromagnetische inverse verstrooiingstheorie.

De belangrijkste bijdragen van dit proefschrift zijn 1) de introductie van een nieuwe "cross-correlated error" term en 2) de introductie van het "sum-of-norm" geregulariseerde reconstructie algoritme. De betekenis van de eerste ligt in het feit dat de voorgestelde foutterm een aanvulling vormt op de vrijheidsgraad die verborgen zit in de klassieke "state error + data error" functionaal. In de optimaliseringsbenaderingen heeft de "data error" term de neiging om de onbekende eigenschappen van de objecten direct uit de meetgegevens aan te passen, terwijl de "state error" term tracht te waarborgen dat de herstelde resultaten voldoen aan Maxwell's vergelijkingen in het velddomein. Met andere woorden, de oplossing moet zowel in het meetdomein als in het velddomein een geschikte oplossing zijn. Er is echter nog steeds een vrijheidsgraad, omdat een kleine mismatch in het velddomein niet is gerelateerd in het meetdomein. De voorgestelde "cross-correlated error" is een begrenzing die het effect heeft de mismatch in het velddomein onder controle te krijgen in het meetdomein. Daarom kunnen we zeggen dat deze nieuwe foutterm een omwenteling teweegbrengt in de formulering van de minimalisatie functionaal in inversietechnieken op basis van de optimalisatietheorie. Het belang van het laatste is dat het voorgestelde reconstructie schema ons in staat stelt om de gezamenlijke informatie die verborgen is in de formulering van meerdere inverse bronproblemen op te diepen, zonder enige significante additionele rekenkracht.

Hoewel de "sum-of-norm" regularisatie niet noodzakelijkerwijs de beste regularisatiebegrenzing is voor sommige gecompliceerde verstrooiers, vertoont deze ten minste twee verbeteringspunten: 1) voor een invers bronprobleem kunnen voordelen worden verkregen door het gebruik van verschillende invallende velden; 2) de "sum-of-norm" regularisatie leidt tot een beter oplossend vermogen als gevolg van de gezamenlijke verwerking van de meervoudige contrastbronvectoren.

De onderzoeks-resultaten in dit proefschrift zijn ook van toepassing op akoestische inverse verstrooiingsproblemen. Toepassing van de kwalitatieve en kwantitatieve reconstructie technieken die in dit proefschrift zijn ontwikkeld op de experimentele data in andere gebieden van de inversie van golfvelden zou zeer interessant zijn als toekomstig onderzoekswerk.

ACKNOWLEDGEMENTS

This thesis concludes four years of my research in the Microwave Sensing, Signals and Systems (MS3) group. I would like to express my gratitude to those who have given their support during my Ph.D. study.

My utmost gratitude first goes to my promotor, Prof. Alexander Yarovoy, who offered me the opportunity to conduct this Ph.D. research. In retrospect, I would not forget his repeated revision to my slides and the encouragement in his eyes when I stepped onto the stage in a conference. Nor would I forget his constant push just at the right time without making me stressful and the merriment from the bottom of his heart every time I have made a small step forward. I appreciate every talk with him in which he always generously shared his knowledge and ideas with an open mind. I am also very grateful to my daily supervisor, Dr. Bert Jan Kooij. It was a casual and short chat with him in the corridor that made me decide to switch to this research topic without hesitation. A few days later, he became my daily supervisor. I came to find that he is always kind and warm as a friend and family. I benefit a lot from his guidance in all aspects of my research. It has been so enjoyable and fruitful working with him.

I would like to thank my dear former and present colleagues from MS3 group for the happy time I have spent with everyone: Oleg Krasnov, Pascal Aubry, Dinh Tran, Fred van der Zwan, Hans Driessen, Peter Swart, Tian Jin, Sakamoto Takuya, Faruk Uysal, Zhenhai Xu, Yuan He, Inna Ivashko, Nadia Haider, Alexey Narykov, Teun de Groot, Fotios Katsilieris, Dmitriy Penkin, Jianping Wang, Harun Cetinkaya, Nikita Petrov, Albert Oude Nijhuis, Shravan Shirodkar, Iraklis Giannakis, Nikola Bogdanović, Sharef Neemat, Arun Muraleedharan, Shengzhi Xu, Jan Puskely, Rossiza Gourova, Yanki Aslan, Nannan Chen, Max Schöpe, Minaksie Ramsoekh. Particular thanks to Minke van der Put for her kind help in dealing with lots of administrative issues and Etienne Goossens for assisting me to run the 3-D inversion program on the server. I would also like to thank Dr. Wonseok Shin for his patient and unconditional support via emails in the use of his electromagnetic scattering solver package. I would like to extend my gratitude to my committee members: Prof. dr. T. Isernia, Prof. dr. C. Pichot, Prof. ir. F. le Chevalier, Prof. dr. ir. E. C. Slob, Prof. dr. ir. C. P. A. Wapenaar, for their thorough reviews and precious comments towards the improvement of this thesis.

I am grateful in particular to my dear brothers: Xiaozhe Wang, Haicheng Liu, Chuan Lin, Shuo Li, for turning our apartment into a cozy home where I have been living during the four years of my entire Ph.D. career. Thanks also to all my friends in or not in The Netherlands. I hope that all of them will know how much they have influenced this thesis even if I could not list everyone here.

Last but not the least, I am indebted to my parents for their unconditional love and support during all the years of my studying abroad. Nothing else that can be dedicated to you so far except this thesis. Love you forever!

Shilong Sun
Delft, 12 December 2017

List of Publications

Journal Papers

1. **S. Sun**, G. Zhu, and T. Jin, "Novel methods to accelerate CS radar imaging by NUFFT," *IEEE Transactions on Geoscience and Remote Sensing*, vol. 53, no. 1, pp. 557–566, 2015

2. **S. Sun**, B. J. Kooij, T. Jin, and A. G. Yarovoy, "Cross-correlated contrast source inversion," *IEEE Transactions on Antennas and Propagation*, vol. 65, no. 5, pp. 2592–2603, 2017

3. **S. Sun**, B. J. Kooij, and A. G. Yarovoy, "A linear model for microwave imaging of highly conductive scatterers," *IEEE Transactions on Microwave Theory and Techniques*, vol. PP, no. 99, pp. 1–16, 2017

4. **S. Sun**, B. J. Kooij, and A. G. Yarovoy, "Linearized 3-D electromagnetic contrast source inversion and its applications to half-space configurations," *IEEE Transactions on Geoscience and Remote Sensing*, vol. 55, no. 6, pp. 3475–3487, 2017

5. **S. Sun**, B. J. Kooij, A. G. Yarovoy, and T. Jin, "A linear method for shape reconstruction based on the generalized multiple measurement vectors model," *IEEE Transactions on Antennas and Propagation*, 2017. (submitted)

6. **S. Sun**, B. J. Kooij, and A. G. Yarovoy, "Extension of the GMMV-based linear method to quantitative inverse scattering," *IEEE Antennas and Wireless Propagation Letters*, vol. 17, no. 1, pp. 94–97, 2018

7. **S. Sun**, B. J. Kooij, and A. G. Yarovoy, "Inversion of multi-frequency data with the cross-correlated contrast source inversion method," *Radio Science*, 2017. (submitted)

Conferences Papers

1. **S. Sun**, B. J. Kooij, T. Jin, and A. G. Yarovoy, "Simultaneous multi-frequency TE/TM polarization inversion based on FDFD for ground penetrating radar," in *2015 8th International Workshop on Advanced Ground Penetrating Radar (IWAGPR)*, pp. 1–5, Jul. 2015

2. **S. Sun**, B. J. Kooij, T. Jin, and A. G. Yarovoy, "Through-wall imaging by TE and TM hybrid polarization inversion based on FDFD and frequency hopping scheme," in *IET International Radar Conference 2015*, pp. 1–4, Oct. 2015 (**Best Paper Award**)

3. T. Jin, **S. Sun**, and A. G. Yarovoy, "A generalized electromagnetic wave penetrating propagation model for CS imaging in through-the-wall radar," in *IET International Radar Conference 2015*, IET, Oct. 2015

4. **S. Sun**, B. J. Kooij, and A. G. Yarovoy, "Solving the PEC inverse scattering problem with a linear model," in *URSI International Symposium on Electromagnetic Theory (EMTS)*, pp. 144–147, Aug. 2016

5. X. Wang, **S. Sun**, J. Wang, A. G. Yarovoy, B. Neducza, and G. Manacorda, "Real GPR signal processing for target recognition with circular array antennas," in *2016 URSI International Symposium on Electromagnetic Theory (EMTS)*, pp. 818–821, Aug. 2016

6. **S. Sun**, B. J. Kooij, and A. G. Yarovoy, "Processing the experimental Fresnel data by the GMMV-based shape reconstruction method," in *International Conference on Electromagnetics in Advanced Applications (ICEAA)*, pp. 1–4, Sep. 2017

About the Author

Shilong Sun was born in Zhangqiu, Shandong, China, in 1988. He received the B.S. and M.S. degrees in information and communication engineering from the National University of Defense Technology, Changsha, China, in 2011 and 2013, respectively.

He joined the Microwave Sensing, Signals and Systems group, Delft University of Technology (The Netherlands) in 2013, where he started working towards his Ph.D. degree in the field of electromagnetic inverse scattering problems.